Single Neuron Dynamics — Models Linking Theory and Experiment

Jan Benda

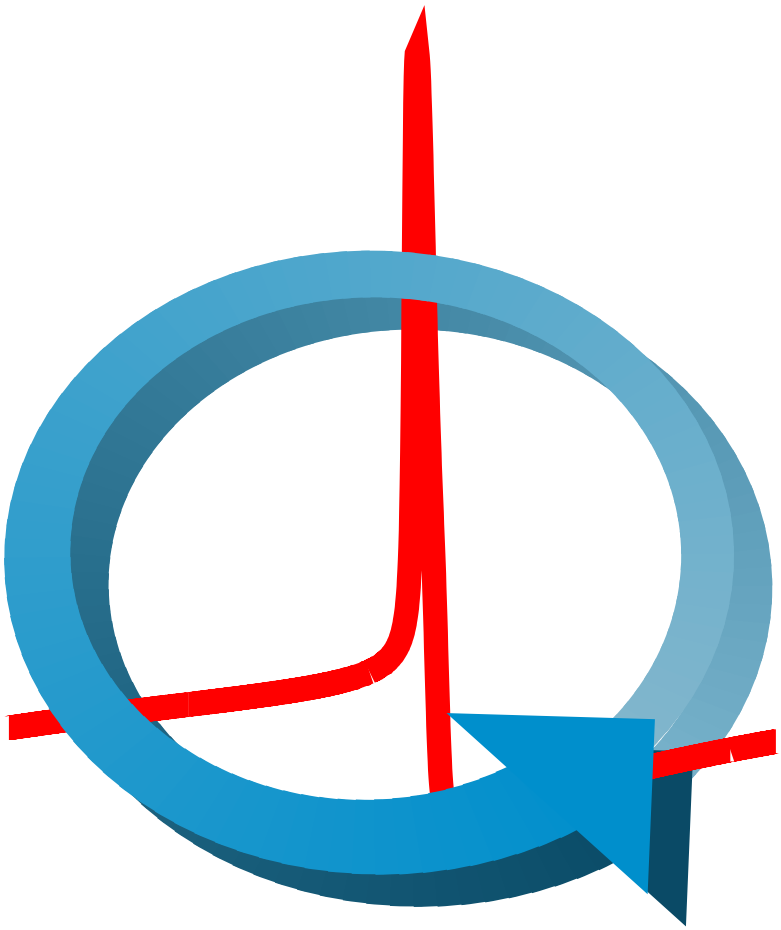

Single Neuron Dynamics — Models Linking Theory and Experiment

D I S S E R T A T I O N

zur Erlangung des akademischen Grades
doctor rerum naturalium
(Dr. rer. nat.)
im Fach Biophysik

eingereicht an der
Mathematisch-Naturwissenschaftlichen Fakultät I
der Humboldt-Universität zu Berlin

von
Herrn Dipl.-Phys. Jan Benda
geboren am 2.12.1970 in Freiburg i. Br.

Präsident der Humboldt-Universität zu Berlin:
Prof. Dr. Jürgen Mlynek

Dekan der Mathematisch-Naturwissenschaftlichen Fakultät I:
Prof. Dr. Bernhard Ronacher

Gutachter:

1. Prof. Dr. Andreas V.M. Herz
2. Prof. Dr. Klaus Pawelzik
3. Prof. Dr. Martin Egelhaaf

Tag der mündlichen Prüfung: 18. Januar 2002

Contents

Contents **I**

List of Figures **III**

List of Tables **VII**

List of Symbols **IX**

1 Introduction **1**

I Theory **5**

2 Spiking Neurons **7**
2.1 Conductance-based models 9
2.2 Time scales of neural dynamics 13
2.3 Reduction of the number of dynamical variables 13
2.4 Class-I versus class-II neurons 19
2.5 Summary 27

3 Modeling Spikes **29**
3.1 Firing frequency as a phase velocity 32
3.2 More about phase velocities 39
3.3 Saddle-node bifurcation and the θ-model 44
3.4 Oscillations and phase-resetting curves 48
3.5 Phase oscillators in the sub-threshold regime 52
3.6 Outlook: Two-dimensional models 56
3.7 Discussion 58
3.8 Summary 60

4 Spike-Frequency Adaptation **61**
4.1 From channels to firing frequency 65
4.2 Defining the parameters of the adaptation models 78
4.3 Signal transmission properties 83
4.4 Combination with spike-generator 93
4.5 Discussion 94
4.6 Summary 100

5 Spike-Train Analysis **103**
5.1 Local interspike-interval distribution . . . 104
5.2 Spike jitter and precision . . . 107
5.3 Summary . . . 111

II Experiments **113**

6 Auditory Receptor Neurons of Locusts **115**
6.1 Introduction . . . 116
6.2 Methods . . . 117
6.3 Results . . . 121
6.4 Discussion . . . 131
6.5 Summary . . . 136

7 Intensity invariance in an auditory interneuron **137**
7.1 Introduction . . . 138
7.2 Methods . . . 140
7.3 Results . . . 146
7.4 Discussion . . . 153
7.5 Summary . . . 158

8 Conclusion **159**

A Conductance-Based Models **163**
A–1 Hodgkin-Huxley model . . . 163
A–2 Traub-Miles model . . . 164
A–3 Modified Traub-Miles model . . . 165
A–4 Connor model . . . 166
A–5 Crook model . . . 167

B Deutschsprachige Zusammenfassung **169**
B–1 Einleitung . . . 169
B–2 Spikende Neurone . . . 169
B–3 Modellierung spikender Neurone . . . 170
B–4 Dynamik der Feuerraten-Adaptation . . . 170
B–5 Analyse von Spike-Folgen . . . 170
B–6 Auditorische Rezeptorneurone von Heuschrecken . . . 171
B–7 Intensitätsinvarianz eines auditorischen Interneurons . . . 171
B–8 Schlußfolgerung . . . 171
B–9 Leitfähigkeitsmodelle . . . 171

Bibliography **173**

Acknowledgments **183**

List of Figures

1.1 The language of neurons. 2
1.2 Male of the grasshopper *Chortippus biguttulus*. 4

2.1 Signal flow in a neuron. 9
2.2 Ion currents through channels in the cell membrane. 10
2.3 The current-voltage relation for sodium and potassium ions. 11
2.4 A spike simulated by the Hodgkin-Huxley model. 12
2.5 Time constants of various gating variables. 14
2.6 Equivalent potentials. 15
2.7 The reduced Hodgkin-Huxley model. 17
2.8 Repetitive spiking in class-I and class-II model neurons. 18
2.9 f-I-curves of class-I and class-II model neurons. 19
2.10 Latencies of class-I and class-II model neurons. 20
2.11 Phase shift of a periodically spiking neuron. 21
2.12 Phase-resetting curves. 21
2.13 Saddle-node bifurcation. 22
2.14 Saddle-node bifurcation in a class-I neuron (Traub-Miles). 22
2.15 Supercritical Hopf bifurcation. 23
2.16 Hopf bifurcation in a class-II neuron (Hodgkin-Huxley). 23
2.17 Spike clustering in a noisy class-II neuron. 24
2.18 Limit cycles for different input currents I. 25
2.19 Amplitudes of spikes. 26

3.1 Modeling the generation of spikes. 31
3.2 Spikes and oscillations. 32
3.3 Limit cycle of an oscillation. 32
3.4 Stimuli used to test the phase models. 34
3.5 Comparison of a phase oscillator with the Traub-Miles model. 35
3.6 Performance of the non-leaky phase oscillator. 36
3.7 Low-pass filter effect of the spike generator. 37
3.8 Transfer function of the non-leaky phase oscillator. 38
3.9 Phase angles on limit cycles. 40
3.10 Transformed phase angles in conductance-based models. 41
3.11 Properties of the leaky phase oscillator. 42
3.12 Performance of the leaky phase oscillator. 43
3.13 f-I-curves of integrate-&-fire neurons. 44
3.14 Square-root f-I-curves. 45
3.15 Properties of the modified θ-model. 46
3.16 Performance of the θ-model. 47

3.17 Response functions of the phase models. 49
3.18 Response functions of two class-I neuron models. 51
3.19 Performance of the θ-model for stimuli close to threshold. 52
3.20 Latencies in relation to the corresponding interspike intervals. 53
3.21 Resting phases calculated from latencies. 54
3.22 Fixed points and limit cycles. 55
3.23 Transformation to a two-dimensional phase model. 56

4.1 Different mechanisms of spike-frequency adaptation. 63
4.2 The phenomenon of spike-frequency adaptation. 65
4.3 f-I-curves and time constants of an adapting neuron. 66
4.4 The dynamics of an adaptation current. 68
4.5 Averaging the membrane potential. 69
4.6 Properties of the M-type-current gating variable. 70
4.7 Averaging the dynamics of the M-type current gating-variable. 72
4.8 Encoder adaptation for two different transduction functions $g(J)$. 76
4.9 The depressing synapse. 79
4.10 Recovery from adaptation. 81
4.11 Time constants of encoder and transducer adaptation. 82
4.12 Adapted f-I-curves. 84
4.13 Linearization of the steady-state f-I-curve. 86
4.14 Influence of the $\gamma(f)$-term on f-I-curves. 87
4.15 Transfer function of adaptation. 89
4.16 Time-derivative detection. 91
4.17 Suppression of background noise by adaptation. 92

5.1 The local *ISI*-distribution. 106
5.2 Measures of spike-jitter. 109
5.3 Firing frequency, spike jitter, precision and firing rate. 110

6.1 Measuring the threshold-curve of an auditory receptor neuron. 118
6.2 Sigmoidal functions used to fit the f-I-curves. 119
6.3 f-I-curves and latencies of low-frequency receptors. 122
6.4 Adaptation time-constants of a low-frequency receptor. 124
6.5 Measuring an adapted f-I-curve. 125
6.6 Adapted f-I-curves of receptor neurons. 126
6.7 Phase-resetting curves of a low-frequency receptor. 127
6.8 Performance of the adaptation model for a white-noise stimulus. 128
6.9 The adaptation model and the smoothing effect of the spike dynamics. . 129
6.10 Performance of the adaptation model for calling songs. 130
6.11 Distribution of stimulus amplitudes compared to the neuron's f-I-curve. 131

7.1 The auditory system of crickets. 139
7.2 Response of an AN1 to constant stimulation. 141
7.3 Responses of an AN1 to different intensities. 142
7.4 f-I-curves of an AN1. 143
7.5 Measuring an adapted f-I-curve. 144
7.6 Time constants of adaptation. 146
7.7 Adapted f-I-curves. 147

7.8 Compression of adapted f-I-curves. 148
7.9 Intensity invariance. 149
7.10 Relative modulation depths for different intensities. 150
7.11 Performance of the adaptation model. 151
7.12 Model performance for white-noise stimuli. 152
7.13 Model performance for pulse patterns. 152
7.14 The amplitude of the transfer function of an AN1. 153
7.15 Adaptation to repeated pulses. 157

List of Tables

2.1 Properties of class-I and class-II neurons. 27

4.1 Encoder and transducer adaptation. 101

6.1 Properties of f-I-curves of low-frequency receptor neurons. 123

7.1 Properties of f-I-curves of the AN1. 145

List of Symbols

This is a summary of symbols, which are used frequently in this thesis. Many symbols appearing only in one section are not included.

symbol	dimension	description	chapter	page
t	ms	time		
V	mV	membrane potential	2	9
g	$\mathrm{mS/cm^2}$	conductance of a population of ion channels	2	10
E	mV	reversal potential of an ionic current	2	10
C	$\mu\mathrm{F/cm^2}$	membrane capacitance	2	11
I	$\mu\mathrm{A/cm^2}$	input current	2	11
m	1	activation variable (of sodium current)	2	12
h	1	inactivation variable (of sodium current)	2	12
x	1	arbitrary gating variable	2	14
$\tau_x(V)$	ms	time constant of gating variable x	2	12
$x_\infty(V)$	1	steady-state variable of gating variable x	2	12
V_x	mV	equivalent potential of gating variable x	2	14
U	mV	representative potential of recovery variables	2	16
T	ms	interspike interval (ISI)	2	18
f	Hz	firing frequency	2	20
$f(I)$	Hz	f-I-curve	2	20
Δt	ms	latency to first spike after stimulus onset	2	18
T_0	ms	unperturbed interspike interval	2	21
φ	1	phase of a perturbation	2	21
$\Delta\varphi$	1	resulting phase shift	2	21
$\Delta\varphi(\varphi)$	1	phase-resetting curve	2	21
φ	1	phase angle $0 \leq \varphi < 1$	3	33
$\dot{\varphi}$	Hz	phase velocity	3	33
ψ	1	phase angle $\sim$ time	3	40
ΔI	–	perturbation of the input I	3	48
$Z(\varphi)$	$1/[\Delta I]$	response function depending on arbitrary φ	3	48
$z(t)$	$1/[\Delta I]$	response function depending on time t	3	49
ν	Hz	measureable firing frequency	3	38
θ	1	phase angle $-\pi \leq \theta < \pi$	3	45
μ	$\mu\mathrm{A/cm^2}$	mean of Gaussian white-noise input	3	34
σ	$\mu\mathrm{A/cm^2}$	standard deviation of Gaussian white-noise input	3	34
f_c	Hz	cut-off frequency of Gaussian white-noise input	3	34
I_{th}	$\mu\mathrm{A/cm^2}$	threshold current of f-I-curve	3	31
$f_0(I)$	Hz	onset f-I-curve	4	66

symbol	dimension	description	chapter	page
$f_\infty(I)$	Hz	steady-state f-I-curve	4	66
$f(I,A)$	Hz	adapted f-I-curve	4	84
I	–	input (general), or input current	4	63
J	–	physical stimulus	4	63
$p(T)$	1/ms	true distribution of interspike intervals	5	105
$\tilde{p}(T)$	1/ms	distribution of interspike intervals over time t	5	105
r	Hz	firing rate as spikes per time bin	5	107
σ_J	ms	spike jitter	5	108
π	Hz	spike precision	5	109
λ	ms	latency of the system	6	120
f_{exp}	Hz	experimentally measured firing frequency	6	121
σ_{exp}	Hz	modulation depth of the measured firing frequency	6	121
σ_{diff}	Hz	mean squared difference of f_{exp} and the predicted firing frequency from a model	6	121
p.e.	%	prediction error	6	121

1

Introduction

"Biology is the most beautiful part of chemistry and physics."

(Ad Kalmijn, 2001)

The basic element of all nervous systems is the neuron. Although the complexity of nervous systems is very different, many fundamental properties of neurons are common to almost all neurons. The similarities reach from proteins forming ion channels, to their morphology with thin and branched processes (dendrites and axons), and the membrane potential as the carrier of information. Neurons receive input from other neurons or, as receptor neurons, they are stimulated directly by physical input from the outside world. On the level of single neurons, basic computational operations like summation, integration, differentiation, and multiplication can be applied to these inputs. These operations are an effect of the dynamics of the single neuron. In this thesis, some important aspects of single neuron dynamics are investigated theoretically, and the resulting models are applied on data from real neurons.

The capability of animals to interact appropriately with their environment is the result of many neurons organized in neural networks. Receptor neurons of various sensory systems transduce physical stimuli of the outside world into changes of their membrane potentials — the "language of neurons" (see Fig. 1.1). This representation of stimuli is further processed in subsequent stages of the nervous system. The information from different sensory modalities is integrated, completed, and generalized, possibly with the help of associative memories. Objects are recognized and classified. Depending on the context and the motivation of the animal, motor neurons are finally activated to produce an appropriate reaction to the situation. The animal behaves in its environment.

In lower animals like polyps or jellyfish, neurons are distributed homogeneously in their epithelium and allow only very basic reflexes. In arthropods, neurons have specific functions and are organized as a segmental nervous system, resulting in already remarkable abilities. For example, grasshoppers recognize their mates based on the temporal structure of their songs. Desert ants have a highly developed navigation system. Dragonflies detect small prey over distances of a few meters and catch it with impressive flight-maneuvers. Honeybees can be trained to distinguish between certain colors or patterns.

In vertebrates, the nervous system is centralized in the brain. Vertebrates stand out by their greatly enhanced behavioral flexibility, learning ability, and memory capabilities. In higher vertebrates and especially humans, an enlarged neocortex is accompanied by

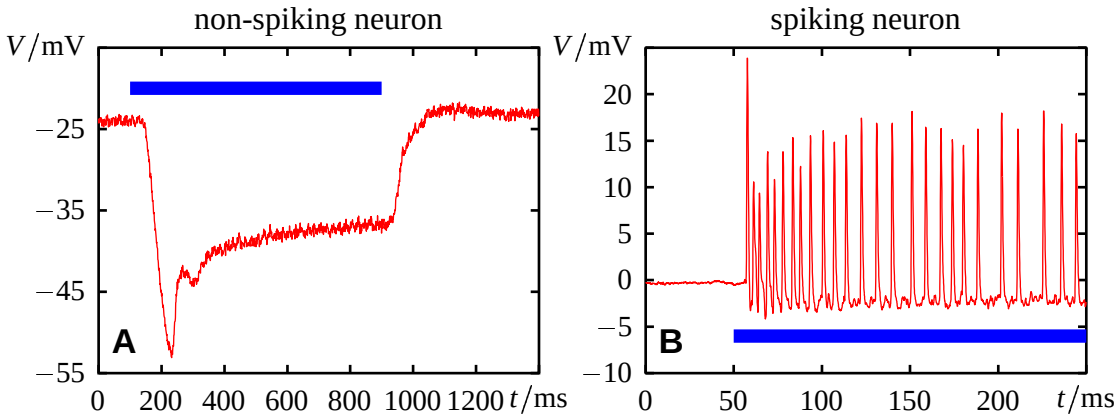

Figure 1.1: THE LANGUAGE OF NEURONS. The voltage that can be measured over the membrane of a neuron carries the information. A quantity is coded either in different values of the membrane potentials (non-spiking neuron A) or in the timing or frequency of so called spikes (spiking neuron B). **A** The membrane voltage V of a horizontal cell, a non-spiking neuron of a turtle retina. The stimulus, a flash of light, is marked by the horizontal bar. The cell responses with a graded hyperpolarization. **B** Intracellular recording of a locust auditory receptor neuron stimulated by a sound wave with constant amplitude (horizontal bar) as an example for a spiking neuron. The spikes are stereotyped deflections of the membrane potential V of about one millisecond duration. They are much faster than the initial transient of the non-spiking cell in A. Note the enlarged time scale in comparison to A.

creativity, self-awareness, and intelligence.

Against this background, the following questions occur: What is the role of a single neuron in these computations? How do its properties influence the processing of signals? Can specific phenomena like the generation of spikes or spike-frequency adaptation be described by phenomenological models, which are derived from microscopic mechanisms?

On the one hand, from about one century of experimental research, many experimental facts have been gathered about molecular mechanisms, morphology, connections, and organization of neurons. Based on this knowledge, realistic and complex models have been developed, which often simulate neurons on a very detailed level. On the other hand, since the middle of the twentieth century, physicists and engineers have been exploring the power of (abstract) neurons for processing and storing of information theoretically. This branch of research is now well established as the theory of neural networks (Hertz et al., 1991). In this area of research, very simple models of neurons are used, which do not aim at reproducing all aspects of real neurons. The recent development of the field of Computational Neuroscience triggered intermediate approaches, which are closer to experimental findings, and which are at the same time applicable to theoretical investigations (Koch, 1999).

This thesis aims to use the detailed biophysical knowledge about neurons to set up phenomenological models, which cover the main functional aspects of single neurons. The parameters of the models should be easily accessible in experiments, i.e. from the timing of the spikes only (not from the details of the voltage trace). The performance of the models is then tested experimentally by comparison with real neurons. Since these models are mathematically relatively simple, they are well suited for discussing signal transmission properties of the neurons, i.e. their role in information processing.

In the first part, models for the generation of spikes and for spike-frequency adaptation are proposed and their general properties are discussed. To keep things simple, properties of the dendritic tree are completely neglected. Only the dynamics of the spike generator is examined in this thesis.

Chapter 2 serves as a short introduction to the field of spiking neurons emphasizing their functional aspects. The starting point for these investigations is given by conductance-based models, which date back to the work of Hodgkin & Huxley (1952). These detailed models summarize a lot of our knowledge about neurons in a system of differential equations. This makes a variety of tools from the theory of dynamical systems (Guckenheimer & Labouriau, 1993; Strogatz, 1994) applicable to the analysis of neural dynamics. The slow processes underlying spike-frequency adaptation can be separated from the fast dynamics of the generation of spikes. Bifurcation theory shows and verifies the observation of Hodgkin (1948) that there exist basically two functional different classes of spiking neurons (Rinzel & Ermentrout, 1998). A comparison with experimental data reveals that most neurons are class-I neurons.

These observations set the framework for chapter 3, where an attempt is made to set up a model for the generation of spikes, whose parameters can be measured from the timing of spikes, which are evoked by simple stimuli. Phase oscillators have been introduced as abstract models of neurons (Hansel et al., 1993). Here, phase oscillators are modified to make them applicable as models of real neurons. For this purpose the neuron's f-I-curve, defined as the dependence of the firing frequency f on the intensity I of a constant stimulus, is included into these models. The timing of the spikes generated by the phase oscillators is compared with simulations of two conductance-based models.

Spike-frequency adaptation as a slow process of neural dynamics is investigated in chapter 4. This phenomenon can be observed in many neurons. The goal of this chapter is to provide a model for spike-frequency adaptation which allows to quantify the effect of adaptation on signal-transmission properties of a neuron. For that purpose, a model for the firing frequency of an adapting neuron is derived from various biophysical mechanisms responsible for adaptation. Its parameters, which can be summarized in two f-I-curves and the time-constant of adaptation, can be obtained experimentally from spike-time recordings.

In chapter 5, the last chapter of the theory part, the calculation of the firing frequency is examined. This is important for comparing the models for spike-frequency adaptation with experimental data. In addition, a measure for the precision of spikes is proposed.

The different models that have been introduced in the first part are tested on experimental data in the second part of the thesis. Neurons of the auditory system of grasshoppers (Fig. 1.2) are well suited for this purpose for three reasons: First, their auditory system is simple enough to successfully investigate its functionality. It consists of relatively few and identifiable neurons. On the other hand, it is complex enough to perform interesting computations, like the recognition of con-specific songs, which is well known from numerous behavioral experiments (von Helversen, 1997; Hennig & Weber, 1997). Second, especially the receptor cells are perfect candidates for the models from the theory part, since they transform the input sound-wave directly into a sequence of spikes, without any processing on a dendritic tree. Third, the stimulation of these cells with sound waves can be controlled well, and stable recordings of sufficient length are possible.

Response properties of auditory receptor cells of the grasshopper *Locusta migratoria* are investigated in chapter 6. They exhibit spike-frequency adaptation which can be well

Figure 1.2: MALE OF THE GRASSHOPPER *Chortippus biguttulus*. Acridid grasshoppers rasp their hind-legs on their wings to produce a song. Their ears are located at the sides of the abdomen directly behind the thorax. One ear can be seen in the photograph as the narrow dark field between the lower edge of the wing and the upper edge of the hind-leg.

described by the model from chapter 4. Adaptation in these receptor neurons helps to suppress background noise of the stimulus during short gaps, which are important elements of the grasshopper's calling songs (von Helversen, 1997).

A first order interneuron of the cricket *Teleogryllus oceanicus*, which pools the responses of receptor neurons, is examined in chapter 7. Even though the models are not designed for such a small network, they still predict the firing frequency of this interneuron well. The activity of this neuron is almost independent of the mean stimulus intensity. This phenomenon can be explained by the adaptation process, which shifts the neuron's f-I-curve to the appropriate intensity.

The intention of this work is to go all the way from the knowledge of microscopic properties of neurons to simple phenomenological models and back to real neurons, with the goal to unravel some of their computational properties. Their applications to quantify neural dynamics as well as their limits are demonstrated on two examples of neurons from the auditory system of grasshoppers and crickets.

Part I

Theory

2

Spiking Neurons

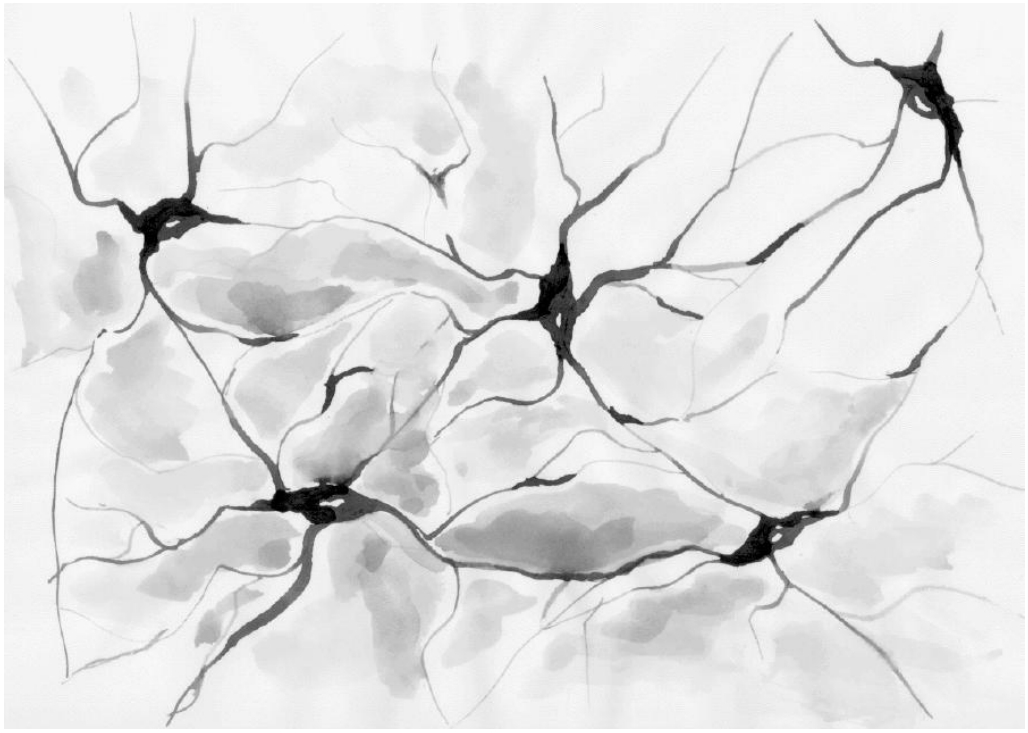

Contents

2.1 Conductance-based models ***9***

2.1.1 Ion currents *10*

2.1.2 Membrane equation *11*

2.1.3 Gating variables *11*

2.2 Time scales of neural dynamics ***13***

2.3 Reduction of the number of dynamical variables ***13***

2.3.1 Equivalent potential *14*

2.3.2 Grouping *16*

2.3.3 Reduction *16*

2.4 Class-I versus class-II neurons ***19***

2.4.1 Firing frequency *20*

2.4.2 Latencies *20*

2.4.3 Phase-resetting curve *24*

2.4.4 Bifurcation *24*

2.4.5 Spike threshold *25*

2.4.6 Spike amplitudes *26*

2.4.7 Real neurons *26*

2.5 Summary ***27***

Cover: Neurons. A drawing by Uta Grünert.

Neurons are basic elements of information processing in animals. They receive continuously input from other neurons via synapses or are directly stimulated by physical stimuli, if they are receptor neurons. The input is collected on the dendritic tree, were it is low-pass filtered or even actively processed through dendritic nonlinearities.. At the soma the resulting ionic current is transformed into a sequence of “spikes”, fast and nearly uniform deflections of the membrane potential. These spikes or “action potentials” travel down the axon and serve as input for other neurons (see Fig. 2.1).

The transformation of some ionic current into spikes is a central step in neural information processing. In the first section of this chapter a short introduction to conductance-based models is given, which describe the detailed biophysical mechanisms of this transformation process. After discussing the different time scales in a neuron in the second section, the scheme for reducing the number of variables in conductance-based models of Kepler et al. (1992) is briefly sketched (section 2.3). Finally in section 2.4 properties of two basic classes of spiking neurons are discussed. The concepts introduced here will become important in the following chapter, where simple models of the generation of spikes are presented, and in chapter 4, which covers spike-frequency adaptation.

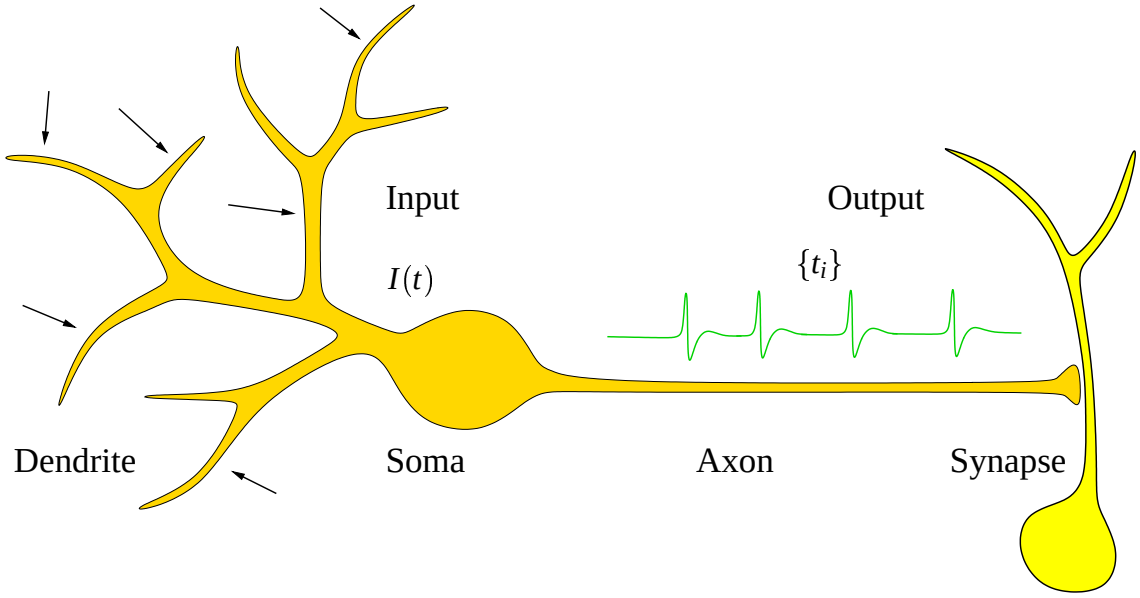

Figure 2.1: SIGNAL FLOW IN A NEURON. A neuron receives various inputs on its dendritic tree (sketched as arrows), where they are processed and summarized. The resulting ionic current $I(t)$ flows into the soma. There, the current is transformed into a sequence of spikes $\{t_i\}$ traveling down the axon. Synapses transmit these spikes to other neurons.

2.1 Conductance-based models

Like any other cell a neuron has a double-lipid layer as a membrane, which separates the cytoplasm from the extracellular space (Madigan et al., 1997). In this membrane specialized proteins are embedded. Ion pumps build up concentration gradients of different types of ions over the membrane. The concentration of potassium ions inside the cell is higher than outside, while for sodium, calcium and chloride ions it is the other way around. Some of the membrane proteins form pores, which allow ions to flow through the membrane. Such ion channels can be highly selective for different ion types. The efflux of positively charged potassium ions through potassium channels down the concentration gradient builds up an electric field over the membrane. The membrane potential V, at which the electrical field is strong enough to prevent potassium ions to further flow outside the cell, is the reversal potential $E_K \approx -80\,\text{mV}$ of potassium. The influx of sodium ions depolarizes the membrane toward the reversal potential of sodium $E_{Na} \approx +50\,\text{mV}$. The resting potential of about $-60\,\text{mV}$ is more close to the potassium reversal-potential. The values of these potentials are only clues; they differ from cell to cell. Some of the ion channels are voltage gated, i.e. their probability to be open depends on the membrane potential V (see Fig. 2.2). Such channels are necessary for the generation of spikes. Other channels open or close depending on the concentration of intracellular calcium or transmitter molecules in synapses, for example (see the textbooks Hille, 1992; Johnston & Wu, 1997; Koch, 1999, for more details).

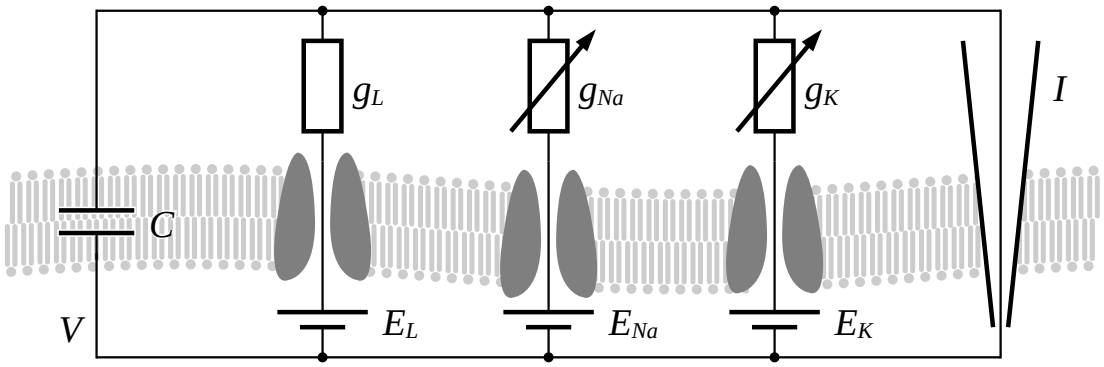

Figure 2.2: ION CURRENTS THROUGH CHANNELS IN THE CELL MEMBRANE. A schematic drawing of a patch of a neuron's membrane is shown. The double-lipid layer separates charge and therefore acts like a capacitor C. Different types of ion channels are embedded into the membrane, which are highly selective to ionic currents. In a good approximation the currents through these channels can be modeled by a conductance g and a battery E, which is the reversal potential of the current, reflecting the electrochemical gradient over the membrane. There is a leakage current with constant conductance g_L and reversal potential E_L. Some of the channels are voltage gated, i.e. their conductance depends on the membrane potential V. Such channels are responsible for the generation of spikes. The sodium current (captured by g_{Na} and E_{Na}) initiating a spike is activated by depolarization. A spike in turn inactivates the sodium current and activates a potassium current (g_K and E_K), forcing the membrane potential back to rest. An additional current I can be injected by a microelectrode.

2.1.1 Ion currents

Ions flowing through the channels represent an electric current over the cell membrane. The total current density i_k through a whole population of ion channels of a specific type k is described by the Goldmann-Hodgkin-Katz (GHK) current-equation (Johnston & Wu, 1997)

$$i_k(V) = P_k z_k^2 \mathrm{F} \frac{V}{\xi} \frac{C_{k_{in}} - C_{k_{out}} \mathrm{e}^{-z_k V/\xi}}{1 - \mathrm{e}^{-z_k V/\xi}} \tag{2.1}$$

where P_k is the permeability of the membrane due to the considered channels, which may depend on membrane voltage. The charge of the ion is denoted by z_k. With the Faraday constant $\mathrm{F} = 96485\,\mathrm{C/mol}$, the ideal gas-constant $\mathrm{R} = 8.3144\,\mathrm{J\,K^{-1}\,mol^{-1}}$ and the temperature T the factor ξ is defined as $\xi = \mathrm{R}T/\mathrm{F}$. Since the concentrations $C_{k_{in}}$ and $C_{k_{out}}$ of the ions inside and outside the cell differ in general, the current-voltage relation described by the GHK-equation (2.1) is nonlinear. However, in physiologically relevant voltage ranges (about -100 to $40\,\mathrm{mV}$) it can be approximated by a linear relation (Johnston & Wu, 1997)

$$i_k = g_k(V - E_k) \tag{2.2}$$

where g_k is the total conductance of the channels per membrane area and E_k is the reversal potential, reflecting the electrochemical gradient over the membrane (see Fig. 2.3).

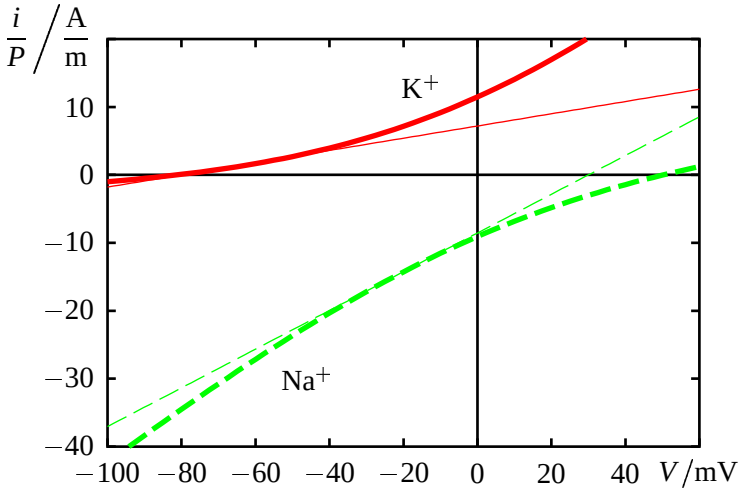

Figure 2.3: THE CURRENT-VOLTAGE RELATION FOR SODIUM AND POTASSIUM IONS. Drawn are two graphs of the GHK current-equation (2.1). The concentrations $[\mathrm{Na}]_{in} = 0.015\,\mathrm{M}$, $[\mathrm{Na}]_{out} = 0.109\,\mathrm{M}$, $[\mathrm{K}]_{in} = 0.124\,\mathrm{M}$ and $[\mathrm{K}]_{out} = 0.005\,\mathrm{M}$ are chosen to provide realistic reversal potentials: $E_{\mathrm{Na}} = +50\,\mathrm{mV}$ and $E_{\mathrm{K}} = -80\,\mathrm{mV}$. The thin lines are possible linearizations (2.2).

2.1.2 Membrane equation

Due to Kirchhoff's law all the currents over the membrane have to be summed up resulting in the membrane or current-balance equation[1]:

$$C\dot{V} = \sum_{k=1}^{M} g_k(E_k - V) + I\,. \tag{2.3}$$

The term on the left hand side is the current charging the membrane with capacitance C. $\dot{V}$ denotes the time derivative $\mathrm{d}V/\mathrm{d}t$ of the membrane potential V. The input current I either is injected by a microelectrode or is the current from the dendritic tree. The membrane equation (2.3) is the basic equation of conductance-based neuron models. These models differ in the number M of ionic currents considered and in the way, how the conductances are modeled.

The membrane equation as given in (2.3) is a model of a point neuron, i.e. the spatial properties of the neuron are completely neglected. For some neurons, especially for receptor neurons, this is a good approximation. Multi-compartmental models are needed to take the spatial structure of a neuron into account. These models combine many single-compartment equations (2.3) by means of the cable equation (Segev, 1992; Segev & Burke, 1998; Schutter & Smolen, 1998). In this thesis, however, the spatial structure of neurons is neglected and the membrane equation (2.3) is the starting point for the following analysis.

2.1.3 Gating variables

Hodgkin and Huxley were the first who measured the properties of ionic currents in the giant axon of the squid and summarized their results in a conductance-based model

[1] Usually the parameter values of conductance-based models are given per membrane area, therefore the unit of the input current I is $\mu\mathrm{A}/\mathrm{cm}^2$.

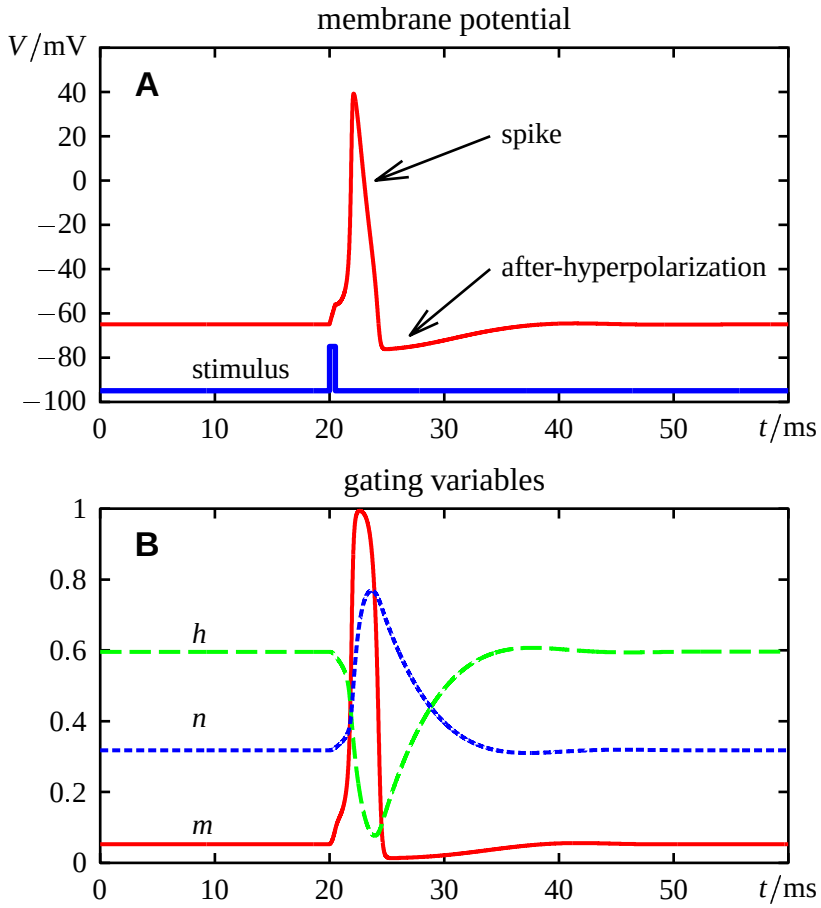

Figure 2.4: A SPIKE SIMULATED BY THE HODGKIN-HUXLEY MODEL. **A** A spike is triggered by a current pulse of 20 μA/cm^2 and 0.5 ms duration, applied at $t = 20$ ms. The spike is the short deflection of the membrane potential V. Right after the spike there is an after-hyperpolarization where the membrane potential is below the resting potential. **B** The time courses of the gating variables corresponding to the spike shown in A. The increase of the membrane potential caused by the current pulse is sufficient to activate the sodium current by its m gating-variable. The sodium current raises the membrane potential, a spike is generated. At high potentials the potassium current is activated via its gating variable n and the sodium current is inactivated by h. The spike is terminated. The increased potassium current after a spike is responsible for the after-hyperpolarization.

(Hodgkin & Huxley, 1952, see appendix A–1 for a definition of the model). They also introduced the concept of gating variables to model voltage gated channels. Each current may have an activation-variable m and an inactivation-variable h. The conductance g of the current is given by a maximum conductance $\bar{g}$ times integer powers p and q of the gating variables m and h:

$$g = \bar{g} m^p h^q \tag{2.4}$$

(for clarity the indices k at each variable are omitted). The dynamics of the gating variables are described by first order differential equations

$$\tau_m(V)\dot{m} = m_\infty(V) - m \tag{2.5}$$

$$\tau_h(V)\dot{h} = h_\infty(V) - h\,. \tag{2.6}$$

The time constants, τ_m and τ_h, as well as the steady-state variables, m_∞ and h_∞, depend on the membrane potential V.

Ionic currents which are not voltage-gated are combined to the so called "leakage current"

$$I_L = \bar{g}_L(E_L - V) \; . \tag{2.7}$$

Its conductance g_L is constant and the corresponding reversal potential is typically near the neuron's resting potential.

With this formalism Hodgkin and Huxley were able to reproduce the local spiking behavior of the axonal membrane in the squid (Hodgkin & Huxley, 1952; Guttman & Barnhill, 1970). See also Fig. 2.4 for an example.

The procedure of measuring the properties of each current, i.e. $\bar{g}$, E, τ_n, m_∞, τ_h and h_∞, requires voltage-clamp experiments and the use of drugs to selectively block the different types of channels. It is a high experimental effort to get all the necessary parameters to define a conductance-based model for a specific neuron. It would, therefore, be very helpful for studying the functional role of specific neurons to have a model with parameters, that can directly and more easily be measured.

In this and the following two chapters various conductance-based models are used to visualize and analyze properties of spiking neurons. Their specifications are put together in appendix A.

2.2 Time scales of neural dynamics

As a first step towards a simplified model of a spiking neuron, the dynamics of the activation and inactivation variables can be grouped with respect to their time constants as in Fig. 2.5.

The sodium current has a very fast activation variable m, which is responsible for the initiation of a spike, whose time constant τ_m is below one millisecond. Then there are several variables, called recovery variables, which terminate the spike. These are the sodium inactivation h, the activation of the potassium current (the so called "delayed rectifier") n (Hodgkin & Huxley, 1952) and the activation of the calcium current s (Jaffe et al., 1994). These variables have time constants below ten milliseconds. The variables of the A-current, a different type of potassium current, are acting within this range, too (Connor & Stevens, 1971; Connor et al., 1977; Numann et al., 1987).

These two types of fast gating variables are necessary for the generation of spikes. If a neuron with only such variables is stimulated with a constant input, it fires regularly with a constant firing frequency (Hodgkin & Huxley, 1952; Connor & Stevens, 1971; Morris & Lecar, 1981). To investigate the dynamics of the generation of spikes it is thus sufficient to study neurons that only exhibit those fast gating variables. In section 2.4 basic properties of such neurons are summarized, which are important for the models proposed in chapter 3. Slower variables are necessary to induce phenomena like spike-frequency adaptation or bursting. This is discussed in chapter 4.

2.3 Reduction of the number of dynamical variables

Replacing gating variables with similar time constants by a single variable reduces the large number of variables of a conductance-based model. Such a reduced model can

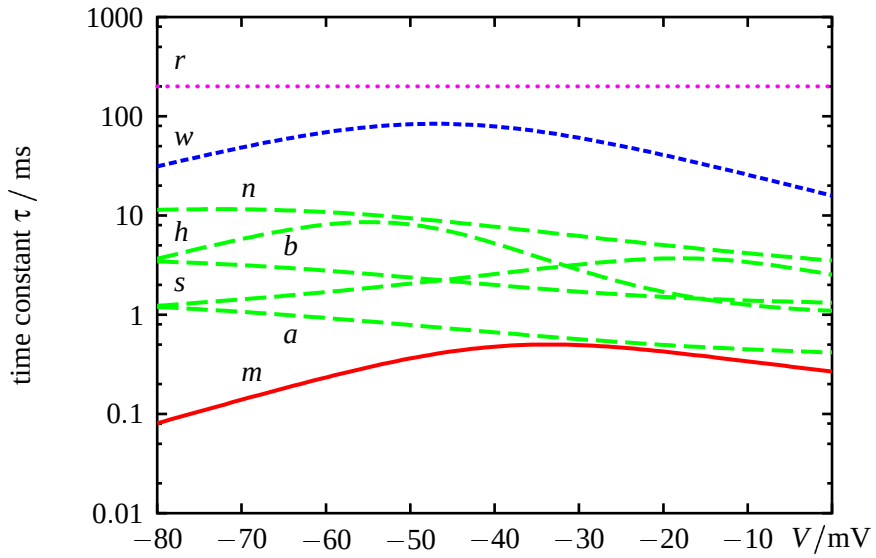

Figure 2.5: TIME CONSTANTS OF VARIOUS GATING VARIABLES. The activation variable of the sodium current *m* with a time constant below one millisecond is the fastest of all time constants. The sodium inactivation *h*, the potassium activation *n*, activation and inactivation of the A-current, and the activation of the calcium current *s* have time constants below 10 milliseconds. Both groups of gating variables are responsible for the spiking behavior of a neuron. Slower variables like those of the M-type current *w* or the inactivation-variable *r* of the calcium current cause spike-frequency adaptation and facilitation, or bursting. The *m*, *h*, *n*, *a*, and *b* gates are taken from the Connor model (Connor et al., 1977), *r*, *s*, and *w* from the Crook model (Crook et al., 1998). See appendix A for a definition of these models. Note the logarithmic scale of the time constants.

be analyzed more easily and helps to uncover the basic principles of a spiking neuron. Various studies proposed low-dimensional models as an approximation of a full conductance-based model. While the Fitzhugh-Nagumo model (Fitzhugh, 1961) only conceptually reproduced the Hodgkin-Huxley model, the similar model of Hindmarsh & Rose (1982) matched experimental data quite well. More recent studies started from detailed conductance-based models. They treated the sodium activation-variable *m* as instantaneous and combined empirically the two recovery variables *h* and *n* (Morris & Lecar, 1981; Awiszus, 1992; Abbott & Kepler, 1990).

After a more intuitive approach (Abbott & Kepler, 1990), Kepler et al. (1992) presented an optimal strategy for combining variables in conductance-based models. This approach is briefly sketched in the following paragraphs. The concept of the equivalent potential and the resulting low-dimensional systems are used in this and the following chapter.

2.3.1 Equivalent potential

As a first step on the way to a reduction of the number of variables the gating variables x are transformed to their equivalent potential V_x. It is defined by the inverse steady-state variable $x_\infty^{-1}(V)$ of the gating variable x

$$V_x = x_\infty^{-1}(x) \tag{2.8}$$

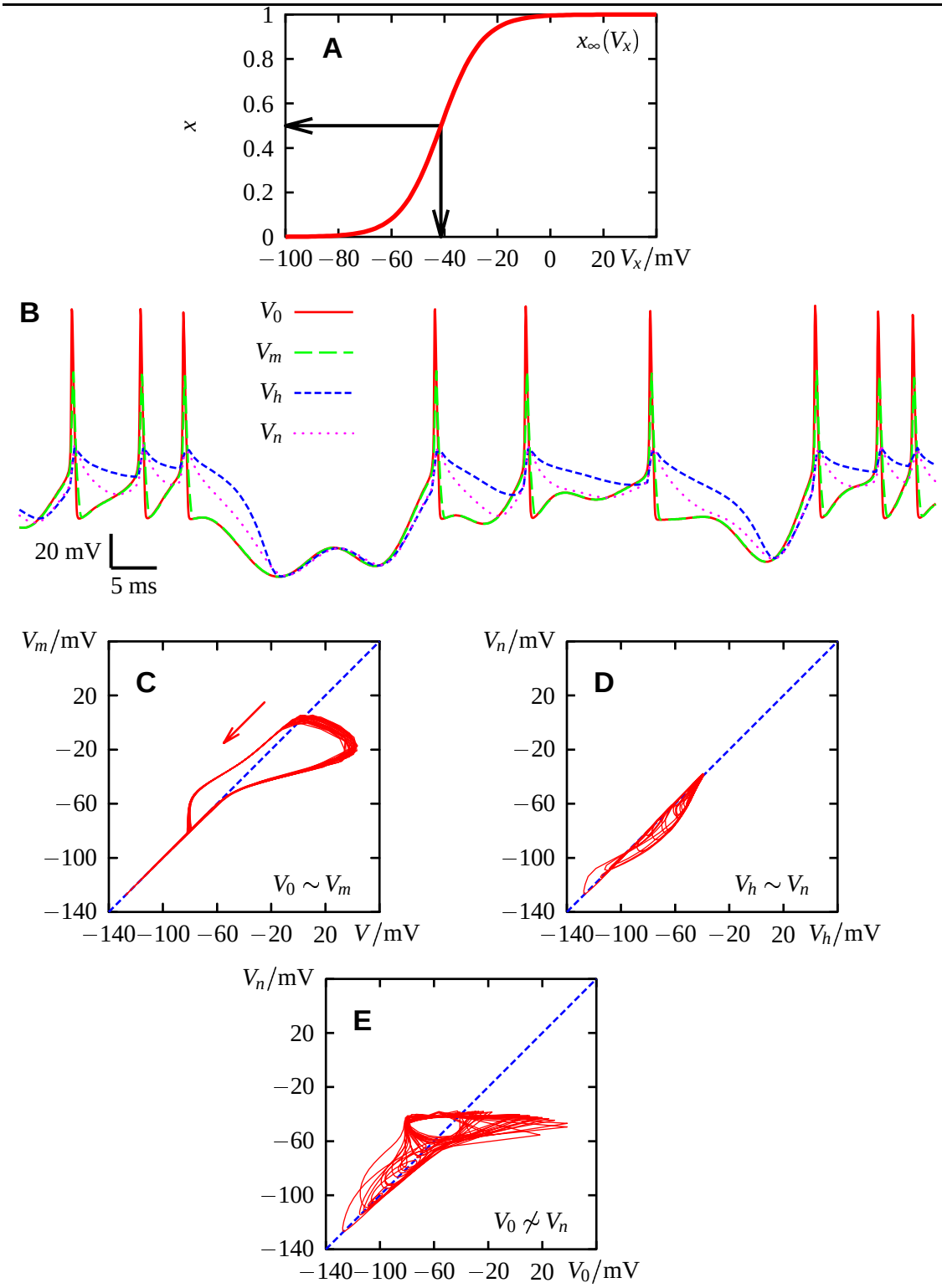

Figure 2.6: EQUIVALENT POTENTIALS. **A** Definition of the equivalent potential of a gating variable x via its steady-state variable $x_\infty(V)$. **B** Time courses of the equivalent potentials of all four variables of the Traub-Miles model evoked by a random stimulus. V_0 denotes the membrane potential of the original model. **C, D & E** Comparison of the equivalent potentials from B. **C** The membrane potential V_0 is most of the time nearly identical to activation-variable m of the sodium activation. They differ only during spikes (loop). Thus, both variables can be combined to a representative membrane potential V. **D** The gating variables h and n can be combined to a single recovery variable U. **E** The membrane potential and the equivalent potential of the potassium gating variable V_n are not similar at all.

and makes the gating variables comparable to the membrane potential V. The definition of the equivalent potentials is illustrated in Fig. 2.6 A. Time courses of the equivalent potentials for all four variables of the Traub-Miles model evoked by a random stimulus are superimposed in panel B and compared to each other in panels C, D & E. See appendix A–2 for a definition of the Traub-Miles model.

2.3.2 Grouping

The next step is to detect variables with similar time courses. In the example shown in Fig. 2.6 B the four variables fall into two distinct groups. The sodium activation-variable m has a very small time constant, thus most of the time its equivalent potential is identical to the membrane potential. Only during spikes they differ (loop in panel C). The other group consist of the two recovery variables h (sodium inactivation-variable) and n (potassium activation-variable). They have similar time constants and the time courses of their equivalent potentials are similar, too (panel D). All four variables cannot be combined into a single variable, since, for example, the equivalent potential V_n of the potassium activation-variable n is not correlated with the membrane potential (panel E).

The clustering of variables into groups is based on sharing both a common time scale and a common sign of influence on the ionic current, i.e. $\mathrm{sign}(\partial\tilde{F}/\partial V_i) = \mathrm{sign}(\partial\tilde{F}/\partial V_j)$ in (2.11) below (Kepler et al., 1992). For this reason the two variables a and b of the A-current of the Connor model cannot be combined, since they have opposite effects on the membrane current.

2.3.3 Reduction

The final step is to linearly combine variables with similar dynamics. The fast sodium activation-variable m can be combined with the membrane potential V_0 to a representative membrane potential V

$$V := \alpha_0 V_0 + \alpha_m V_m \,. \tag{2.9}$$

The coefficients α_0 and α_m are constrained to sum to one. Slow variables like h and n can be combined to a single recovery variable U

$$U := \alpha_h V_h + \alpha_n V_n + \ldots \,. \tag{2.10}$$

Even slower variables may be combined to additional representative potentials in the same way as it is shown here for the U variable.

After expanding the time derivatives of V and U to first order in the corrections $\delta_i = V_i - V$ ($i = 0,\ m$) and $\delta_j = V_j - U$ ($j = h,\ n$), the coefficients α_i and α_j can be chosen so that the first order corrections δ_i and δ_j vanish and the expansion is valid to second order. The resulting reduced set of differential equations is

$$\begin{aligned} \frac{C}{\alpha_0}\dot{V} &= \sum_{k=1}^{M} \bar{g}_k m_{\infty_k}^{p_k}(V_{m_k}) h_{\infty_k}^{q_k}(V_{h_k})(E_k - V) + I := \tilde{F}(V, V_i) + I \approx F(V, U) + I \\ \dot{U} &= \sum_{j=1}^{N} \alpha_j \frac{x_{\infty_j}(V) - x_{\infty_j}(U)}{\tau_j(V)\ \mathrm{d}x_{\infty_j}(U)/\mathrm{d}U} \,. \end{aligned} \tag{2.11}$$

The first equation is the membrane equation (2.3) summing up all M ionic currents I_k. Their gating variables m_k and h_k are replaced by their steady-state variables m_{∞_k} and h_{∞_k}

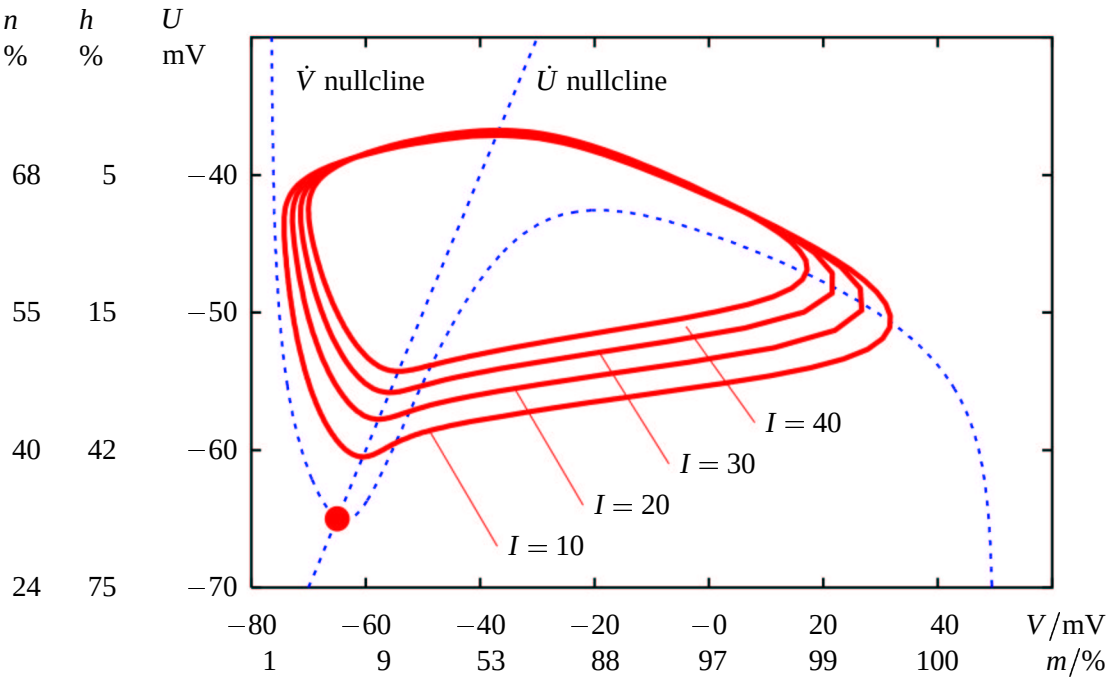

Figure 2.7: THE REDUCED HODGKIN-HUXLEY MODEL. A phase portrait of the Hodgkin-Huxley model reduced by the scheme of Kepler et al. (1992) as described in the text is shown. Similar to the Traub-Miles model in Fig. 2.6 the sodium activation-variable m is combined with the membrane potential to a representative membrane potential V on the abscissa. To each value of V corresponds a value of the gating variable m. The two remaining gating variables h of the sodium current and n of the potassium current are combined to a recovery variable U. Each value of U is associated with corresponding values of these two gating variables. The dashed lines are the $\dot{V}$ and $\dot{U}$ nullclines for an input current $I = 0$. They intersect at $V = -65\,\mathrm{mV}$ resulting in a stable fixed point (filled circle) — the resting potential. The $\dot{U}$ nullcline is always given by the line $V = U$. The input current I changes only the $\dot{V}$ nullcline. For sufficiently high input currents stable limit cycles emerge — the neuron fires periodically. Four such limit cycles for different input currents as indicated in $\mu\mathrm{A/cm}^2$ are shown. Note that the amplitude of a spike depends on the input current.

---

depending on the corresponding equivalent potentials V_{m_k} and V_{h_k}. These equivalent potentials V_i are replaced by the appropriate representative potentials V or U. The coefficient α_0 in the first equation of (2.11) is given by

$$\alpha_0 = \frac{\frac{C}{\tau_m(V)} + \frac{\partial F}{\partial V} - \sqrt{\left(\frac{C}{\tau_m(V)} - \frac{\partial F}{\partial V}\right)^2 - 4\frac{C}{\tau_m(V)}\frac{\partial F}{\partial m_\infty}\frac{\mathrm{d}m_\infty}{\mathrm{d}V}}}{2\left(\frac{\partial F}{\partial V} + \frac{\partial F}{\partial m_\infty}\frac{\mathrm{d}m_\infty}{\mathrm{d}V}\right)} \,. \tag{2.12}$$

The second equation in (2.11) sums over N the gating variables x_j, which are combined within the representative potential U. The coefficients

$$\alpha_j = \frac{\frac{\partial \tilde{F}}{\partial V_j}}{\sum_{i=1}^{N} \frac{\partial \tilde{F}}{\partial V_i}} \tag{2.13}$$

weigh the influence of the corresponding equivalent potential V_j on the membrane equation.

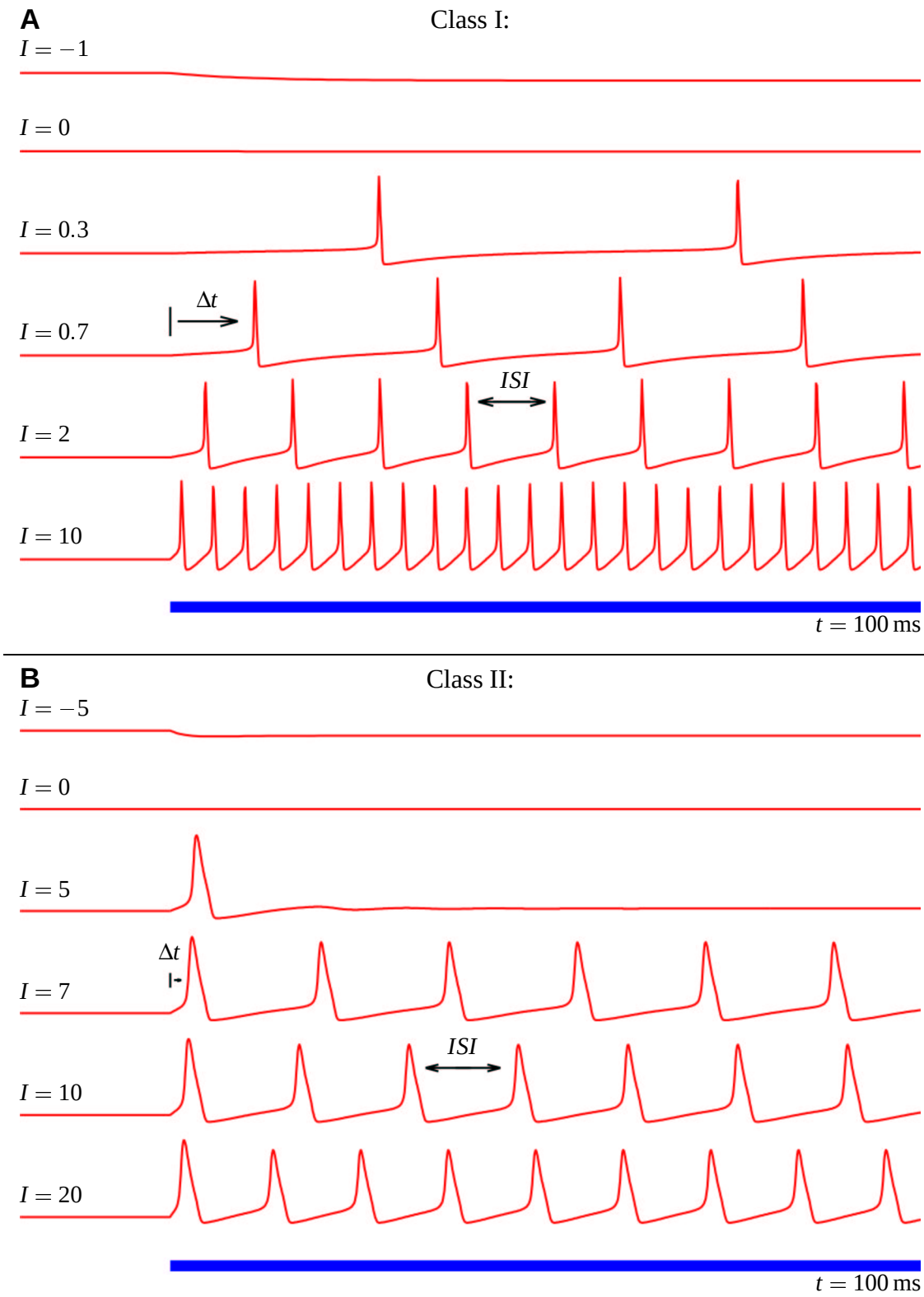

Figure 2.8: REPETITIVE SPIKING IN CLASS-I AND CLASS-II MODEL NEURONS. Traces of the membrane potential computed from **A** the Traub-Miles model and **B** the Hodgkin-Huxley model for different constant input currents (bottom bar) as indicated (units are $\mu A/cm^2$). The interspike interval *ISI* is defined as the time between two succeeding spikes. The latency Δt is the time from the onset of the stimulus to the first spike. Note that only a single spike is evoked by a current of $I = 5\,\mu A/cm^2$ of the Hodgkin-Huxley model.

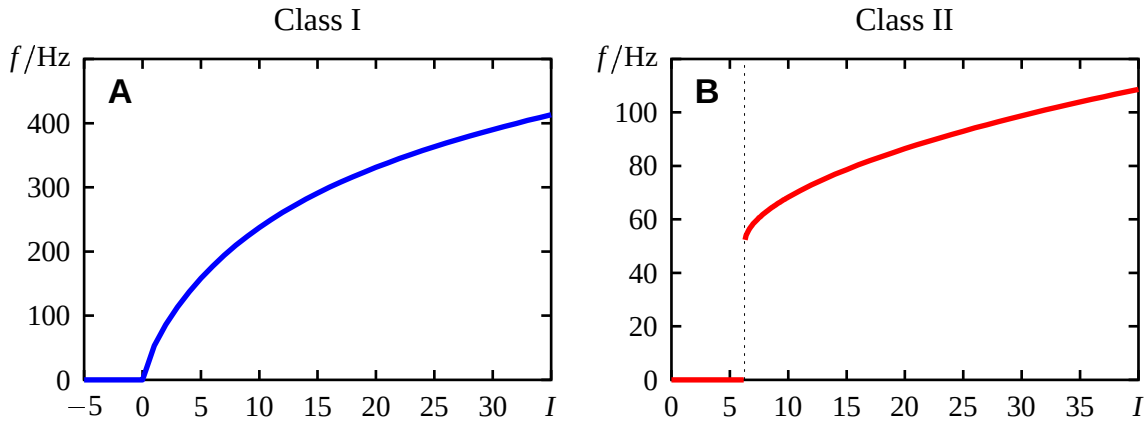

Figure 2.9: f-I-CURVES OF CLASS-I AND CLASS-II MODEL NEURONS. Plotting the firing frequency f as the reciprocal of the *ISI* against the strength of the constant input current I results in the f-I-curve. **A** In class-I neurons, like the Traub-Miles model shown here, the f-I-curve is continuous. **B** f-I-curves of class-II neurons, like the Hodgkin-Huxley model, exhibit a discontinuous jump to a non-zero firing frequency at the threshold current I_{th} (vertical line).

In Fig. 2.7 a phase portrait of the Hodgkin-Huxley equations reduced to two variables is shown. On the abscissa the membrane potential is drawn, which also represents the state of the m-gating variable. Both the h and the n-gating variables are combined to the recovery variable U on the ordinate. The dynamics of this reduced Hodgkin-Huxley model approximates the one of the full four-dimensional model very well (Kepler et al., 1992).

Combining all gating variables with similar dynamics reduces the number of variables, but does not reduce the number of parameters needed for the definition of the dynamics (2.11) of the remaining representative potentials. However, neglecting all processes with time constants greater than ten milliseconds, a simple two dimensional set of differential equations remains, which describes the essentials of generating spikes.

2.4 Class-I versus class-II neurons

Some years before Hodgkin and Huxley published their extraordinary work in 1952, it was already known that there are basically two types of excitable neurons, which were called class-I and class-II neurons (Hodgkin, 1948). They differ in some basic properties in their response to constant currents. Phase space analysis revealed two different bifurcation types for these two classes of excitable neurons (Rinzel & Ermentrout, 1998). From a functional point of view this is a very important finding.

In the following the differences of the two types of neurons as they were described by Hodgkin (1948), Hansel et al. (1995) and Ermentrout (1996) are demonstrated. Note that these differences mainly concern the transition from rest to repetitive spiking. Then the two different types of bifurcations for these two types of neurons are discussed. To illustrate the differences the Traub-Miles model as an example for a class-I neuron and the Hodgkin-Huxley model as an example for a class-II neuron are used. Both models are defined in appendix A.

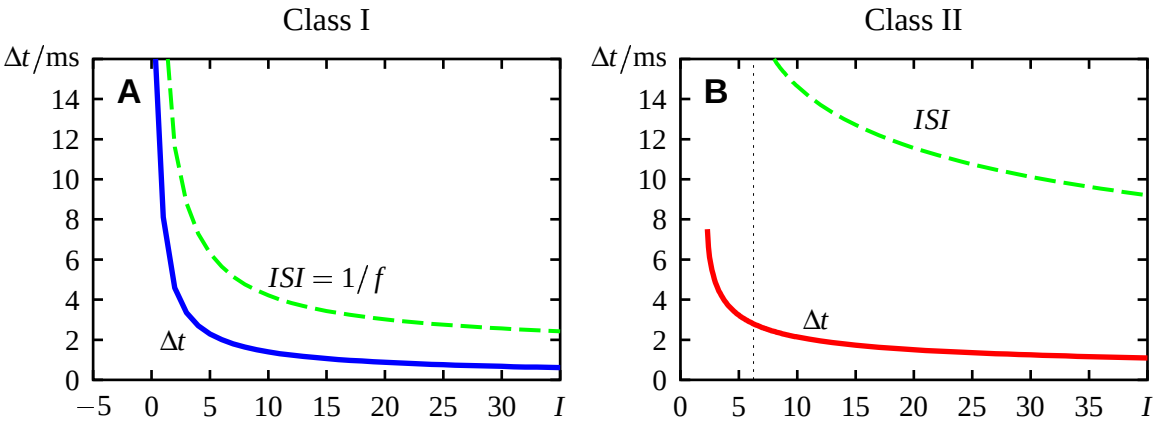

Figure 2.10: LATENCIES OF CLASS-I AND CLASS-II MODEL NEURONS. **A** Latencies Δt in the Traub-Miles model (as an example of a class-I neuron) can be arbitrary long. They are of the same order of magnitude as the corresponding *ISI*. **B** In class-II neurons, like the Hodgkin-Huxley model, latencies are finite and short compared to the corresponding *ISI*. Only the latencies of single spikes evoked by low currents, which do not induce repetitive firing, increase with decreasing input current (to the left of the vertical line).

2.4.1 Firing frequency

Injecting constant currents of different intensities into a neuron results in voltage traces as shown in Fig. 2.8 for a class-I (panel A) and a class-II neuron (panel B). Both neurons have in common that they start to spike for strong enough input currents. They spike periodically with a period T, which is referred to as the interspike interval (*ISI*). The reciprocal *ISI* is the firing frequency f of the neuron. For small or negative currents the membrane potential stays at a fixed value. The minimum current necessary to evoke periodic spiking is the threshold current I_{th}.

The main difference between the two classes is the type of transition from the non-spiking state to repetitive spiking. Class-I neurons are able to spike with arbitrary low frequencies, while periodic spiking in class-II neurons sets in with a non-zero frequency.

This behavior can be summarized in firing-frequency-versus-input-intensity-curves (f-I-curves, $f(I)$), where the firing frequency $f = 1/T$ is plotted against the intensity of the injected current I (see Fig. 2.9). The f-I-curve of the class-I neuron is monotonically increasing and reaches very high values. The f-I-curve of the class-II neuron has a discontinuous jump and is relatively insensitive to the current strength compared to the class-I neuron.

2.4.2 Latencies

Another difference pointed out by Hodgkin (1948) is the latency of the first spike after onset of an input current (see Fig. 2.10). In class-I neurons the latency can be very long (Koch et al., 1995) and is of the order of the corresponding interspike interval. Latency in class-II neurons is much shorter compared to the interspike intervals and is nearly independent of the input strength (see for example figure 1 in Fricker & Miles, 2000). While f-I-curves describe the steady-state behavior of a neuron for stimuli above threshold, latencies give additional information about the transition from rest to repetitive firing.

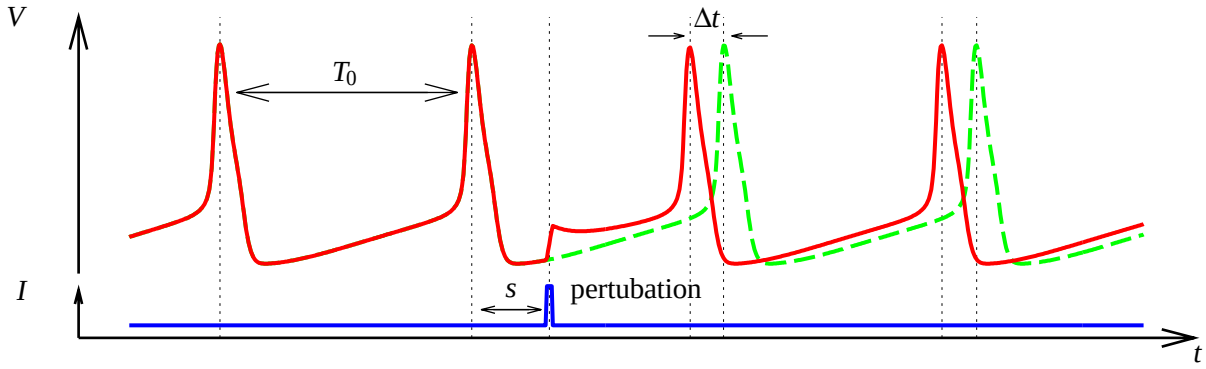

Figure 2.11: PHASE SHIFT OF A PERIODICALLY SPIKING NEURON. Given a constant input current I the neuron is spiking periodically with some period T_0. At time s relative to a spike a short and small perturbation is delivered. The succeeding spikes (solid line) are shifted relative to the unperturbed response (dashed line) by some time Δt (time of the perturbed spike minus time of the unperturbed spike), but still have a period of T_0. Perturbing at different phases $\varphi = s/T_0$ results in different phase shifts $\Delta\varphi = \Delta t/T_0$. The phase shift $\Delta\varphi$ is positive, if the perturbation advances the following spike as illustrated, and negative, if the following spike is delayed.

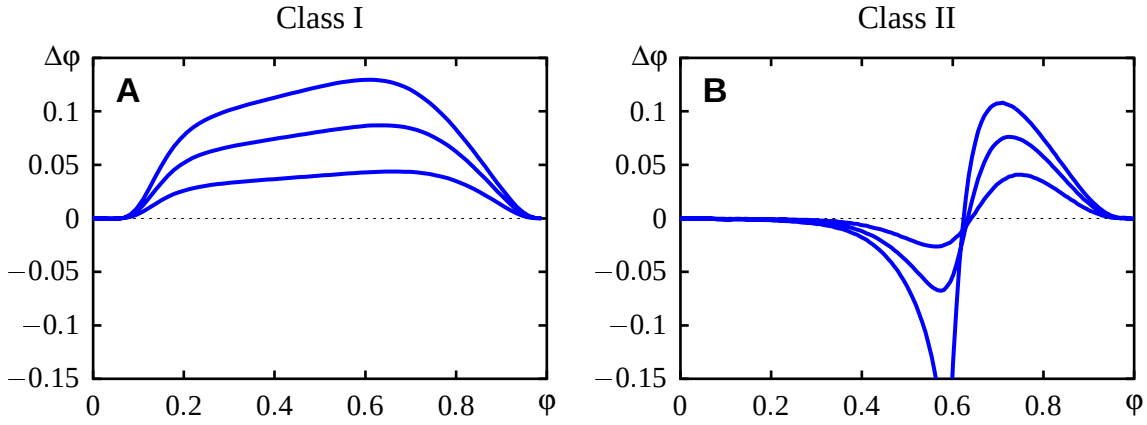

Figure 2.12: PHASE-RESETTING CURVES. At $\varphi = 0$ and $\varphi = 1$ are the maxima of the spikes. Phase-resetting curves for three perturbation intensities $\Delta I = 5, 10,$ and $15\,\mu\text{A/cm}^2$, each of 0.25 ms duration, are shown. **A** The Traub-Miles model as an example for a class-I neuron has mono-phasic phase-resetting curves. All positive perturbations advance the following spike. Only during the spikes in a small range of phases the neuron is insensitive to inputs. The input current was $I = 4\,\mu\text{A/cm}^2$, and resulted in a firing period of 7.29 ms. **B** The Hodgkin-Huxley model representing a class-II neuron has a biphasic phase-resetting curve. Up to almost a phase of $\varphi = 0.4$ perturbations do not have any effect. In a following short range $\Delta\varphi$ is negative, thus the period is increased. If the perturbation is strong enough, the oscillation can be even stopped. Only during the last third of the period the following spike will be advanced. The input current was $I = 10\,\mu\text{A/cm}^2$, and resulted in a period of 14.63 ms.

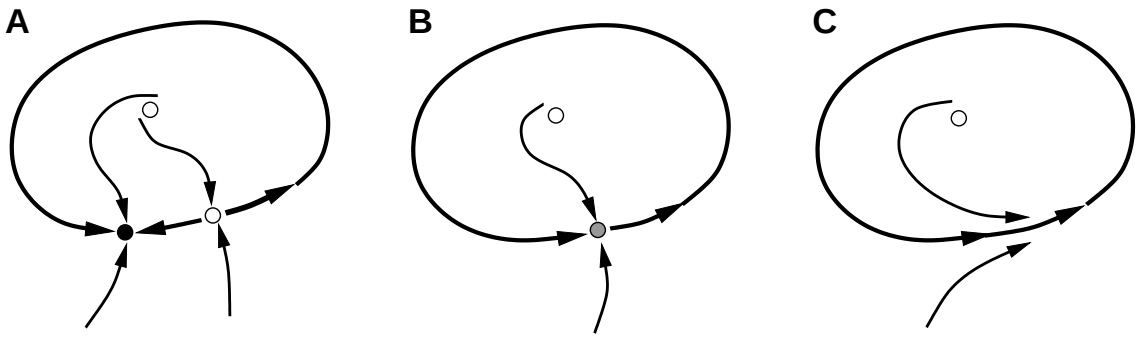

Figure 2.13: SADDLE-NODE BIFURCATION. **A** Below bifurcation there exist three fixed points. A stable node (black circle), a saddle (lower white circle) and an unstable spiral (upper white circle). Small perturbations of the rest state decay back to the stable fixed point, while a strong perturbation beyond the saddle causes a large excursion of the solution before returning to the equilibrium — a spike. Such a trajectory is called a periodic pseudo-orbit. **B** Right at the bifurcation the stable node collapses with the saddle, resulting in an unstable fixed point associated with a homoclinic orbit with zero frequency. **C** Above bifurcation the node and the saddle vanish and a stable limit cycle remains — the neuron fires periodically.

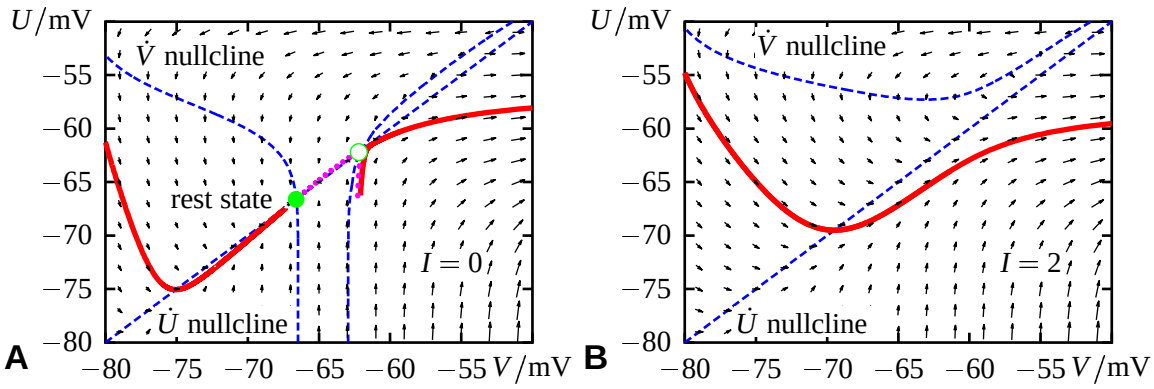

Figure 2.14: SADDLE-NODE BIFURCATION IN A CLASS-I NEURON (TRAUB-MILES). **A** Below the firing threshold the $\dot{V}$ nullcline (dashed line) intersects three times the $\dot{U}$ nullcline (circles, two are visible, the third is outside the panel to the right). The leftmost intersection is a stable fixed point (filled circle); the vectors of the flow-field are all pointing toward it. The middle intersection is a saddle point (open circle). Trajectories starting from below first approach the saddle and then turn either toward the stable fixed point directly (dotted line) or leave the panel to the right, circle round (which is a spike) and approach the fixed point from the left (solid line). A separatrix separates the spiking trajectories from the silent ones. **B** For super-threshold currents the two fixed points vanish. There is no longer a stable fixed point in the system. Instead the spiking trajectory is now a stable limit cycle (solid line): the neuron is firing periodically.

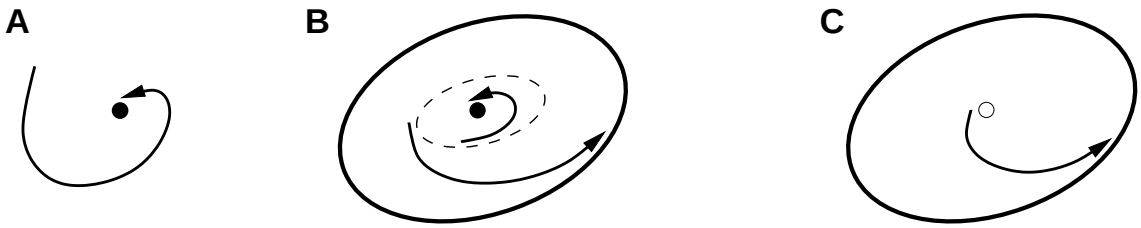

Figure 2.15: SUPERCRITICAL HOPF BIFURCATION. **A** First there is only a single stable fixed point. **B** With increasing bifurcation parameter a stable limit cycle emerges in coexistence with the stable fixed point. The basins of attraction are separated by an unstable limit cycle as indicated by the dashed line. **C** This separatrix shrinks toward the fixed point until at the Hopf bifurcation this fixed point looses stability and the stable limit cycle remains.

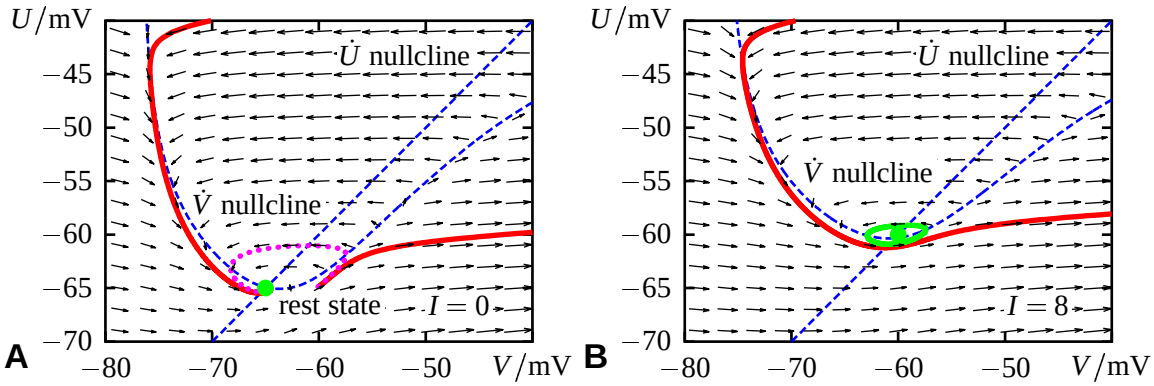

Figure 2.16: HOPF BIFURCATION IN A CLASS-II NEURON (HODGKIN-HUXLEY). **A** The $\dot{V}$ and $\dot{U}$ nullclines (dashed lines) intersect at one point only. For sub-threshold currents the fixed point is stable (filled circle). Small perturbations produce damped oscillations back to the fixed point (dotted line). Larger perturbations may induce a single (or several) spike (solid line) before the fixed point is reached again. In contrast to the saddle-node bifurcation there exists no separatrix associated with a saddle (Izhikevich, 2000). **B** With increasing strength of the input current, the trajectory of the spike becomes a stable limit cycle, which coexists with the still stable fixed point. The basin of attraction of the fixed point (loop around fixed point) decreases until the fixed point looses stability and a stable limit cycle remains.

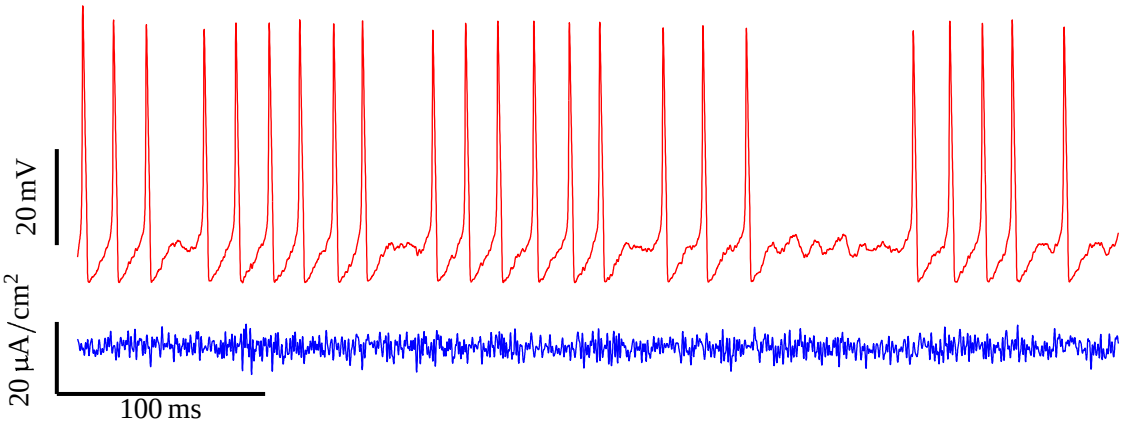

Figure 2.17: SPIKE CLUSTERING IN A NOISY CLASS-II NEURON. A spike train of a Hodgkin-Huxley model evoked by a noisy stimulus. The mean of the Gaussian white-noise stimulus was 7 $\mu A/cm^2$, its standard deviation 2 $\mu A/cm^2$ and the cut-off frequency 1000 Hz. The system jumps between the stable fixed point and the stable limit cycle of the noiseless system. This leads to clustered spikes.

2.4.3 Phase-resetting curve

Besides the f-I-curves, which provide information about the period of the oscillation for a constant current I, the so called "phase-resetting curve" characterizes the influence of perturbations on this oscillation. As illustrated in Fig. 2.11, without any perturbation the neuron fires with period T_0. A perturbation delivered at a given time s after a spike may advance or delay the occurrence of the following spikes by Δt relative to the unperturbed spikes. The perturbed interspike interval is then $T = T_0 - \Delta t$. The phase-resetting curve $\Delta\varphi(\varphi)$ is the phase shift $\Delta\varphi = \Delta t/T_0$ as a function of the phase $\varphi = s/T_0$ of the perturbation.

Ermentrout (1996) has proved, that the phase-resetting curve of a system at a saddle-node bifurcation like a class-I neuron is always positive, indicating that any positive perturbation advances the spikes (see Fig. 2.12). From simulation studies of class-II neurons it is known that they have biphasic phase-resetting curves (Hansel et al., 1995). In the middle part of the interspike interval, perturbations delay the following spike, while later perturbations advance it (see Fig. 2.12).

2.4.4 Bifurcation

The reason for these two completely different qualitative behaviors of neurons is the type of bifurcation. As shown by Rinzel & Ermentrout (1998) class-I neurons have a saddle-node bifurcation, while class-II neurons undergo a subcritical Hopf bifurcation (see also Izhikevich, 2000).

The generic form of a saddle-node bifurcation is demonstrated in Fig. 2.13 and in Fig. 2.14. For subthreshold input currents a stable node representing the resting potential lies directly on a periodic pseudo-orbit, which is the trajectory of a spike. At threshold the node loses stability and the pseudo-orbit becomes a stable limit cycle. The period is infinitely long, since the limit cycle passes the intersection of the two nullclines, where the derivatives equal zero. With increasing input current the nullclines no longer intersect, leading to increasing derivatives at the location of the former node. Therefore the

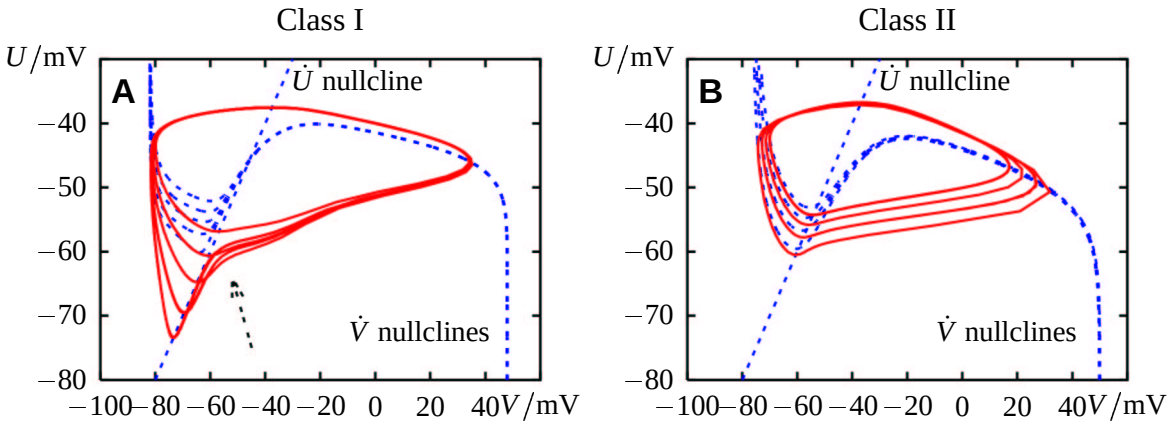

Figure 2.18: LIMIT CYCLES FOR DIFFERENT INPUT CURRENTS I. **A** The Traub-Miles model (class-I) and **B** the Hodgkin-Huxley model (class-II). Increasing the input current shifts only the minimum of the $\dot{V}$ nullcline upwards. Therefore differences between the limit cycles are mostly restricted to this region. The inner cycles correspond to high current levels.

period of the limit cycle decreases (Strogatz, 1994). The latency is of the same order of magnitude as the corresponding *ISI* since the trajectory first has to pass the "ghost" of the saddle, where — like on a limit cycle — it spends most of its time. Perturbations cannot move the system nearer to the "ghost" of the saddle-node, since they cross it anyway. Therefore perturbations cannot slow the movement down.

For the case of a subcritical Hopf bifurcation a stable limit cycle appears around the fixed point, far away from the intersection of the nullclines. Therefore at least one derivative on the limit cycle is always greater than zero leading to a finite period and to a short latency. This is shown in Fig. 2.15 and Fig. 2.16 for a Hodgkin-Huxley neuron. The coexistence of both a stable fixed point and a stable limit cycle induces hysteresis. In the presence of noise this leads to spike clustering as illustrated in Fig. 2.17 (figures 4–6 in Alonso & Klink (1993), figure 8 in Haman et al. (2000)). The noise switches the trajectory from the basin of attraction of the fixed point to that of the limit cycle and *vice versa* (Schneidman et al., 1998). This phenomenon cannot be observed in class-I neurons. In addition, a perturbation can push the system from a limit cycle towards the fixed point. Therefore the movement is slowed down, resulting in a negative phase shift.

2.4.5 Spike threshold

Due to the separatrix associated with the saddle, class-I neurons have a precisely defined threshold for the initiation of a spike. Crossing this separatrix generates a spike with full amplitude. Since the flow-field is uniquely defined by the input current I, the separatrix also depends on I. Furthermore the separatrix does not have to be a simple voltage threshold. In general it can be a more complicated function in the neuron's phase space. Note, that crossing this threshold is not identical with immediately emitting a spike. It may take a while until the trajectory has passed the saddle point and eventually produces the spike (Gutkin & Ermentrout, 1998).

Class-II neurons do not have a well defined threshold. Instead they have a whole threshold set. They can generate spikes with arbitrary amplitudes, depending on where in the threshold set they start (Cole et al., 1970). However, this threshold set is usually very small so that in practice (adding just some noise) class-II neurons show a quasi-threshold behavior (Izhikevich, 2000).

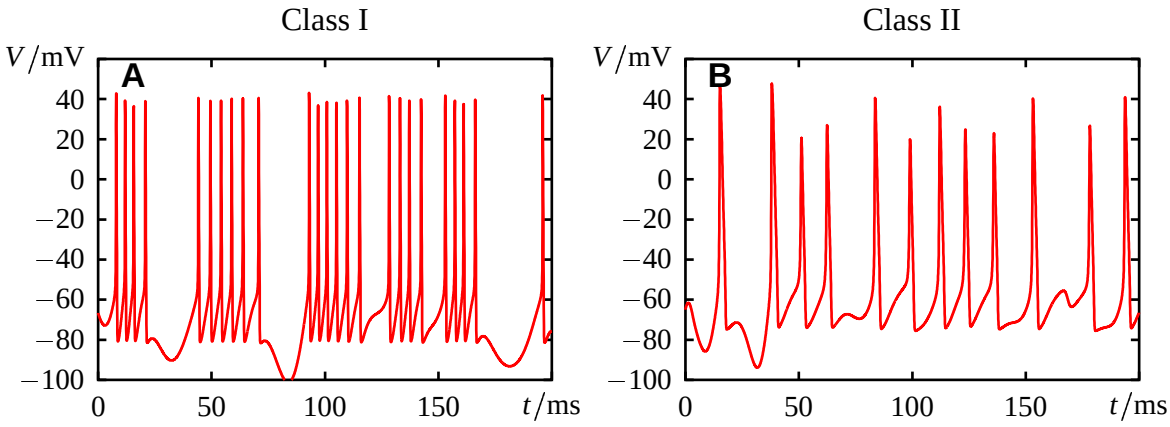

Figure 2.19: AMPLITUDES OF SPIKES. **A** In the Traub-Miles model (class I) spike amplitudes are approximately constant, while **B** in the Hodgkin-Huxley model (class II) they vary strongly. Shown are the voltage traces to different Gaussian white noise stimuli with a cut-off frequency of 50 Hz.

2.4.6 Spike amplitudes

For different super-threshold currents the limit cycles of a class-I and a class-II neuron differ mainly in the part of the spike upstroke (Fig. 2.18). While in the class-I example the limit cycles change only before the onset of the spike, the limit cycles of the class-II neuron differ also in the spike upstroke. This leads to spikes with different amplitudes as demonstrated in Fig. 2.19. There is no proof for this phenomenon, but it can be understood qualitatively. The flow-field of the former saddle of a class-I neuron still attracts the trajectories (arrow in Fig. 2.18 A), thus the various orbits converge after passing the saddle. In contrast the flow-field of a class-II neuron is dominated completely by the limit cycles, which are not influenced by the fixed point, resulting in trajectories more parallel to each other.

2.4.7 Real neurons

To my knowledge there are only a few neurons identified to be class-II neurons, as for example cortical interneurons (Alonso & Klink, 1993; Gloveli et al., 1997; Koch, 1999). The Hodgkin-Huxley equations, which are the most prominent example of a class-II neuron, describe properties of a patch of axonal membrane and not the spike initiating zone, which from a computational point of view is much more relevant. In contrast, the majority of neurons have a class-I f-I-curve. For example neocortical pyramidal and sparsely spiny stellate neurons (McCormick et al., 1985), CA1 interneurons (Lacaille & Williams, 1990), and layer III cells of the medial enthorhinal cortex (Gloveli et al., 1997). Thus, it is in general much more realistic to use a class-I neuron model instead of the Hodgkin-Huxley equations for simulation studies.

It has to be noted that due to noise the discontinuity in the class-II f-I-curves in real neurons may be smeared out (Schneidman et al., 1998; Koch, 1999). It is therefore harder to distinguish class-I from class-II neurons based only on their f-I-curves. However, other properties like latencies, phase-resetting curves or spike clustering still allows separating these two types of neurons.

Table 2.1: PROPERTIES OF CLASS-I AND CLASS-II NEURONS.

	Class I	Class II
firing frequency	arbitrary low	frequency band
latency	arbitrary long	short
phase shift	advance	delay & advance
bifurcation	saddle node	Hopf
noise	jitter	clustering
threshold	separatrix	threshold set
spike amplitudes	fixed	variable
conductance-based models	Traub et al. (1991) Morris & Lecar (1981) Connor et al. (1977) Bower (1989)	Hodgkin & Huxley (1952) Morris & Lecar (1981)
real neurons	Pyramidal cells	cortical interneurons

A summary of the differences of class-I and class-II neurons as discussed in the text. The conductance based models as well as the real neurons listed here are only a few examples. For references to the examples of real neurons see section 2.4.7.

2.5 Summary

- Conductance-based models provide a detailed biophysical description of the dynamics of ionic currents in neurons.
- The time scales of different gating variables can be grouped.
- With the scheme for reducing the number of variables of Kepler et al. (1992) conductance-based models can be simplified.
- Two classes of neurons can be distinguished on the basis of f-I-curves, latencies, and phase-resetting curves as summarized in tab. 2.1.
- Class-I neurons start spiking through a saddle-node bifurcation, while class-II neurons have a subcritical Hopf bifurcation.

3

Modeling Spikes

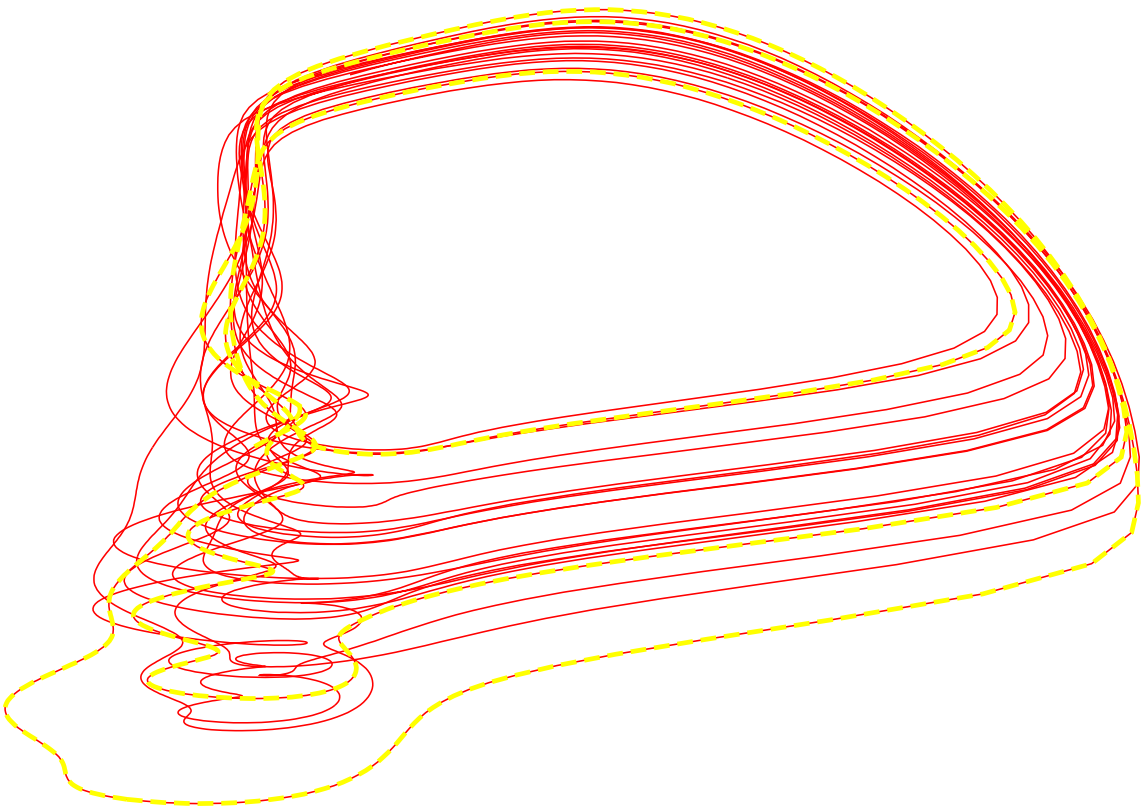

Contents

3.1 Firing frequency as a phase velocity **32**
3.1.1 The non-leaky phase oscillator 33
3.1.2 Performance of the non-leaky phase oscillator 33
3.1.3 Signal-transmission properties of firing frequencies 37
3.2 More about phase velocities **39**
3.2.1 The leaky phase oscillator 42
3.2.2 Performance of the leaky phase integrator 42
3.2.3 Relation to the integrate-&-fire model 43
3.3 Saddle-node bifurcation and the θ-model **44**
3.3.1 Performance of the θ-model 46
3.4 Oscillations and phase-resetting curves **48**
3.4.1 Phase-resetting curves of phase oscillators 48
3.5 Phase oscillators in the sub-threshold regime **52**
3.5.1 Performance of the θ-model near threshold 52
3.5.2 Possible latencies of phase oscillators 53
3.5.3 Fixed points calculated from latencies 54
3.6 Outlook: Two-dimensional models **56**
3.7 Discussion **58**
3.7.1 Spiking in the super-threshold regime 58
3.7.2 Prediction of super-threshold properties from bifurcation . . 58
3.7.3 Spiking near threshold 59
3.7.4 Two-dimensional models 59
3.7.5 Class-II neurons 60
3.8 Summary **60**

Cover: Trajectory of the Hodgkin-Huxley model stimulated with Gaussian white-noise (mean $2\,\mu\mathrm{A}/\mathrm{cm}^2$, standard deviation $17\,\mu\mathrm{A}/\mathrm{cm}^2$, cut-off frequency 400 Hz, duration 400 ms). The abscissa is the membrane potential V, the ordinate the recovery variable U.

Conductance-based models as introduced in the previous chapter provide a very detailed description of neural dynamics. The time course of the membrane potential and of all gating variables can be computed from conductance-based models for arbitrary stimuli. However, solely the timing of the resulting spikes is what matters, since these determine the input to the postsynaptic neurons. The detailed time course of the membrane potential in spiking neurons is irrelevant for the transmitted information. In addition, the experimental effort to measure properties of ion-channels needed to define a conductance-based model for a specific type of neuron is high.

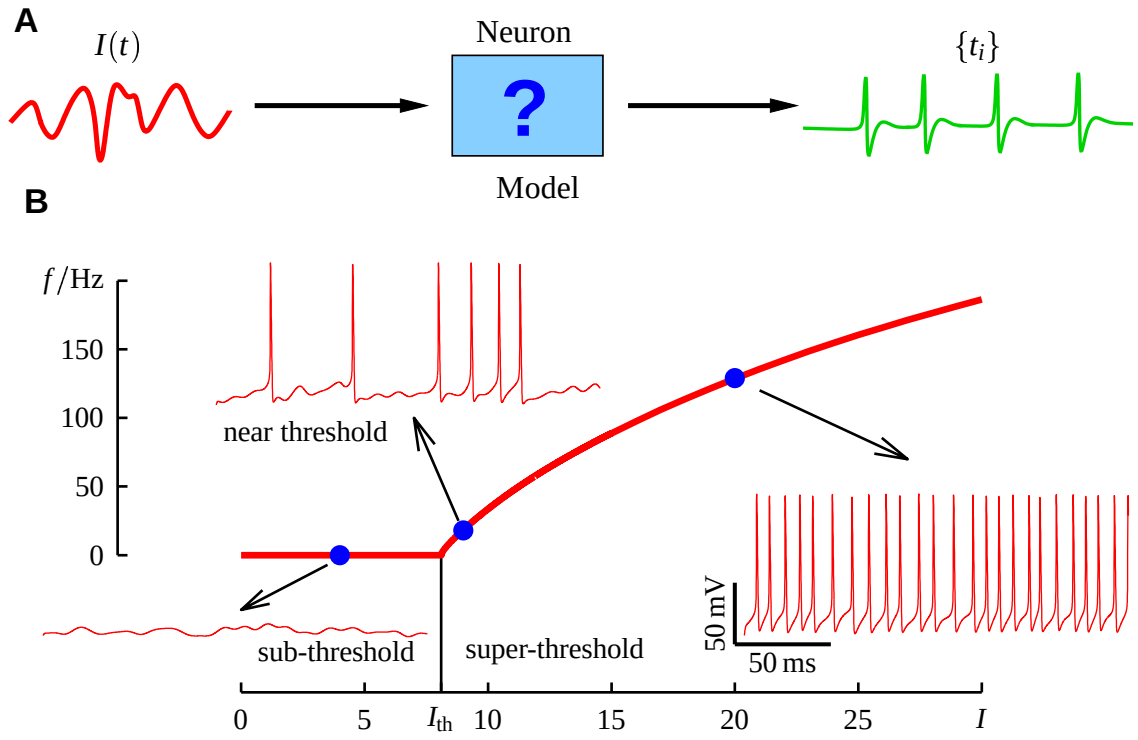

Figure 3.1: MODELING THE GENERATION OF SPIKES. **A** An ionic current $I(t)$ is transformed into a sequence of spikes $\{t_i\}$ at the spike initiating zone of a neuron. The aim of this chapter is to introduce models for this transformation process (box). **B** Shown is the f-I-curve of the Connor model and three simulated voltage traces (insets), which were evoked by Gaussian white-noise stimuli with standard deviation $4\,\mu\mathrm{A/cm^2}$, cut-off frequency 100 Hz and different mean values of 4, 9 and $20\,\mu\mathrm{A/cm^2}$ (dots). Input currents I are separated by the neuron's f-I-curve into two different regimes. No spikes are produced in the sub-threshold regime (left inset), where the input currents stay below the threshold current I_{th}. The neuron fires repetitively in the super-threshold regime (right inset) for currents above threshold I_{th}. Currents fluctuating around threshold I_{th} occasionally evoke spikes (upper left inset) when they are super-threshold.

More abstract models than conductance-based models are introduced in this chapter. They focus on the timing of spikes instead on the precise time course of the membrane potential (Fig. 3.1 A). Their parameters are defined by macroscopic properties directly. Instead of adjusting some microscopic parameter to fit a macroscopic property, the latter is used directly as a parameter for the models. The neuron's f-I-curve plays an important role, since it can be measured easily and characterizes basic nonlinear properties of a neuron. A model not reproducing the neuron's f-I-curve fails to predict even the right firing frequency for constant stimuli.

The dynamics of the spike generating mechanisms is exclusively discussed in this chapter. Slower processes like spike-frequency adaptation are not considered here. Their discussion is given in chapter 4.

The dynamics of a spiking neuron has two regimes (Fig. 3.1 B). In the sub-threshold regime, where the input current stays below the threshold current of the neuron's f-I-curve, no spikes are generated and stable fixed points exist. The super-threshold regime is characterized by the existence of stable limit cycles, which correspond to the spikes. The type of bifurcation of the transition from the quiescent to the oscillating regime determines various functional properties of a neuron as summarized in the previous chapter.

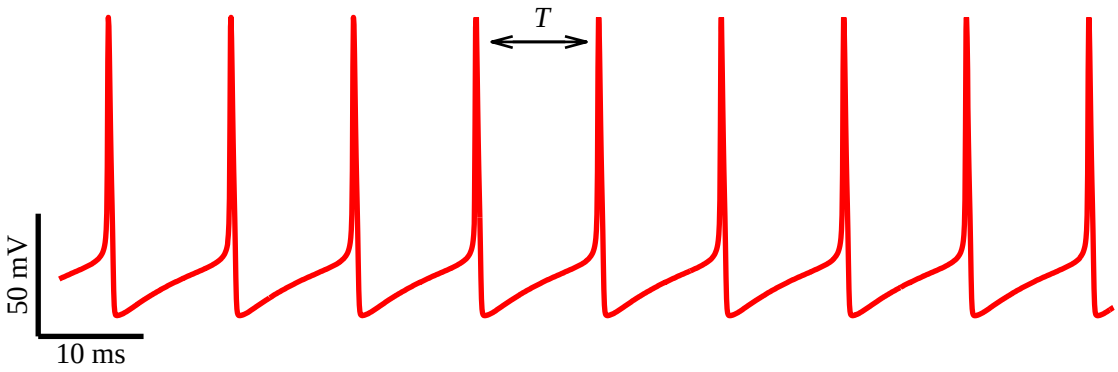

Figure 3.2: SPIKES AND OSCILLATIONS. A neuron with only fast gating variable fires periodically, if it is stimulated with a constant input. This is an oscillation with period T. Shown is the voltage trace of the Traub-Miles model evoked by a current of $I = 2\,\mu\text{A/cm}^2$.

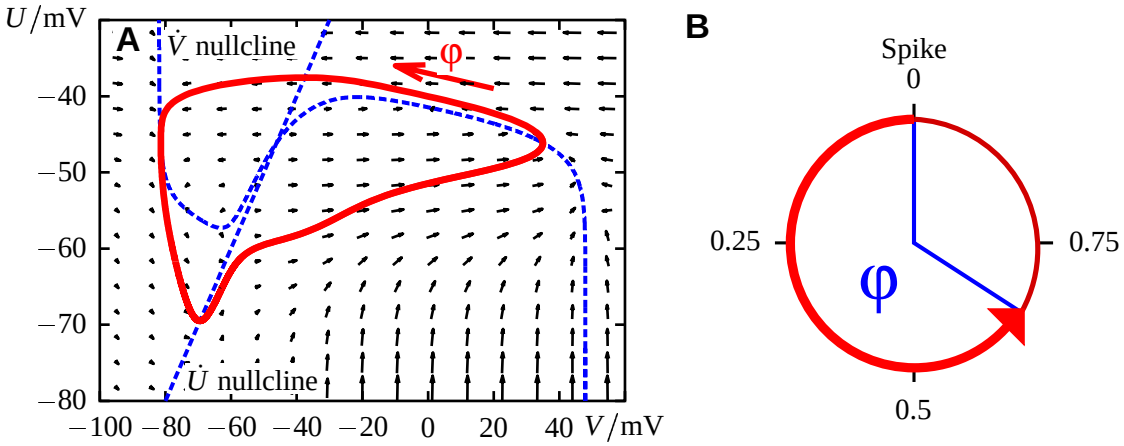

Figure 3.3: LIMIT CYCLE OF AN OSCILLATION. **A** The solid line is the limit cycle of the Traub & Miles model corresponding to the periodic spike train of Fig. 3.2. The membrane potential V is plotted on the x-axis. The two recovery variables h and n are combined into the representative potential U on the y-axis. The flow field is sketched by the arrows and the two nullclines are plotted as dashed lines. **B** The movement on a limit cycle like in A is a one-dimensional circular dynamics. Each location on the circle can be defined by a phase angle φ. A phase angle of $\varphi = 1 = 0$ corresponds to the peak of a spike (rightmost extension of the trajectory shown in A).

In the following four sections the super-threshold dynamics especially of class-I neurons is explored. The interaction with the sub-threshold regime is investigated in section 3.5.

3.1 Firing frequency as a phase velocity

Consider a deterministic neuron with only fast gating variables, like the Hodgkin-Huxley model or the Traub-Miles model. If such a neuron is stimulated with a constant input current I, it will fire regularly as in Fig. 3.2. Each interspike interval has the same duration T, and the voltage trace from one spike to the next is repeated periodically. This is an oscillation. The neuron fires with a frequency $f = 1/T$.

In the phase space of a dynamical system like a neuron the trajectory of an oscillation follows a closed orbit, which is a stable limit cycle. The limit cycle of the oscillation from

Fig. 3.2 is shown in Fig. 3.3 A. The membrane potential is plotted on the x-axis and the two recovery variables h of the sodium inactivation and n of the potassium activation are combined into the representative potential U on the y-axis (see variable reduction-scheme of Kepler et al. (1992) described in detail in section 2.3). Cycling on this orbit yields the periodic voltage trace of Fig. 3.2.

Each location on the limit cycle is uniquely defined by a phase angle φ of the oscillation (Fig. 3.3 B). The phase angle φ can be defined to be zero at the peak of a spike, which corresponds to the rightmost extension of the limit cycle in Fig. 3.3 A. The phase increases while moving on the limit cycle until it reaches the value one after exactly one cycle.

The speed of the movement on such a limit cycle is the phase velocity $\dot{\varphi}$, which is the time derivative $\mathrm{d}\varphi/\mathrm{d}t$ of the phase angle. The dependence of the phase velocity on the phase angle

$$\boxed{\begin{array}{rcll} \dot{\varphi} & = & g(\varphi;I) & ; \quad \varphi < 1 \\ \varphi & = & 0 & ; \quad \varphi = 1 \;\rightarrow\; \text{spike} \end{array}} \tag{3.1}$$

completely defines the one-dimensional dynamics on the limit cycle for a given input current I. The phase φ is integrated until it reaches one. Then a spike is produced and the phase is reset to zero. Provided the system stays on its limit cycles for all time-dependent inputs $I(t)$, the phase oscillator (3.1) sufficiently describes the generation of spikes.

3.1.1 The non-leaky phase oscillator

The dependence of the firing frequency f on the input current I is described by the neuron's f-I-curve $f(I)$. The f-I-curve gives the period $T = 1/f(I)$ of the limit cycle corresponding to the constant input current I. If the firing frequency is increased, the system has to move around the limit cycle faster to complete one cycle in a shorter time. The simplest model, which just reproduces the neuron's f-I-curve, is the non-leaky phase oscillator

$$\boxed{\begin{array}{rcll} \dot{\varphi} & = & f(I) & ; \quad \varphi < 1 \\ \varphi & = & 0 & ; \quad \varphi = 1 \;\rightarrow\; \text{spike} \end{array}} \tag{3.2}$$

where the phase velocity is directly given by the f-I-curve $f(I)$ of the neuron.

For the trivial case of a constant stimulus I the non-leaky phase oscillator (3.2) is an exact model for periodic spike trains like in Fig. 3.2. The time of one period

$$T = \int_0^1 \frac{\mathrm{d}\varphi}{f(I)} \tag{3.3}$$

equals $1/f(I)$ as required.

3.1.2 Performance of the non-leaky phase oscillator

Stimuli $I(t)$ of neurons are depending on time t. Cortical neurons receive input via synapses. The summated postsynaptic currents result in a fast fluctuating input current $I(t)$ to the spike generator with frequency components upto roughly 1000 Hz. Therefore,

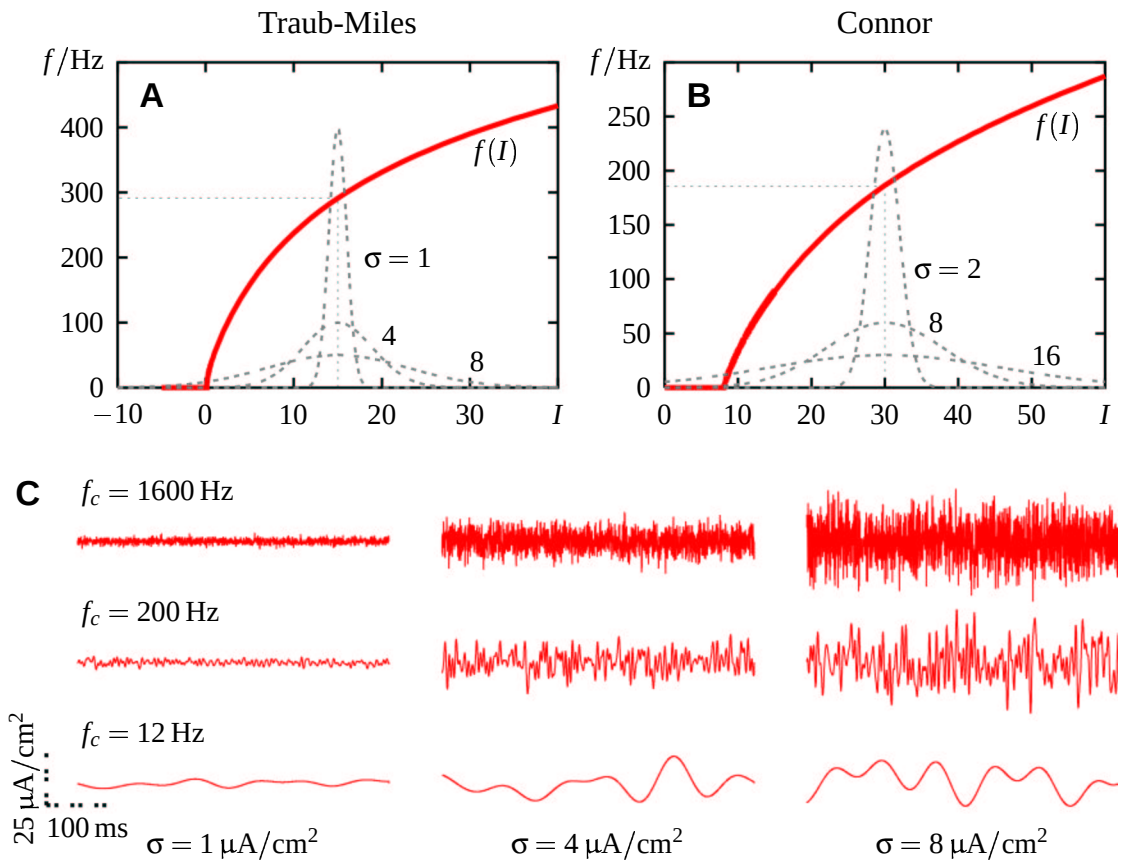

Figure 3.4: STIMULI USED TO TEST THE PHASE MODELS. **A** The f-I-curve $f(I)$ of the Traub-Miles model and the distributions of three Gaussian white-noise stimuli with mean $\mu = 15\,\mu\text{A/cm}^2$ and standard deviations σ as indicated in $\mu\text{A/cm}^2$. The firing frequency evoked by this mean current is $f = 291\,\text{Hz}$. **B** The f-I-curve of the Connor model and the distributions of three Gaussian white-noise stimuli with mean $\mu = 30\,\mu\text{A/cm}^2$. The firing frequency evoked by this mean current is $f = 186\,\text{Hz}$. **C** Examples of the Gaussian white-noise stimuli with three different cut-off frequencies f_c and standard deviations σ as used for the tests on the Traub-Miles model.

the capability of a model to reproduce the timing of spikes evoked by such time dependent stimuli, is of great importance.

To quantify the power of a phase model in predicting the timing of spikes it was tested on conductance-based models. In this chapter the Connor and the Traub-Miles model are used as a reference (see appendix A for a definition). Both are models of class-I neurons and they differ in the A-current, which is included in the Connor model. Gaussian white-noise stimuli with a mean intensity μ, standard deviation σ and cut-off frequency f_c were used as the input current for both the conductance-based model and the phase oscillator (3.1). The relation of these stimuli to the f-I-curves of the Connor and the Traub-Miles model and some example stimuli are illustrated in Fig. 3.4. Note that with these stimuli the results for the Traub-Miles model and the Connor model are not directly comparable. The firing frequency evoked by the mean intensity of the stimuli differs by approximately 100 Hz and the stimuli with high standard deviations are closer to threshold of the Connor model than of the Traub-Miles model.

A comparison of the non-leaky phase model with the Traub-Miles model is illustrated in Fig. 3.5 for one particular stimulus. First, the conductance-based model was integrated (second-order Runge-Kutta method (Press et al., 1992), step-width 0.001 ms)

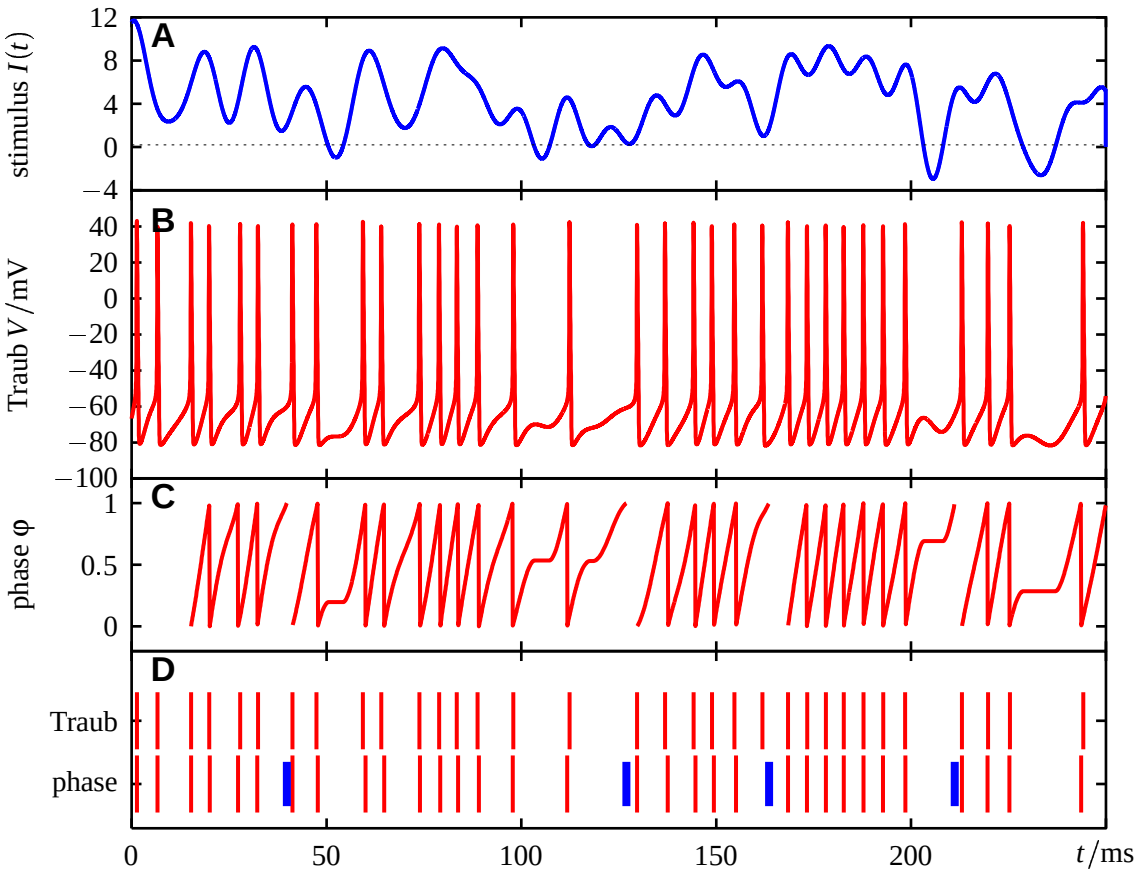

Figure 3.5: COMPARISON OF A PHASE OSCILLATOR WITH THE TRAUB-MILES MODEL. **A** The stimulus used for this particular example (Gaussian white-noise with mean $5\,\mu A/cm^2$, standard deviation $3\,\mu A/cm^2$, and cut-off frequency 100 Hz). **B** The voltage trace evoked by this stimulus simulated with the Traub-Miles model. **C** The phase angle of a non-leaky phase oscillator (3.2) was calculated for the same stimulus using the f-I-curve of the Traub-Miles model. **D** The spikes as detected from the voltage trace of the Traub-Miles model in B (upper row, number of spikes $N_1 = 33$) and from the non-leaky phase oscillator (bottom row, number of spikes $N_2 = 32$). The four thick and short spikes indicate spikes of the phase oscillator, which were more than one millisecond apart from the corresponding spike of the Traub-Miles model. At such failures the phase model was reset and its integration was continued at the following spike of the Traub-Miles model (gaps in C). At total $N_c = 28$ spikes were predicted correctly within $\pm$ one millisecond, resulting in $\Gamma = 80\%$ (without the initial three spikes).

and the spikes were detected from the generated voltage trace. The integration of the phase model (Euler method, step-width 0.001 ms) was started at the third spike of the conductance-based model. The timing of each spike generated by the phase model was compared with the corresponding spike of the conductance-based model. If they differed by more than half a millisecond, the integration of the phase model was stopped and started again at the following spike of the conductance-based model. The performance of the phase model was quantified by relating the number N_c of correctly predicted spikes (within the time window Δt of ± 0.5 ms) to the total number of spikes N_1 and N_2 evoked by the conductance-based model and the phase model, respectively. For that purpose the coincidence rate

$$\Gamma = \frac{KN_c - N_1N_2}{\frac{1}{2}(N_1+N_2)(K-N_1)} \tag{3.4}$$

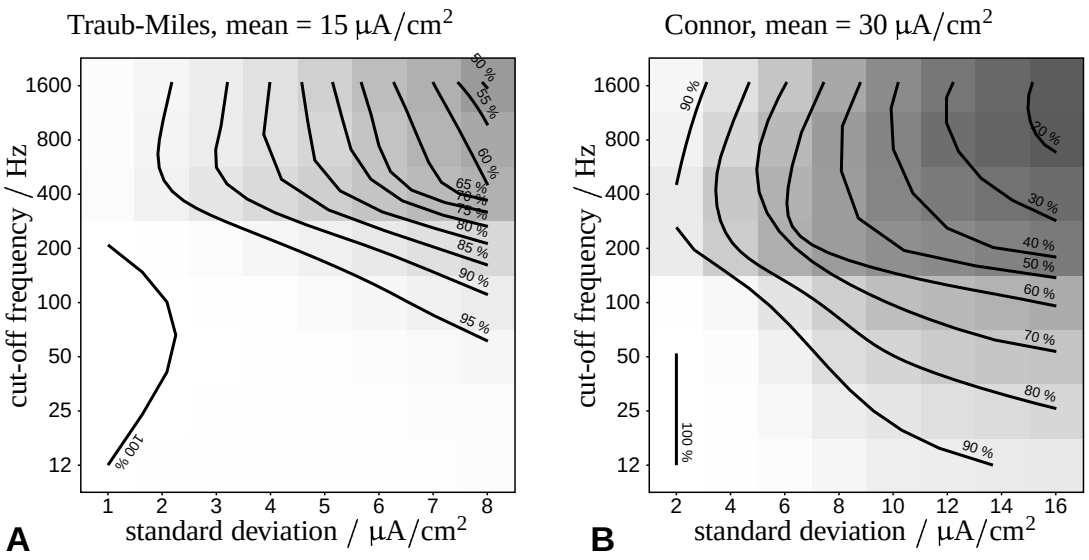

Figure 3.6: PERFORMANCE OF THE NON-LEAKY PHASE OSCILLATOR. Shown is the coincidence rate Γ (3.4) for various Gaussian white-noise stimuli. On the abscissa the standard deviation of these stimuli is indicated. The cut-off frequency is drawn on the ordinate. See Fig. 3.4 for some examples of the stimuli and their relation to the f-I-curves of the neuron models. Each of the stimuli was 2 s long and the coincidence rate Γ was averaged over 10 runs of different realizations of these stimuli. Spikes within ± 0.5 ms were counted as coincident. **A** Performance of the non-leaky phase oscillator (3.2) tested on the Traub-Miles model using stimuli with mean 15 $\mu A/cm^2$. For moderate stimuli with cut-off frequencies below 100 Hz the non-leaky phase oscillator predicts more than 95 % of the spikes correctly. **B** The spikes of the Connor model for stimuli with mean 30 $\mu A/cm^2$ are predicted worse. This is partly due to the lower mean firing rate of below 200 Hz evoked by these stimuli.

was calculated, which corrects for spike coincidences by chance (Kistler et al., 1997). $K = 0.5T/\Delta t$ and T is the stimulus duration. Γ equals 100 % if each spike was predicted correctly. The averaged coincidence rates Γ over 10 runs of different 2 s long realizations of each Gaussian white-noise stimulus are summarized in contour plots like in Fig. 3.6.

Alternatively, the phase model could have been integrated independently from the conductance-based model, i.e. without resetting it on failures to predict the spikes within the time window Δt. However, resetting the phase model on failures is the better choice for the purpose of this chapter. First, the coincidence rate with resetting measures how long the model on average is able to predict the spikes correctly, instead of emphasizing the number of spikes needed to recover from failures. Second, the resolution of the coincidence rate is finer, since without resetting the number of incorrectly predicted spikes increases, and Γ drops very fast to zero. Third, the coincidence rate is mainly used to compare the performance of different phase models, rather than to give absolute measures of their performance.

The performance of the non-leaky phase oscillator (3.2) for the Connor and especially the Traub-Miles model is astonishingly good. Stimuli slower than the mean firing frequency are predicted with high fidelity. However, the non-leaky phase oscillator fails to predict faster and strongly fluctuating stimuli.

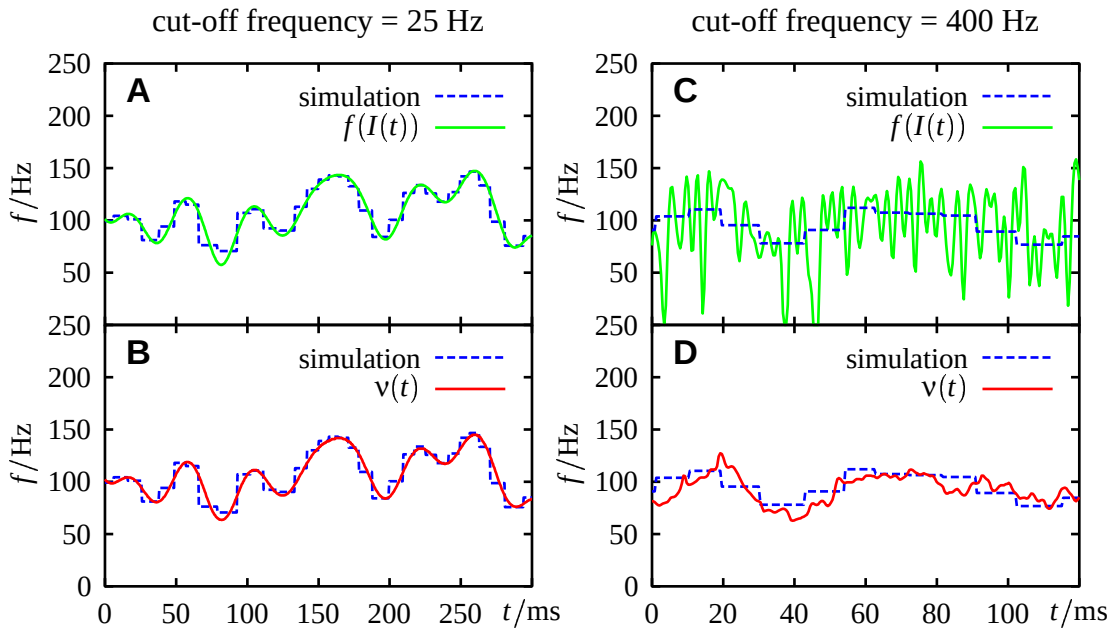

Figure 3.7: LOW-PASS FILTER EFFECT OF THE SPIKE GENERATOR. The Connor model was used to simulate the response of a neuron to Gaussian white-noise stimuli with mean and standard deviation of 16 and 4 $\mu A/cm^2$, respectively. Spikes were detected and the firing frequency as the inverse of the interspike intervals was calculated (simulation: dashed lines). **A & C** The simulated firing frequency was compared with the firing frequency which is obtained by mapping the stimulus through the neuron's f-I-curve $f(I)$ (solid line). **B & D** The mapped firing frequency $f(I)$ was smoothed by the running average (3.6) to account for the low-pass filter effect of the spike generator ($\nu(t)$, solid line). **A** For a slow stimulus with cut-off frequency 25 Hz $f(I(t))$ closely follows the firing frequency measured from the simulation, since the mean firing frequency of about 100 Hz is about four times larger than the cut-off frequency of the stimulus. **B** Applying the running average (3.6) has almost no effect. **C** Firing frequencies evoked by a stimulus with cut-off frequency 400 Hz. In contrast to the slow stimulus used in A, the mapping of this fast stimulus fluctuates much faster than the simulated firing frequency. Here the cut-off frequency of the stimulus is about four times larger than the mean firing frequency. **D** Applying the running average (3.6) enhances the match with the simulated firing frequency.

3.1.3 Signal-transmission properties of firing frequencies

An important aspect of signal transmission via spikes is the low-pass filter effect of the spike generator. Fluctuations of the stimulus between two succeeding spikes in general cannot be resolved from the spike train. A particular interspike interval could result from a constant stimulus or from a fluctuating stimulus. The situation is similar as for the sampling theorem, which states that a signal has to be sampled with twice its highest frequency component in order to preserve all information. For a neuron, the samples are the interspike intervals (*ISI*). Thus, only frequency components of the stimulus smaller than half of the corresponding firing frequency $f = 1/ISI$ can be transmitted if no assumptions about the stimulus are made. Usually, spikes and interspike intervals evoked by dynamic stimuli are unequally spaced in time. Spikes can be close together, resulting in small interspike intervals and large firing frequencies. If the interspike intervals are large, then the firing frequency is low. Therefore, this low-pass filter effect has not a fixed cut-off frequency. It rather depends on the actual firing frequency. At high firing frequencies faster fluctuations of the stimulus can be transmitted than at low firing frequencies.

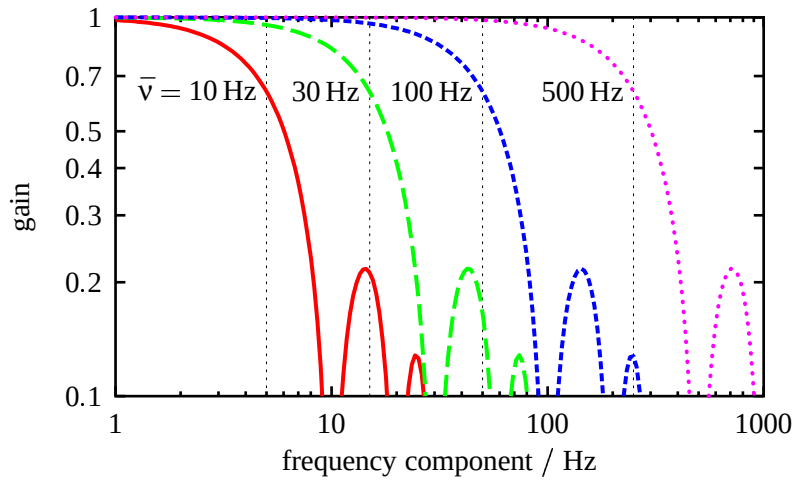

Figure 3.8: TRANSFER FUNCTION OF THE NON-LEAKY PHASE OSCILLATOR. Plotted is the gain, which is the absolute value of the transfer function (3.8), for different values of the mean firing frequency $\bar{\nu}$ as indicated. The vertical dotted lines mark the values $\bar{\nu}/2$, where the gain is about 64%.

This effect is illustrated in Fig. 3.7. The stimulus mapped through the neurons f-I-curve $f(I(t))$ is compared with the firing frequency obtained from the spikes (panel A & C). Input and output firing frequency match pretty well as long as the cut-off frequency of the stimulus is less than half of the firing frequency. If the stimulus is faster, then the input $f(I(t))$ fluctuates much more than the output firing frequency.

These considerations can be quantified by means of the non-leaky phase oscillator. Integrating the differential equation of the non-leaky phase oscillator (3.2) from one spike to the next yields

$$\int_0^1 \mathrm{d}\varphi = 1 = \int_{t-T(t)/2}^{t+T(t)/2} f(t')\,\mathrm{d}t'\,, \tag{3.5}$$

where $T(t)$ is the interspike interval at time t and $f(t) = f(I(t))$ is the stimulus mapped through the neurons f-Icurve. The reciprocal of $T(t)$ is the observed firing frequency $\nu(t) = 1/T(t)$, which can be measured given the spikes. How to estimate $\nu(t)$ from several spike trains evoked by the same stimulus is discussed in chapter 5. In contrast to $\nu(t)$, the firing frequency $f(t)$ given by the neuron's f-I-curve cannot be derived from the spike trains directly. Dividing (3.5) by $T(t)$ results in

$$\nu(t) = \frac{1}{T(t)} \int_{t-T(t)/2}^{t+T(t)/2} f(t')\,\mathrm{d}t'\,. \tag{3.6}$$

Neglecting the discrete nature of spike timing, (3.6) is a running average over $f(t)$ defined for each time t. This equation is the mathematical formulation of the considerations from above. The input $f(t)$ is smoothed — it is low-passed filtered — by the running average (3.6). The width of the averaging window $T(t)$ corresponds to the actual interspike interval, which is given by the firing frequency $\nu(t) = 1/T(t)$. Thus, the averaging window is small at high firing frequencies ν and vice versa. Note that (3.6) is an implicit equation for the output firing-frequency $\nu(t)$, since $T(t)$ on the right hand side equals $1/\nu(t)$.

The resulting interspike intervals T can be written as a mean interspike interval $\bar{T}$ plus a deviation. Assuming the fluctuations of $f(t)$ to be small, the deviations of the resulting interspike intervals $T(t)$ from the mean interspike interval $\bar{T}$ are small, too. Neglecting the

deviations on the right hand side of (3.6) only, yields an explicit equation for the output firing-frequency $\nu(t)$

$$\nu(t) = \frac{1}{T}\int_{t-\bar{T}/2}^{t+\bar{T}/2} f(t')\,\mathrm{d}t' \,. \tag{3.7}$$

An important aspect of this approach is that the usage of the neuron's f-I-curve covers already some of the nonlinearities of the spike generator. In that the firing frequency $f(t)$ is considered as the input directly, these nonlinearities are avoided.

For equation (3.7) the transfer function $H(\omega)$ can now be calculated for different mean interspike intervals $\bar{T}$, i.e. mean firing frequencies $\bar{\nu} = 1/\bar{T}$:

$$H(\omega) = \frac{\mathcal{F}[\nu(t)]}{\mathcal{F}[f(t)]} = \frac{2\bar{\nu}}{\omega}\sin\left(\frac{\omega}{2\bar{\nu}}\right) \,. \tag{3.8}$$

$\mathcal{F}[f(t)]$ is the Fourier-transform of the input, $\mathcal{F}[\nu(t)]$ is the Fourier-transform of the output, and the angular frequency ω is 2π times the frequency component of the input $f(t)$. The gain as the absolute value of this transfer function is illustrated in Fig. 3.8. For $\nu = \bar{\nu}/2$, the gain is about 64%. Thus, a neuron firing at some firing frequency acts like a low-pass filter with a cut-off frequency at about one half of this firing frequency. Fluctuations of the stimulus $I(t)$ between two succeeding spikes cannot be transmitted. Note that this analysis assumes the fluctuations of the mapped input $f(I)$ to be small.

3.2 More about phase velocities

The non-leaky phase model (3.2) reproduces no more than the neuron's f-I-curve. It is a reasonable model to describe the spikes evoked by approximately constant stimuli above threshold of the f-I-curve. However, it fails to reproduce responses to fast and strong fluctuating inputs. One reason for this failure is the missing dependence of the phase velocity on the phase angle. To get an impression of this dependence, the phase velocity on limit cycles in conductance-based models is explored in this section.

A specific phase angle φ can be assigned for each location on a limit cycle by relating its distance along the cycle from a reference point to the whole circumference of the limit cycle. All variables of the conductance-based model have to have the same units, in order to calculate distances on the limit cycle. A suitable possibility is taking their equivalent potentials as defined by (2.8) on page 14. Once phase angles are numerically assigned to various limit cycles, isophases can be drawn into the phase space by connecting equal phase angles from the different limit cycles. A limit cycle together with such isophases of the Traub-Miles model in its reduced two-dimensional version is illustrated in Fig. 3.9 A. Starting with $\varphi = 0$ at the top of a spike, the isophases for phase angles of multiples of 0.05 are marked by the thick lines. The dots are equally spaced in time ($\Delta t = 0.2$ ms).

Knowing for each location on a limit cycle the phase angle φ and the corresponding time t, the phase velocity can be calculated as the time derivative of the phase angle (Fig. 3.9 B). The phase velocity depends strongly on the phase angle and is influenced by the input current I. During the spike there are two regions with a very high phase velocity, while between the spikes ($0.5 < \varphi < 0.6$) it is very low.

The method described above is only one possibility to assign phases on a limit cycle. Different possibilities of phase assignments can be transformed into one another. A

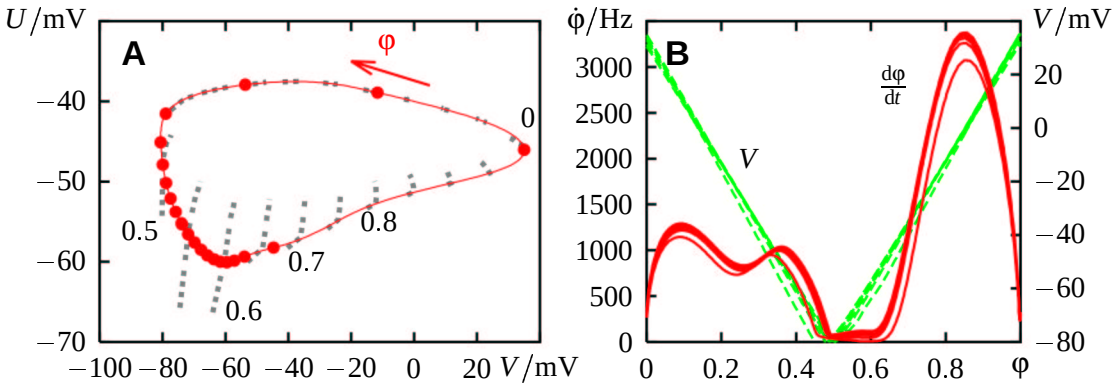

Figure 3.9: PHASE ANGLES ON LIMIT CYCLES. **A** The closed loop is the limit cycle of a reduced Traub-Miles model for an input current of $I = 11\,\mu\text{A/cm}^2$. The dots mark the state of the system at every 0.2 ms. The lower right and upper part of the limit cycle is the spike. The system moves through this part very fast (~ 1 ms). The system spends most of the time on the remaining part of the limit cycle between the spikes. Distances on the limit cycle relative to its circumference define phase angles φ. The thick lines are isophases separated by $\Delta\varphi = 0.05$ calculated on several limit cycles for different input currents. Since the U axis is scaled differently than the V-axis the isophases appear unequally spaced. **B** The resulting phase velocity $\dot{\varphi}$ in dependence on the phase angle φ (solid lines) for input currents $I = 2$, 12, 22, 32, 42, and $52\,\mu\text{A/cm}^2$. The corresponding membrane potential V is plotted for orientation (dashed lines).

special transformation is the following, which for a particular limit cycle transforms the phases into time t.

Any phase model (3.1) with parameter I

$$\dot{\varphi} = g(\varphi; I)\ ,\ \ 0 \le \varphi < 1 \tag{3.9}$$

can be transformed with

$$\frac{d\psi}{d\varphi} = \frac{1}{g(\varphi; I^*)\int_0^1 \frac{d\varphi'}{g(\varphi', I^*)}} \tag{3.10}$$

to a new phase oscillator with phase ψ for a particular reference value I^* of the parameter I. The dynamics (3.9) in the new variable ψ reads

$$\dot{\psi} = \frac{d\psi}{d\varphi}\dot{\varphi} = \frac{g(\varphi; I)}{g(\varphi; I^*)\int_0^1 \frac{d\varphi'}{g(\varphi', I^*)}}\ ,\ \ 0 \le \psi < 1\ . \tag{3.11}$$

For the reference value I^* this equals the non-leaky phase oscillator

$$\dot{\psi} = f(I^*) = const\ , \tag{3.12}$$

where $\psi(t)$ is proportional to time t. In general, however, $\dot{\psi}$ in (3.11) does depend on the phase angle ψ for different values of the parameter I.

Such a transformation was applied on the phase velocities from Fig. 3.9 B. The resulting phase velocities of the new phase variable ψ are displayed in Fig. 3.10 B. The highest value of the input current I used, which evoked the fastest oscillation, was used as the reference parameter I^*. As can be seen in panel A, the isophases of the new phase angle φ are now concentrated on the slow part of the limit cycle. Consequently the spikes are now restricted to less than a third of the phase angles (panel B). The phase velocity

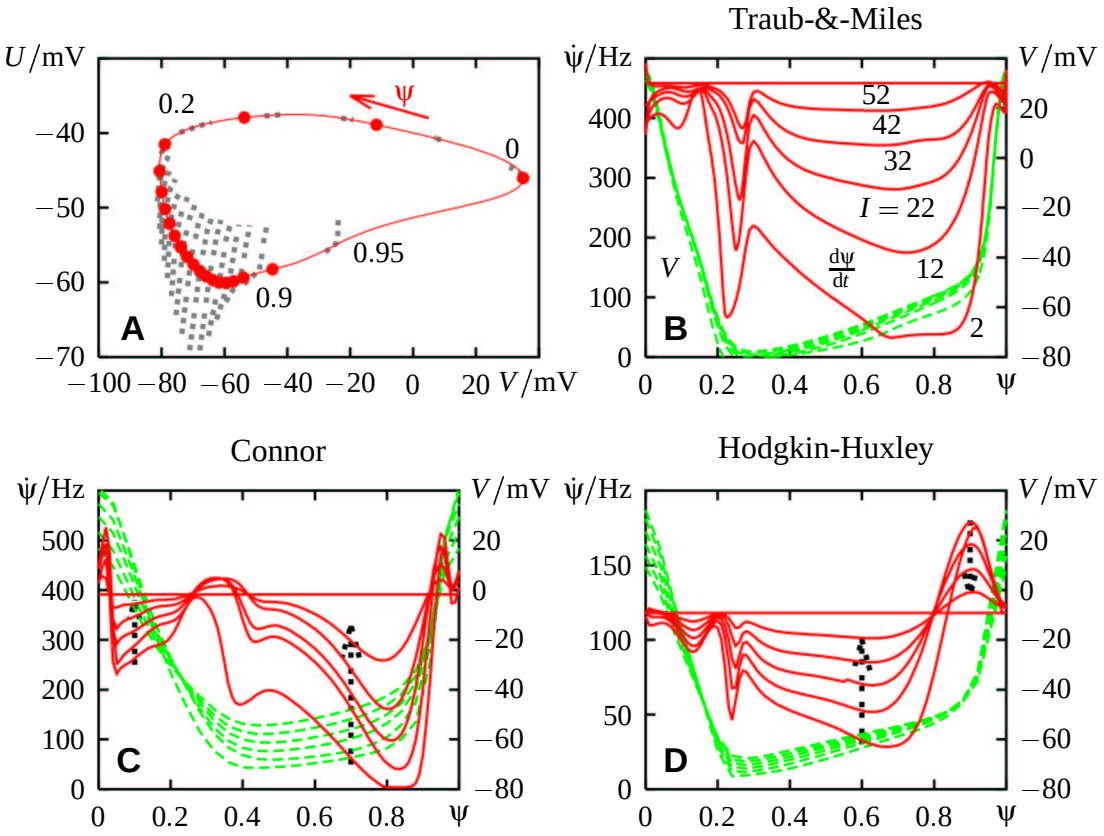

Figure 3.10: TRANSFORMED PHASE ANGLES IN CONDUCTANCE-BASED MODELS. **A** The phase angle φ in Fig. 3.9 was transformed using (3.10) with $I^* = 52\,\mu\mathrm{A/cm^2}$. The same limit cycle as in Fig. 3.9 A for $I = 11\,\mu\mathrm{A/cm^2}$ is shown together with the isophases (thick lines) of the transformed phase angle ψ. **B** The velocities $\dot{\psi}$ (solid lines) of the transformed phase angle of the Traub-Miles model for limit cycles caused by different input currents as indicated (in $\mu\mathrm{A/cm^2}$). By definition the phase velocity for $I^* = 52\,\mu\mathrm{A/cm^2}$ is constant and equals the firing frequency. The corresponding membrane potentials V are plotted for comparison (dashed lines). **C** Phase velocities (solid lines) of the Connor-model as a further example for a class-I neuron. The input currents used were 10, 30, 50, 70, 90, and 110 $\mu\mathrm{A/cm^2}$, and the reference current was $I^* = 110\,\mu\mathrm{A/cm^2}$. Arrows indicate the direction of increasing input intensity. The threshold current is at $I_{\mathrm{th}} = 8.1\,\mu\mathrm{A/cm^2}$. **D** Phase velocities (solid lines) of the Hodgkin-Huxley model as an example for a class-II neuron. The input currents used were 7, 17, 27, 37, 47, and 57 $\mu\mathrm{A/cm^2}$, and the reference current was $I^* = 57\,\mu\mathrm{A/cm^2}$. The threshold current of the Hodgkin-Huxley model is at $I_{\mathrm{th}} = 6.2\,\mu\mathrm{A/cm^2}$.

for $I^* = 52\,\mu\mathrm{A/cm^2}$ is constant by construction. However, the phase velocities still depend on the phase angle for all other input currents. The phase velocity decreases during the interspike interval and almost instantaneously steps to a high value at the beginning of a spike. Since the firing frequency increases with input current, the phase velocity increases, too.

The phase velocities of a further class-I and a class-II model neuron are compared in Fig. 3.10 C & D. The phase velocity decreases in both models with increasing phase angle. In addition, the phase velocity also increases with input intensity, if it is below the phase velocity of the reference current I^*. Velocities above the reference decrease with input intensity. One significant difference between class I (B & C) and class II (panel D) is that

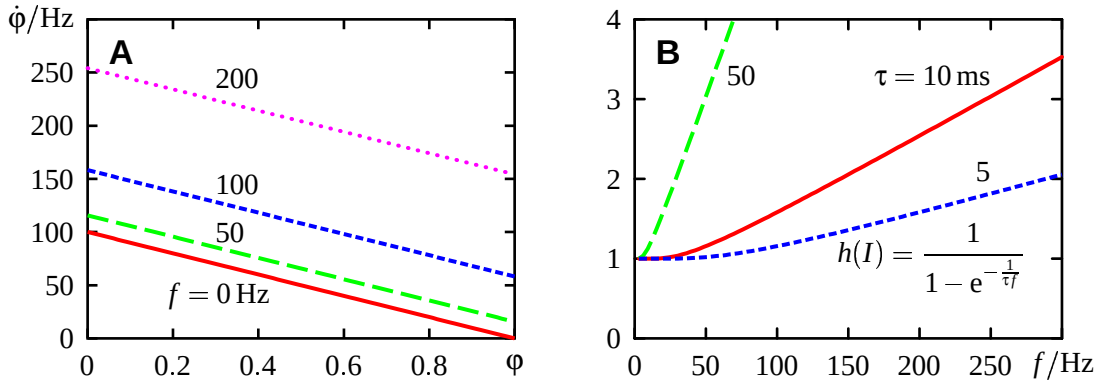

Figure 3.11: PROPERTIES OF THE LEAKY PHASE OSCILLATOR. **A** The dependence of the phase velocity $\dot{\varphi}$ on the phase angle φ for different firing frequencies as indicated in Hz and $\tau = 10\,\text{ms}$. The phase velocities of the leaky phase oscillator roughly resemble the observed dependence on the phase angle in Fig. 3.10, in that they decrease with increasing phase. **B** The dependence of the inhomogeneity $h(I)$ of the leaky phase oscillator (3.13) on the firing frequency for three different values of the time constant as indicated in milliseconds.

for small input currents class-I neurons have phase velocities very close to zero directly before the onset of the spike. This reflects the ghost of the saddle in their phase space and is the reason for the infinitely long periods near threshold.

3.2.1 The leaky phase oscillator

The non-leaky phase oscillator (3.2) can now be improved with the experience gained in the last section about the dependence of phase velocities on phase in conductance-based models. A crude but very simple way to sketch the dependence of the phase velocity on phase of the models from Fig. 3.10, is the following:

$$\dot{\varphi} = -\varphi/\tau + h(I) \tag{3.13}$$

The phase velocity decreases linearly with increasing phase. The slope of this dependence is $1/\tau$, which is independent of the input current I. The offset $h(I)$ is set by the input I. Forcing this phase model to obey the f-I-curve results in

$$\boxed{\begin{aligned} \tau\dot{\varphi} &= -\varphi + \frac{1}{1-\mathrm{e}^{-\frac{1}{\tau f(I(t))}}} \quad ; \quad \varphi < 1 \\ \varphi &= 0 \quad ; \quad \varphi = 1 \rightarrow \text{spike} \end{aligned}} \tag{3.14}$$

In the following this phase model is referred to as the leaky phase oscillator. It has a time constant τ as the only additional parameter to the neuron's f-I-curve. The basic properties of the leaky phase oscillator are illustrated in Fig. 3.11.

3.2.2 Performance of the leaky phase integrator

The performance of the leaky phase oscillator is indeed better than the performance of the non-leaky phase oscillator (see Fig. 3.12). However, the spikes evoked by stimuli with cut-off frequencies higher than the mean firing frequency are still predicted with low coincidence rate.

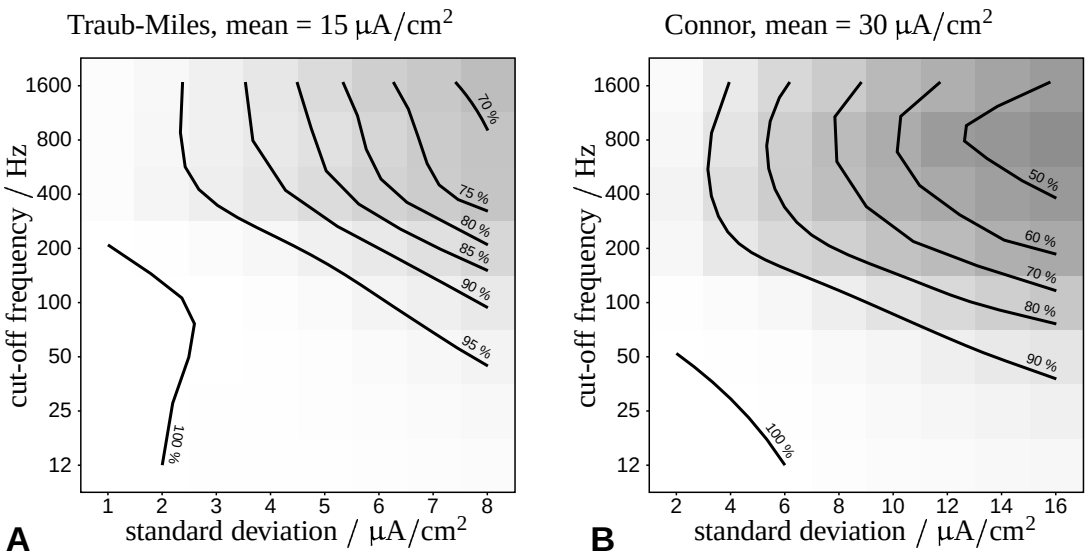

Figure 3.12: PERFORMANCE OF THE LEAKY PHASE OSCILLATOR. The performance of the leaky phase oscillator (3.14) is much better in comparison to the performance of the non-leaky phase oscillator in Fig. 3.6. Especially the performance to stimuli with high cut-off frequencies and standard deviations is improved.

3.2.3 Relation to the integrate-&-fire model

The integrate-&-fire model is commonly used in both analytical and numerical investigations of neural networks. Driven by the input current I it integrates the membrane voltage V. If it crosses a threshold V_{th}, a spike is elicited and V is reset to V_0:

$$\begin{aligned} \tau\dot{V} &= -V + RI \quad ; \quad V < V_{\text{th}} \\ V &= V_0 \qquad\quad ; \quad V = V_{\text{th}} \rightarrow \text{ spike}\,. \end{aligned} \tag{3.15}$$

τ and R are the time constant and the resistance of the neuron's membrane, respectively. The integrate-&-fire model is a linear membrane equation extended by a voltage threshold, which mimics partly the nonlinearities arising from voltage gated ion channels in order to generate spikes. For input currents I sufficiently below threshold, the neuron's membrane is indeed linear (Koch, 1999).

The f-I-curve of the integrate-&-fire model

$$f(I) = \frac{1}{\tau \ln \frac{RI - V_0}{RI - V_{\text{th}}}} \tag{3.16}$$

is determined by V_{th} and V_0, as well as τ and R. These are properties of the neuron in its non-spiking regime. At threshold $I_{\text{th}} = V_{\text{th}}/R$ the slope of the f-I-curve is infinity (see Fig. 3.13 A).

However, the integrate-&-fire model fails to reproduce the spiking behavior of a neuron, if its parameters τ, R, V_0 and V_{th} are taken as the membrane properties at rest and as the spike threshold. Troyer & Miller (1997) adjusted the reset potential closer to the threshold potential in order to explain the high gain of natural f-I-curves. Stevens & Zador (1998b) introduced a time dependent membrane resistance, which they measured during repetitive firing. Further properties like an absolute or relative refractory period, can be added to the integrate-&-fire model (3.15) to fit it to experimental data (see Fig. 3.16 B).

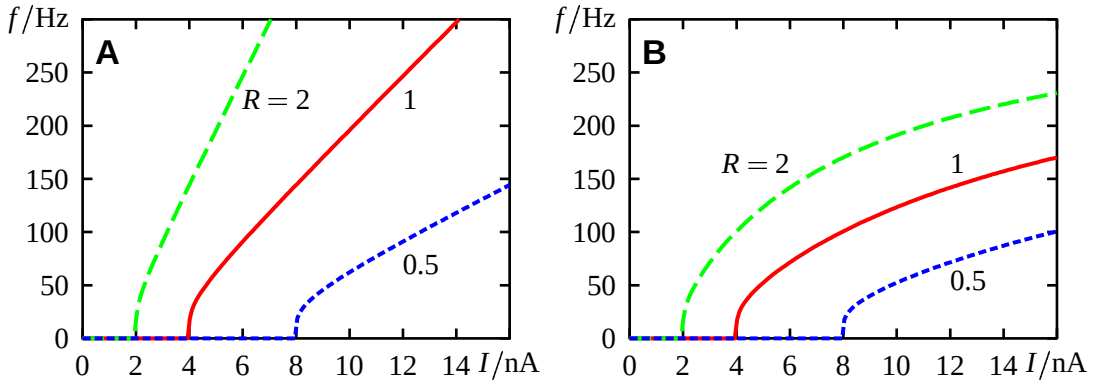

Figure 3.13: f-I-CURVES OF INTEGRATE-&-FIRE NEURONS. Parameters are $\tau = 10\,\text{ms}$, $V_0 = 0\,\text{mV}$, and $V_{\text{th}} = 4\,\text{mV}$. The f-I-curves are drawn for different values of R in MΩ as indicated. **A** The f-I-curves of a standard integrate-&-fire neuron (3.15) increases approximately linearly for large I. **B** Adding a fixed refractory period of 3 ms bounds the f-I-curves below 333 Hz.

With a transformation of the membrane potential V to a dimensionless variable φ

$$\varphi = \frac{V - V_0}{V_{\text{th}} - V_0} \tag{3.17}$$

the integrate-&-fire model can be rewritten as a leaky phase oscillator

$$\tau\dot{\varphi} = -\varphi + \frac{RI - V_0}{V_{\text{th}} - V_0}\,. \tag{3.18}$$

This interpretation of the integrate-&-fire neuron as a phase oscillator sheds new light onto its parameters. Instead of defining properties of the membrane at rest (τ, R, V_0) and a spike threshold V_{th}, they define the dependence of the phase velocity on phase φ. From this point of view, additional parameters (Stevens & Zador, 1998b) or unusual parameter values (Troyer & Miller, 1997) help to approximate the real phase velocities in order to enhance the performance of the integrate-&-fire model in the super-threshold regime. Then, however, these parameters describe the super-threshold properties and may differ from the parameter values of the membrane at rest.

3.3 Saddle-node bifurcation and the θ-model

A useful hint for an appropriate parameterization of a phase model can be obtained by analyzing the type of bifurcation from the fixed point (resting potential) to oscillation (repetitive firing). As discussed in the previous chapter, neurons can be grouped into two classes according to their type of bifurcation. Class-I neurons start to oscillate via a saddle-node bifurcation, while class-II neurons go through a Hopf bifurcation.

In class-I neurons right at the bifurcation, where the node loses stability, the trajectories are attracted by the homoclinic orbit of the saddle. Above the bifurcation this orbit turns into a stable limit cycle like the one shown in Fig. 3.9 A. Approximating the flow field at its saddle to second order in the direction of the homoclinic orbit, results in the normal form

$$\dot{x} = a(I - I_{\text{th}}) + bx^2\,;\;\; a, b \in \mathbb{R} \tag{3.19}$$

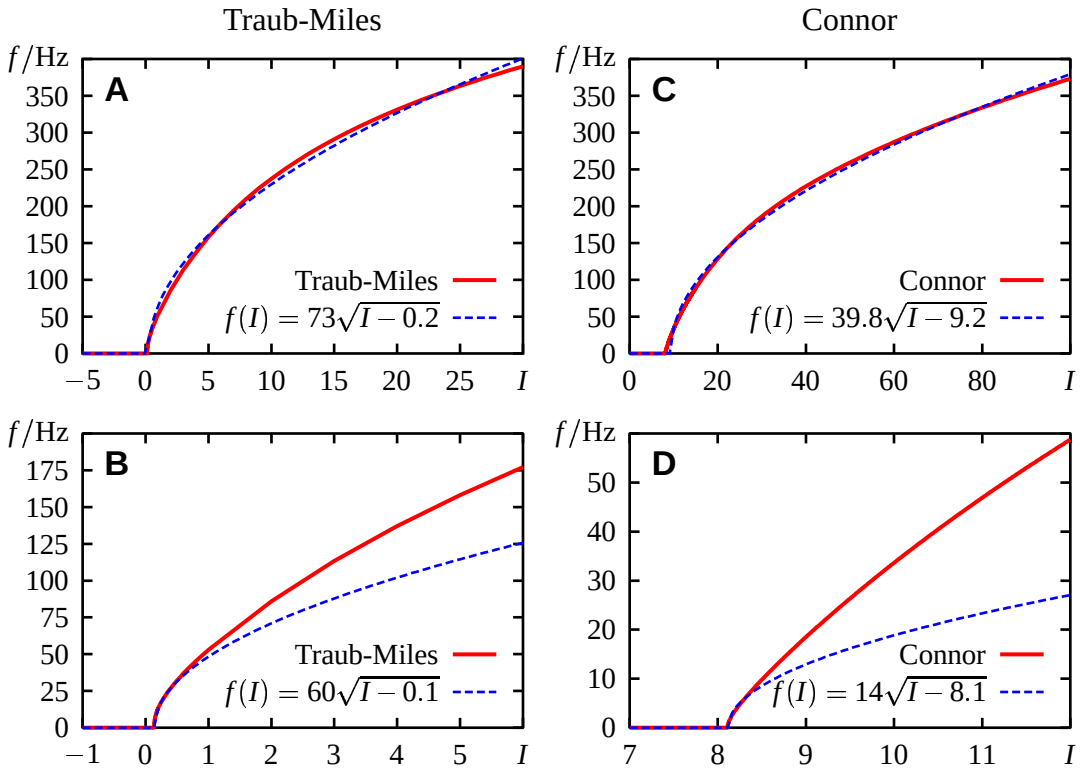

Figure 3.14: SQUARE-ROOT f-I-CURVES. The f-I-curves simulated by two class-I conductance-based models compared with the square-root relation as expected from the saddle-node bifurcation. **A & B** f-I-curve of the Traub-Miles model. **A** The overall dependence of the firing frequency on the input current I is well described by the square-root relation (3.21) of the θ-model. **B** Fitting the square root for currents $I < 0.5\,\mu\text{A/cm}^2$ close to the threshold $I_{\text{th}} = 0.1\,\mu\text{A/cm}^2$ only, indeed results in an excellent approximation in this region, but fails to describe the f-I-curve for higher currents. **C & D** f-I-curve of the Connor model. **C** Overall description of the whole f-I-curve. **D** Focusing on the very vicinity $I < 8.4\,\mu\text{A/cm}^2$ of the threshold $I_{\text{th}} = 8.1\,\mu\text{A/cm}^2$, results in a perfect match of the square-root relation (3.21) to the f-I-curve. For higher currents, however, the f-I-curve increases faster and more linearly than the square root.

of a saddle-node bifurcation (Strogatz, 1994; Hoppensteadt & Izhikevich, 1997). The input current I plays the role of the bifurcation parameter. I_{th} is the threshold of the f-I-curve were the saddle-node bifurcation occurs. Ermentrout (1996) applied this idea to class-I neurons. After a variable transformation he arrived at the so called θ-model[1]

$$\begin{aligned} \tau\dot{\theta} &= (1-\cos\theta) + (1+\cos\theta)c(I-I_{\text{th}}) \quad ; \quad -\pi \le \theta < \pi \\ \theta &= -\pi \quad ; \quad \theta = \pi \rightarrow \text{spike}\,, \end{aligned} \tag{3.20}$$

where τ and c are two parameters $\in \mathbb{R}^+$.

The θ-model is another simple phase oscillator as a model of a spiking neuron. In contrast to the non-leaky and the leaky phase oscillator (3.2) and (3.14), it is based on the saddle-node bifurcation of class-I neurons and therefore has high predictive power. For example, the f-I-curve of the θ-model is the square-root of the input current I relative to threshold I_{th}:

$$f(I) = \frac{\sqrt{c}}{\pi\tau}\sqrt{I - I_{\text{th}}}\,. \tag{3.21}$$

[1] To describe the model dynamics in real time instead of slow time, a slightly different parameterization of the θ-model has been used.

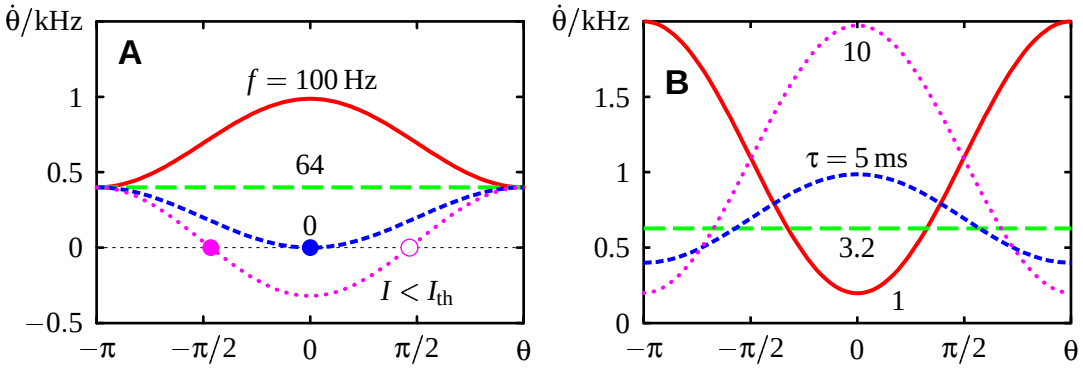

Figure 3.15: PROPERTIES OF THE MODIFIED θ-MODEL. **A** Dependence of the phase velocity $\dot{\theta}$ on the phase angle θ for different input firing frequencies as indicated. The time constant τ is set to 5 ms. At a firing frequency of $f = 0$ Hz the graph of the phase velocity touches the θ-axis at $\theta = 0$. For even lower input currents $I < I_{\text{th}}$ the original model (3.20) exhibits two fixed points. A stable one at negative phase angles (filled circle) and an unstable fixed point at positive phase angles (open circle). Bringing the system above the unstable fixed point leads to a spike before it settles at the stable fixed point. For inputs above threshold ($f > 0$) the phase-velocity curve is always above zero. No fixed points exist and spikes are generated periodically. **B** Graphs of the phase velocity for $f = 100$ Hz and different values of the time constant τ as indicated.

This relation describes many f-I-curves of both conductance-based models and real neurons fairly well. This square-root dependence is compared in Fig. 3.14 with the f-I-curves simulated with the Traub-Miles model (panel A & B) and the Connor model (panel C & D). Indeed, close to the bifurcation the square-root relation (3.21) matches perfectly the f-I-curves (B & D). The overall dependence of the firing frequency on the input current can be approximately described by (3.21), too, but with different parameter values (A & C). This inconsistency is a hint that the θ-model is valid only in the very vicinity of the bifurcation.

Deviations of the square-root relation from the real f-I-curves decrease the performance of the θ-model. To account for these differences, (3.21) can be solved for $I - I_{\text{th}}$ and inserted into (3.20):

$$\begin{aligned} \tau\dot{\theta} &= (1-\cos\theta) + (1+\cos\theta)(\pi\tau f(I))^2 \quad ; \quad -\pi \le \theta < \pi \\ \theta &= -\pi \quad ; \quad \theta = \pi \rightarrow \text{spike} \end{aligned} \tag{3.22}$$

In this version the θ-model reproduces exactly the neuron's f-I-curve for constant stimuli I. The dependence of the phase velocity $\dot{\theta}$ on phase is symmetric with respect to $\theta = 0$. The relation of the time constant τ to the firing frequency $f(I)$ determines whether the phase velocity during the spikes is faster or slower than in between the spikes. For $f(I) = 0$ the θ-model has a single fixed point at $\theta = 0$. The properties of this phase oscillator are illustrated in Fig. 3.15.

3.3.1 Performance of the θ-model

The performance of the θ-model for time-dependent stimuli is tested in Fig. 3.16. The θ-model predicts the spikes of the Traub-Miles model with high accuracy even for very strong and fast fluctuating stimuli. However, it predicts the spikes of the Connor model

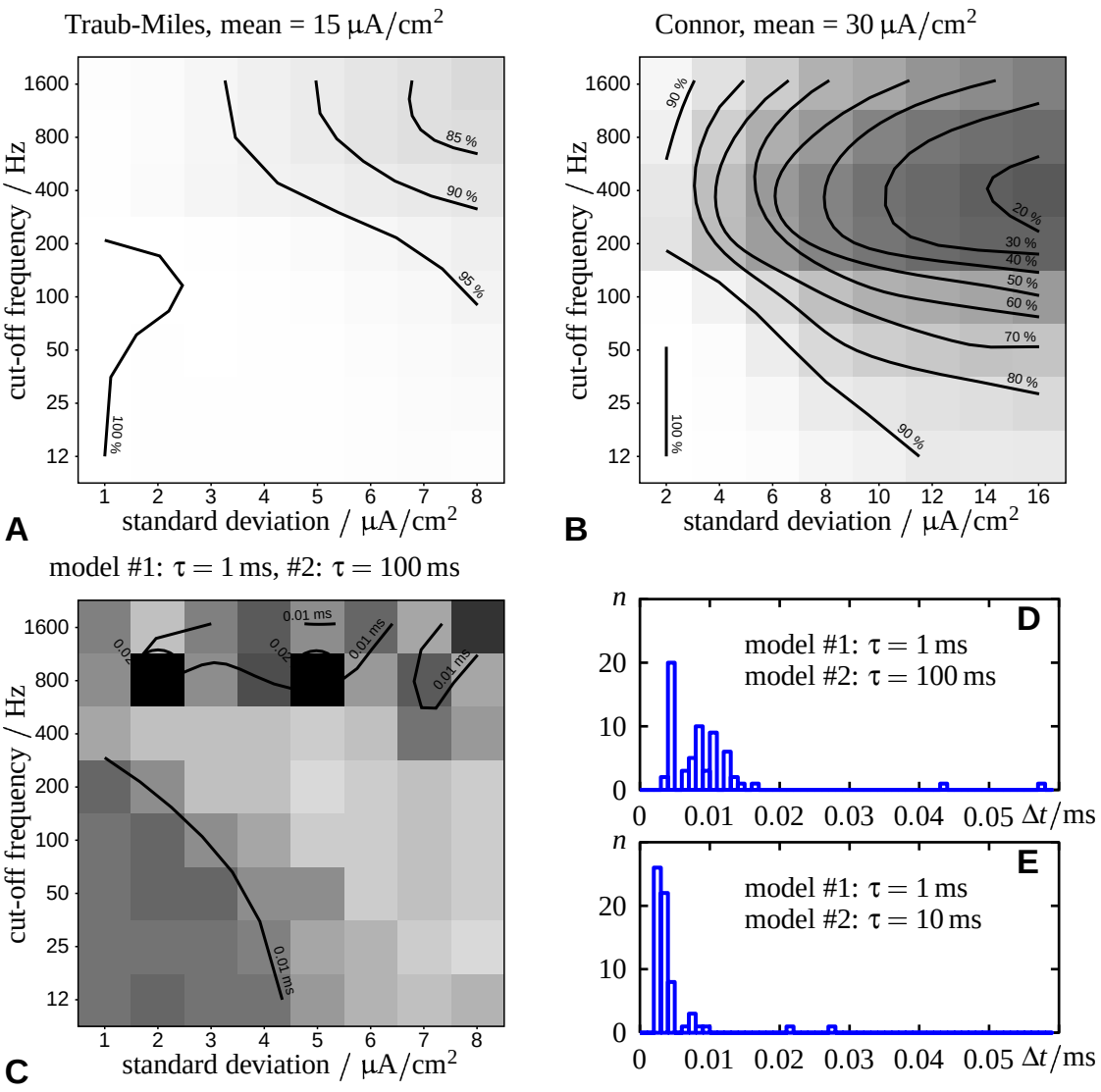

Figure 3.16: PERFORMANCE OF THE θ-MODEL. **A** The performance tested on the Traub-Miles model is greatly enhanced compared to the performance of the leaky phase oscillator shown in Fig. 3.12 A. The worst performance at the stimulus with standard deviation $\sigma = 8\,\mu\text{A/cm}^2$ and cut-off frequency $f_c = 1.6\,\text{kHz}$ is still better than 80 %. **B** In contrast, the performance tested on the Connor model is worse than the one of the leaky phase oscillator shown in Fig. 3.12 B, and similar to the performance of the non-leaky phase oscillator in Fig. 3.12 B. **C, D & E** Within the $\pm 0.5\,\text{ms}$ window two θ-models with different time constants τ as indicated predict the same spikes. However, the predicted spikes are not exactly identical. In the plots the averaged distances of corresponding spikes are displayed. **C** The averaged distances in milliseconds resulting from testing one θ-model with $\tau = 1\,\text{ms}$ against a θ-model with $\tau = 100\,\text{ms}$. The performance was tested with Gaussian white-noise stimuli with standard deviations and cut-off frequencies as indicated, and mean $\mu = 10\,\mu\text{A/cm}^2$. The f-I-curve of the Traub-Miles model was used for the models. **D** A histogram of the averaged distances of the spikes from C. Most differences are below 0.02 ms. **E** A histogram of spike distances from two θ-models with time constants $\tau = 1\,\text{ms}$ and $\tau = 10\,\text{ms}$. The same stimuli as in C were used.

worse than the leaky phase oscillator and with similar fidelity as the non-leaky phase oscillator (compare with Fig. 3.6 and Fig. 3.12).

Interestingly the performance of the θ-model is almost independent of the time constant τ. To further check this, two θ-models, which differed only by their values of the time constant τ, were tested against each other in Fig. 3.16 C & D. Indeed, they produce very similar timing of spikes within ± 0.5 ms for the entire range of stimuli used, regardless of their time constant of $\tau = 1$, 10, or 100 ms. The reason for this is the independence of the response function $z(t)$ of the time constant (see below). However, the spikes are not identical. On average they differ by about less than 0.01 ms.

3.4 Oscillations and phase-resetting curves

Until now, the phase oscillators (3.2), (3.14) and (3.22) were only compared with phase velocities simulated on conductance-based models as the ones in Fig. 3.10. The reason was that the dependence of the phase velocity on the phase angle cannot be measured directly from a real neuron. However, the phase velocity determines how a perturbation applied at a given phase effects the timing of the next spike. This can be quantified by measuring the phase-resetting curve as introduced in the previous chapter on page 21.

3.4.1 Phase-resetting curves of phase oscillators

Imagine the general one-dimensional phase oscillator (3.1)

$$\dot{\varphi} = g(\varphi; I) \tag{3.23}$$

driven by some input $I(t)$. For a small perturbation $\Delta I(t)$ of a constant stimulus $I = I_0$, the right hand side can be expanded to first order

$$\dot{\varphi} \approx g(\varphi; I_0) + \left.\frac{\partial g(\varphi; I)}{\partial I}\right|_{I=I_0} \cdot \Delta I(t) \; . \tag{3.24}$$

With the transformation

$$\frac{\mathrm{d}\varphi}{\mathrm{d}\psi} = g(\varphi; I_0) \tag{3.25}$$

the differential equation (3.24) in the new phase variable ψ reads

$$\dot{\psi} = 1 + Z(\varphi; I_0)\Delta I(t) \; . \tag{3.26}$$

Without perturbation, ψ equals the time t. The expression multiplying the perturbation $\Delta I(t)$,

$$\boxed{Z(\varphi; I_0) = \frac{\left.\frac{\partial g(\varphi; I)}{\partial I}\right|_{I=I_0}}{g(\varphi; I_0)}} \tag{3.27}$$

is called the response function. It is the phase-resetting curve $\Delta\varphi(\varphi)$ for infinitely small perturbations ΔI. Note, that $Z(\varphi)$ depends on the original phase variable φ. Phase-resetting curves which can be measured experimentally depend on time t. Therefore, the

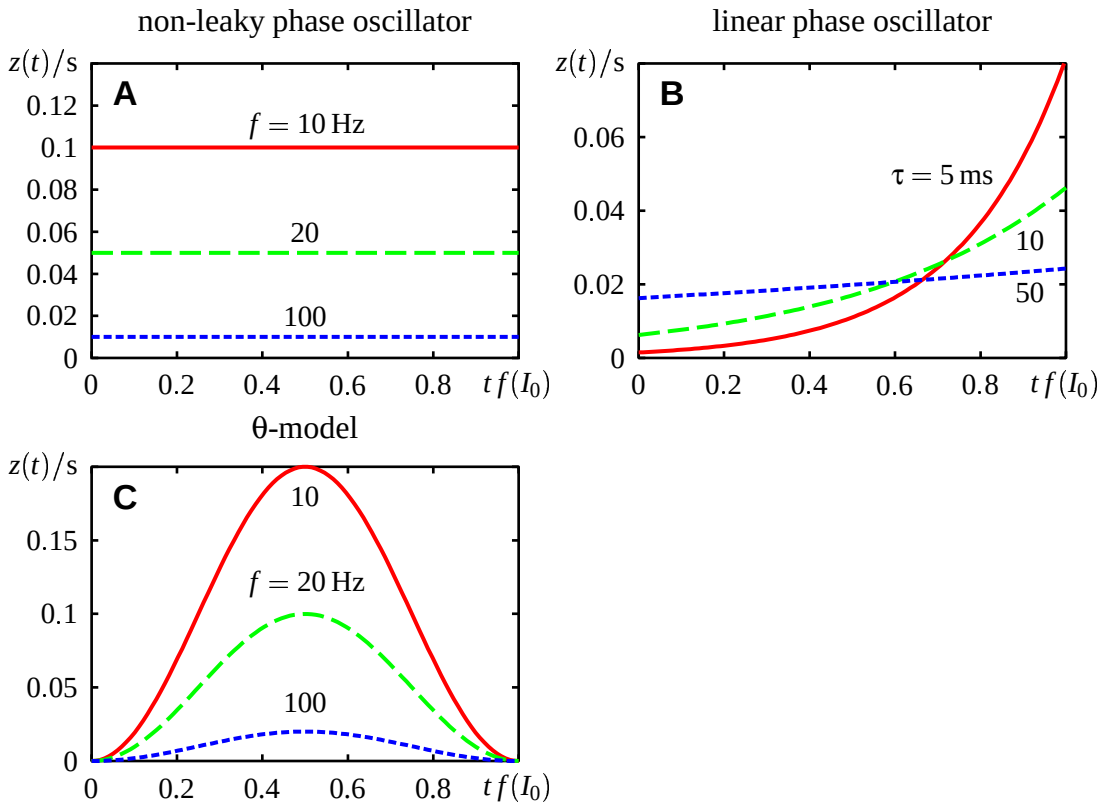

Figure 3.17: RESPONSE FUNCTIONS OF THE PHASE MODELS. **A** Response functions of the non-leaky phase oscillator (3.2) for different values of the unperturbed firing frequency as indicated. **B** Response functions of the leaky phase oscillator (3.14) for a firing frequency $f(I_0) = 50\,\mathrm{Hz}$ and different values of τ as indicated. **C** Response functions of the θ-model for different firing frequencies $f(I_0)$ as indicated. The response functions of the θ-model are independent of the value of the time constant τ.

solution $\varphi(t)$ has to be known in order to make them comparable. The response function $z(t)$ depending on time t is defined as

$$z(t;I_0) = Z(\varphi_0(t);I_0)\,, \tag{3.28}$$

where $\varphi_0(t)$ is the solution of the phase equation (3.23) without perturbation, i.e. $I(t) = I_0$.

The response functions for the three phase oscillators can be calculated with this scheme, if the firing frequency $f(I)$ is viewed as the input variable. The response function is independent of φ for the non-leaky phase oscillator (3.2) (Fig. 3.17 A):

$$z_n(t;I_0) = 1/f(I_0)\,. \tag{3.29}$$

The leaky phase oscillator (3.14) has an exponential response function (Fig. 3.17 B)

$$z_l(t;I_0) = \frac{1}{\tau f^2(I_0)\left(\mathrm{e}^{\frac{1}{\tau f(I_0)}} - 1\right)}\ \mathrm{e}^{t/\tau} \tag{3.30}$$

and the one of the θ-model (3.22) is symmetric and is independent of the time constant τ

$$z_\theta(t;I_0) = \frac{1}{f(I_0)}(1+\cos(2\pi t\, f(I_0)) \tag{3.31}$$

(Fig. 3.17 C).

The independence of the response function of the θ-model of the time constant τ is one reason for the observed independence of the performance of this model on the value of its time constant in Fig. 3.16. The other reason for this "lost time constant" is that the f-I-curve of a class-I neuron is approxiamtely a square-root function of the input: $f(I) = \sqrt{c(I - I_{\text{th}})}$ (3.21). Since the f-I-curve enters the θ-model quadratically, the inhomogeneity of the θ-model for such an f-I-curve depends linearly on the input I:

$$\tau\dot{\theta} = (1 - \cos\theta) + (1 + \cos\theta)\pi^2\tau^2 c(I - I_{\text{th}}) \,. \tag{3.32}$$

Because of this linear dependence on the input, the expansion of the phase oscillator to first order in the input (3.24) does not only approximate the original model for small perturbations $\Delta I(t)$ of the stimulus around a reference stimulus I_0, it rather equals the original model:

$$\tau\dot{\theta} = (1 - \cos\theta) + (1 + \cos\theta)\pi^2\tau^2 c(I_0 - I_{\text{th}}) + (1 + \cos\theta)\pi^2\tau^2 c\Delta I(t) \,. \tag{3.33}$$

Transforming this equation to a new phase variable ψ using the transformation (3.25), yields

$$\dot{\psi} = 1 + z(\psi; I_0)\Delta I(t) \quad \text{with} \quad z(\psi; I_0) = \frac{1}{2I_0}(1 + \cos(2\pi f(I_0)\psi)) \,, \tag{3.34}$$

where $z(\psi; I_0)$ is the response function. This phase oscillator is independent of the time constant τ. Note that this equation is equivalent to the original phase oscillator (3.32) for *arbitrary* perturbations $\Delta I(t)$. The very small differences in the timing of spikes of two θ-models with different time constants (Fig. 3.16 C, D & E) may be attributed to the deviations of the f-I-curve of the Traub-Miles model from a square-root function (Fig. 3.14 A & B).

To make measurements of phase-resetting curves compareable with the response functions of the phase oscillators, the resulting interspike interval T of a short perturbation ΔI at time t and duration Δt has to be calculated. Separating variables in (3.26) and integrating over one cycle of the phase variable ψ, which ranges from 0 to the duration T_0 of the unperturbed interspike interval, yields

$$T = \int_0^T \mathrm{d}t = \int_0^{T_0} \frac{\mathrm{d}\psi}{1 + z(\psi; I_0)\Delta I(\psi)} \,. \tag{3.35}$$

The right hand side can be expanded to first order if the perturbation ΔI is sufficiently small

$$T = \int_0^{T_0} \mathrm{d}\psi - \int_0^{T_0} z(\psi; I_0)\Delta I(\psi)\,\mathrm{d}\psi \,. \tag{3.36}$$

The perturbation occurs at time $\psi = t$ and has a very short duration Δt. The perturbed interspike interval is then approximately

$$T = T_0 - z(t; I_0)\Delta I(t)\Delta t \,. \tag{3.37}$$

Rearranging and dividing by T_0 finally results in the phase shift

$$\Delta\varphi(t) := \frac{T_0 - T}{T_0} = \frac{z(t; I_0)\Delta I(t)\Delta t}{T_0} \,. \tag{3.38}$$

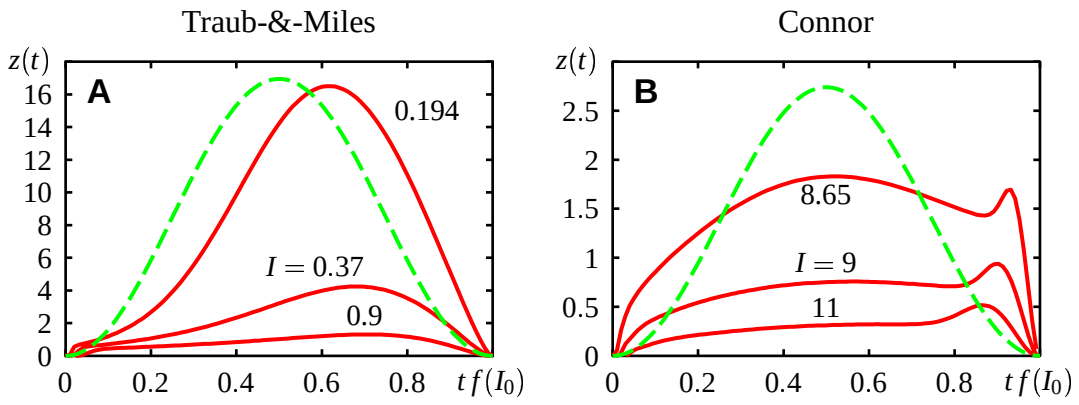

Figure 3.18: RESPONSE FUNCTIONS OF TWO CLASS-I NEURON MODELS. First, phase-resetting curves $\Delta\varphi$ were measured with short current pulses ΔI for different input currents I_0 as indicated in $\mu A/cm^2$ (solid lines) corresponding to firing frequencies of 12.5, 25, and 50 Hz. From the data the response function $z(t)$ was calculated using (3.39). For comparison the response function of the θ-model (3.22) for $f_0 = 12.5\,\text{Hz}$ is shown (dashed line). Since the response function of the θ-model originally has been calculated for perturbations of the firing frequency, it was multiplied with the corresponding derivative of the f-I-curve of the conductance-based model in order to make it comparable with the response function of the conductance-based model. The unit of the response functions is $cm^2/\mu A$. **A** Perturbations of $\Delta t = 0.2\,\text{ms}$ duration and $\Delta I = 2\,\mu A/cm^2$ were used to measure the phase-resetting curves $\Delta\varphi$ of the Traub-Miles model. With increasing input current I_0 the height of the response function decreases and their peak shifts to later phases φ. Except of this shift their shape is similar to the corresponding response function of the θ-model (3.31). **B** Response functions of the Connor model are quite different. They have a prominent peak at $\varphi \approx 0.9$, which is not expected from the θ-model. However, with decreasing input current I_0 a broad peak in the middle arises, making the response function more similar to the one of the θ-model (3.31). To measure the phase-resetting curves $\Delta\varphi$ perturbations of $\Delta t = 0.2\,\text{ms}$ duration and $\Delta I = 4\,\mu A/cm^2$ were used.

Vice versa, the response function $z(t)$ is related to the phase-resetting curve $\Delta\varphi$ measured with small perturbations of duration Δt and strength ΔI by

$$z(t;I_0) = \frac{\Delta\varphi(t)}{f(I_0)\Delta I \Delta t}\,, \tag{3.39}$$

where $f(I_0) = 1/T_0$ is the frequency of the unperturbed oscillation.

The response functions measured in two conductance-based models of class-I neurons for different input intensities I_0 are shown in Fig. 3.18. The response functions of the Traub-Miles model for currents near the threshold are well approximated by the prediction of the θ-model (3.31). In contrast, the response functions of the Connor model are much broader and show an additional peak at $\varphi \approx 0.9$, which is not expected from the θ-model. Thus, for increasing input current the response functions are more similar to the one of the leaky phase oscillator (3.30) shown in Fig. 3.17 B. However, for currents nearer to the threshold the response functions of the Connor model tend towards the one of the θ-model, too (Ermentrout, 1996).

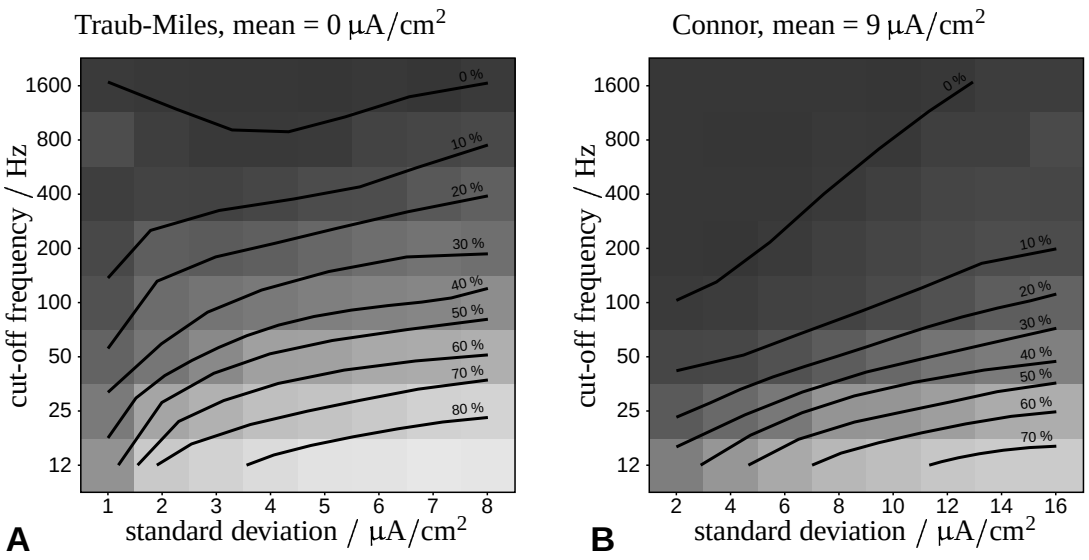

Figure 3.19: PERFORMANCE OF THE θ-MODEL FOR STIMULI CLOSE TO THRESHOLD. The performance for both **A** the Traub-Miles model and **B** the Connor model is generally very poor. It is better for low cut-off -frequencies and surprisingly increases slightly with higher standard deviations of the Gaussian white-noise stimuli.

3.5 Phase oscillators in the sub-threshold regime

f-I-curves and response functions are properties of a neuron in its oscillating regime. These two properties sufficiently describe the super-threshold dynamics, as shown above. However, they do not carry any information about the dynamics for sub-threshold input currents. Stable fixed-points exist in the sub-threshold regime, which correspond to the resting potential. The location of these fixed points depend on the sub-threshold current.

The phase oscillators defined by f-I-curves do not have appropriate fixed points. For sub-threshold stimuli where $f(I)$ equals zero, the non-leaky phase oscillator (3.2) stops integrating and stays at the phase angle φ, where it just was. The leaky phase oscillator (3.14) has a fixed point at $\varphi = 1$, independent of the value of the input current. Applying any input above threshold would immediately generate a spike, which is not very realistic. The θ-model (3.22) has its fixed point at $\theta = 0$, i.e. the latency to a spike evoked by a constant input current I above threshold is exactly one half of the corresponding interspike interval $1/f(I)$.

3.5.1 Performance of the θ-model near threshold

The original θ-model (3.20), however, is defined for both sub- and super-threshold stimuli in the vicinity of the threshold I_{th}. For sub-threshold stimuli it exhibits one stable and one unstable fixed point as it is illustrated in Fig. 3.15 A. To test the performance of the θ-model, in Fig. 3.19 input currents fluctuating around the threshold current I_{th} were used. For currents above threshold the θ-model (3.22) defined directly by the neuron's f-I-curve was taken, and for sub-threshold currents the original model (3.20) was used, with its parameters c and I_{th} set to fit the f-I-curve. Even for small standard deviations of the input current in the very vicinity of the threshold current I_{th} the performance of this model is astonishingly poor, as illustrated in Fig. 3.19. It follows that the flow-field of

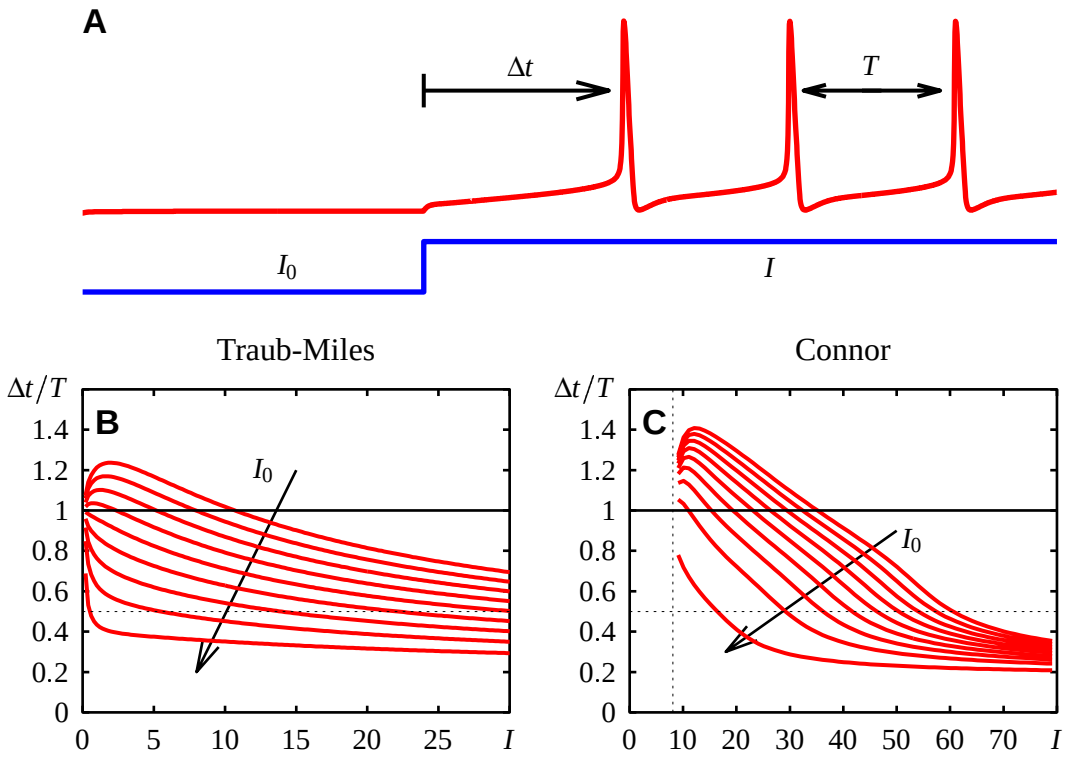

Figure 3.20: LATENCIES IN RELATION TO THE CORRESPONDING INTERSPIKE INTERVALS. **A** First the neuron is relaxed to a sub-threshold current I_0. Then a current I above threshold is switched on. The latency $\Delta t(I_0, I)$ is the time to the first spike evoked by this stimulus. The following periodic spike train has a period $T(I)$. **B & C** Latencies Δt related to the interspike intervals T in dependence on I for different sub-threshold currents I_0. All currents are given in $\mu A/cm^2$. The solid horizontal line marks the maximum possible latency $\Delta t = T$ of a phase model. The dashed line at $\Delta t = T/2$ is the minimum latency of the θ-model. **B** Latencies of the Traub-Miles model. The current threshold is at $I_{th} = 0.1\ \mu A/cm^2$ (see Fig. 3.14 A). For the sub-threshold current I_0 values ranging from -3.2 to $0.0\ \mu A/cm^2$ incremented by $0.4\ \mu A/cm^2$ were used. Only latencies from sub-threshold currents I_0 not too close (!) to threshold are in accordance with the θ-model. The latencies from very low sub-threshold currents exceed the corresponding interspike intervals. **C** Latencies of the Connor model, which has its current threshold I_{th} at $8.1\ \mu A/cm^2$ (see Fig. 3.14 B). For the sub-threshold current I_0 values ranging from -6.62 to $7.8\ \mu A/cm^2$ incremented by $1.8\ \mu A/cm^2$ were used. The latencies deviate even more from the expectations of the θ-model.

the θ-model for sub-threshold inputs cannot be extrapolated from its properties above threshold. Besides the f-I-curve and the phase-resetting curves a third measure is needed to characterize also the sub-threshold dynamics of a neuron.

3.5.2 Possible latencies of phase oscillators

A neuron settles at a stable fixed point (resting potential) for a constant sub-threshold stimulus. Each fixed point of a phase model (3.1) corresponds to a resting phase $\varphi_0(I_0)$ depending on the sub-threshold input current I_0. Switching on a constant current I above threshold generates a spike after some latency $\Delta t(I_0, I)$. This latency depends on the sub-threshold current I_0, which determines the fixed point, and on the super-threshold stimulus I, which determines the flow-field generating the spike.

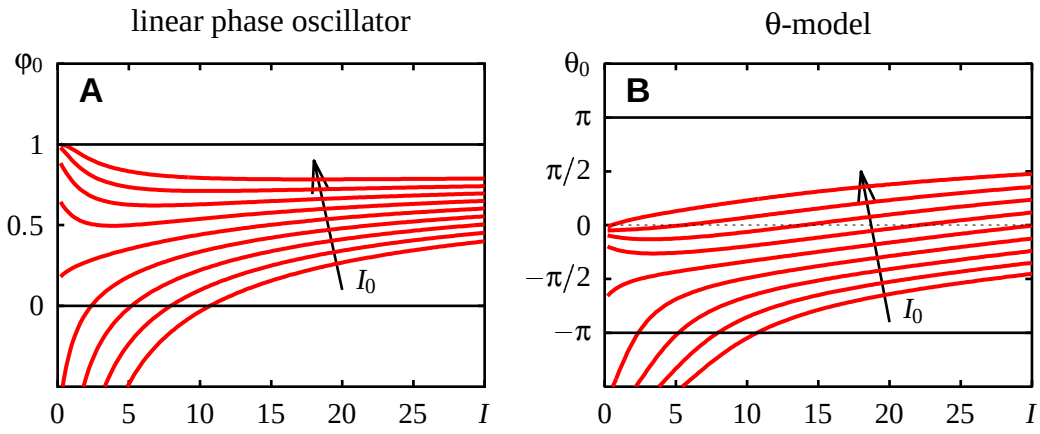

Figure 3.21: RESTING PHASES CALCULATED FROM LATENCIES. **A** The resting phases φ_0 calculated from latencies according to (3.41) for the leaky phase oscillator. Shown are the results from the same latencies of the Traub-Miles model as shown in Fig. 3.20 B. The horizontal lines mark the minimum and maximum phase angle of the leaky phase oscillator (3.14). The resting phases depend strongly on the value of the super-threshold current I. This is not in accordance with the assumption of the fixed points lying directly on the periodic orbits. **B** The resting phases θ_0 calculated for the θ-model using (3.42). The results from the same data used in A are plotted. The minimum and maximum phase angles are indicated by the solid horizontal lines. The dashed line marks the maximum possible resting phase of the θ-model. Especially for currents near the threshold the resting phases θ_0 depend strongly on I, thus contradicting the assumptions of one-dimensionality of the θ-model.

The resting phases φ_0 of a phase model have to lay in the range of one period, i.e. $0 \leq \varphi_0 < 1$. Thus, the latencies have to be smaller than the period $T = 1/f(I)$ of the corresponding oscillation evoked by the super-threshold stimulus I. The latencies of the θ-model are even longer than one half of the interspike interval T, since it is symmetric with respect to $\theta = 0$ and its stable fixed point is at negative phases θ (Fig. 3.22 A). The latencies related to the corresponding interspike intervals are shown in Fig. 3.20. Both the Traub-Miles model and the Connor model have latencies which are smaller than half of the corresponding interspike interval. This is the case for sub-threshold currents I_0 very close to threshold and/or very high values of the super-threshold stimulus. The requirement of the latency to be shorter than the corresponding interspike interval is violated by latencies from very low sub-threshold currents. This explains only partly the poor performance of the θ-model in Fig. 3.19, since most latencies of the Traub-Miles model actually are within the required range.

3.5.3 Fixed points calculated from latencies

Latencies can be used to determine the resting phase φ_0 for every sub-threshold current I_0, given a particular phase model $\dot{\varphi} = g(\varphi; I)$. For super-threshold input currents I, the latencies $\Delta t(\varphi_0(I_0), I)$

$$\Delta t(\varphi_0, I) = \int_{\varphi_0}^{1} \frac{\mathrm{d}\varphi}{g(\varphi; I)} \tag{3.40}$$

can be calculated for any resting phase φ_0 and super-threshold current I. Thus, given the latencies $\Delta t(I_0, I)$ measured in a particular neuron, by means of the inverse function of

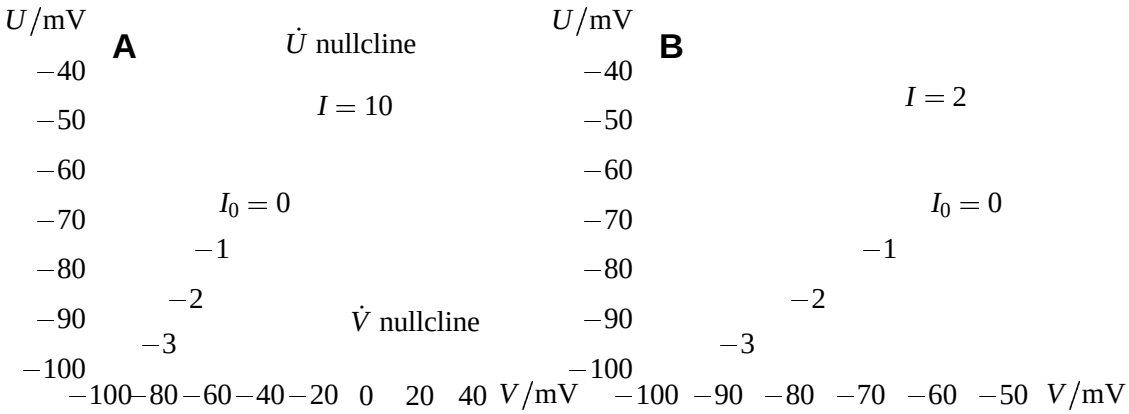

Figure 3.22: FIXED POINTS AND LIMIT CYCLES. The dots indicate four different fixed points of the Traub-Miles model. These fixed points correspond to sub-threshold currents $I_0 = -3$, -2, -1, and $0\,\mu\text{A}/\text{cm}^2$. The solid lines are the trajectories starting from these fixed points towards the limit cycle of a super-threshold current I. Compare them with the latencies shown in Fig. 3.20 B. The dashed lines are the corresponding nullclines. **A** All fixed points are far away from the limit cycle for $I = 10\,\mu\text{A}/\text{cm}^2$. The trajectories first move along the $\dot{U}$-nullcline, before they reach the limit cycle. In this example the resulting latencies, however, are not longer than a whole period of the limit cycle. **B** The same situation as in A, but with a limit cycle for $I = 2\,\mu\text{A}/\text{cm}^2$ more closely to threshold $I_{\text{th}} = 0.1\,\mu\text{A}/\text{cm}^2$. The trajectories starting from the lower fixed points move very closely to the $\dot{U}$-nullcline. Therefore, their movement is very slow, resulting in latencies even longer than the period of the limit cycle. The fixed point corresponding to $I_0 = 0\,\mu\text{A}/\text{cm}^2$ lies inside the limit cycle. Its latency is shorter than half of the period of the limit cycle.

(3.40) the corresponding resting phases $\varphi_0(I_0)$ can be determined. If such a model is a valid description of a neuron, the resulting resting phases should be independent of the super-threshold current I used to evoke the spikes.

The resting phase given the latency $\Delta t(I_0, I)$ and the interspike interval $T(I)$ for the leaky phase oscillator (3.14) is

$$\varphi_0(I_0) = \frac{1 - \mathrm{e}^{-\frac{T(I) - \Delta t(I_0, I)}{\tau}}}{1 - \mathrm{e}^{-\frac{T(I)}{\tau}}}\,, \tag{3.41}$$

and for the θ-model (3.22)

$$\theta_0(I_0) = 2\mathrm{atan}\left(\pi \frac{\tau}{T(I)} \tan\left(\pi\left(\frac{1}{2} - \frac{\Delta t(I_0, I)}{T(I)}\right)\right)\right) \tag{3.42}$$

However, as shown in Fig. 3.21 for both the leaky phase oscillator and the θ-model, the resting phases are not independent of I. Only for sub- and super-threshold currents very close to the threshold current, the resting phases of the θ-model are close to $\theta_0 = 0$ as predicted, and the dependence of θ_0 on I is not too strong. Thus, the latencies observed in conductance-based models are not in accordance with the phase models, i.e. the sub-threshold dynamics is not in accordance with the super-threshold dynamics.

The assumption of a one-dimensional movement in the neuron's phase space implies that every fixed point lies directly on the periodic orbits. Trajectories starting from several fixed points towards two limit cycles are shown in Fig. 3.22. The fixed points indeed are far away from the periodic orbits. The trajectories move close to the $\dot{U}$ nullcline towards the periodic orbit. The flow-field at the fixed points is therefore very different from the

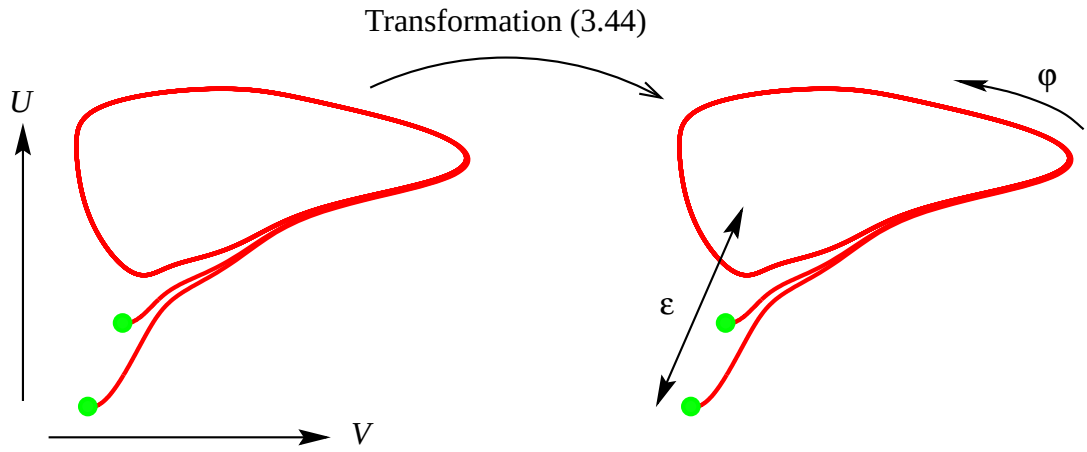

Figure 3.23: TRANSFORMATION TO A TWO-DIMENSIONAL PHASE MODEL. The two variables V and U of the original conductance-based model can in principle be transformed by (3.44) into a phase angle φ and a deviation from the limit cycles ε. The dynamics of the phase angle models the initiation of spikes, while ε is mainly responsible for the sub-threshold dynamics.

flow-field on the limit cycles. Thus, movement on the limit cycles has a completely different dynamics than around the fixed points. Therefore, the assumption of a one-dimensional dynamics made for all the phase models introduced in this chapter fails.

3.6 Outlook: Two-dimensional models

To combine the super-threshold dynamics on limit cycles with the sub-threshold dynamics, a two dimensional model is needed. In addition to the phase variable φ, which accounts for the dynamics on limit cycles, a second variable ε is necessary for the sub-threshold dynamics far away from the limit cycles.

Recall the original equations of conductance-based models in their reduced version (2.11) from chapter 2. For a periodically spiking neuron they are given by

$$\begin{aligned} \dot{V} &= F(V,U;I) \\ \dot{U} &= G(V,U)\,. \end{aligned} \tag{3.43}$$

With an invertible nonlinear transformation

$$\begin{aligned} \varphi &= \varphi(V,U) \\ \varepsilon &= \varepsilon(V,U;I) \end{aligned} \tag{3.44}$$

the membrane potential V and the recovery variable U can be mapped onto a phase angle φ and a deviation ε from the limit cycles as illustrated in Fig. 3.23.

$$\begin{aligned} V &= V(\varphi,\varepsilon;I) \\ U &= U(\varphi,\varepsilon;I) \end{aligned} \tag{3.45}$$

is the corresponding inverse transformation of (3.44). The mapping of the phase angles φ is independent of I. For example, such a mapping is shown in Fig. 3.10 A. It can be extended to the whole V-U space. The mapping of the deviation ε must depend on the input I, since the orbits of the limit cycles depend on I, too (see Fig. 2.18). In the new

variables φ and ε the dynamics reads

$$\begin{aligned} \dot{\varphi} &= \frac{\partial\varphi}{\partial V}\dot{V} + \frac{\partial\varphi}{\partial U}\dot{U} &&=: P(\varphi,\varepsilon;I) \\ \dot{\varepsilon} &= \frac{\partial\varepsilon}{\partial V}\dot{V} + \frac{\partial\varepsilon}{\partial U}\dot{U} + \frac{\partial\varepsilon}{\partial I}\dot{I} &&=: E(\varphi,\varepsilon;I) + \tilde{E}(\varphi,\varepsilon;I)\dot{I}\,. \end{aligned} \tag{3.46}$$

where (3.43) and (3.44) was used. In contrast to the original equations (3.43), the time derivatives of both variables depend on the input I. The one-dimensional phase models discussed in this chapter are a special case of (3.46), with the distance from the limit cycles ε always equal to zero ($P(\varphi,\varepsilon;I) \equiv g(\varphi;I)$).

For a constant current I above threshold I_{th} the deviation ε relaxes to zero. The time constant of this process may depend on the phase, since the flow-field in the vicinity of the limit cycles is very different depending on the location. Thus, a linear approximation of $E(\varphi,\varepsilon;I)$ would be $-\varepsilon/\tau(\varphi;I)$, where the time constant $\tau(\varphi;I)$ determines the speed of the relaxation of ε.

However, as illustrated in Fig. 3.22 the fixed points for sub-threshold stimuli are far away from any of the limit cycles. Therefore an additional term $\gamma(I)$ accounting for the appropriate fixed point is needed, which is large for sub-threshold currents only. It does not have to depend strongly on the phase angle φ, since for sub-threshold currents the phase φ approximately does not change very much.

The last term of the differential equation for ε, $\tilde{E}(\varphi,\varepsilon;I)\dot{I}$, accounts for the different locations of the limit cycles depending on I. Since the performance of the one-dimensional phase models for currents above threshold is very good, this term might be negligible.

It is hard to imagine how the deviation ε actually affects the dynamics of the phase angle, but it is the key to match the latencies of the original models. Altogether, from (3.46) remains the simplification

$$\begin{aligned} \dot{\varphi} &= P(\varphi,\varepsilon;I) \\ \dot{\varepsilon} &= -\frac{\varepsilon}{\tau(\varphi;I)} + \begin{cases} \gamma(I) & ; \quad I < I_{\text{th}} \\ 0 & ; \quad I \geq I_{\text{th}} \end{cases} \end{aligned} \tag{3.47}$$

The sub-threshold equation for ε now is a linear differential equation. Since below the activation of the sodium current, the membrane of a neuron indeed is linear (Koch, 1999), this equation might be identified with the linear membrane equation for the membrane potential V

$$\tau\dot{V} = -V + RI\,, \tag{3.48}$$

where R is the membrane resistance, C is the membrane capacitance and $\tau = RC$ is the membrane time-constant. The resting potential for $I = 0$ is set to zero. However, the dependence of the linear membrane equation (3.48) on the phase angle φ is missing.

The two-dimensional model (3.47) reflects the two regimes of neural dynamics (recall Fig. 3.1 B). Below the threshold current the dynamics is mainly governed by the equation for ε. If the current crosses threshold, the phase equation comes into play and finally triggers a spike. If the current stays above threshold, the dynamics is mainly determined by the phase equation. Both equations differ, and both are necessary for a complete description of the spiking behavior of a class-I neuron. The interaction of the dynamics of both regimes is very important for inputs fluctuating around the neuron's threshold.

How the deviation ε couples into the phase equation remains to be analyzed. Then, in addition to the f-I-curve, response functions and latencies, a paradigm has to be found for measuring the necessary parameter of the two-dimensional model (3.47), based solely on spikes.

3.7 Discussion

Spiking neurons are nonlinear oscillators. For super-threshold input currents they exhibit stable limit cycles. In this chapter phase oscillators as suitable models for their dynamics on limit cycles were discussed. However, neural dynamics for sub-threshold inputs is of a completely different quality, which cannot be inferred from super-threshold properties.

3.7.1 Spiking in the super-threshold regime

The non-leaky phase oscillator (3.2) performed very well for stimuli with cut-off frequencies below the mean firing frequency. Such stimuli are approximately constant during a single interspike interval. Any phase oscillator (3.1) can be transformed by means of (3.10) into the non-leaky phase oscillator (3.2) for a particular input current I^*. This reference current can be set to the mean input current during each interspike interval. Thus, any general phase oscillator (3.1) can be transformed appropriately to the non-leaky phase oscillator (3.2) for each interspike interval. This corresponds to the zero order expansion of the general phase oscillator (3.26). In fact, the non-leaky phase oscillator is a canonical model for each dynamical system in the vicinity of its limit cycle (Hoppensteadt & Izhikevich, 1997).

Stimuli fluctuating faster and more strongly cannot be approximated as constant during an interspike interval. Besides their frequency the different properties of the neuron's limit cycles for different input currents I become important. Thus, a more detailed description of the dynamics on the limit cycles is necessary. The leaky phase oscillator (3.14) is an empirical model describing roughly the phase velocity in conductance based models. The θ-model is a phase oscillator derived from the properties of the saddle-node bifurcation of class-I neurons (Ermentrout, 1996). Both models further improve the performance of the non-leaky phase oscillator.

Another reason for the simple phase oscillators to fail is that the limit cycles differ in their location in phase space (compare with Fig. 2.18). Strongly fluctuating inputs may push the system outside the vicinity of a limit cycle. Thus, the flow-field outside the limit cycles may play a role, too. However, the excellent performance of the θ-model in predicting spikes of the Traub-Miles model demonstrates that a good description of the dynamics on the limit cycles may be sufficient.

3.7.2 Prediction of super-threshold properties from bifurcation

The θ-model was derived from the properties of a saddle-node bifurcation (Ermentrout, 1996). It predicted a square-root dependence of firing frequency on input current, and a symmetric response function.

In the limit of the input current approaching the threshold current, f-I-curves, response functions and latencies of class-I neurons like the Traub-Miles model and the Connor model are very close to the predictions of the θ-model, thus confirming that they have a saddle-node bifurcation. With increasing distance of the input current from threshold the properties of the conductance-based models differ more and more from the predictions based on the saddle-node bifurcation.

These differences emerge in the Connor model very soon, while the properties of the Traub-Miles model deviate less from its properties at bifurcation. The response function

of the Connor model becomes more similar to the exponential response function of the leaky phase oscillator. Whether this behavior of the Connor model has to be attributed to the inactivation variable of the A-current has to be investigated. At least this variable constitutes a third dimension in the Kepler-reduced Connor model (Kepler et al., 1992).

Reyes & Fetz (1993) measured phase-resetting curves of cortical neurons. They found both the symmetrical type of phase-resetting curves of the θ-model and the exponential type of the leaky phase oscillator. So, both the θ-model and the leaky phase oscillator are representative models according to their response functions.

3.7.3 Spiking near threshold

While the phase oscillators predict spikes in the super-threshold regime very well, their performance drops dramatically as soon as the stimuli fluctuate around threshold. In addition there is a mismatch of the latencies in relation to the corresponding firing frequencies, which contradicts the predictions of the phase models. Both issues demonstrate that the sub-threshold dynamics cannot be extrapolated from super-threshold properties. Vice versa, the super-threshold behavior cannot be predicted from sub-threshold properties. This was shown for the integrate-&-fire model by Stevens & Zador (1998b) for a cortical neuron. The membrane resistance, capacitance and resting potential measured by means of sub-threshold inputs, resulted in a completely wrong f-I-curve of the integrate-&-fire model in comparison with the f-I-curve measured experimentally.

The common notion of a voltage threshold for the initiation of spikes is a one-dimensional model for the sub-threshold regime. The integrate-&-fire model is the most prominent example for such a model. However, Koch et al. (1995) recognized in their simulation study of a class-I model-neuron that there also exist a current threshold. A short and sufficiently strong current pulse can induce a spike, which occurs after some delay. This corresponds to pushing the system beyond the separatrix associated with a saddle (see Fig. 2.14).

3.7.4 Two-dimensional models

One-dimensional models in general fail to predict spikes of class-I neurons. Note also, that from a conceptionally point of view, integrate-&-fire models are sub-threshold models and thus can never explain the neuron's super-threshold properties. On the other hand, the phase oscillators introduced in this chapter are based on the super-threshold dynamics, and fail in the sub-threshold regime. If one-dimensional models are not sufficient, then at least two-dimensional model are needed for a more realistic description of the spiking dynamics. This is not surprising, since a two-dimensional dynamical system is required to enable oscillations, i.e. spikes.

The importance of realistic models of neural dynamics is stressed by the work of Gutkin & Ermentrout (1998). They used the θ-model as a more realistic model for class-I neurons compared to the integrate-&-fire model or random-walk models. With the properties of this model it was possible to explain much more of the high variability of spike-trains in cortical neurons than expected from simpler models (Shadlen & Newsome, 1998).

3.7.5 Class-II neurons

The situation may be different for class-II neurons. Recall that the latencies of class-II neurons are approximately independent of input intensity (Fig. 2.10). Therefore, the phase equation for the super-threshold regime only has to supply this fixed delay. Since this latency is short, the role of the super-threshold equation in initiating a spike might be negligible. However, the super-threshold equation also handles the absolute and relative refractory period after a spike. These are important, but the dynamics during the refractory period is very stereotyped.

In their spike-response model, Kistler et al. (1997) convolve the input with a kernel, which may depend on the time of the previous spike, to calculate the membrane potential. If this potential reaches a threshold a spike is simulated by a stereotyped voltage trace which is added on the voltage trace. The performance of the spike-response model to predict spikes of the Hodgkin-Huxley model indeed is good (Kistler et al., 1997). Whether this one-dimensional nonlinear model is able to reproduce the super-threshold behavior of a class-II neuron was not shown. With the stimuli they used to test their model, mainly the sub-threshold dynamics of the model was tested.

3.8 Summary

- The neuron's f-I-curve determines completely a non-leaky phase oscillator $\dot{\varphi} = f(I(t))$, which predicts the timing of spikes well for currents fluctuations slower than an interspike interval.
- A spiking neuron acts like a low-pass filter with its cut-off frequency determined by the actual firing frequency.
- Exploring the dynamics on limit cycles in conductance-based models leads to the leaky phase oscillator, which gives a new interpretation of the integrate-&-fire neuron.
- Analyzing the properties of the saddle-node bifurcation of class-I neurons results in the θ-model as proposed by Ermentrout (1996).
- Latencies measured in class-I conductance-based models contradict the latencies predicted by phase oscillators.
- The dynamics of the sub-threshold regime cannot be extrapolated from the dynamics on limit cycles of the super-threshold regime.
- Two-dimensional models are needed to combine the sub-threshold dynamics with the dynamics on limit cycles for class-I neurons.

4

Dynamics of Spike-Frequency Adaptation

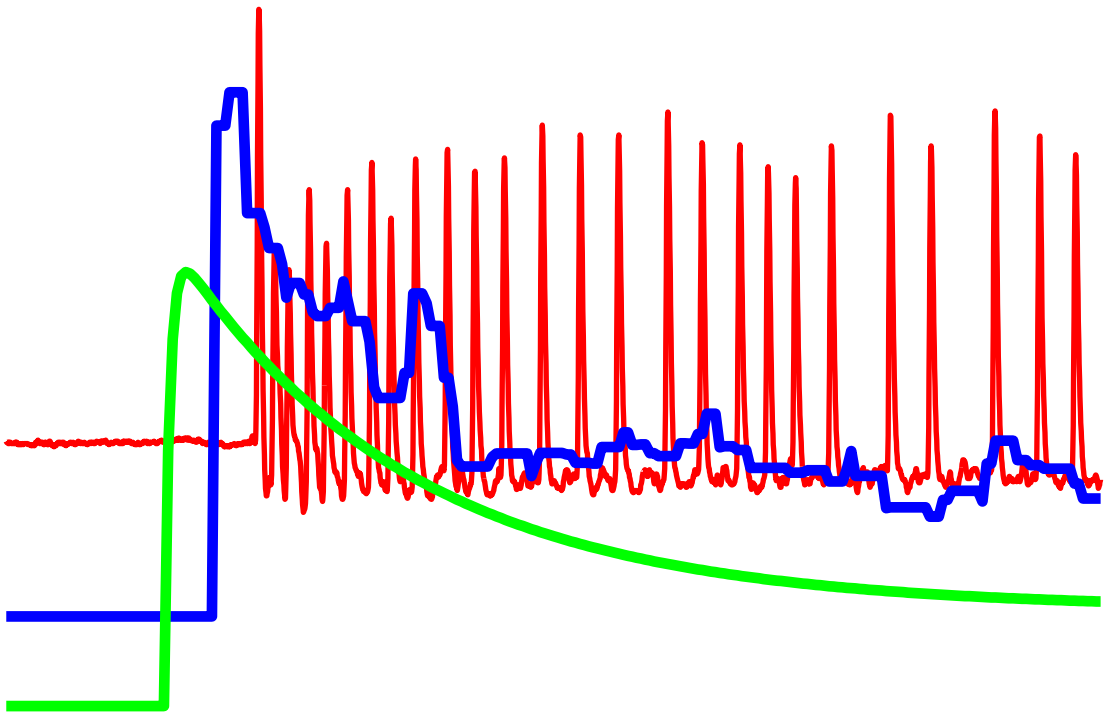

Contents

4.1 From channels to firing frequency ***65***
4.1.1 Encoder adaptation *66*
M-type currents *70*
AHP-currents *73*
Slow recovery from inactivation *74*
General model for encoder adaptation *75*
Physical stimulus as input *75*
4.1.2 Transducer adaptation *77*
4.1.3 Depressing synapses *78*
4.2 Defining the parameters of the adaptation models ***78***
4.2.1 Steady-state strength of adaptation *79*
Encoder adaptation *79*
Transducer adaptation *79*
4.2.2 The $\gamma(f)$ - term *80*
4.2.3 Time constants of adaptation *80*
4.3 Signal transmission properties ***83***
4.3.1 Adapted f-I-curves *83*
4.3.2 Linear adaptation and linear steady-state f-I-curves *85*
4.3.3 High-pass filter properties due to adaptation *88*
4.3.4 Time-derivative detection *90*
4.3.5 Nonlinear effects *90*
4.4 Combination with spike-generator ***93***
4.4.1 Adaptation and spike dynamics *94*
4.5 Discussion ***94***
4.5.1 Models of spike-frequency adaptation *94*
4.5.2 Assumptions of the model for encoder adaptation *95*
4.5.3 Biophysical mechanisms of spike-frequency adaptation . . . *97*
4.5.4 Transducer adaptation and depressing synapses *99*
4.5.5 Functional role of adaptation *99*
4.6 Summary ***100***

Cover: Voltage trace recorded in an adapting auditory receptor of *Locusta migratoria*. Overlaid is the time course of the firing frequency and a fit of the adaptation model.

Spike-frequency adaptation is a widespread phenomenon in spiking neurons, exhibited by almost any type of neuron in vertebrates as well as in invertebrates, in peripheral

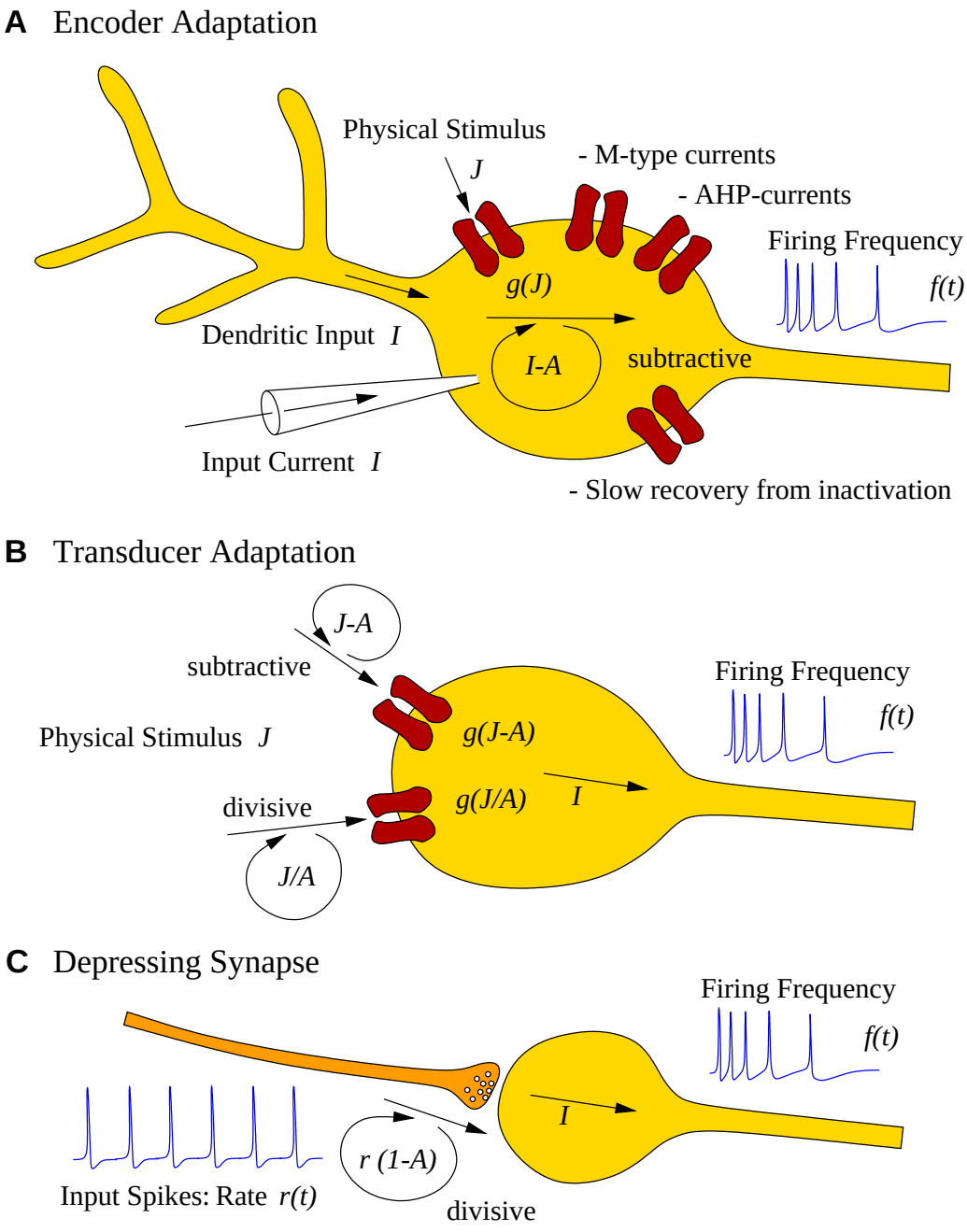

Figure 4.1: DIFFERENT MECHANISMS OF SPIKE-FREQUENCY ADAPTATION. **A** Various types of slow ionic currents (M-type, AHP, recovery from inactivation) act subtractive on the input current I. They cause spike-frequency adaptation in dependence on the output firing frequency $f(t)$ of the spike generator. This type of adaptation is referred to as "encoder adaptation" in this thesis. The input current I is either injected by a microelectrode, or is the current from the dendritic tree, or flows through a conductance $g(J)$, which is changed by the transduction of a physical stimulus J. **B** In receptor neurons the transduction process of a physical stimulus J into a change of a conductance $g(J)$ may adapt (transducer adaptation). This type of adaptation depends on the input intensity J. It acts on the input J either subtractive or divisive. **C** A continous stimulation of a synapse with a spike train may gradually reduce its efficiency. Such depressing synapses act divisive on the input rate $r(t)$. The postsynaptic current is reduced, and the resulting output spikes show spike-frequency adaptation.

as well as in central neurons. For example, it was observed in rat pyramidal neurons (Gustafsson & Wigström, 1981; Lanthorn et al., 1984; Barkai & Hasselmo, 1994), rat motoneurons (Granit et al., 1963), cat layer V cells of the sensorimotor cortex (Stafstrom et al., 1984), pyramidal tract cells of the cat (Koike et al., 1970), cat motoneurons (Kernell, 1965), cat auditory-nerve fiber (Javel, 1996), arthropod stretch receptors (Edman et al., 1987a; French, 1989b), auditory receptors in noctuid moths (Coro et al., 1998) and locusts (Michelsen, 1966).

Adapting neurons respond to a prolonged constant stimulation with a decaying firing frequency. The final firing frequency levels out at some value below the initial one, or the neuron may even stop spiking after a while. The time scales associated with spike-frequency adaptation range from tens of milliseconds (Madison & Nicoll, 1984; Schwindt et al., 1988; Storm, 1989; Engel et al., 1999; Sah & Clements, 1999; Stocker et al., 1999) to several seconds (Edman et al., 1987a; French, 1989b; Hocherman et al., 1992).

There are many different mechanism causing spike-frequency adaptation. Focusing on single cell properties and neglecting network effects like recurrent inhibition, these mechanisms can be summarized in three basic groups (see Fig. 4.1).

First, there exist slow ionic currents, which directly influence the initiation of spikes in dependence on the generated firing frequency. For this adaptation mechanism the term "encoder adaptation" is used throughout this thesis. Three main groups of such ionic currents can be distinguished: M-type currents, which are caused by slow, voltage-dependent, high-threshold potassium channels (Brown & Adams, 1980; Halliwell & Adams, 1982), AHP-currents mediated by calcium-dependent potassium channels (Madison & Nicoll, 1984), and slow recovery from inactivation, e.g. of the fast sodium channel (Fleidervish et al., 1996). Properties of these and other ionic currents are presented in detail in the discussion.

Second, the transduction process of a physical stimulus into a change of a membrane conductance may adapt itself in dependence on the stimulus intensity. This type of adaptation is important for receptor neurons. It is referred to as "transducer adaptation".

Third, neurons usually receive their input via synapses, which may adapt as well. Such synapses are known as depressing synapses.

Various modeling studies on spike-frequency adaptation have already been performed, most of them based on conductance based models of a specific cell, thus focusing on a special encoder-adaptation mechanism (Cartling, 1996a; Wang, 1998; Ermentrout, 1998). In this chapter an attempt is made to formulate a general model for different biophysical mechanisms inducing encoder adaptation. Analyzing the effects of various slow ionic currents on the neuron's intensity-response curve (f-I-curve), a universal phenomenological model for encoder adaptation is derived. Its parameters can be easily accessed experimentally by measuring the neuron's f-I-curves. Comparable models are derived for some types of transducer adaptation as well as for depressing synapses.

Based on the model, signal transmission properties due to spike-frequency adaptation can be quantified from the neuron's f-I-curves. For encoder adaptation and some types of transducer adaptation spike-frequency adaptation acts subtractive on the input (section 4.3.1) and turns the neuron into a high-pass filter (section 4.3.3). Depending on the adaptation time-constant and the shape of the neuron's f-I-curves, the response of the neuron resembles the time-derivative of the stimulus (section 4.3.4). Together with the inherent threshold-property of the spike-generator, adaptation is more than just filtering out the mean intensity of the stimulus. It also leads to effects like suppression of background-

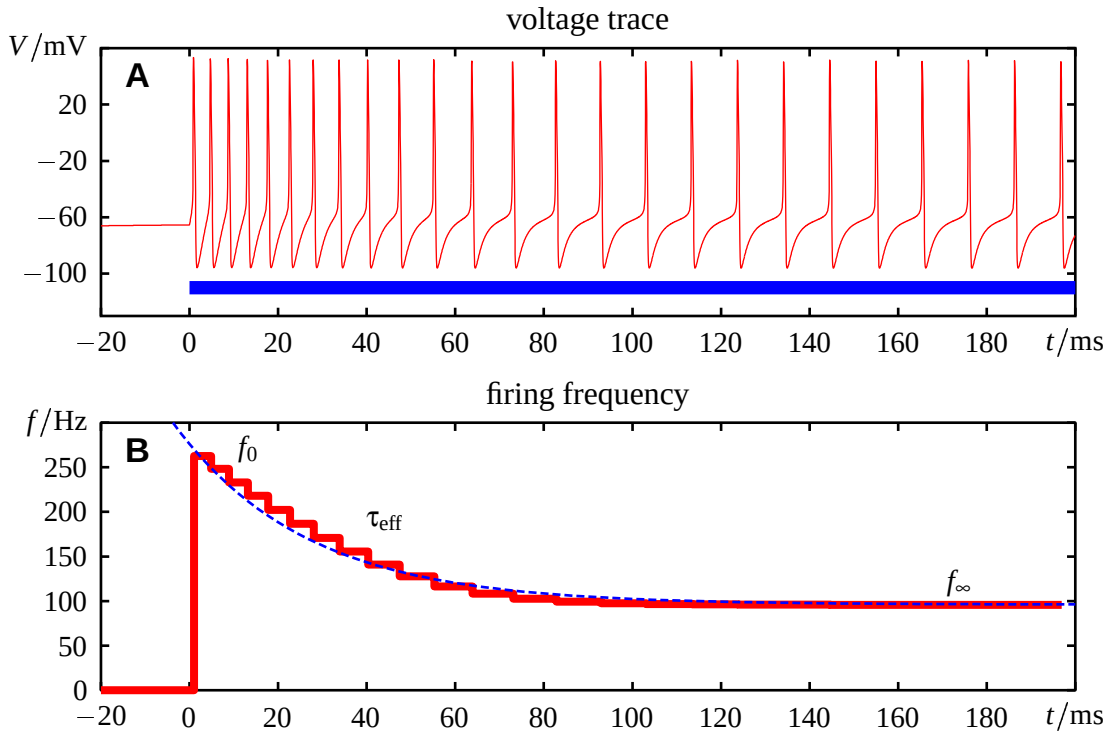

Figure 4.2: THE PHENOMENON OF SPIKE-FREQUENCY ADAPTATION. **A** The voltage trace of a modified Traub-&-Miles model with AHP-current evoked by a constant stimulus ($I = 18$) as indicated by the solid bar. **B** The corresponding instantaneous firing frequency as the reciprocal of the interspike intervals. The onset response f_0 decays with some time-constant τ_{eff} down to a steady-state value f_∞. This decay is approximately exponential (dashed line).

noise and forward-masking as demonstrated in section 4.3.5.

For the illustrations the modified Traub-Miles models as well as the Crook models are used. Either an M-type current or an AHP-current was added to simulate spike-frequency adaptation. The definitions of the models are summarized in appendix A.

4.1 From channels to firing frequency

The phenomenon spike-frequency adaptation is illustrated in Fig. 4.2. Assume a neuron to be completely unadapted. Its initial response to the onset of a constant stimulus reflects the properties of the non-adapted neuron, i.e. the fast processes of the spike generator alone. This is covered by the neuron's onset f-I-curve $f_0(I)$, which describes the initial firing frequency f_0 in dependence of the stimulus intensity I (see Fig. 4.3). Then the firing frequency decays to some steady-state value — the neuron adapts. From these values the steady-state f-I-curve $f_\infty(I)$ can be drawn. The decay of the firing frequency is approximately exponential and is characterized by some effective adaptation time-constant τ_{eff}. As will be shown, this time constant may differ from the one of the underlying process and may depend on input intensity or firing frequency.

In the following, phenomenological models for spike-frequency adaptation are derived from different biophysical mechanisms. First, three possibilities of encoder adaptation are investigated in detail and a general firing-frequency model is introduced. Then, similar models of subtractive transducer adaptation and depressing synapses are proposed.

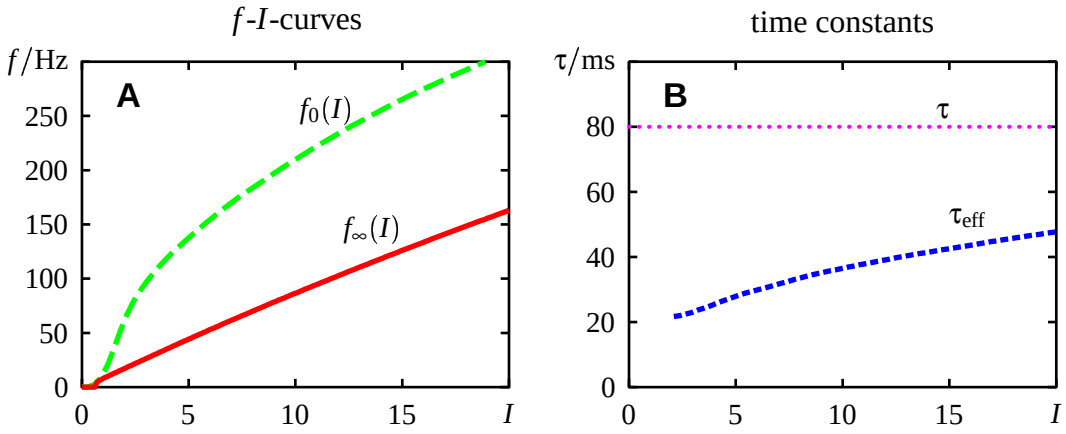

Figure 4.3: f-I-CURVES AND TIME CONSTANTS OF AN ADAPTING NEURON. **A** The onset and the steady-state f-I-curve, $f_0(I)$ and $f_\infty(I)$, constructed from the modified Traub-&-Miles model with AHP-current (same model neuron as in Fig. 4.2). The linear steady-state f-I-curve is an effect of linear adaptation. This linearization is discussed in section 4.3.2. **B** The effective time constant τ_{eff} of the decay of the firing frequency for different input intensities I. It is much smaller than the time constant of the calcium removal ($\tau = 80$ ms), which sets the dynamics of adaptation in this model. Furthermore τ_{eff} depends on input intensity.

4.1.1 Encoder adaptation

Encoder adaptation is caused by different types of ionic channels, which decrease the sensitivity of the spike generator. It is therefore an intrinsic mechanism of the neuron and can be studied by current injections.

The aim of the following analysis is, first, to investigate how adaptation acts on the neuron's f-I-curve and, second, to derive a one-dimensional differential equation for the state of adaptation. In combination this approach results into a simple model for the firing frequency of an adapting neuron, which is defined by the neuron's f-I-curves.

As discussed in the previous chapter, the spike encoding process of a non-adapting neuron is mainly defined by the firing frequency given by the neurons f-I-curve:

$$f(t) = f_0(I(t)) \,, \tag{4.1}$$

where the injected current $I(t)$ is the input. This relation captures the dynamics of all the currents involved in the generation of spikes, i.e. the current balance equation for the membrane potential V

$$C\dot{V} = \sum_i g_i(E_i - V) + I \,, \tag{4.2}$$

which sums up the ionic currents through channels with total conductance g_i and reversal potential E_i (recall chapter 2 for details).

Consider an adaptation current

$$I_a = -\bar{g}_a a(V - E_a) \tag{4.3}$$

with maximum conductance $\bar{g}_a$, reversal potential E_a and gating variable a, which obeys some additional differential equation. According to Kirchoff's law this current has to be added to the current balance equation (4.2):

$$C\dot{V} = \sum_i g_i(E_i - V) + I - \bar{g}_a a(V - E_a) \,. \tag{4.4}$$

Therefore, the adaptation current can be viewed as an additional input current. The firing frequency of the neuron is then given by

$$f(t) = f_0(I + I_a) = f_0(I - \bar{g}_a a(V - E_a)) \,. \tag{4.5}$$

This is the starting point for the discussion of different mechanisms of encoder adaptation. However, in this form (4.5) is rather useless, since it depends still on the membrane potential V. In the following, the adaptation current is transformed to depend on the firing frequency f. Then the corresponding dynamics of the adaptation gating-variable is investigated for each of the discussed adaptation mechanisms. Nevertheless, (4.5) gives a first hint that adaptation may just shift the neuron's unadapted f-I-curve $f_0(I)$ in dependence on the adaptation gating-variable a.

Two properties of the adaptation current (4.3) are important to eliminate its dependence on the membrane potential V. First, the dynamics of the adaptation gating-variable a is slow compared to the dynamics of the generation of spikes (4.2) (see for example Fig. 4.4 C). Second, adaptation currents are small compared to the sodium and potassium currents during a spike. Thus, the adaptation gating-variable a is a slow variable, which is weakly coupled into the fast spike dynamics (4.2). The slow and the fast sub-systems of such dynamics can be treated separately (Strogatz, 1994). The time course of the slow adaptation gating-variable $a(t)$ can be replaced by its running average $\langle a \rangle_T (t)$ defined by

$$a(t) \approx \langle a \rangle_T (t) := \frac{1}{T(t)} \int_{t-T(t)/2}^{t+T(t)/2} a(t') \mathrm{d}t' \,, \tag{4.6}$$

where the interspike intervals $T(t)$ are the periods of the fast spike generation. Note that the interspike intervals have to be short compared to the time constant of the adaptation dynamics, to allow the distinction of a fast and a slow dynamics. In other words, the approximation of the adaptation dynamics to be slow is valid for sufficiently high firing frequencies only.

Caused by the time-varying driving force $V(t) - E_a$ the adaptation current I_a strongly fluctuates during spikes (see Fig. 4.4 D). Therefore it is not a good approximation to replace the whole adaptation current I_a (4.3) by its running average $\langle I_a \rangle$. However, phase-resetting curves of neurons show that during the spike and during the refractory period, fluctuations of the input have almost no effect on the firing behavior (see Fig. 2.12 and section 3.4). What matters for the generation of spikes is the time course of the adaptation current between the spikes. There it fluctuates much less than during the spikes, and it could be substituted by a suitable average, which emphasizes the interspike interval and neglects the spike. The best way to do so is to use the response function $z(t)$ as the weight for an average over one interspike interval T

$$I_a(t) \approx \langle I_a \rangle_z (t) := \frac{1}{T(t)} \int_{t-T(t)/2}^{t+T(t)/2} \tilde{z}(t') I_a(t') \mathrm{d}t' \tag{4.7}$$

(compare with (3.36) on page 50). $\tilde{z}(t)$ is the response function $z(t)$ normalized to one. Since the maximum conductance $\bar{g}_a$ is constant, and the averaged gating variable $\langle a \rangle$ is approximately constant during an interspike interval, the adaptation current can be replaced by

$$I_a \approx -\bar{g}_a \langle a \rangle \langle V - E_a \rangle_z \,. \tag{4.8}$$

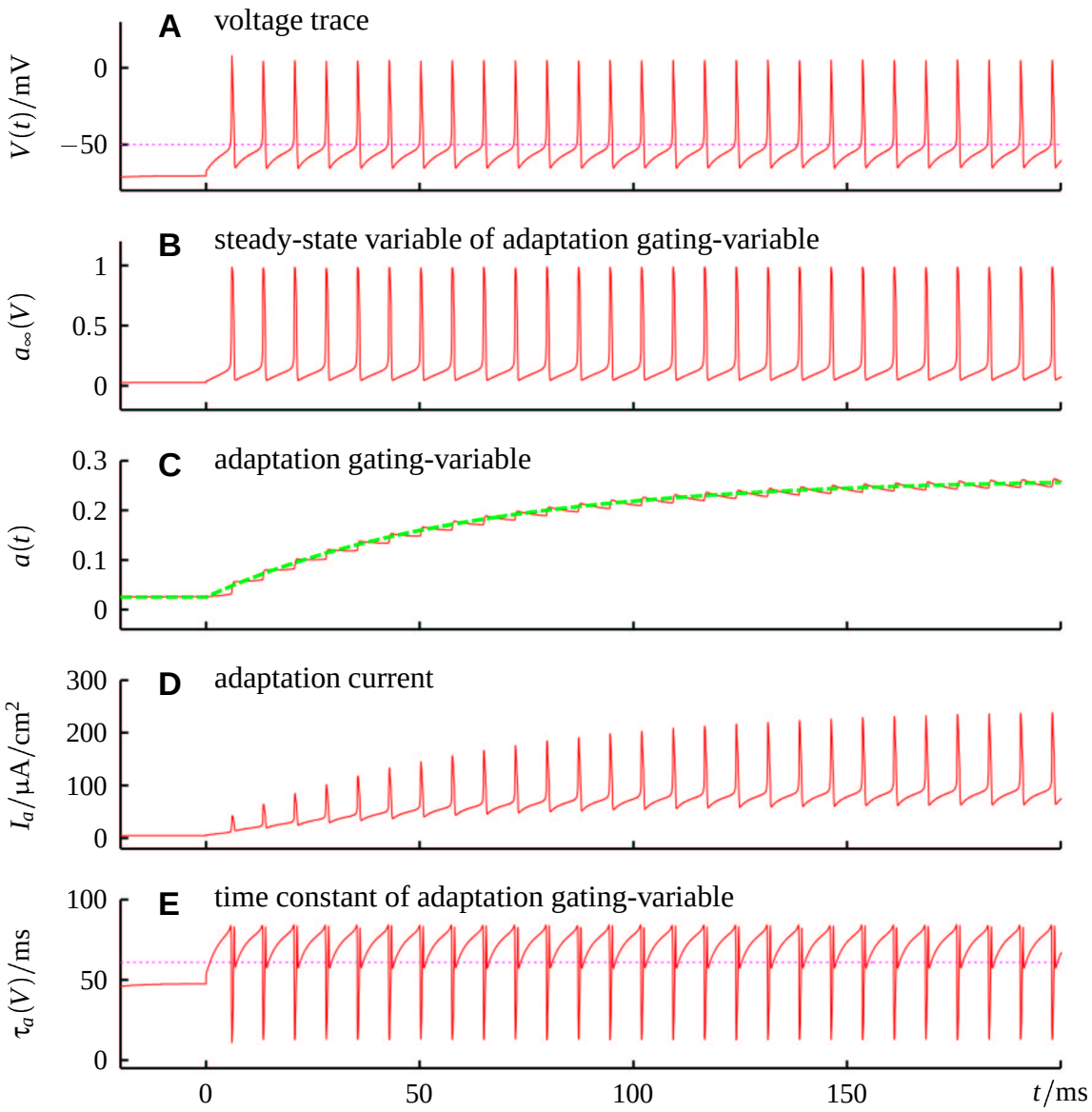

Figure 4.4: THE DYNAMICS OF AN ADAPTATION CURRENT. Variables of the Crook model stimulated with a constant current starting at $t = 0$. Only the sodium, potassium and calcium currents are included in the membrane equation. Therefore the firing frequency is constant and does not adapt. The variables shown in panel B – E are the one of an M-type current activated by the voltage trace shown in A. However, the resulting adaptation current I_a is not included in the membrane equation (4.2), thus it has no effect on the spike-train. The steady-state variable $a_\infty(V)$ and the time constant $\tau_a(V)$ used to model the M-type current are shown in Fig. 4.6. **A** The voltage trace. The dotted line marks the potential above which $a_\infty(V)$ is activated. **B** The time course of $a_\infty(V)$ resulting from the voltage trace in A. **C** Due to $a_\infty(V)$ the adaptation gating-variable a is incremented at each spike. Between the spikes a decays with the time constant $\tau_a(V)$ shown in E. The time course of a can be well approximated by its mean $\langle a \rangle$ (dashed line), which is an exponential with a time constant of 61 ms. **D** The adaptation current $I_a = \bar{g}_a a(V - E_a)$. Note its large fluctuations caused by the spikes and the after-hyperpolarization. **E** The time constant $\tau_a(V)$. It also fluctuates very strongly during the spikes. The dotted line is the time constant describing the mean gating variable in C.

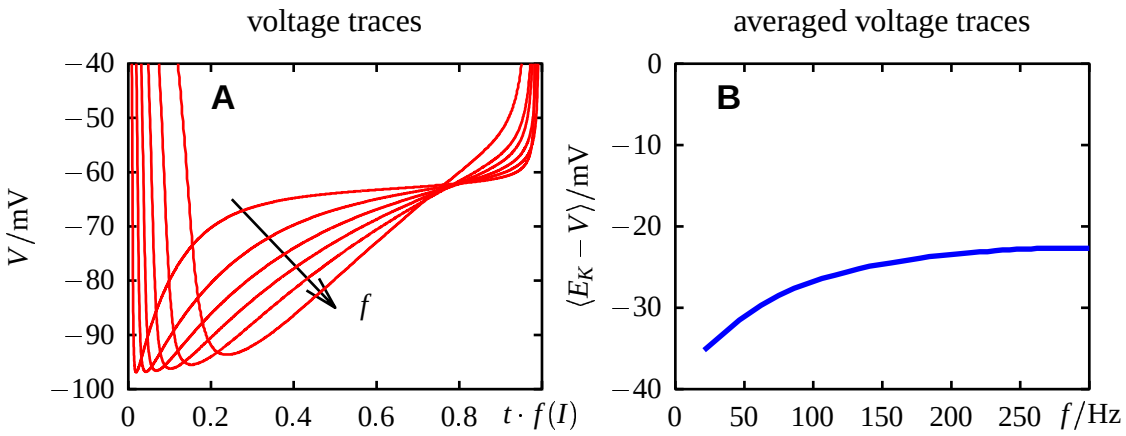

Figure 4.5: AVERAGING THE MEMBRANE POTENTIAL. **A** Time course of the membrane potential during the interspike intervals for different firing frequencies f of the same model used in Fig. 4.2 and 4.3 (modified Traub-&-Miles with AHP-current). For low firing frequencies the membrane potential stays longer near about $-65\,\mathrm{mV}$. More time at more hyperpolarized potentials is spent with increasing firing frequency. The corresponding firing frequencies to the voltage traces are 20, 46, 75, 115, 178, and 302 Hz. **B** Averaged driving force $\langle E - V \rangle_z$ using the weighted average (4.7). For high firing frequencies the averaged driving force is approximately independent of the firing frequency f.

The membrane potential V, as one of the variables of the fast spike generating dynamics, occurs now inside an average only, i.e. its detailed time course is not of importance. One-dimensional phase oscillators are capable of predicting spikes simulated by conductance-based models fairly well, as demonstrated in the previous chapter. Thus, during repetitive firing the neuron's trajectory stays close to stable limit cycles. The limit cycles are determined by the input current. Associated with each of these limit cycles is a certain period of oscillation — an interspike interval. Given the firing frequency $\nu(t) = 1/T$ as the reciprocal interspike interval, the corresponding limit cycle is known. Since the system stays close to the limit cycles, the time course of the membrane potential $V(t)$ is determined by the limit cycle, and in turn by the input current. Thus, averages of functions depending on the membrane potential $V(t)$ can be approximated by functions depending on the firing frequency $\nu(t)$. This is an essential approximation, which is used frequently in the following to eliminate the membrane potential $V(t)$ or other fast variables of the spike generator.

Therefore, the average $\langle V - E_a \rangle_z$ in (4.8) can be replaced by a function depending on $\nu(t)$:

$$\langle V - E_a \rangle_z \approx \rho(\nu)\,. \tag{4.9}$$

How the time course of the voltage trace depends on firing frequency can be seen in Fig. 4.2 and 4.5, as well as in various experimental studies, for example Schwindt (1973) and Avoli et al. (1994). The values of the membrane potential between two spikes depend not strongly on firing frequency, especially if the differences are compared to the absolute values of the membrane potential. Therefore the average $\langle V - E_a \rangle_z$ (4.9) is expected to be essentially constant in ν, while higher order terms are much smaller. To emphasize this, (4.9) is rewritten to

$$\langle V - E_a \rangle_z \approx \tilde{\rho}[1 + \gamma(\nu)] \tag{4.10}$$

where $\tilde{\rho}$ is now a constant and $\gamma(\nu)$ captures the dependence on the firing frequency ν.

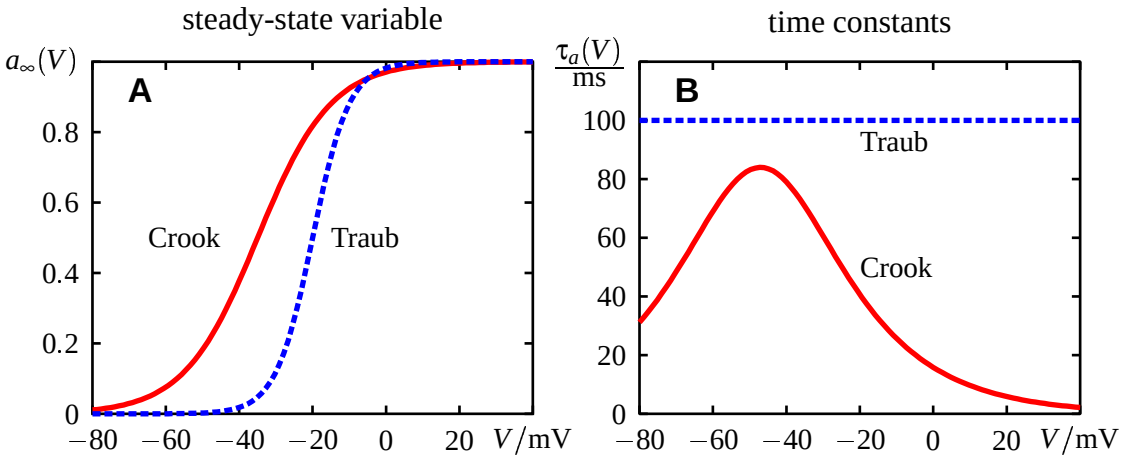

Figure 4.6: PROPERTIES OF THE M-TYPE-CURRENT GATING VARIABLE. **A** The dependence of the activation function $a_\infty(V)$ on the membrane potential V as defined in the Crook model (Crook et al., 1998) and the modified Traub-&-Miles model (Traub et al., 1991). While in the Crook model the M-current is activated already at rest, in the modified Traub-&-Miles model it is only activated during spikes. **B** The time constant $\tau_a(V)$ in the Crook model depends realistically on the membrane potential V. In the modified Traub-&-Miles model it is assumed to be constant.

The constant $\tilde{\rho}$ is positive, since a potassium adaptation-current, for example, has a reversal potential E_a, which is always below the membrane potential V. Thus, $\langle V - E_a \rangle_z$ is positive.

As outlined in the previous chapter, the observed firing frequency $\nu(t)$ in general differs from firing frequencies $f(t)$, like the ones given by (4.5), which are just a mapping of the stimulus through the neuron's f-I-curve. The neuron integrates over $f(t)$ and therefore $\nu(t)$ is slower than $f(t)$. However, due to the small value of $\gamma(\nu)$ the firing frequency $\nu(t)$ in (4.10) can be replaced by $f(t)$ without changing the result too much.

Denoting $\bar{g}\langle a \rangle_T \tilde{\rho}$ as the state of adaptation $A(t)$, a general equation is obtained for the firing frequency of a neuron with encoder adaptation:

$$\boxed{f(t) = f_0\Big(I - A[1+\gamma(f)]\Big)} \,. \tag{4.11}$$

This result already shows how adaptation influences the neuron's f-I-curve. As expected from (4.5), the onset f-I-curve $f_0(I)$ is indeed shifted due to adaptation ($-A$), but it is also distorted by the $\gamma(f)$-term.

The dynamics for the state of adaptation $A(t)$ still has to be derived. Since the biophysical mechanisms of the different possibilities of encoder adaptation differ, they are treated separately in the following sections.

M-type currents

M-type currents are slow voltage dependent potassium currents (Brown & Adams, 1980; Halliwell & Adams, 1982; Marrion, 1997; Wang et al., 1998; Selyanko & Brown, 1999; Schroeder et al., 2000). Their dynamics for the adaptation gating-variable a is given by

$$\tau_a(V)\frac{\mathrm{d}a}{\mathrm{d}t} = a_\infty(V) - a \,. \tag{4.12}$$

The steady-state variable $a_\infty(V)$ is a sigmoidal function of the membrane potential V with values ranging from zero to one. The transition region of $a_\infty(V)$ is at high potentials, where the time constant $\tau_a(V)$ decreases (see Fig. 4.6). Thus, this current is activated during a spike. Between the spikes, M-type currents deactivate slowly. Since they are potassium currents, they lower the sensitivity of the spike generator to input currents (see 4.4).

In order to set up the dynamics of the state of adaptation A needed for the model (4.11), a differential equation for the averaged gating variable $\langle a \rangle_T$ has to be derived. For this purpose the differential equation of the adaptation gating-variable a (4.12) is first divided by $\tau_a(V)$ and then averaged:

$$\left\langle \frac{\mathrm{d}a}{\mathrm{d}t} \right\rangle_T = \left\langle \frac{a_\infty(V)}{\tau_a(V)} \right\rangle_T - \left\langle \frac{a}{\tau_a(V)} \right\rangle_T . \tag{4.13}$$

Since a is slow, the operations of averaging over time and taking the time-derivative can be exchanged[1]. The last term in (4.13) can be factorized, provided $a(t)$ and $1/\tau_a(t)$ are uncorrelated. This can be expected for the following reasons:

As stated above, the steady-state variable $a_\infty(V)$ has its transition region at high potentials. From the Hodgkin-Huxley formalism is known that the time constant $\tau_a(V)$ is given by $a_\infty(V)$, divided by the corresponding rate constant $\alpha(V)$ for the transition of the channels from their closed state to open (Johnston & Wu, 1997). Since $\alpha(V)$ is monotonically increasing, $\tau_a(V)$ has a maximum value somewhere above the cells resting potential (see Fig. 4.6 B). This results in a fast fluctuating time course of the time constant τ_a during spikes, as can be seen in Fig. 4.4 E. Therefore, the slow time course of the gating variable a is almost uncorrelated to $1/\tau_a$, and the average $\langle a/\tau_a \rangle_T$ can be split into the product $\langle a \rangle_T \cdot \langle 1/\tau_a \rangle_T$.

Dividing (4.13) by $\langle 1/\tau_a \rangle_T$ results in the desired differential equation for $\langle a \rangle_T$

$$\frac{1}{\langle 1/\tau_a(V) \rangle_T} \frac{\mathrm{d}\langle a \rangle_T}{\mathrm{d}t} = \frac{1}{\langle 1/\tau_a(V) \rangle_T} \left\langle \frac{a_\infty(V)}{\tau_a(V)} \right\rangle_T - \langle a \rangle_T . \tag{4.14}$$

As discussed already for equation (4.9) above, averages over functions depending on the membrane potential V can be replaced by functions depending on the firing frequency ν. So, for (4.14) a time constant $\tilde{\tau}(\nu) \approx 1/\langle 1/\tau_a \rangle_T$ and a steady-state variable $\alpha(\nu) \approx 1/\langle 1/\tau_a \rangle_T \langle a_\infty/\tau_a \rangle_T$ is obtained. (4.14) is a linear first order differential equation, which acts like a low pass filter on the steady-state variable $\alpha(\nu)$. Therefore, the slow $\nu(t)$ can be in a good approximation replaced by the faster $f(t)$. Then (4.14) becomes

$$\tilde{\tau}(f) \frac{\mathrm{d}\langle a \rangle_T}{\mathrm{d}t} = \alpha(f) - \langle a \rangle_T . \tag{4.15}$$

[1] The average and the time derivative of a in general cannot be exchanged, since the length of the averaging window $T(t)$ depends in time t. Instead

$$\left\langle \frac{\mathrm{d}a}{\mathrm{d}t} \right\rangle_T = \frac{\mathrm{d}\langle a \rangle_T}{\mathrm{d}t} - \frac{\mathrm{d}T/\mathrm{d}t}{T} \left(\frac{a(t+T/2) + a(t-T/2)}{2} - \langle a \rangle_T \right) .$$

However, since changes in a are assumed to be much slower than T, $(a(t+T/2) + a(t-T/2))/2 - \langle a \rangle$ tends to zero. Therefore, the second term of the right hand side can be neglected and the average can be exchanged with the derivative

$$\left\langle \frac{\mathrm{d}a}{\mathrm{d}t} \right\rangle_T \approx \frac{\mathrm{d}\langle a \rangle_T}{\mathrm{d}t} .$$

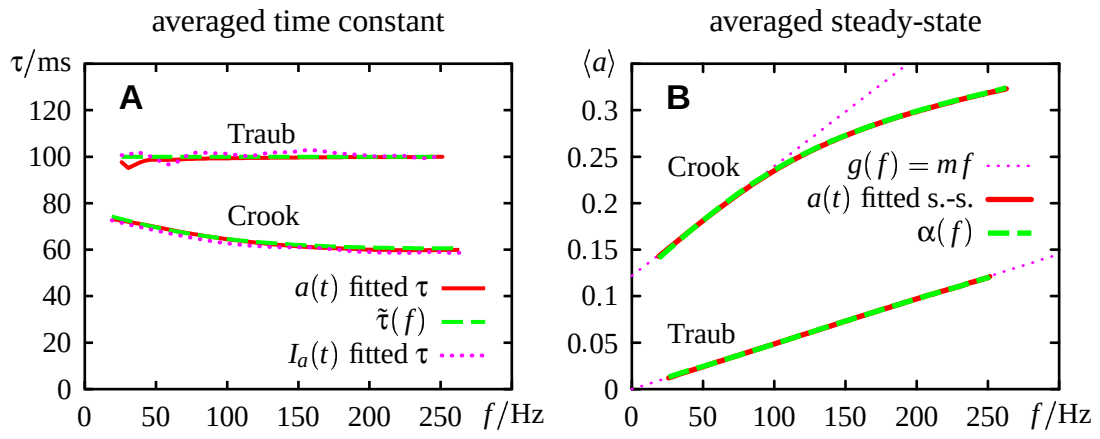

Figure 4.7: AVERAGING THE DYNAMICS OF THE M-TYPE CURRENT GATING-VARIABLE. Doing the same simulation as in Fig. 4.4 (M-type current not included in the membrane equation) for different firing frequencies f allows one to measure the adaptation time-constant and the steady-state variable as a function of f. The different results for the modified Traub-&-Miles and the Crook model are compared. See Fig. 4.6 for the different properties of their M-currents. **A** The adaptation time-constant fitted from the time course of the adaptation gating-variable $a(t)$ (Fig. 4.4 C), as the average $\tau(f) = 1/\langle 1/\tau_a(V)\rangle_T$ of $\tau_a(V)$ over a single interspike interval, and fitted from the time course of the resulting adaptation current I_a (Fig. 4.4 D). The latter corresponds to the time constant of the adaptation dynamics (4.16). All three measures agree quite well. Since in the modified Traub-&-Miles model the time constant is assumed to be constant, the adaptation time constant does not depend on the firing rate f. The situation is different with a voltage-dependent time constant like in the Crook model. The adaptation time constant then depends on firing frequency. **B** The steady-state variable of adaptation measured from the time course of the adaptation gating-variable $a(t)$ (Fig. 4.4 C), and as the average $\alpha(f) = 1/\langle 1/\tau_a\rangle_T \langle a_\infty/\tau_a\rangle_T$ of $a_\infty(V)$ over a single interspike interval. For comparison, the best fitting straight lines $g(f) = mf$ are plotted (dotted lines). In the modified Traub-&-Miles model, the M-current is only activated during spikes, and therefore the steady-state variable of the adaptation gating-variable $\alpha(f)$ is proportional to the firing frequency f. In the Crook model, the M-current is also activated by potentials at rest and between the spikes. This results in a nonlinear dependence of $\alpha((f)$ on firing frequency. However, the offset can be removed and added to the leak-current in the membrane equation (4.2). Then $\alpha(f)$ can be well approximated by a straight line for small firing frequencies.

The averaged $\langle 1/\tau_a\rangle_T$ mainly depends on the time course of $\tau_a(V)$ between the spikes, which in turn is determined by the corresponding time course of the membrane potential. Thus, the time constant $\tilde{\tau}(f)$ is expected to depend only weakly on f, corresponding to the situation for the driving force $V - E_a$ (4.10) discussed above. To emphasize this, $\tilde{\tau}(f)$ is rewritten as $\tau(1+\varepsilon(f))$, where τ is a constant and $\varepsilon(f)$ captures all the dependencies on the firing frequency f.

For the steady-state variable $a_\infty(V)$ the situation is different. It nearly vanishes between the spikes. Therefore the average $\langle a_\infty/\tau_a\rangle_T$ is determined mainly by the time course of the membrane potential during the spikes. The shapes of the spikes are approximately always the same, resulting in $\alpha(f)$ to be basically proportional to the firing frequency f.

Multiplying (4.15) with $\bar{g}\rho$ and denoting $A_\infty(f) = \bar{g}\rho_a\alpha(f)$, finally a linear differential equation for the state of adaptation $A = \bar{g}\rho_a\langle a\rangle$ is obtained:

$$\boxed{\tau[1+\varepsilon(f)]\dot{A} = A_\infty(f) - A} \,. \tag{4.16}$$

Together with (4.11) this is a complete description of the firing frequency $f(t)$ of an adapting neuron evoked by arbitrary stimuli $I(t)$.

AHP-currents

A very important adaptation mechanism is due to the AHP-current, a calcium dependent potassium current (Madison & Nicoll, 1984). Basically, spikes induce an influx of calcium through voltage-gated calcium channels, which increases the intracellular concentration of free calcium. This calcium is removed with a slow time-constant (tens of milliseconds). The amount of AHP-current depends on the intracellular calcium concentration. Since it is a potassium current, it reduces the firing frequency — the neuron adapts.

First, there are the voltage gated calcium channels of the N-, P-, Q-, L- and T-type. They are all activated very fast by depolarizations induced by spikes (about one millisecond, Kay & Wong, 1987; Jaffe et al., 1994). N-, P-, Q- and L-type channels have a high activation threshold while T-type channels have a low threshold (Jaffe et al., 1994). Recent calcium imaging studies show that the amount of calcium influx per spike is in good approximation constant and indeed is mediated by the calcium channels (Markram et al., 1995; Schiller et al., 1995; Helmchen et al., 1996; Borst & Helmchen, 1998; Smetters, 1999). Calcium-induced calcium release may also contribute to the calcium transients induced by spikes (Sandler & Barbara, 1999). Altogether, the processes of calcium influx are very fast and therefore are captured by the unadapted f-I-curve $f_0(I)$.

Calcium is removed again from the cytoplasm with a slow time constant τ_{Ca}. This process is the result of buffering, diffusion, and calcium pumps. The endoplasmatic reticulum serves as an important calcium buffer and exhibits its own dynamics (see Berridge (1998) for a review). Diffusion of free calcium in the cytoplasm is a three-dimensional process and calcium pumps can carry a sizeable current in dependence on calcium concentration (Schutter & Smolen, 1998). In its simplest form, all these processes are combined in a single differential equation for the concentration of the intracellular free calcium $[\mathrm{Ca}^{2+}]$

$$\frac{\mathrm{d}[\mathrm{Ca}^{2+}]}{\mathrm{d}t} = -\beta I_{\mathrm{Ca}} - [\mathrm{Ca}^{2+}]/\tau_{\mathrm{Ca}} \tag{4.17}$$

(Traub et al., 1991). The concentration of intracellular calcium is increased proportionally to the calcium influx I_{Ca}. The time constant τ_{Ca} of the calcium removal determines the time scale of this type of adaptation. It is equivalent to the time constant τ_a of the M-type current discussed above.

Finally, depending on intracellular calcium concentration a potassium current is activated (Brown & Griffith, 1983; Madison & Nicoll, 1984)

$$\begin{aligned} I_{\mathrm{AHP}} &= \bar{g}_{\mathrm{AHP}} q (V - E_{\mathrm{K}}) \\ \tau_q([\mathrm{Ca}^{2+}])\dot{q} &= q_\infty([\mathrm{Ca}^{2+}]) - q \end{aligned} \tag{4.18}$$

This medium after-hyperpolarization (mAHP)-current is responsible for spike-frequency adaptation. Due to the calcium dynamics (4.17) $q_\infty([\mathrm{Ca}^{2+}])$ is changing slowly, too. The time constant τ_q of this current is much faster than the one of the calcium removal. Thus the gating variable q can be replaced by its steady-state variable $q_\infty([\mathrm{Ca}^{2+}])$. Similar to the M-type current, there is now a single differential equation for the adaptation process (here the one for the calcium dynamics), which gates a potassium current. The only difference is that the adaptation variable $[\mathrm{Ca}^{2+}]$ enters the adaptation current (4.18) through a nonlinear function $q_\infty([\mathrm{Ca}^{2+}])$. However, as analysis of various models show, $q_\infty([\mathrm{Ca}^{2+}])$ is

a first order Michaelis-Menten-function and takes only small values (Crook et al., 1998; Ermentrout, 1998). Therefore it can be approximated by the proportionality $c \cdot [\mathrm{Ca}^{2+}]$, and the adaptation strength in this case is $A = \bar{g}_a \rho_a c \left\langle [\mathrm{Ca}^{2+}] \right\rangle$. Averaging the dynamics of the intracellular calcium concentration (4.17) results in the same equation (4.16) as for the M-type current.

Slow recovery from inactivation

Slow recovery from inactivation of fast sodium channels was reported in stretch-receptor neurons of several arthropod species (cockroach: French (1989b), lobster: Edman et al. (1987a), crayfish: Purali & Rydqvist (1998)) as well as in mammalian pyramidal cells (Fleidervish et al., 1996; Martina & Jonas, 1997). An additional inactivation process, which is much slower than the Hodgkin-Huxley-type inactivation (Hodgkin & Huxley, 1952), induces use-dependent removal of excitable sodium channels. This results in spike-frequency adaptation (Fleidervish et al., 1996). The time constants of this slow inactivation process range from 133 ms (Martina & Jonas, 1997) and 450 ms (Fleidervish et al., 1996) in mammals to more than a second in arthropods (Edman et al., 1987a; French, 1989b; Edman et al., 1987a). Evidence of slow inactivation was also reported from the persistent sodium current $I_{\mathrm{Na,P}}$ (Fleidervish et al., 1996).

The fast sodium current I_{Na} is gated by an activation variable m and two inactivation variables h and s:

$$\begin{aligned} I_{\mathrm{Na}} &= -\bar{g}_{\mathrm{Na}} m^3 h s (V - E_{\mathrm{Na}}) \\ \tau_m(V)\dot{m} &= m_\infty(V) - m \\ \tau_h(V)\dot{h} &= h_\infty(V) - h \\ \tau_s(V)\dot{s} &= s_\infty(V) - s \,. \end{aligned} \tag{4.19}$$

The time constant τ_m of the activation gating-variable m is shorter than one millisecond, τ_h of the inactivation variable h has values of a few milliseconds (Hodgkin & Huxley, 1952; Martina & Jonas, 1997). In contrast, the time constant τ_s of the slow inactivation process is very slow (several 100 ms).

Replacing the slow inactivation gating-variable s by $1 - a$ results in

$$\begin{aligned} I_{\mathrm{Na}} &= -\bar{g}_{\mathrm{Na}} m^3 h (V - E_{\mathrm{Na}}) + \bar{g}_{\mathrm{Na}} m^3 h a (V - E_{\mathrm{Na}}) \\ \tau_s(V)\dot{a} &= 1 - s_\infty(V) - a \,. \end{aligned} \tag{4.20}$$

The sodium current has been formally split into two components. The first one depends only on the two fast gating variables m and h. It is responsible for initiation of spikes and therefore contributes to the unadapted f-I-curve $f_0(I)$. The second component depends on the two fast gating variables m and h, too, and in addition on the slow gating variable a. This component is therefore the reason for adaptation. The differential equation for a is very similar to the one of an M-like current discussed above. Its time constant $\tau_s(V)$ is voltage dependent and much slower than the the spike generating processes. The steady-state variable $1 - s_\infty(V)$ is activated at depolarized potentials during spikes. Thus, the same differential equation (4.15) is obtained for the averaged gating variable $\langle a \rangle_T$.

The adaptation current $\bar{g}_{\mathrm{Na}} m^3 h a (V - E_{\mathrm{Na}})$ differs from the general one given in (4.3) by the additional fast gating variables m and h. They have to be included in the averaging process (4.7) of the adaptation current. As for the membrane potential, the time courses of the fast variables $m(t)$ and $h(t)$ are determined by the limit cycles during repetitive spiking. Averaging over any combination of such variables results also in a function

depending on the firing rate f:

$$\left\langle \bar{g}_{\mathrm{Na}} m^3 h \langle a \rangle_T (V - E_{\mathrm{Na}}) \right\rangle_z \approx - \langle a \rangle_T \bar{g}_{\mathrm{Na}} \tilde{\rho} [1 + \gamma(f)] \tag{4.21}$$

The reversal potential of sodium E_{Na} is always above the membrane potential. Thus, the driving force $V - E_{\mathrm{Na}}$ is always negative. This is expressed in (4.21) by the negative sign. The constant $\tilde{\rho}$ is then positive.

The multiplication of a with $m^3 h$ makes the strength of the adaptation due to slow inactivation very small, since m is very small most of the time. On the other hand, the maximum conductance $\bar{g}_{\mathrm{Na}}$ of sodium currents is very high, thus compensating for the effect of small m.

There also exist slow inactivating potassium currents with a time constants of about one second (see for example Edman et al., 1987a; Storm, 1988; Delord et al., 2000). They result in positive adaptation, i.e. they increase the firing frequency during constant stimulation ($\tilde{\rho} < 0$).

General model for encoder adaptation

In summary, all three mechanisms responsible for encoder adaptation discussed above, result in exactly the same equations (4.11) and (4.16) for a phenomenological description of adaptation of the firing frequency $f(t)$:

$$\boxed{\begin{aligned} f &= f_0 \Big(I - A[1 + \gamma(f)] \Big) \\ \tau[1 + \varepsilon(f)] \dot{A} &= A_\infty(f) - A \end{aligned}} \tag{4.22}$$

The output firing frequency $f(t)$ is determined by the input current $I(t)$ and the state of adaptation $A(t)$. On this macroscopic level the different adaptation mechanisms are indistinguishable.

Physical stimulus as input

Until now an electrical current I was assumed to be the input to the neuron. This is the usual situation in current-clamp experiments. However, in reality neurons receive their input via changes in conductances. Especially receptor neurons are stimulated by physical stimuli resulting in conductance changes, but also synaptic input is mediated via changes in conductances. To account for such inputs, the input current I has to be replaced by a current $g_i(J)(E_i - V)$, where $g_i(J)$ is the conductance mediating the physical stimulus J and E_i is the corresponding reversal potential. Note, that the transduction of the physical stimulus $g_i(J)$ in this context can be understood directly, as in a receptor cell, or as the result of feed-forward processing over several neurons.

Again, the aim is to eliminate the V dependence of $g_i(J)(E_i - V)$. Using the same arguments as for the adaptation current (phase-resetting curve, equation (4.7)) and assuming either $g_i(t)$ to be slow or to be uncorrelated to the membrane potential[2], $E_i - V$ can be replaced by its average, which is some function $\rho_i(f)$ depending on the firing

[2]Note, that a weak input g_i, resulting in a very low firing frequency, is correlated with the membrane potential $V(t)$. However, at higher firing frequencies, the dynamics of $V(t)$ is dominated by the spike generating process, which uncorrelates V from g_i.

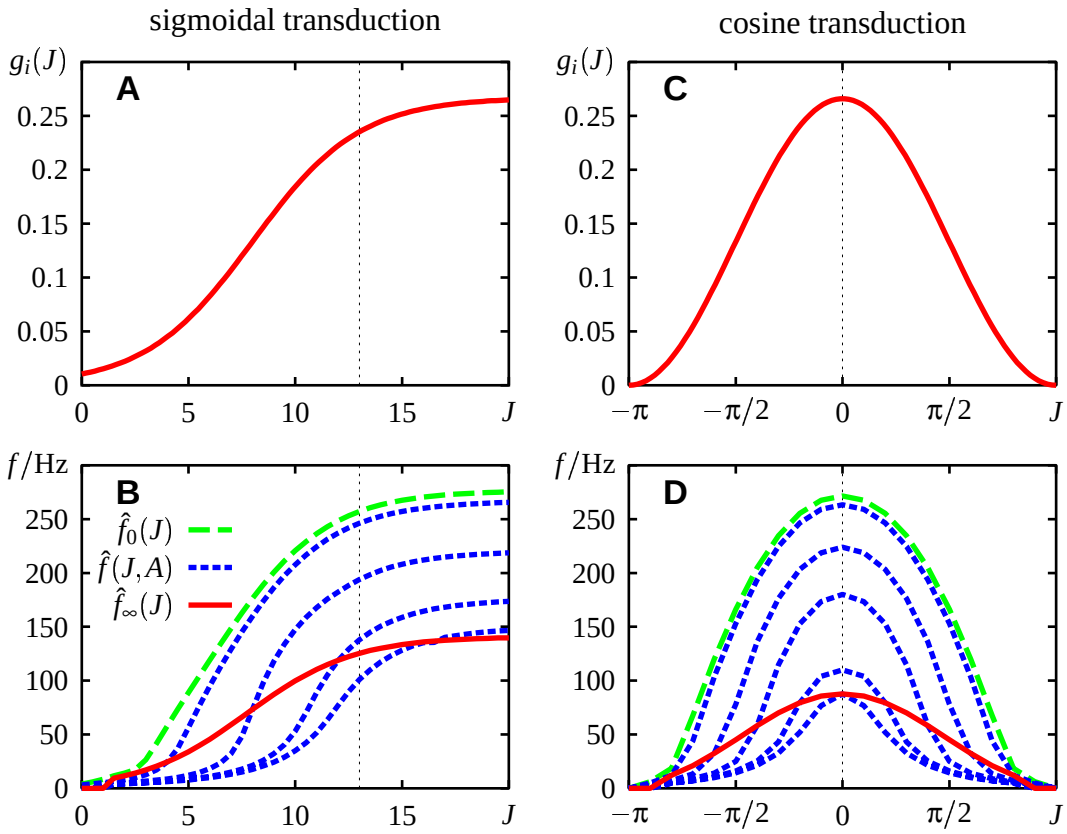

Figure 4.8: ENCODER ADAPTATION FOR TWO DIFFERENT TRANSDUCTION FUNCTIONS $g(J)$. A transduction-current $I = g_i(J)(0-V)$ was added to the membrane equation of the modified Traub-&-Miles model with AHP-current. **A** Sigmoidal transduction of the physical stimulus J into the conductance $g_i(J)$ (measured in μS/cm^2). The upper limit of the linear transition range is indicated by the dotted line. **B** The resulting f-J-curves $\hat{f}(J,A)$ for different strength of adaptation compared with the unadapted and the steady-state f-J-curve, $\hat{f}_0(J)$ and $\hat{f}_\infty(J)$, respectively. In the linear regime (upto the dotted line) the adapted f-I-curves are mainly shifted to the right, as it is the case for an injected current as input, but all of them saturate at the same input intensity (vertical line). **C** Orientation selective cells in the visual system or direction selective cells in the auditory system, for example, may have a cosine dependency of the conductance on the stimulus like $g(J) = 1+\cos(J)$. **D** Due to the symmetry of the conductance, the f-I-curves are symmetric to $J = 0$. Therefore, the adapted f-I-curves $\hat{f}(J,A)$ appear to be shifted downwards.

frequency f. In receptor neurons the reversal potential E_i is usually high compared to the resting potential of the neuron, to have a significant exciting effect of the stimulus J. Hence, the dependence of the time course of the membrane potential $V(t)$ on the firing frequency $f(t)$ is small compared to the absolute value of the averaged distance $\langle E_i - V\rangle_z$. This leads to an approximately constant function $\rho_i(f) \approx \tilde{\rho}_i$. Then the intensity-response function $\hat{f}_0(J)$ to the physical stimulus J is related to the current-response curve $f_0(I)$ by

$$\hat{f}_0(J) \approx f_0(g_i(J)\tilde{\rho}_i)\,. \tag{4.23}$$

Encoder adaptation is acting subtractive on the input current. The relation of the physical stimulus to its evoked membrane current in general is nonlinear due to $g_i(J)$. For this reason, the equations for encoder adaptation (4.22) cannot be taken over by just replacing the current input I by the physical input J.

However, if $g_i(J)$ is a sigmoidal function of J, its dynamical range can be approxi-

mated by a linear function $g_i(J) \approx mJ + b$. In this case, adaptation acts indeed subtractive on the physical stimulus J:

$$f(t) \approx f_0\Big(\tilde{\rho}_i(mJ+b) - A\Big) = f_0\Big(\tilde{\rho}_i m(J - A/m/\tilde{\rho}_i) + \tilde{\rho}_i b\Big) = \hat{f}_0(J - \hat{A}) \,, \qquad (4.24)$$

where the strength of adaptation is now $\hat{A} = A/m/\tilde{\rho}_i$ and for simplicity $\gamma(f)$ is neglected. At the saturation of $g_i(J)$, the f-I-curve $\hat{f}_0(J)$ has to saturate, too, since increasing input J no longer increases the conductance g_i. Therefore, the input strength where g_i and the f-I-curve saturates, cannot be changed by encoder adaptation. So, for a sigmoidal function $g_i(J)$ the neuron's f-J-curve is shifted due to adaptation only in the range of its transition. This is illustrated in Fig. 4.8 A & B.

A different common scenario is a cyclic dependence of the conductance on the stimulus, e.g. $g(J) = 1 + \cos(J)$, where J is some angle. Such dependencies can be found in orientation selective cells in the early visual pathway, where the input is the orientation angle of a bar. Also, there are neurons in the auditory pathway of vertebrates, which are tuned to a certain phase difference between left and right ear. There is no prominent linear region in $g(J)$. As a consequence, the shift of the f-I-curve induced by encoder adaptation is completely obscured by the nonlinearity of $g(J)$. The resulting adapted f-I-curves appear to be shifted downwards (see Fig. 4.8 C and D).

4.1.2 Transducer adaptation

In receptor cells a different type of adaptation can be observed in addition to encoder adaptation. It occurs in the transduction of the physical stimulus J.

For example, in vertebrate hair cells it is well known from voltage clamp experiments that the transducer current shows adaptation, which results in a shift of the response function (Hille, 1992; Holt et al., 1997). In voltage clamp this input current is proportional to the conductance g_i mediating the physical stimulus J (i.e. deflection of the hair bundle) via Ohm's law. Adopting the formalism derived above for encoder adaptation, the time course of the conductance $g_i(t)$ is given by the unadapted response $g_{i,0}(J)$ shifted due to the state of adaptation A:

$$g_i(t) = g_{i,0}(J(t) - A(t)) \qquad (4.25)$$

This type of adaptation is directly acting on the input $J(t)$.

The dynamics for A is

$$\tau_i(J)\dot{A} = A_\infty(J) - A \,, \qquad (4.26)$$

where the time constant τ_i and the steady-state variable A_∞ now depends on the input J (Ricci et al., 1998).

The spike generator of the neuron transforms the state of the conductance g_i into spikes. This process is characterized by its f-J-curve $\hat{f}_0(J) = f_0(g_i(J)(E_i - V))$, which can be measured directly as a function of the input J. Due to (4.25) transducer adaptation acts subtractive on the input

$$f(t) = \hat{f}_0(J(t) - A(t)) \qquad (4.27)$$

with the dynamics of A given by (4.26). In contrast to encoder adaptation it is driven by the input intensity J and not by the resulting firing frequency f.

Adaptation in photoreceptors induced by the interaction of cyclic GMP and free calcium is subtractive, too (Schnapf et al., 1990).

4.1.3 Depressing synapses

Since the work of Tsodyks & Markram (1997), the phenomenon of depressing synapses is quantitatively characterized. In a mean-field version (Tsodyks et al., 1998), the post-synaptic current $I(t)$ of a population of synapses is given by

$$\begin{aligned} I(t) &= \tau_{rec} A_{SE} U_{SE} x(t) r(t) \\ \dot{x} &= \frac{1-x}{\tau_{rec}} - U x r(t) \,, \end{aligned} \tag{4.28}$$

where τ_{rec} is the recovery time-constant of the synaptic resources, A_{SE} is the absolute synaptic strength, $x(t)$ are the available synaptic resources, U_{SE} is the fraction of the available synaptic resources $x(t)$, which is utilized by each spike, and $r(t)$ is the input firing rate. Rearranging the differential equation of $x(t)$ and substituting x by $1-A$ yields

$$\begin{aligned} I(t) &= \tau_{rec} A_{SE} U_{SE} r(t) (1 - A(t)) \\ \frac{\tau_{rec}}{1+U_{SE}\tau_{rec} r(t)} \dot{A} &= 1 - \frac{1}{1+U_{SE}\tau_{rec} r(t)} - A \,. \end{aligned} \tag{4.29}$$

In this version A is again a state of adaptation. It equals zero for the completely recovered (unadapted) synapse and increases due to depression. Its dynamics obeys a single linear differential equation with an effective time constant

$$\tau_{\text{eff}}(r) = \frac{\tau_{rec}}{1 + U_{SE}\tau_{rec} r} \tag{4.30}$$

and a steady-state variable

$$A_\infty(r) = 1 - \frac{1}{1 + U_{SE}\tau_{rec} r} \,, \tag{4.31}$$

both depending on the input rate $r(t)$ (see Fig. 4.9 A).

The postsynaptic current (4.29) is identically with the input current of the neuron's unadapted f-I-curve

$$f(t) = f_0\Big(\tau_{rec} A_{SE} U_{SE} r(t) (1 - A(t))\Big) \,. \tag{4.32}$$

The notable difference to the model of encoder adaptation (4.22) is that adaptation due to depressing synapses acts multiplicatively on the input $r(t)$. Depressions has a divisive effect on the input-output-curves (Fig. 4.9 B).

In the following discussion of parameters and signal transmission properties it is focused on the subtractive type of adaptation only.

4.2 Defining the parameters of the adaptation models

The equations for the adaptation of the firing frequency derived above still rely on A_∞, τ, $\varepsilon(f)$ and $\gamma(f)$. Until now, these functions are still defined by the microscopic properties of a specific adaptation mechanism. In this section it is shown, how they can be obtained from macroscopic measurements.

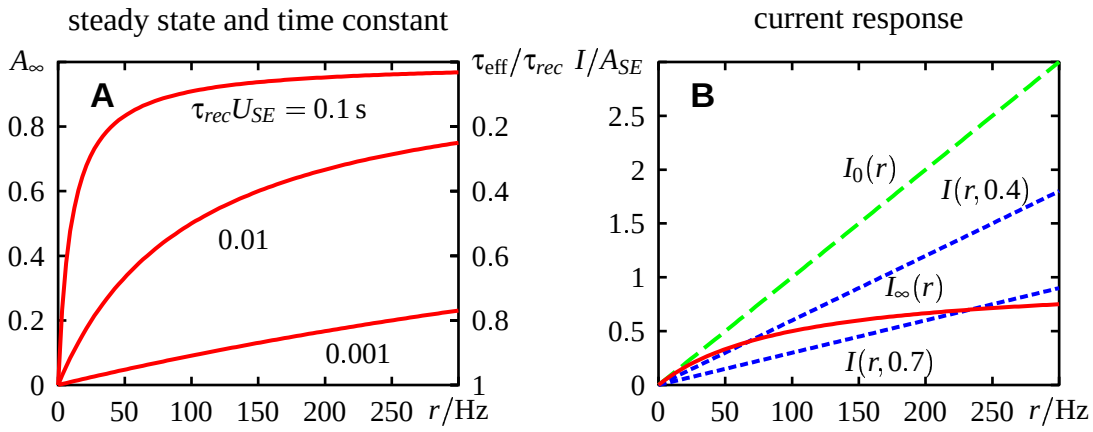

Figure 4.9: THE DEPRESSING SYNAPSE. **A** The steady-state variable $A_\infty(r)$ of the depressing synapse in dependence on the firing rate $r(t)$ of the input spikes for different values of $\tau_{rec}U_{SE}$ as indicated (in seconds). The effective time constant depends similarly on the input rate $r(t)$ (note the reversed scale). **B** The onset response of the completely recovered synapse $I_0(r)$ depends linearly on the input rate $r(t)$ ($\tau_{rec}U_{SE} = 0.01$ s). Depression scales the instantaneous response down (shown for two different states of adaptation $A = 0.4$ and $A = 0.7$). $I_\infty(r)$ is the steady-state response of the synapse to a constant input rate r.

4.2.1 Steady-state strength of adaptation

To define the steady-state strength of adaptation A_∞, the steady-state f-I-curve $f_\infty(I)$ can be used by definition. In the steady-state the firing frequency f is given by $f_\infty(I)$ and the state of adaptation A equals A_∞. Plugging this into the equation for the adapted firing frequency (4.11) and solving for A_∞ results in

$$A_\infty(f_\infty) = \frac{I - f_0^{-1}(f_\infty)}{1+\gamma(f_\infty)}\,, \tag{4.33}$$

where f_0^{-1} is the inverse function of the onset f-I-curve.

Encoder adaptation

For encoder adaptation A_∞ has to be a function depending on the firing frequency f only. The input intensity I is determined by f_∞ via $I = f_\infty^{-1}(f_\infty)$. Then the right hand side of (4.33) is solely a function of the steady-state firing frequency f_∞, which holds for any firing frequency f:

$$A_\infty(f) = \frac{f_\infty^{-1}(f) - f_0^{-1}(f)}{1+\gamma(f)}\,. \tag{4.34}$$

Transducer adaptation

For transducer adaptation A_∞ is a function depending on the input J only. Just using the input dependence of the steady-state f-I-curve $\hat{f}_\infty(J)$ and setting $\gamma(f)$ in (4.33) to zero results in

$$A_\infty(J) = J - \hat{f}_0^{-1}(\hat{f}_\infty(J))\,. \tag{4.35}$$

4.2.2 The $\gamma(f)$ - term

To determine the $\gamma(f)$-term at least one f-I-curve $f(I,A)$ of the neuron being at a certain constant state of adaptation A is needed (see Fig. 4.12). Given such an adapted f-I-curve, $\gamma(f)$ can be obtained from the implicit equation (4.11) for the adapted firing frequency:

$$\gamma(f) = \frac{I - f_0^{-1}(f(I,A))}{A} - 1 \tag{4.36}$$

In this equation A is the distance of the unadapted f-I-curve and the steady-state f-I-curve at the firing frequency given by the intersection of the adapted f-I-curve $f(I,A)$ and the steady-state f-I-curve $f_\infty(I)$. Then $\gamma(f)$ is small in a region around the steady-state firing frequency. Thus, it can be neglected for small fluctuations of the input I.

4.2.3 Time constants of adaptation

In addition to the onset, the steady-state f-I-curve, and the γ-term, the adaptation time-constant τ has to be known in order to apply the adaptation model on experimental data. Furthermore, transducer and encoder frequency adaptation have to be distinguished in receptor neurons stimulated with their appropriate physical stimulus. To address these questions the relation of the effective time constant τ_{eff} to the adaptation time-constant τ in (4.22) or (4.26) has to be explored. The effective time constant τ_{eff} is the time constant which can be obtained from the exponential decay of the firing frequency during constant stimulation. For simplicity the possible dependence of the adaptation time-constant on the firing frequency is neglected in the following.

In general the adaptation time-constant τ is not identical with the effective time constant τ_{eff}. One reason is the nonlinear shape of the onset f-I-curve $f_0(I)$ and the $\gamma(f)$-term, which obscures the time course of A. For encoder adaptation the dependence of the steady-state strength of adaptation $A_\infty(f)$ on the firing frequency f is the main reason for a difference between τ and τ_{eff}. This already causes a decay constant τ_A of the strength of adaptation A to be different from the adaptation time-constant τ (see below). As a consequence the time course of the firing frequency in general is not strictly exponential and its effective time constant τ_{eff} differs from the adaptation time-constant τ.

Knowing the onset f-I-curve $f_0(I)$ and $\gamma(f)$ permits to calculate the time course of the state of adaptation $A(t)$ using (4.11) to overcome the effects of $f_0(I)$ and $\gamma(f)$ on $A(t)$:

$$A = \frac{I - f_0^{-1}(f)}{1 + \gamma(f)} \tag{4.37}$$

By means of this equation the time course of the state of adaptation can be computed without knowing the adaptation time-constant and mechanism, provided the inverse function of $f_0(I)$ exist, i.e. the firing frequency has to be greater than zero. From the exponential-like decay of the state of adaptation $A(t)$ for constant stimuli I, a time constant τ_A can be obtained. For transducer adaptation, τ_A equals τ for all input intensities I (see Fig. 4.11 C).

For encoder adaptation the dependence of A_∞ on the firing frequency still makes τ_A different from τ. However, if the firing frequency equals zero, i.e. the stimulus is subthreshold, A_∞ equals zero and from the differential equation (4.16) for A remains $\tau\dot{A} = -A$, which describes an exponential recovery of the state of adaptation A with time constant

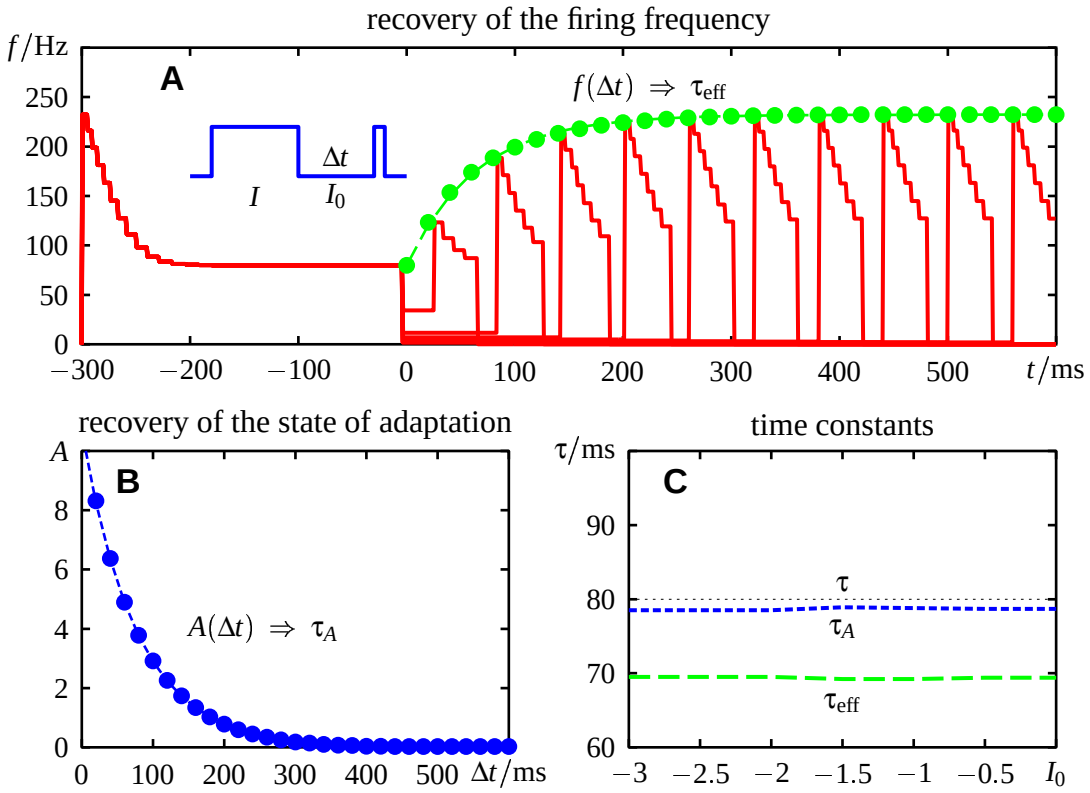

Figure 4.10: RECOVERY FROM ADAPTATION. **A** The stimulus protocol for measuring recovery from adaptation is sketched in the inset. First a 300 ms adaptation stimulus is applied to adapt the neuron into a certain state of adaptation A (the modified Traub-&-Miles model with AHP-current is used as a model neuron). After a delay Δt a test stimulus is applied. The solid line is the time course of the firing frequency evoked by such stimuli with different delays Δt. The peak-response of the neuron to the test stimulus is measured (dots). **B** Using the unadapted f-I-curve $f_0(I)$ the corresponding values of the state of adaptation A can be calculated from the peak responses in A by means of (4.37). **C** Fitting an exponential function to the state of adaptation as a function of the delay $A(\Delta t)$, a time constant τ_A is obtained, which is very close to the adaptation time-constant τ (dotted line). In contrast, the time constant τ_{eff} measured from the firing frequency $f(\Delta t)$ underestimates τ.

$\tau_A = \tau$. Since f equals zero, the time course of A cannot be computed directly by means of (4.37). Instead, $A(t)$ has to be determined from the onset firing frequency evoked by a short test stimulus with given intensity I at different times after the offset of an adaptation stimulus using (4.37). By fitting an exponential function into $A(t)$ the adaptation time constant τ is obtained (see Fig. 4.10 C and Fig. 4.11 D).

However, measuring the time constant τ from recovery from adaptation is a long procedure. Eliminating A in (4.16) using (4.11) and (4.34), and expanding the f-I-curves at the steady-state firing frequency $f_\infty(I)$ (not input intensity I! $f_\infty^{-1}(f) \approx I + \mathrm{d}f_\infty^{-1}/\mathrm{d}f(f_\infty(I))(f - f_\infty(I))$ and $f_0^{-1}(f) \approx f_0^{-1}(f_\infty(I)) + \mathrm{d}f_0^{-1}/\mathrm{d}f(f_\infty(I))(f - f_\infty(I))$ results in a linear differential equation for the firing frequency $f(t)$

$$\tau_{\text{eff}}(I)\,\dot{f} = f_\infty(I) + \tau_{\text{eff}}(I)\,f_0'(f_0^{-1}(f_\infty(I)))\dot{I} - f \tag{4.38}$$

for both encoder and transducer adaptation. The effective time constant τ_{eff} is the one of the exponential decay of the firing frequency $f(t)$. For transducer adaptation, τ_{eff} is

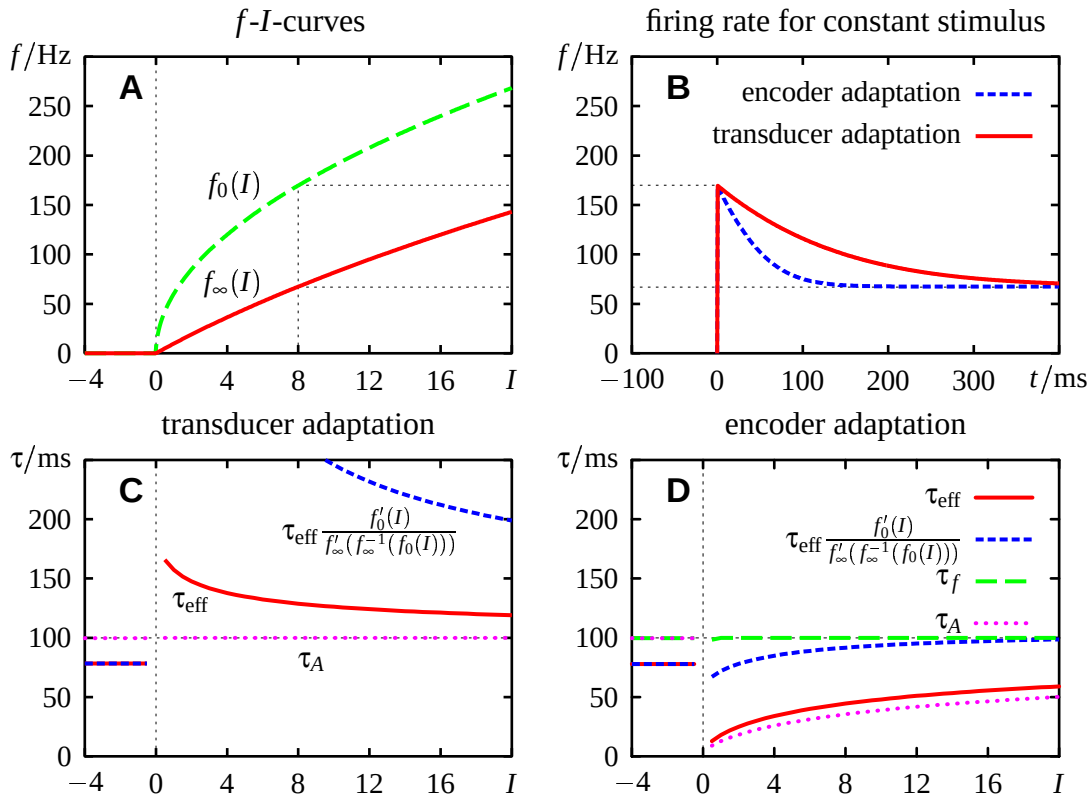

Figure 4.11: TIME CONSTANTS OF ENCODER AND TRANSDUCER ADAPTATION. **A** The onset and the steady-state f-I-curve used for the simulation: $f_0(I) = 60\sqrt{I}$ and $f_\infty(I) = 60\sqrt{I + 0.1^2 60^2/4} - 0.1 \cdot 60^2/2$. **B** Response $f(t)$ of the transducer and encoder adaptation model to a constant stimulus with intensity $I = 8$ starting at $t = 0$. The f-I-curves shown in A and an adaptation time constant $\tau = 100$ ms were used. Note the much faster decay of the firing frequency for encoder adaptation. **C & D** Time constants obtained from both types of adaptation for various stimulus intensities I. For sub-threshold stimuli ($I < 0$), the time constants were measured from recovery from adaptation. The effective time constant τ_{eff} is directly measured from the firing frequency $f(t)$ by means of an exponential fit. For encoder adaptation τ_{eff} corrected by the factor $f_0'(I)/f_\infty'(f_\infty^{-1}(f_0(I)))$ from (4.40) should result in a good estimate of the adaptation time-constant τ. The time constant τ_A of the decay of the state of adaptation $A(t)$ computed from the response $f(t)$ by means of (4.37) and $f_0(I)$. **C** Transducer adaptation: The measured time constant τ_{eff} is larger than the adaptation time-constant τ. This difference is caused only by the nonlinear shape of the onset f-I-curve $f_0(I)$. For the same reason τ_A equals τ for all stimulus intensities I. The correction of τ_{eff} even enhances the difference to the true adaptation time-constant. It is meaningless for transducer adaptation. **D** Encoder adaptation: The measured time constant τ_{eff} is smaller than the adaptation time-constant τ. Near the threshold at $I = 0$ it tends to zero. For super-threshold stimuli τ_A is also very different from τ. However, the corrected τ_{eff} is very close to the real adaptation time-constant τ. An alternative way to get the value of τ is to use the f-I-curves from A and the model for encoder adaptation to compute the time course of the firing frequency $f(t)$ numerically for different stimulus intensities and time constants, and fit it to the data. The time constant τ_f obtained from such a procedure gives the exact value of the adaptation time-constant. Note, that this only works exactly provided the adaptation time-constant does not depend on firing frequency. For sub-threshold stimulus intensities τ_A, measured from recovery from adaptation, reveals the exact value of τ, too.

identical to the adaptation time-constant τ, while for encoder adaptation it is

$$\tau_{\text{eff}}(I) = \tau \frac{f'_\infty(I)}{f'_0(f_0^{-1}(f_\infty(I)))} \tag{4.39}$$

It is scaled by the relative slopes of the f-I-curves at the firing frequency $f_\infty(I)$. This is the right expansion for small deviations from the steady-state firing frequency. However, τ_{eff} is usually measured from applying a constant stimulus to the unadapted neuron as in Fig. 4.2. The value of the τ_{eff} depends strongly on the initial phase of the response far away from the steady-state. It might be better to expand the f-I-curves at $f_0(I)$ instead at $f_\infty(I)$. Then for transducer adaptation τ_{eff} still equals τ but for encoder adaptation τ_{eff} becomes

$$\tau_{\text{eff}}(I) = \tau \frac{f'_\infty(f_\infty^{-1}(f_0(I)))}{f'_0(I)} \tag{4.40}$$

This is a generalization of the formula given by Ermentrout (1998) for arbitrary f-I-curves. Especially right above the firing threshold of the onset f-I-curve $f_0(I)$, its slope is much larger than the corresponding slope of the steady-state f-I-curve. The resulting effective time constant can be very small, provided τ is constant. Recall the time constant resulting from the M-type current of the Crook model shown in Fig. 4.7 A. This adaptation time constant is not constant, it increases for small firing frequencies, thus counteracting the effect of the f-I-curves.

The relation (4.40) of τ_{eff} and τ for encoder transduction can be used the other way around to compute an estimate of the adaptation time-constant τ from the measured effective time constant τ_{eff} as in Fig. 4.11. If the resulting τ is still strongly dependent on the input intensity, then a dependence of the time constant on the firing frequency f has to be taken into account, i.e. $\varepsilon(f)$ cannot be neglected.

Subtractive transducer and encoder adaptation can be distinguished based on the intensity-dependence of their time-constants (see Fig. 4.11). For transducer adaptation the time constant τ_A of the decay of the state of adaptation A should be a smooth function of the input intensity, while for encoder adaptation it shows a distinct drop at the firing threshold. The corrected time constant from (4.40) results for encoder adaptation in more similar values between the sub- and super-threshold range, while for transducer adaptation it enhances the difference. Note that the true adaptation time-constant may in a way depend on stimulus intensity or firing frequency obscuring these differences. Especially an adaptation time-constant like the one of the M-type current shown in Fig. 4.7 A, which decreases with increasing firing frequency, would minimize the difference between time constants of encoder and transducer adaptation.

4.3 Signal transmission properties

With the phenomenological models (4.22) and (4.27) for subtractive spike-frequency adaptation, signal transmission properties of a neuron due to adaptation can now be quantified.

4.3.1 Adapted f-I-curves

Two types of f-I-curves have to be distinguished. First, there are the f-I-curves $f(I,A)$ of the neuron for a given strength of adaptation A. These f-I-curves describe the instan-

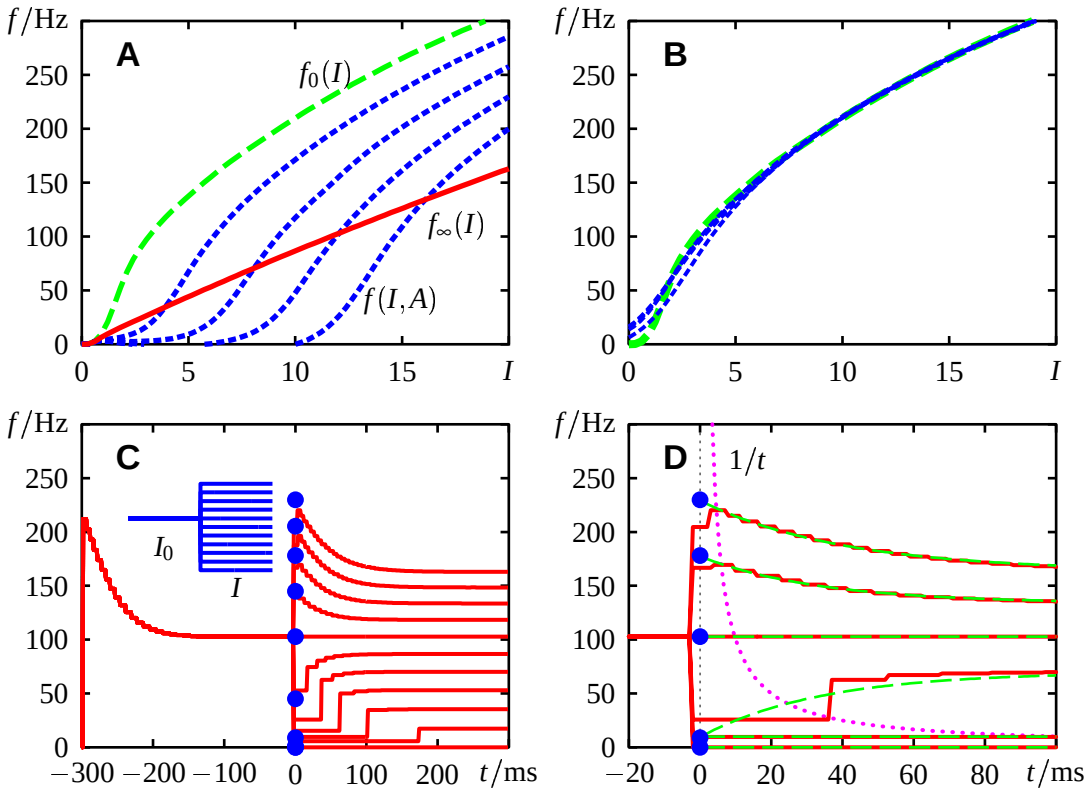

Figure 4.12: ADAPTED f-I-CURVES. **A** The adapted f-I-curves $f(I,A)$ in comparison with the unadapted f-I-curve $f_0(I) \equiv f(I,0)$ and the steady-state f-I-curve $f_\infty(I)$ for the same neuron as in Fig. 4.3. **B** The adapted f-I-curves $f(I,A)$ shifted on top of the unadapted f-I-curve. As expected, these f-I-curves are very similar. The deviations below $I = 5$ are due to the difficulties to measure the adapted f-I-curves as described in the following. **C** The firing frequencies evoked by the protocol for measuring an adapted f-I-curve (inset). In this example the neuron is first adapted to $I_0 = 12$ (conditioning pulse $t < 0$). Then the input is stepped to different intensities I (test pulse $t > 0$) to test the initial response of the adapted neuron to these intensities (dots). The responses to higher test intensities show sharp peaks, which decay back to a new steady-state. Lower test intensities result in decreased responses, which raise due to recovery from adaptation to the corresponding steady-state values. **D** A closer look at the responses in C reveals that the initial responses especially for lower stimulus intensities are ill defined. Since the neuron responds with repetitive firing to the conditioning pulse, there might be a spike at $t = 0$ or shortly before. Thus, the lowest firing rate that can be measured before a spike at time t is $f = 1/t$ (dotted line). As a consequence, firing frequencies measured below the $1/t$-line are an overestimation of the real response of the neuron. For a better estimate exponential functions are fitted into responses (dashed lines) and their value at $t = 0$ is taken as the initial response of the neuron. From these values the adapted f-I-curve as shown in A are constructed.

taneous response of the neuron. A special case of such f-I-curves is the onset f-I-curve $f_0(I)$, which is the response of the unadapted neuron with $A = 0$. Second, there is the steady-state f-I-curve $f_\infty(I)$. It is the response of the neuron after some time, when it is fully adapted to the applied stimulus intensity. For each intensity I of the steady-state f-I-curve the corresponding strength of adaptation A is different.

How do the f-I-curves for a given strength of adaptation A look like? Neglecting the $\gamma(f)$-term, (4.11) simplifies to $f(t) = f_0(I - A)$. Depending on the state of adaptation A,

the unadapted f-I-curve is just shifted to higher or lower input intensities, according to the sign of A. In (4.10) the sign of A is given by $\tilde{\rho}$ via $V - E_a$. For a potassium adaptation-channel like for M-type or AHP-currents, V is always greater than E_a, and therefore A is positive. The f-I-curve is shifted to higher input intensities, i.e. the sensitivity of the neuron decreases.

Such adapted f-I-curves can be measured by first applying a constant stimulus I_0 in order to specifically adapt the neuron. Then the stimulus is stepped to different test intensities I, and the adapted f-I-curve can be constructed from the onset firing frequencies evoked by these test stimuli (see Fig. 4.12 for details).

To analyze the influence of the $\gamma(f)$-term on the adapted f-I-curves, f_0 in (4.11) is expanded to first order at $I - A$, where $\gamma(f) = 0$ (see section 4.2.2)

$$f(t) \approx f_0(I-A) - f_0'(I-A) \cdot A\gamma(f(t)) \,. \tag{4.41}$$

Assuming $\gamma(f) = \tilde{\gamma} f$, an explicit equation for the firing frequency of the adapting neuron is obtained:

$$f(t) \approx \frac{f_0(I-A)}{1 + A\tilde{\gamma} f_0'(I-A)} \,. \tag{4.42}$$

The first order effect of the $\gamma(f)$-term is a compression or amplification of the neuron's f-I-curve due to the divisor $1 + A\tilde{\gamma} f_0'(I-A)$, depending on the signs of A and $\tilde{\gamma}$ (see Fig. 4.14).

4.3.2 Linear adaptation and linear steady-state f-I-curves

Alternatively, one can ask what the steady-state f-I-curve looks like, given a specific dependence of the steady-state adaptation A_∞ on the firing frequency. This question was addressed by the study of Ermentrout (1998) for encoder adaptation. He showed that adaptation linearizes the steady-state f-I-curve. In the following, this issue is analyzed more generally.

In the steady-state, the firing frequency f is given by the steady-state f-I-curve $f_\infty(I)$, and the state of adaptation A equals A_∞. From (4.11) an implicit equation for the steady-state f-I-curve is obtained:

$$f_\infty(I) = f_0\Big(I - A_\infty(f_\infty)[1 + \gamma(f_\infty)]\Big) \,. \tag{4.43}$$

This can be more generalized by letting the state of adaptation A act through a function $g(A)$. For example, such a nonlinear dependence on the concentration of calcium, which represents the state of adaptation, is possible, as mentioned above in deriving the adaptation dynamics of an AHP-current. The implicit equation for the steady-state f-I-curves then reads

$$f_\infty(I) = f_0\Big(I - g(A_\infty(f_\infty))[1 + \gamma(f_\infty)]\Big) =: f_0\Big(I - h(f_\infty)\Big) \,. \tag{4.44}$$

All the terms depending on f_∞ on the right hand side can be summarized in a single general function $h(f_\infty)$. This function combines the dependencies on the firing frequency due to the steady-state adaptation $A_\infty(f)$, the $\gamma(f)$-term, as well as a possible nonlinear dependence of the adaptation current on the state of adaptation A.

Implicitly differentiating (4.44) with respect to I yields

$$\frac{\mathrm{d}f_\infty(I)}{\mathrm{d}I} = f_0'\Big(I - h(f_\infty)\Big) \cdot \left(1 - h'(f_\infty)\frac{\mathrm{d}f_\infty}{\mathrm{d}I}\right) \,, \tag{4.45}$$

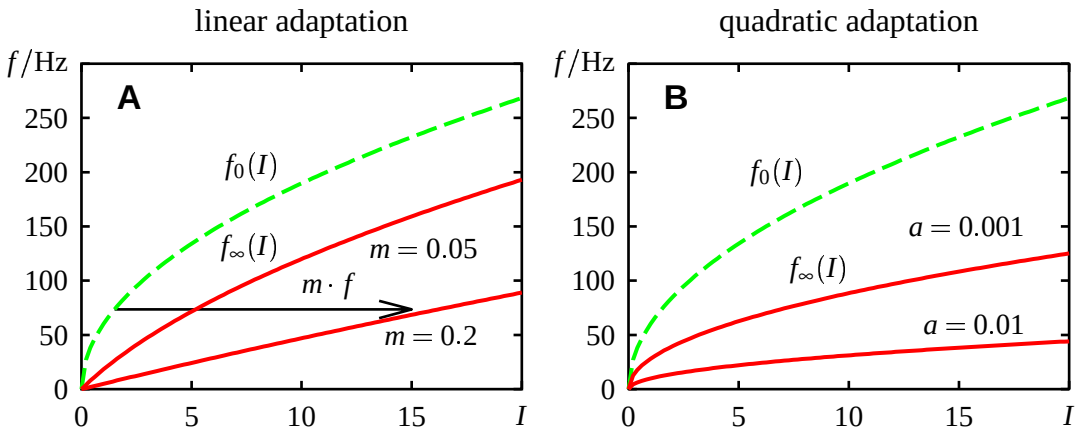

Figure 4.13: LINEARIZATION OF THE STEADY-STATE f-I-CURVE. As an example, the effect of encoder adaptation on an onset f-I-curve given by $f_0(I) = c\sqrt{I}$ is shown. **A** Linear adaptation $A_\infty(f) = m \cdot f$ with increasing adaptation ($m = 0.05$ and 0.2) linearizes and compresses the steady-state f-I-curve. The steady-state f-I-curve is only linear as long as the firing frequency is so small that the onset f-I-curve is approximately a vertical line. **B** Quadratic adaptation $A_\infty(f) = a \cdot f^2$ scales the onset f-I-curve down. It does not linearize $f_\infty(I)$.

where the prime $'$ denotes the derivative with respect to the argument. Solving for the derivative of the steady-state f-I-curve reveals

$$\frac{\mathrm{d}f_\infty(I)}{\mathrm{d}I} = \frac{f_0'(I - h(f_\infty))}{1 + h'(f_\infty)\, f_0'(I - h(f_\infty))} \,. \tag{4.46}$$

The steady-state f-I-curve linearly depends on input current I, if its slope — its derivative (4.46) with respect to I — is independent of then input I via $f_\infty(I)$. To satisfy this condition, the derivative of the function h_∞ has to be constant. That is, adaptation is only allowed to depend linearly on firing frequency. This is the case for $\gamma(f) = 0$ and for $g(A_\infty(f)$ linearly depending on firing frequency f. Since the steady-state adaptation A_∞ most likely is already proportional to the firing frequency (Fig. 4.7 B), $g(A)$ has to be the identity. With these conditions the equation for the steady-state f-I-curve reads

$$f_\infty(I) = f_0\Big(I - m \cdot f_\infty\Big) \,, \tag{4.47}$$

where m is a proportionality constant. This set of conditions is called "linear adaptation" in the following, since in the steady-state the state of adaptation depends only linearly on firing frequency.

Furthermore, the derivative of the onset f-I-curve in (4.46) has to be constant, too, in order for the steady-state f-I-curve to be linear. Therefore, the onset f-I-curve has to be a straight line. Thus, only linear adaptation keeps the steady-state f-I-curve of a linear onset f-I-curve linear.

A second possibility is that the onset f-I-curve starts with a very high slope. This is the case for class-I neurons, whose onset f-I-curve in the vicinity of their threshold is a square-root function of the input current (Ermentrout, 1996). Then the derivative of the steady-state f-I-curve at small inputs I becomes

$$\frac{\mathrm{d}f_\infty(I)}{\mathrm{d}I} \approx \frac{1}{h'(f_\infty)} \tag{4.48}$$

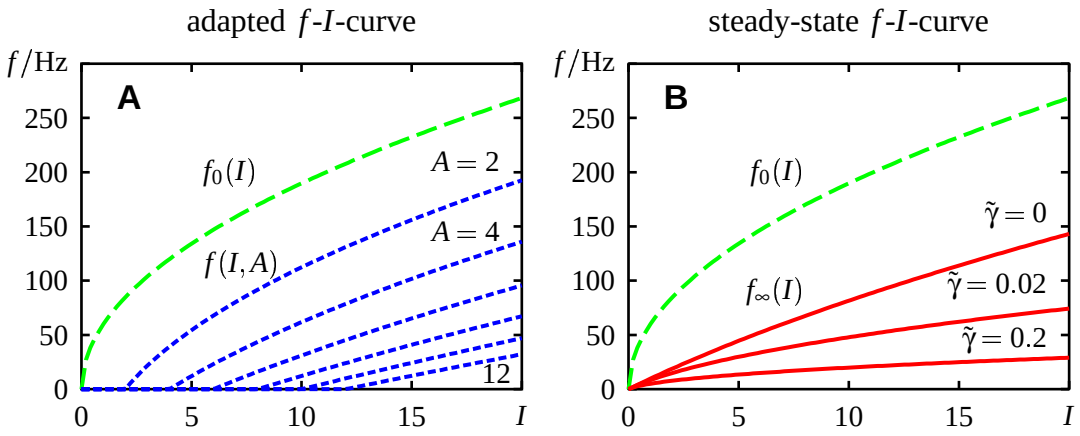

Figure 4.14: INFLUENCE OF THE $\gamma(f)$-TERM ON f-I-CURVES. **A** With linear $\gamma(f) = 0.02f$ and increasing state of adaptation $A = 2$, 4, 6, 8, 10, 12, the adapted f-I-curves $f(I,A)$ are linearized and compressed. **B** The linearizing effect of linear adaptation $A_\infty(f) = 0.1f$ on the steady-state f-I-curve $f_\infty(I)$ is abolished by a linear $\gamma(f)$-term ($\gamma(f) = \tilde{\gamma}f$, $\tilde{\gamma} = 0$, 0.02, 0.2).

Provided the derivative of $h(f)$ is constant (see above), then the resulting steady-state f-I-curve is linear in a region close to threshold (see Fig. 4.13).

For an onset f-I-curve depending like a square root on the input current

$$f_0(I) = c\sqrt{I}\,, \tag{4.49}$$

the following explicit equation for the steady-state f-I-curve is obtained (Ermentrout, 1998):

$$f_\infty(I) = c\sqrt{I + \frac{m^2c^2}{4}} - \frac{mc^2}{2}\,. \tag{4.50}$$

This corresponds to the onset f-I-curve shifted to the left and down. Thus, the steady-state f-I-curve starts no longer with infinite slope, as the onset f-I-curve does (see Fig. 4.13 A).

In the same manner, the influence of the $\gamma(f)$-term on the shape of the adapted f-I-curves can be reexamined. The only term introducing a dependency on the firing frequency in the argument of the onset f-I-curve is the $\gamma(f)$-term itself, since the state of adaptation A is fixed:

$$f(I,A) = f_0\Big(I - A[1+\gamma(f)]\Big)\,. \tag{4.51}$$

Implicitly differentiating with respect to I gives

$$\frac{\mathrm{d}f(I,A)}{\mathrm{d}I} = \frac{f_0'\Big(I - A[1+\gamma(f)]\Big)}{1+\gamma'(f)Af_0'\Big(I - A[1+\gamma(f)]\Big)} \tag{4.52}$$

for the slope of the adapted f-I-curve. Analogously to the situation for the steady-state f-I-curve (4.46), this derivative is independent of I, if the derivative of $\gamma(f)$ is constant and the onset f-I-curve is either a straight line or has an infinite slope at threshold. Then the adapted f-I-curve is linearized (see Fig. 4.14). Note that for this scenario the steady-state f-I-curve cannot be linear.

These findings can be summarized the other way around as follows. Observing a linearized steady-state f-I-curve $f_\infty(I)$ implies that $\gamma(f)$ can be neglected and $A_\infty(f)$ depends

linearly on firing frequency f [3]. A nonlinear steady-state f-I-curve requires an influence of the $\gamma(f)$-term or a nonlinear $A_\infty(f)$ or $g(A)$. If the adapted f-I-curves are just shifted versions of the unadapted f-I-curve $f_0(I)$, then the $\gamma(f)$-term can be ruled out, and the nonlinear steady-state f-I-curve is caused by a nonlinear $g(A_\infty(f))$.

4.3.3 High-pass filter properties due to adaptation

The dynamics of both encoder and transducer adaptation, (4.22) and (4.26), is basically linear. The only nonlinearities are introduced by nonlinear f-I-curves and the $\gamma(f)$-term. For linear systems a transfer function can be calculated to specify its signal-transmission properties.

Consider a stimulus $I(t)$ with only small fluctuations. Then the f-I-curves can be linearized around the firing frequency given by the value of steady-state f-I-curve for the mean input $f_\infty(\langle I\rangle)$. The transfer function $H_f(\omega)$ then can be calculated from (4.38), which is linear in the firing frequency $f(t)$. It is defined as the Fourier-transform of the output $\mathcal{F}[f(t)]$ divided by the Fourier-transform of the input $\mathcal{F}[I(t)]$. The angular frequency $\omega = 2\pi f_c$ is proportional to the frequency component f_c of the stimulus $I(t)$. For the steady-state f-I-curve linearized without offset[4] ($f_\infty(I) \approx f'_\infty(\langle I\rangle)\cdot I$) the transfer function becomes

$$H_f(\omega) = f'_\infty \frac{1 - i\omega\tau_{\text{eff}}\, f'_0/f'_\infty}{1 - i\omega\tau_{\text{eff}}} \,. \tag{4.53}$$

Using a sinusoidal stimulus $I(t)$ of frequency ω the resulting time course of the firing frequency is also sinusoidal with the same frequency. Its amplitude is the one of the stimulus multiplied by the amplitude of the transfer function $|H_f(\omega)|$ — the gain:

$$|H_f(\omega)| = f'_\infty \sqrt{\frac{1 + \left(\omega\tau_{\text{eff}}\, f'_0/f'_\infty\right)^2}{1 + \omega^2\tau_{\text{eff}}^2}} \,. \tag{4.54}$$

The phase shift between the input $I(t)$ and the output $f(t)$ is given by the argument of the transfer function

$$\arg(H_f(\omega)) = \operatorname{atan}\left(\frac{\omega\tau_{\text{eff}}(f'_0/f'_\infty - 1)}{1 + \omega^2\tau_{\text{eff}}^2\, f'_0/f'_\infty}\right) \,. \tag{4.55}$$

Both the gain and the phase shift of the transfer function for the firing frequency $H_f(\omega)$ are illustrated in Fig. 4.15 A & B. Low frequency components of the stimulus $I(t)$ up to about $\omega\tau_{\text{eff}} = 0.2$ and its mean are transmitted via the slope of the steady-state f-I-curve ($|H_f(0)| = f'_\infty$). Fast fluctuations of the stimulus with $\omega\tau_{\text{eff}} > 2$ are transmitted much better by the slope of the onset f-I-curve ($\lim_{\omega\tau_{\text{eff}}\to\infty} |H_f(\omega)| = f'_0$). The transition region is marked by a cut-off frequency of $\omega_c\tau_{\text{eff}} \approx 1$. In this region the firing frequency response lags behind the stimulus. So, adaptation acts essentially as a high-pass filter. In addition, low frequency components are transmitted poorly due to the steady-state f-I-curve.

This can be better understood by the action of the state of adaptation A. As already discussed in section 4.3.1 on page 83, increasing A shifts the onset f-I-curve to higher input intensities, making the neuron less sensitive. In which manner and how fast A

[3] There is also the possibility of the nonlinear dependence of the adaptation current on the state of adaptation to cancel out the nonlinearity in $A_\infty(f)$.

[4] The offset adds only a component to the transfer function at $\omega = 0$.

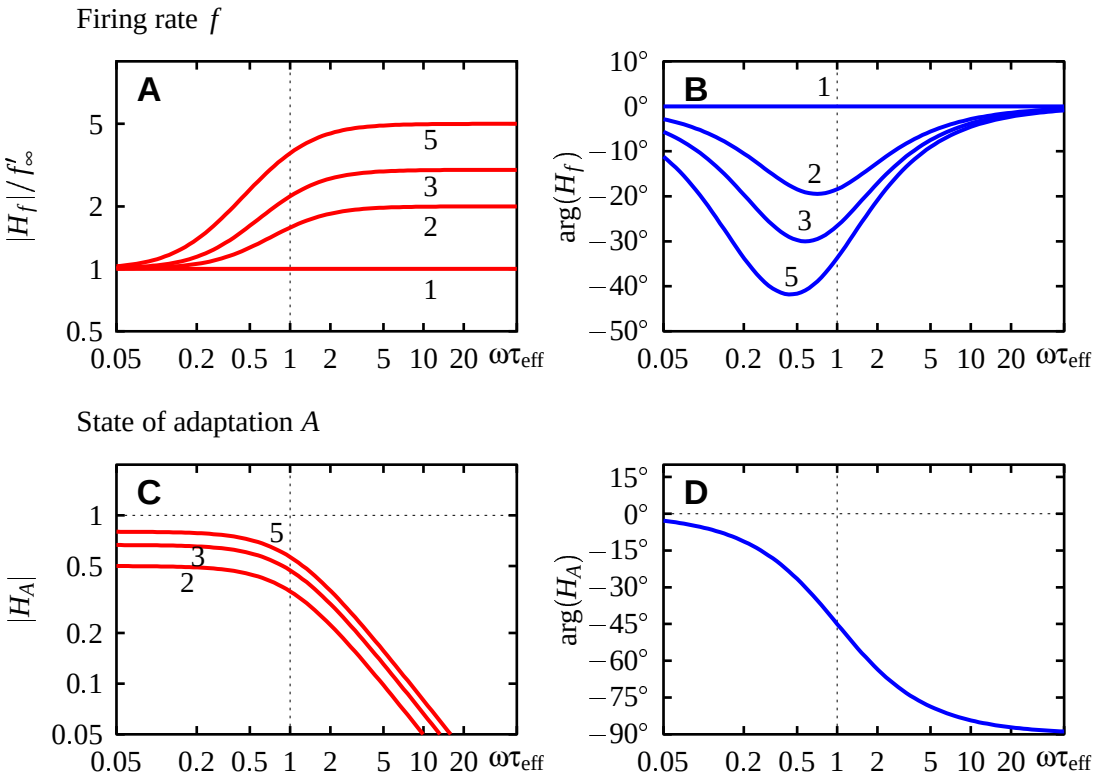

Figure 4.15: TRANSFER FUNCTION OF ADAPTATION. **A** Amplitude (4.54) and **B** phase (4.55) of the transfer function for the firing frequency $f(t)$. Amplitude **C** and phase **D** of the transfer function (4.57) for the state of adaptation $A(t)$. The frequency axis is logarithmic as multiples of the effective time constant τ_{eff}. For $\tau_{\text{eff}} = 160$ ms the values at the frequency axis are in Hertz. The labels indicate the relation of the slopes of the f-I-curves f'_0/f'_∞. The dotted vertical line marks the cut-off frequency $\omega\tau_{\text{eff}} = 1$.

shifts the f-I-curve is given by the dynamics (4.16) or (4.26) of A. Substituting f in A_∞ by (4.11), setting $\gamma(f) = 0$ and linearizing around $f = f_\infty(I)$ results for both types of adaptation in a linear differential equation in A

$$\tau_{\text{eff}}\dot{A} = I - f_0^{-1}(f_\infty(I)) - A\,. \tag{4.56}$$

The effective time constant τ_{eff} is the same as in the linearized equation for the firing frequency (4.38). Linearizing both f-I-curves without offset ($f_0(I) \approx f'_0 \cdot I$ and $f_\infty(I) \approx f'_\infty \cdot I$), (4.56) becomes linear in the input $I(t)$, too:

$$\tau_{\text{eff}}\dot{A} = I(1 - f'_\infty/f'_0) - A\,. \tag{4.57}$$

This is the equation of a first-order low-pass filter. Its transfer function $H_A(\omega)$ is shown in Fig. 4.15 C & D. The state of adaptation follows directly the low frequencies components ($\omega\tau_{\text{eff}} \leq 0.2$) of the stimulus. It shifts the onset f-I-curve appropriately to the corresponding values of the steady-state f-I-curve. As a consequence, these slow components are transmitted via the steady-state f-I-curve. High frequency components ($\omega\tau_{\text{eff}} > 2$) of the stimulus have almost no effect on A, i.e. the adapted f-I-curve stays at its position. Thus, these fast components are transmitted via the onset f-I-curve, which is shifted due to the low frequency components to higher input intensities. By this way, the shift of the onset

f-I-curve compensates for the mean value of the stimulus and optimizes the transmission of fast fluctuations, which results in a high-pass filter.

The transfer functions of both the firing frequency (4.53) and the state of adaptation depend on the effective time constant τ_{eff} and not on the adaptation time-constant τ. Since for encoder adaptation τ_{eff} usually is a function of the input I, the cut-off frequency $\omega_c = 1/\tau_{\text{eff}}$ changes with input intensity, too. For example, the f-I-curves and time constants in Fig. 4.11 D result in a very low effective time constant and thus in a very high cut-off frequency for small positive inputs I, which is not expected from the value of the adaptation time-constant τ. For encoder adaptation the adaptation time-constant τ together with the relative slopes of the onset and steady-state f-I-curve determine the behavior of the adapting neuron.

4.3.4 Time-derivative detection

Recall the linearized equation (4.38) for the firing frequency $f(t)$. The firing frequency exponentially decays to $f_\infty(I) + \tau_{\text{eff}} f_0'(\tilde{I})\dot{I}$ with the effective time constant τ_{eff}. The second term with the time derivative of the input $\dot{I}$ is responsible for the high-pass properties of adaptation. The first term — the steady-state f-I-curve $f_\infty(I)$ — adds the low frequency components of the stimulus to the response. Phasic neurons have per definition a vanishing steady-state f-I-curve. Thus their response is only driven by the time-derivative of the stimulus $\dot{I}$. It depends only on the value of the effective time constant τ_{eff} how closely the firing frequency follows the time-derivative of the stimulus. For encoder adaptation this is illustrated in Fig. 4.16. Since the slope of $f_\infty(I)$ is very small for the phasic neuron, the corresponding effective time constants are very small compared to the phasic-tonic neuron with a steeper steady-state f-I-curve. A vanishing steady-state f-I-curve turns a neuron with encoder adaptation into a time-derivative detector for two reasons: 1) its response is driven only by the time-derivative of the stimulus, and 2) its effective time constant becomes smaller, reducing its low-pass filter effect on $\dot{I}$. However, the absolute response is reduced, too. Inserting the expression (4.39) for the effective time constant into the term with the time-derivative of the stimulus results in $\tau f_\infty'(I)\dot{I}$. Thus, with vanishing $f_\infty(I)$ this term may even vanish, too (as long one deals with linear f-I-curves and constant τ!).

The situation for transducer adaptation is different. There the effective time constant equals the adaptation time-constant. Independently from the steady-state f-I-curve the low-pass filter properties of (4.38) remain the same. The term with the time-derivative of the input is only determined by the slope of the onset f-I-curve, and therefore is larger compared to the situation of encoder adaptation.

In summary there are two counteracting effects. Either for encoder adaptation there is a weak but fast response to the time-derivative of the input, or for transducer adaptation the response is strong but slow.

4.3.5 Nonlinear effects

The most important difference of real f-I-curves to linear f-I-curves is the existence of some threshold of the input I_{th} below that the firing frequency equals zero. This threshold is shifted by adaptation to higher input intensities. Stimuli below the actual threshold are not transmitted at all, they do not evoke spikes. Furthermore, during sub-threshold stimuli

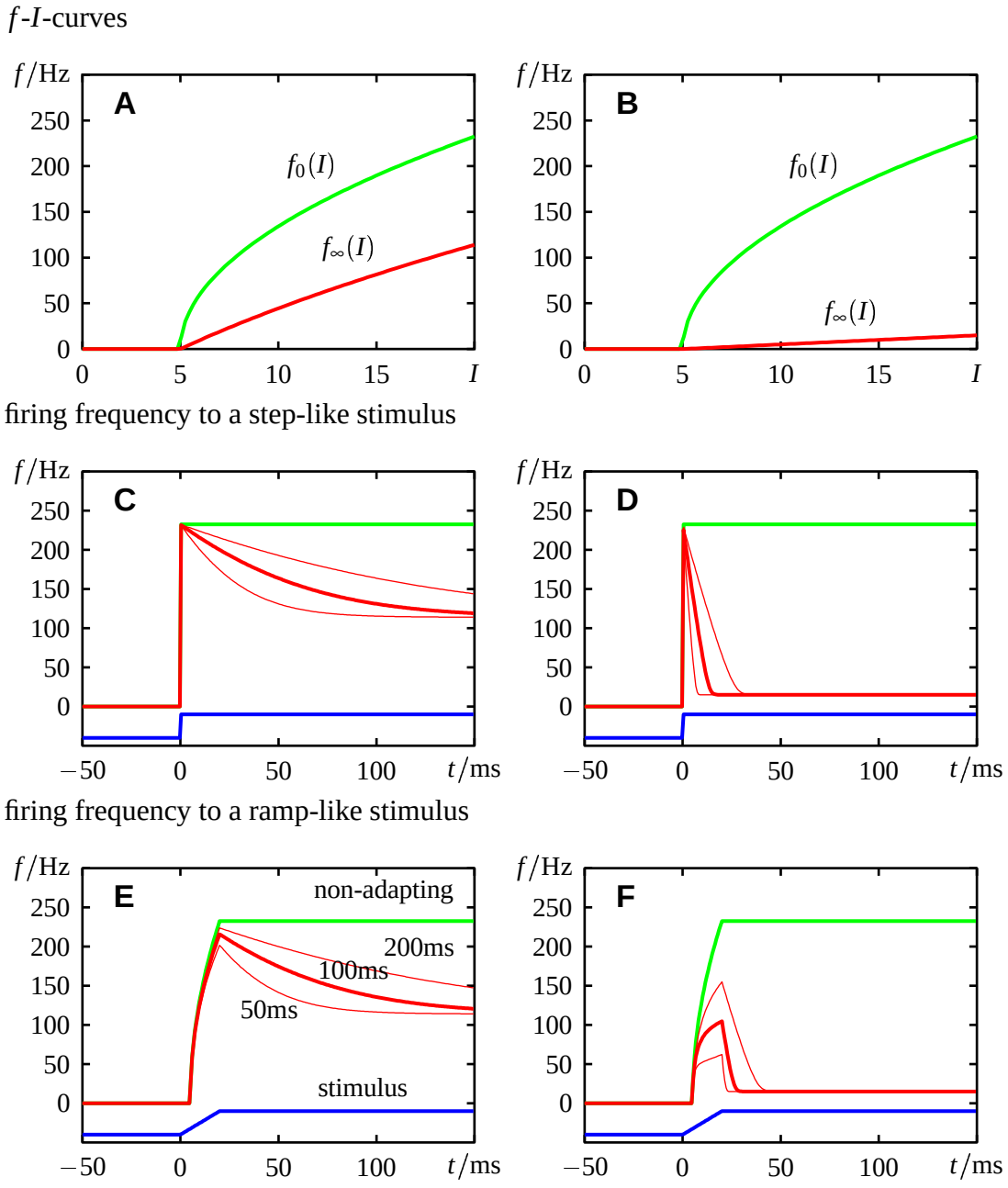

Figure 4.16: TIME-DERIVATIVE DETECTION. The responses of two neurons with the same onset f-I-curve $f_0(I) = 60\sqrt{I}$ to step- and ramp-stimuli, which differ in their adaptation strength. **A** A phasic-tonic neuron with medium adaptation ($A_\infty(f) = 0.1f$), which was used to simulate the responses in C & E. **B** An approximately phasic neuron with strong adaptation ($A_\infty(f) = 10f$), which was used to simulate the responses in D & F. **C & D** Response to the rapid onset of a stimulus for different adaptation time-constants τ as indicated in E, and for a non-adapting neuron. The shorter the adaptation time-constant, the better resembles the phasic neuron the time-derivative of the stimulus. Note that the effective time constant of the phasic neuron is much smaller than the one of the phasic-tonic neuron. This further enhances the time-derivative character of its response. **E & F** Response to a ramp of 20 ms duration. The peak response decreases with smaller adaptation time-constants, since the neuron starts to adapt during the ramp. The response of the phasic neuron with small time constant is very close to a rectangular response, which would be the derivative of the ramp stimulus.

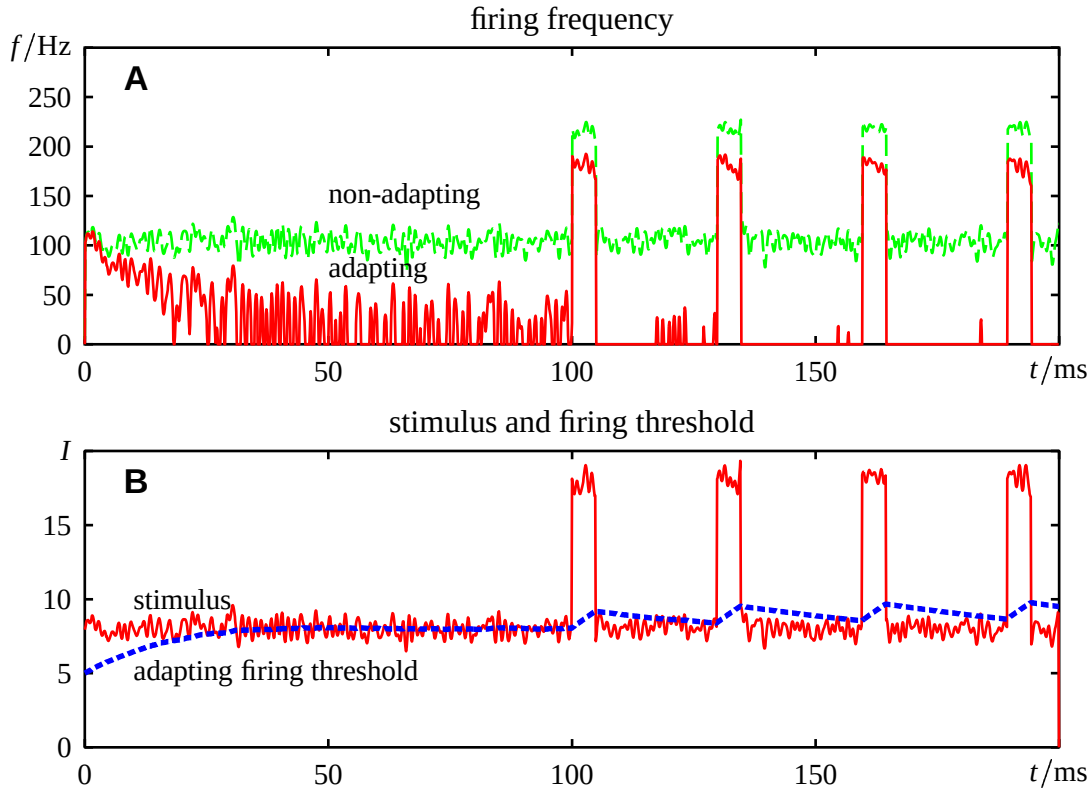

Figure 4.17: SUPPRESSION OF BACKGROUND NOISE BY ADAPTATION. **A** The firing frequency of a non-adapting and an adapting neuron in response to four pulses in the presence of additional background noise, shown in **B**. The noise is switched on at time $t = 0$, i.e. the adapting neuron is not adapted initially. Due to the noise the non-adapting neuron shows a strong activity even when the true signal is absent. The pulses evoke an increase in firing frequency. In contrast the adapting neuron adapts to the noise, but still responds with a low firing frequency to it. During the pulses the neuron adapts further and finally responses only to them. However, the absolute response strength to the pulses is smaller than in the non-adapting neuron. The f-I-curves used were $f_0(I) = 60\sqrt{I-5}$ and $f_\infty(I) = 5(I-5)$. The adaptation time-constant was $\tau = 100\,\text{ms}$. The dashed line in **B** is the firing threshold of the actual f-I-curve, i.e. $A(t) + 5$ (arbitrary units).

the neuron is able to recover from adaptation.

Adaptation together with the threshold of the f-I-curve helps to suppress the transmission of background noise as illustrated in Fig. 4.17. The neuron adapts to the noise alone, but is still active. A strong signal leads to a further adaptation of the neuron. The firing-threshold increases and less of the weaker background noise is transmitted. Especially right after the signal the neuron is silent. Repeating the signal before adaptation has completely recovered, finally holds the threshold above the background noise. The neuron is silent throughout the pauses between the signals. Compared to the response of a non-adapting neuron the absolute response strength to the signals is reduced, too, but the signal-to-noise ratio is enhanced. These effects certainly depend on the duration of the signals d and of the pauses p compared to the effective time-constant τ_{eff} of adaptation of the firing frequency. Very short signals ($d \ll \tau_{\text{eff}}$) do not benefit from adaptation, while very long signals ($d \gg \tau_{\text{eff}}$) do not further enhance this noise-suppressing effect. In contrast, they themselves are attenuated by adaptation. The shorter the pauses ($p < \tau_{\text{eff}}$), the less recovers the neuron from adaptation and it stays quiet for the whole pause. Long

pauses ($p > \tau_{\text{eff}}$) may cause a response of the neuron to the background noise towards the end of the pause. In addition, the signals have to be strong enough to evoke sufficient adaptation. Thus, adaptation only amplifies the signal-to-noise ratio, it does not perform a fancy noise-reduction algorithm.

In summary, adaptation sets the timescale of important signals. Signals which are short compared to the adaptation time-constant are treated as background noise. Too long signals are attenuated due to adaptation. Only repeated signals with durations and pauses of the order of magnitude of the effective time constant of adaptation optimally use the ability of noise-suppression by adaptation.

A special case of this effect is known as forward masking. If a strong stimulus is followed by a weaker one, the response of the weak stimulus is suppressed compared to the response without the preceding strong stimulus. This was discussed in detail by Wang (1998) and Liu & Wang (2001).

4.4 Combination with spike-generator

A key assumption of the analysis of spike-frequency adaptation was a sufficiently high firing frequency compared to the adaptation time-constant. This was necessary to treat the dynamics of adaptation independently of the generation of spikes.

The firing frequency $f(t)$ resulting from the models (4.22) and (4.27) is a simple mapping of the stimulus $I(t)$ through the onset f-I-curve $f_0(I)$. As a consequence, the time course of $f(t)$ fluctuates as fast as the input $I(t)$. However, the transformation of a stimulus into a train of spikes acts like a low-pass filter. Fluctuations between two succeeding spikes of the stimulus $I(t)$ cannot be observed, given the spikes. Thus, the firing frequency $\nu(t)$ measured from the spikes in general is different and slower than the firing frequency $f(t)$ from the model. Only for stimuli, which are approximately constant between two spikes, the firing frequency $f(t)$ from the model approximates the measured one $\nu(t)$ (see Fig. 3.7).

For faster stimuli, at least the firing frequency from the model $f(t)$ has to be fed into a model to generate spikes. From these spikes a firing frequency $\nu(t)$ can be calculated as the reciprocal of the interspike intervals, which then can be compared with the firing frequency measured experimentally.

The simplest way to do this is to use the non-leaky phase oscillator (3.2) from the previous chapter:

$$\begin{aligned} \dot{\varphi} &= f(t) \quad ; \quad \varphi < 1 \\ \varphi &= 0 \quad ; \quad \varphi = 1 \rightarrow \text{spike} \end{aligned} \tag{4.58}$$

It is equivalent to a running average with variable time window $T(t) = 1/\nu(t)$ (3.6):

$$\nu(t) = \frac{1}{T(t)} \int_{t-\frac{1}{2}T(t)}^{t+\frac{1}{2}T(t)} f(t')\, \mathrm{d}t' \tag{4.59}$$

This approach captures a good deal of the low-pass properties of the spike generator, but as shown in the previous chapter it is not the best model. However, if one is only interested in the firing rate $\nu(t)$, this model gives quite a good approximation.

4.4.1 Adaptation and spike dynamics

To overcome the restriction to high firing frequencies, a general model for spike-frequency adaptation is needed, which can be plugged into a model of the generation of spikes directly. Let

$$\dot{\vec{x}} = \vec{g}(\vec{x}, I(t)) \tag{4.60}$$

be a model for the generation of spikes. It is a N-dimensional system of differential equations, which is driven by the input current $I(t)$. Whenever one of the variables $\vec{x}(t)$ crosses a threshold, a spike is produced. This is a general formulation of conductance based models, integrate-and-fire models and the phase oscillators from the previous chapter.

As shown above, for encoder adaptation all considered mechanisms can be reduced to an adaptation current I_a, which is subtractive to the input current $I(t)$ and depends on some adaptation gating-variable. The latter is activated by the spikes. The adaptation model (4.22) has to be transformed back from the firing frequency level to the spikes level. Consider

$$\begin{aligned} \dot{\vec{x}} &= \vec{g}\Big(\vec{x},\, I(t) - y[1+\gamma(\nu)]\Big) \\ \tau[1+\varepsilon(\nu)]\dot{y} &= \tfrac{A_\infty(\nu)}{\nu}\delta(t-t_i) - y\,, \end{aligned} \tag{4.61}$$

where y is a generalized adaptation gating-variable, $\delta(t-t_i)$ is Dirac's delta-function, t_i is the time of the last spike, and $\nu = 1/(t_i - t_{i-1})$ is the firing frequency. Applying the averaging procedures on this equation results exactly in the adaptation model for the firing frequency $f(t)$, since $\langle \delta(t-t_i)\rangle_T = \nu$. Its parameters $\gamma(\nu)$, τ, $\varepsilon(\nu)$ and $A_\infty(\nu)$ are the same as from the adaptation model. Hence, they can be easily measured experimentally.

For transducer adaptation the situation is even simpler, since it is really independent from the spike generator:

$$\begin{aligned} \dot{\vec{x}} &= \vec{g}(\vec{x}, J(t) - A) \\ \tau(J)\dot{A} &= A_\infty(J) - A\,. \end{aligned} \tag{4.62}$$

Here the transduction of the physical stimulus $J(t)$ is part of the spike generator.

4.5 Discussion

In this chapter many different mechanisms of spike-frequency adaptation were investigated. It was possible to derive a universal phenomenological model for many types of encoder adaptation. A similar model for transducer adaptation was introduced, too, and contrasted with properties of depressing synapses. The models are defined by the neuron's f-I-curves and the adaptation time-constant, which can be measured easily in standard experiments. The simplicity of the models allows to make quantitative statements about signal transmission properties of neurons.

4.5.1 Models of spike-frequency adaptation

Most of the modeling studies on spike-frequency adaptation rely on a specific mechanism of encoder adaptation. Among these the AHP-current was most frequently investigated. F. Baldissera linked the after-hyperpolarizations evoked by those currents with spike-frequency adaptation by algebraic summation (Baldissera et al., 1973; Baldissera & Gustafsson, 1974). Doing so he was able to reproduce the steady-state f-I-curve of a

motoneuron. In studies like Hindmarsh & Rose (1984), Rose & Hindmarsh (1989), and Cartling (1995) the slow dynamics of an adaptation current was already treated independently of the fast dynamics of the generation of spikes. B. Cartling formulated a firing frequency model for adaptation based on an AHP-current (Cartling, 1995, 1996a,b). It is closely related to the model proposed here. The main difference is that the corresponding A_∞-term in his equations depends in addition on the state of adaptation A (calcium concentration). Wang (1998) investigated semi-analytically a conductance-based model with calcium dynamics and an AHP-current. He recognized the difference between the adaptation time-constant of the calcium removal τ and the effective time constant τ_{eff} measurable from the exponential decay of the firing frequency. However, since he used a linear model, his relation between these two time constants depends on the relation of the f-I-curves at a given intensity ("percentage adaptation of firing frequency"), neglecting the fact that encoder adaptation depends on firing frequency and not on input intensity. In a general analytical investigation Ermentrout (1998) showed the linearizing effect of linear adaptation on the steady-state f-I-curve. He compared them with simulations of a conductance based model with both an M-type current and an AHP-current. For f-I-curves of the form $f_0(I) = c\sqrt{I}$ he derived a relation between τ and τ_{eff}, which is in agreement with the more general equation (4.40) derived here. Finally, adaptation of integrate-&-fire models was often introduced by an adaptive firing threshold (MacGregor & Oliver, 1974; Liu & Wang, 2001). These approaches were neither verified by the dynamics of conductance-based models nor compared to experimental findings. Liu & Wang (2001) worked out some differences between an adaptive threshold and an adaptation current, which have to be tested on real neurons.

Very abstract models of adaptation as proposed for example by Izhikevich (2000) were not compared to experimental findings. His canonical model of adaptation is a simplification of the model (4.61) with a constant adaptation time-constant, the steady-state adaptation strength proportional to the firing frequency, and no $\gamma(f)$-term. On the other hand, very detailed conductance-based models take all the different mechanisms of calcium dynamics into account, which are important for adaptation due to AHP-currents (Jaffe et al., 1994; Migliore et al., 1995; Schutter & Smolen, 1998).

Here a universal phenomenological model for encoder adaptation is derived from the kinetics of M-type currents, AHP-currents, and slow recovery from inactivation of the fast sodium channels. The existence of such a model shows that the results obtained from specific mechanisms can be generalized to a lot of mechanisms responsible for spike-frequency adaptation. The adaptation mechanisms only have to satisfy a few assumptions, to result in the proposed equations (4.11) and (4.16).

4.5.2 Assumptions of the model for encoder adaptation

The basic assumption is that the adaptation time-constant is long compared to the firing frequency. This enables to treat the adaptation dynamics independently of the spike generation (Cartling, 1996a; Wang, 1998). Since typical adaptation time-constants are larger than 50 ms, the critical firing frequency is below 20 Hz. For peripheral neurons were firing frequencies may exceed 500 Hz, and regular spiking cells in the cortex (Connors & Gutnick, 1990) this is not a critical restriction. However, many central neurons are firing very rarely. If their firing frequency is very low, then adaptation does no longer play any role, since adaptation caused by one spike is fully recovered until the next spike. It is only

a small bandwidth around 10 Hz, where the model might fail. To investigate this region, the interplay of the adaptation current with the spike generator becomes important. They have to be analyzed in combination, for example with the canonical model (4.61).

An important point is that currents are additive in the membrane equation (4.2) due to Kirchoff's law. This is the reason, why the f-I-curves are shifted to higher input intensities. To influence the firing behavior of a neuron, any adaptation mechanism has to add a current to the membrane equation. Exceptions might be modulations of the dynamics of other currents in dependence on the firing frequency. For example, the level of intracellular calcium triggers the expression of genes, and this way might modulate the properties of some ionic currents. However, such processes usually have much longer time scales as the ones considered here in the context of spike-frequency adaptation.

Averaging the driving force of the adaptation current results in a constant $\tilde{\rho}$ plus higher order terms $\gamma(f)$ in the firing frequency f. This result is independent of using Ohm's law or the Goldman-Hodgkin-Katz equation (Johnston & Wu, 1997) to model the current, since only the strong dependence of the driving force on the membrane potential V was used.

The possible f-dependence of the averaged driving force covered by the $\gamma(f)$-term might be negligible, since changes in the membrane potential between the spikes due to different firing frequencies are very small. It was never mentioned by other modeling studies (Ermentrout, 1998; Izhikevich, 2000; Liu & Wang, 2001), and still has to be confirmed experimentally.

It is further assumed that the adaptation current is linearly scaled by the adaptation variable. All models of the kinetics of voltage gated adaptation channels are indeed linear. It is never reported that they have to be raised to some integer power, as it is the case for the Hodgkin-Huxley sodium and potassium channels (Edman et al., 1987a; Fleidervish et al., 1996; Crook et al., 1998; Selyanko & Brown, 1999; Delord et al., 2000). Critical is the dependence of the steady-state variable of the mAHP-current on the intracellular calcium concentration, which might be nonlinear as discussed below. However, observing a linearized steady-state f-I-curve is a strong hint for a linear acting adaptation. Numerous experimental data show in good approximation linearized steady-state f-I-curves (Granit et al., 1963; Koike et al., 1970; Gustafsson & Wigström, 1981; Stafstrom et al., 1984; Lanthorn et al., 1984; Avoli et al., 1994).

The dynamics of adaptation is given by the slow linear first order differential equation of the underlying mechanism. It is only a single one, since faster processes can be separated into the spike generator, and slower ones can be neglected. Only if several equations with similar time constants would be involved in the adaptation mechanism, the proposed model (4.16) fails. To my knowledge, no such single current with two similar time constants exist (Hille, 1992; Koch, 1999). However, as discussed below, in adaptation due to an AHP-current, several differential equations might be indeed involved. Also it is very likely that several currents together are responsible for spike-frequency adaptation (Madison & Nicoll, 1984; Madison et al., 1987; Köhler et al., 1996; Xia et al., 1998; Stocker et al., 1999).

The steady-state strength of adaptation $A_\infty(f)$ can be easily defined by using the steady-state f-I-curve. It is basically proportional to the firing frequency, since the adaptation gating-variable is mostly activated by the spikes. However, if it is also activated by sub-threshold input-intensities, at least a term depending on the input intensity has to be included in $A_\infty(f)$.

Finally, the adaptation time-constant is often assumed to be constant (Ermentrout, 1998; Izhikevich, 2000; Liu & Wang, 2001). For voltage gated adaptation currents (M-type currents and slow recovery from inactivation) this depends on the values of the membrane potential between the spikes. Provided they are independent from firing frequency, then the adaptation time-constant is indeed independent, too. This also needs experimental verification. The time constant of adaptation due to an AHP-current is given by the dynamics of the calcium removal. As discussed below, there are several hints for this time constant to depend on firing frequency.

4.5.3 Biophysical mechanisms of spike-frequency adaptation

These few assumptions are easily satisfied by M-type currents and slow recovery from inactivation as discussed above.

The situation for an mAHP-type current, which is the most prominent current used for modeling studies (Cartling, 1996a; Ermentrout, 1998; Wang, 1998; Liu & Wang, 2001), is more complex. First, there is a possibly nonlinear dependence of the steady-state gating-variable on the calcium concentration. While Ermentrout (1998) and Wang (1998) approximate this dependence by a linear one, in her study of a conductance-based model Engel et al. (1999) argues for an important role of this nonlinearity. As shown in the context of Fig. 4.13, the shape of the steady-state f-I-curves can be linearized only by linear adaptation. A nonlinear steady-state f-I-curve results from a nonlinear adaptation and/or the $\gamma(f)$-term. For experimentally measured f-I-curves it is sometimes hard to distinguish whether the steady-state f-I-curve is nonlinear due to too weak adaptation or due to real nonlinear adaptation (see for example the steady-state f-I-curves in Madison & Nicoll, 1984; Lanthorn et al., 1984). Thus, in general a nonlinear dependence of the steady-state adaptation strength $A_\infty(I)$ cannot be ruled out. Second, there is the assumption of the mAHP-gating variable to be very fast. The modeling study of the AHP-channel gating Hirschberg et al. (1998) gives a hint for long time constants (> 40 ms) of this channel at low calcium concentrations. Its dynamics cannot be neglected if this time constant exceeds the time constant of the calcium dynamics. Instead, the adaptation dynamics at low calcium levels corresponding to low firing frequencies would be dominated by this slow gating of the AHP-current. At higher calcium levels, the calcium removal would be the prominent component. This could result in a dependence of the macroscopically observed adaptation time constant on the firing frequency. Third, even the time constant of the calcium removal seems to depend on firing frequency. Calcium imaging shows a decreasing time constant of the mean intracellular calcium with increasing firing frequency (Schiller et al., 1995; Helmchen et al., 1996). This effect seems to be reproduced by detailed modeling of the calcium dynamics, which includes diffusion, pumps and buffering (Engel et al., 1999), but was neither recognized nor analyzed in detail (Schutter & Smolen, 1998). Forth, the channels mediating the calcium influx during spikes can inactivate and thus reduce the increase of intracellular calcium (Jaffe et al., 1994; Yamada et al., 1998). This makes the dependence of the steady-state strength of adaptation A_∞ on the firing frequency nonlinear. However, such an effect cannot be seen in calcium imaging data (Markram et al., 1995; Schiller et al., 1995; Helmchen et al., 1996; Borst & Helmchen, 1998; Smetters, 1999).

Besides the mAHP-current there exist a slow sAHP-current, which induces after-hyperpolarizations and adaptation on time scales of more than one second (Schwindt

et al., 1988; Hocherman et al., 1992; Sah, 1996; Sah & Clements, 1999; Stocker et al., 1999). There is an ongoing debate about the reasons of its slow dynamics. Several possibilities have been discussed (see Sah & Clements (1999) for a review): 1) the channels mediating the sAHP are spatially separated from the sites of calcium influx and its slow time course reflects diffusion of intracellular free calcium to these channels; 2) the delayed calcium signal is due to calcium-induced calcium release (CICR); 3) the channels themselves have slow kinetics; 4) a calcium activated second messenger system is the reason for the long delay of the sAHP-current. A lot of evidence exist for slow kinetics of the channels mediating the sAHP-current (Hocherman et al., 1992; Sah & Clements, 1999). This would require a differential equation for the gating of the sAHP-current in addition to the one for the calcium dynamics.

The channels mediating M-type currents are composed out of KCNQ2, KCNQ3 and KCNQ5 subunits (Wang et al., 1998; Selyanko & Brown, 1999; Schroeder et al., 2000). It is likely that different combinations of these subunits coexist in a single neuron, which may differ in quantitative aspects of their kinetics, especially in their time constants.

Slow recovery from inactivation seems to be a widespread phenomenon. It can be observed in a lot of different ion channels and can lead to spike-frequency adaptation or to spike-frequency facilitation, i.e. an increase in firing frequency. In contrast to the M-type currents and mAHP-currents, slow inactivation operates on longer time scales of about one second and more. Slow recovery from inactivation of the sodium channels is responsible for spike-frequency adaptation (Edman et al., 1987a; French & Korenberg, 1989; Fleidervish et al., 1996; Martina & Jonas, 1997; Purali & Rydqvist, 1998). Slowly inactivating potassium channels enhance the firing activity (Delord et al., 2000). Also, the calcium channels responsible for the calcium influx during spikes inactivate. This reduces the calcium influx and thus reduces spike-frequency adaptation mediated by AHP-currents on a time scale of several 10 to 100 ms (Jaffe et al., 1994).

Currents activated by hyperpolarizations may also play a role in shaping the macroscopically observed spike-frequency adaptation. Such I_Q or I_h currents are mixed Na^+-K^+-currents with a reversal potential above the cell's resting potential. They are activated by hyperpolarizations at potentials below rest (Halliwell & Adams, 1982; Edman et al., 1987b; Maccaferri et al., 1993). With depolarizing inputs these currents deactivate and contribute to spike-frequency adaptation. There dynamics can be treated similar to the sodium inactivation.

Sanchez-Vives et al. (2000) report a Na^+-activated K^+ current. It induces spike-frequency adaptation on a very long time scale (about 3 to 10 seconds). Since no detailed statements are made about the kinetics of this current, it remains unclear if it fits the adaptation model (4.22). The situation might be similar to the sAHP-current.

Finally, the action of electrogenic pumps has to be considered to be the reason for very slow spike-frequency adaptation (French & Korenberg, 1989; Sanchez-Vives et al., 2000), too. Pump currents act also subtractive on the input current and in their simplest description obey a single linear differential equation. So it is likely that they fit the adaptation model, too.

It should be mentioned that there also exist the opposite phenomenon to spike-frequency adaptation, namely the increase of the firing frequency (Delord et al., 2000). From a mechanistic point of view, it is closely related to spike-frequency adaptation. The model derived here is also applicable to such positive adaptation. The only difference is that the state of adaptation then acts additive on the input current.

4.5.4 Transducer adaptation and depressing synapses

The mechanisms underlying adaptation in the transduction process in receptor neurons may be much more various. For mechano-transduction in hair-cells the shift of the conductance-intensity-curve due to adaptation is well established (Hille, 1992). The divisive effect of adaptation in depressing synapses is due to very basic principles, i.e. a fraction of a resource is used and the recovery process is slow. It is therefore very likely that certain types of transducer adaptation obey this divisive type of adaptation instead of the subtractive type of the hair cells and the photoreceptors. For example, bleaching of pigment in photoreceptors is a source of divisive adaptation (Schnapf et al., 1990). It is also imaginable that even other mechanisms exist for transducer adaptation.

4.5.5 Functional role of adaptation

Based on their functional form, all the different mechanisms causing spike-frequency adaptation can be grouped into subtractive and divisive adaptation. Depressing synapses and some types of transducer adaptation belong to the divisive type. Encoder adaptation and at least transducer adaptation in hair cells act subtractive on the input. Signal transmission properties were analyzed in detail for the subtractive type of adaptation only.

The shape of a neuron's f-I-curve is important for its signal-transmission properties. Stimuli below the firing threshold I_{th} are not transmitted at all, and the slope of the f-I-curve sets the resolution of input modulations. In adapting neurons the f-I-curve is not fixed. Their onset f-I-curve $f_0(I)$ is shifted dynamically due to adaptation. The shape of the onset f-I-curve determines the transmission of fast fluctuating stimuli. Slow stimuli are transmitted via the the steady-state f-I-curve $f_\infty(I)$. The value of the effective time-constant of the decay of the firing frequency separates slow and fast stimuli. It depends on the time constant of the adaptation process and the shape of the onset and steady-state f-I-curves. Statements like adaptation "make the transfer function of neurons logarithmic" (Engel et al., 1999) refer to the steady-state f-I-curve, which is the neuron's transfer function for very slow stimuli only. The same holds for the linearizing effect of adaptation on f-I-curves (Ermentrout, 1998). Adaptation does not change the shape of the onset f-I-curve, which is the important one for fast stimuli.

Subtractive adaptation turns the neuron into a high-pass filter, since the state of adaptation follows only the slow components of the stimulus and is subtracted from the stimulus. This way the mean of the stimulus is removed and only fast fluctuations are transmitted. The result is intensity invariance or, which is the same, contrast constancy. The fidelity of this invariance depends strongly on the steady-state f-I-curve. In the limit of a vanishing steady-state f-I-curve the intensity invariance is achieved best. The time scale is again determined by the effective time constant. If this time constant is small, the firing frequency of the adapting neuron follows the time derivative of the stimulus. This is just another view of the high-pass filter properties due to adaptation with a high cut-off frequency. Thus, small steady-state f-I-curve and a small effective time constant turns the neuron into a time-derivative detector.

In encoder adaptation the effective time constant depends on the relative slopes of the onset and steady-state f-I-curves. Thus, a small steady-state f-I-curve induces a small time constant. However, a dependence of the adaptation time constant on firing frequency may counteract this effect. In transducer adaptation these two parameter are independent.

Together with the threshold property of neuronal f-I-curves spike-frequency adaptation enhances the signal-to-noise ratio of the response to appropriate stimuli. This noise-suppression effect works best for stimuli, which last for a time roughly comparable to the effective time constant, and which are repeated. Forward masking is a special form of this effect (Sobel & Tank, 1994; Wang, 1998; Liu & Wang, 2001).

In order to study the information transfer of neurons, broad-band filtered white-noise stimuli with cut-off frequencies larger than 50 Hz are widely used (Bialek et al., 1991; Machens et al., 2001). Since effective time constants of spike-frequency adaptation are usually larger than 10 ms, the cut-off frequency of the neurons transfer function is well below 16 Hz. Thus, most of the power of such stimuli is above the cut-off frequency of adaptation. Right after the onset of such a stimulus, the neuron adapts and then the state of adaptation approximately stays at a constant level. Therefore using such stimuli does not test the properties of adaptation.

This could explain the curious result of French et al. (2001), who explored paired spider mechanoreceptor neurons. One of them is phasic and the other phasic-tonic. Surprisingly the information transfer measured for these two neurons was nearly identical. An explanation might be that both neurons only differ in their steady-state f-I-curve, but have similar onset f-I-curves. For the broad-band stimuli used for this experiment, only properties of the onset f-I-curve contributed to the signal transmission. Therefore the differences in the steady-state f-I-curves were not tested by the stimuli, resulting in similar information rates.

As shown in Machens et al. (2001) the knowledge of the neuron's firing threshold is essential for improving stimulus reconstruction. For stimuli with strong low frequency components the shift of the f-I-curve and its firing threshold due to adaptation would make the reconstruction worse. The knowledge about the actual f-I-curve as provided by the adaptation model can eliminate the effects of adaptation on stimulus reconstruction.

Finally it should be mentioned that in the context of whole networks of neurons, spike-frequency adaptation plays a significant role, too. Excitatory networks of class-I neurons without adaptation cannot synchronize (Hansel et al., 1995). However, adding spike-frequency adaptation makes synchrony in such networks possible (Crook et al., 1998; Ermentrout et al., 2001). Schwabe et al. (2001) pointed out that adaptation reduces the output firing frequency of the neuron and therefore its excitatory input to other neurons. This reduces competition in a network and is a possible mechanisms to perform optimal coding.

4.6 Summary

- Spike-frequency adaptation of a single neuron may be caused by
  - slow ionic currents of the spike generator (encoder adaptation),
  - adaptation of the transduction process of the stimulus (transducer adaptation),
  - depressing synapses.
- Adaptation can act on the input either
  - subtractive (encoder and transducer adaptation) or
  - divisive (transducer adaptation and depressing synapses).

- The dynamics of adaptation is driven either
  - by the output firing frequency (encoder adaptation) or
  - by the input (transducer adaptation and depressing synapses).
- A universal phenomenological model for subtractive adaptation was derived from various biophysical mechanisms responsible for encoder and transducer adaptation. The model predicts the time course of the firing frequency $f(t)$ and the state of adaptation A evoked by some stimulus $I(t)$:

$$f = f_0\Big(I - A[1-\gamma(f)]\Big) \tag{4.63}$$

$$\tau\dot{A} = A_\infty(I,f) - A \tag{4.64}$$

Encoder and transducer adaptation differ in the expressions for A_∞, $\gamma(f)$ and τ:

Table 4.1: ENCODER AND TRANSDUCER ADAPTATION.

encoder adaptation	transducer adaptation
input current	physical stimulus
$A_\infty(f) = \frac{f_\infty^{-1}(f) - f_0^{-1}(f)}{1+\gamma(f)}$	$A_\infty(I) = I - f_0^{-1}(f_\infty(I))$
$\gamma(f) \geq 0$	$\gamma(f) \sim 0$
$\tau(f) = \tau[1+\varepsilon(f)]$	$\tau(I)$
$\tau_{\text{eff}} = \tau\frac{f'_\infty(I)}{f'_0(f_0^{-1}(f_\infty(I)))}$	$\tau_{\text{eff}} = \tau(I)$

For $\gamma = 0$ and linearized f-I-curves the firing frequency $f(t)$ decays exponentially to constant stimulation with an effective time constant τ_{eff} (see equation (4.38)). Fig. 4.11 summarizes the differences in the effective time constants of encoder and transducer adaptation.

- Both the unadapted and steady-state f-I-curve, $f_0(I)$ and $f_\infty(I)$, respectively, as well as the time constant τ_{eff} can be measured directly from standard experiments (see Fig. 4.2 and 4.3). A linear steady-state f-I-curve is a strong hint for a vanishing $\gamma(f)$-term. In contrast, linearized adapted f-I-curves result from a contribution of the $\gamma(f)$-term (Fig. 4.12 and Fig. 4.14).
- Due to the dynamics of the adaptation strength $A(t)$, the onset f-I-curve is shifted to higher input intensities and, provided $\gamma(f) > 0$, is compressed. Only linear adaptation linearizes the steady-state f-I-curve (see Fig. 4.13).
- Adaptation acts like a high-pass filter with a cut-off frequency at about $\omega\tau_{\text{eff}} = 1$. A vanishing steady-state f-I-curve turns the neuron into a time-derivative detector. Adaptation helps to suppress background noise, expecially for repeated presentation of a stimulus.
- The resulting firing frequency $f(t)$ of the adaptation model (4.63) in general differs from the measurable firing frequency $\nu(t)$. To get an estimate of the time course of $\nu(t)$ from $f(t)$ at least (4.59) has to be applied. The model (4.61) takes the interaction of encoder adaptation and the spike encoder into account.

5

Spike-Train Analysis

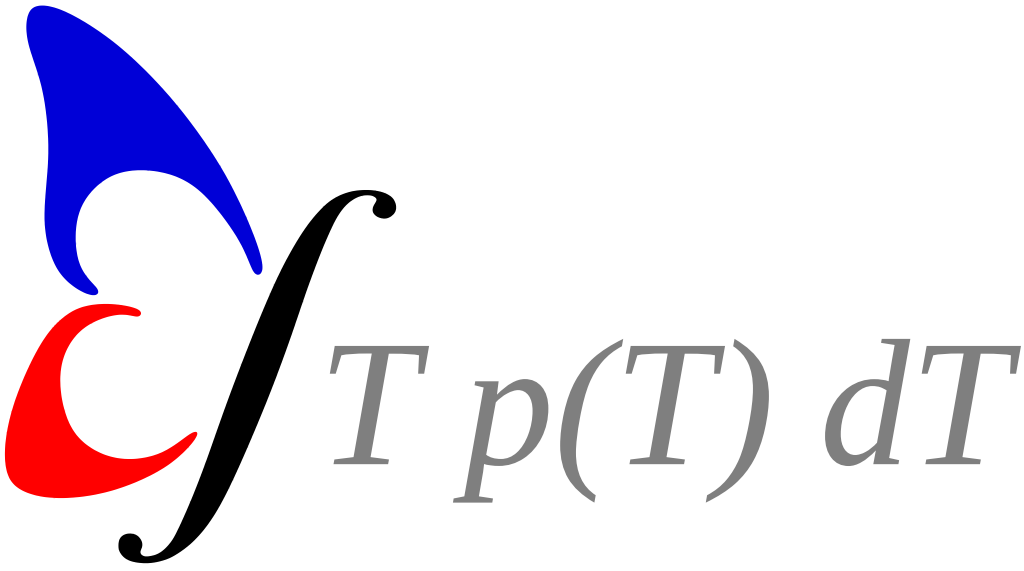

Contents

5.1 Local interspike-interval distribution 104
5.2 Spike jitter and precision 107
5.3 Summary 111

Cover: The logo of the ITB and the integral (5.3) for calculating the mean interspike interval T from the true distribution $p(T)$.

The models for the neuronal dynamics introduced in chapters 2 – 4 were all deterministic. However, real neurons are non-deterministic. Stimulating a neuron repeatedly with the same stimulus results in different spike trains. This stochastic behavior is caused by several sources of noise in the nervous system, such as channel noise (Strassberg & DeFelice, 1993; Chow & White, 1996; Schneidman et al., 1998; White et al., 1998; Steinmetz et al., 2000; White et al., 2000), thermal noise (Stevens, 1972) or noisy synapses (White et al., 2000). Therefore spike trains computed by the previous models cannot be directly compared with those measured in a real neuron, where properties like the mean firing frequency or the precision of the timing of spikes have to be determined from many repeated trials.

The firing frequency used in the context of the phase models in chapter 3 as well as for the adaptation models in chapter 4 was the reciprocal of the interspike interval (*ISI*), i.e. the time from one spike to the next. To compare the firing frequency calculated by these models with spike trains measured in real neurons, the reciprocal interspike interval at each time has to be computed from the data. Higher order statistics like the standard deviation of the interspike-interval distribution at a given time can be used to quantify the effects of noise on the generation of spikes. How to obtain such a local interspike-interval distribution is discussed in the first section. To quantify the precision of spikes at each time t, a simple measure of spike jitter based on the standard deviation of spike timing is proposed in the second section.

5.1 Local interspike-interval distribution

Consider N spike trains, which are all drawn from the same interspike-interval distribution, for example an exponential distribution of a Poisson process as in Fig. 5.1. Creating a histogram of all interspike intervals of these spike trains results exactly in the same distribution $p(T)$ used to generate the spikes. However, a histogram $\tilde{p}(T)$ constructed from the interspike intervals $T_1, T_2, \ldots, T_N$ of each spike train that contain a given time t (horizontal lines in Fig. 5.1 A), does not match the true distribution $p(T)$ (panel C). The reason for this discrepancy is that the number of short interspike intervals is underestimated compared to the number of longer interspike intervals if they are selected by this way. The situation is similar to counting interspike intervals of a single spike train at every multiple of some time step. A long interspike interval is counted more frequently than a short one proportional to its length. Therefore the distribution of the measured *ISI*s, $\tilde{p}(T)$, at time t

is proportional to the true distribution $p(T)$ multiplied by T

$$\tilde{p}(T) \sim p(T)T \,. \tag{5.1}$$

Thus, the true distribution $p(T)$ is the measured distribution $\tilde{p}(T)$ divided by T

$$p(T) = \frac{\tilde{p}(T)/T}{c} = \frac{\tilde{p}(T)/T}{\int_0^\infty \tilde{p}(T)/T \, \mathrm{d}T} \,, \tag{5.2}$$

where $c = \int_0^\infty \tilde{p}(T)/T \, \mathrm{d}T$ is a normalization constant such that $\int_0^\infty p(T)\mathrm{d}T = 1$. The measured distribution $\tilde{p}(T)$ has to be divided by T and normalized in order to get the true distribution $p(T)$. See Fig. 5.1 C for an example of reconstructing the local interspike-interval distribution.

Using this relation, the mean *ISI* with respect to the true distribution $p(T)$

$$\langle T \rangle_p = \int_0^\infty T p(T) \, \mathrm{d}T \tag{5.3}$$

can be calculated in terms of the measured distribution $\tilde{p}(T)$ as

$$\langle T \rangle_p = \int_0^\infty T \frac{\tilde{p}(T)/T}{\int_0^\infty \tilde{p}(T')/T' \, \mathrm{d}T'} \, \mathrm{d}T = \frac{1}{\left\langle \frac{1}{T} \right\rangle_{\tilde{p}}} \,. \tag{5.4}$$

Thus, the mean firing frequency f, defined as the reciprocal of the mean interspike interval (5.4) is given by

$$\boxed{f \equiv \frac{1}{\langle T \rangle_p} = \left\langle \frac{1}{T} \right\rangle_{\tilde{p}} = \frac{1}{N} \sum_{i=1}^{N} \frac{1}{T_i}} \,. \tag{5.5}$$

It is the mean of the reciprocal interspike intervals. It is not, as one might have expected, the reciprocal of the averaged interspike intervals $1/\langle T \rangle_{\tilde{p}}$.

In Fig. 5.1 B both measures are compared using the example of Poisson spike trains. The true interspike-interval distribution of Poisson spikes is $p(T) = r\exp(-rT)$, and the firing frequency is expected to equal the rate r of the Poisson process. However, the measured distribution $\tilde{p}(T)$ of the interspike intervals at a given time t (5.1) is

$$\tilde{p}(T) = \frac{T p(T)}{\int_0^\infty T p(T) \mathrm{d}T} = \frac{T r \mathrm{e}^{-rT}}{\int_0^\infty T r \mathrm{e}^{-rT} \mathrm{d}T} = \frac{T r \mathrm{e}^{-rT}}{1/r} \,, \tag{5.6}$$

and the firing frequency calculated as the reciprocal of the averaged measured interspike intervals is exactly half the rate r of the Poisson process:

$$1/\langle T \rangle_{\tilde{p}} = \frac{1/r}{\int_0^\infty T^2 r \mathrm{e}^{-rT} \mathrm{d}T} = \frac{1}{2} r \,. \tag{5.7}$$

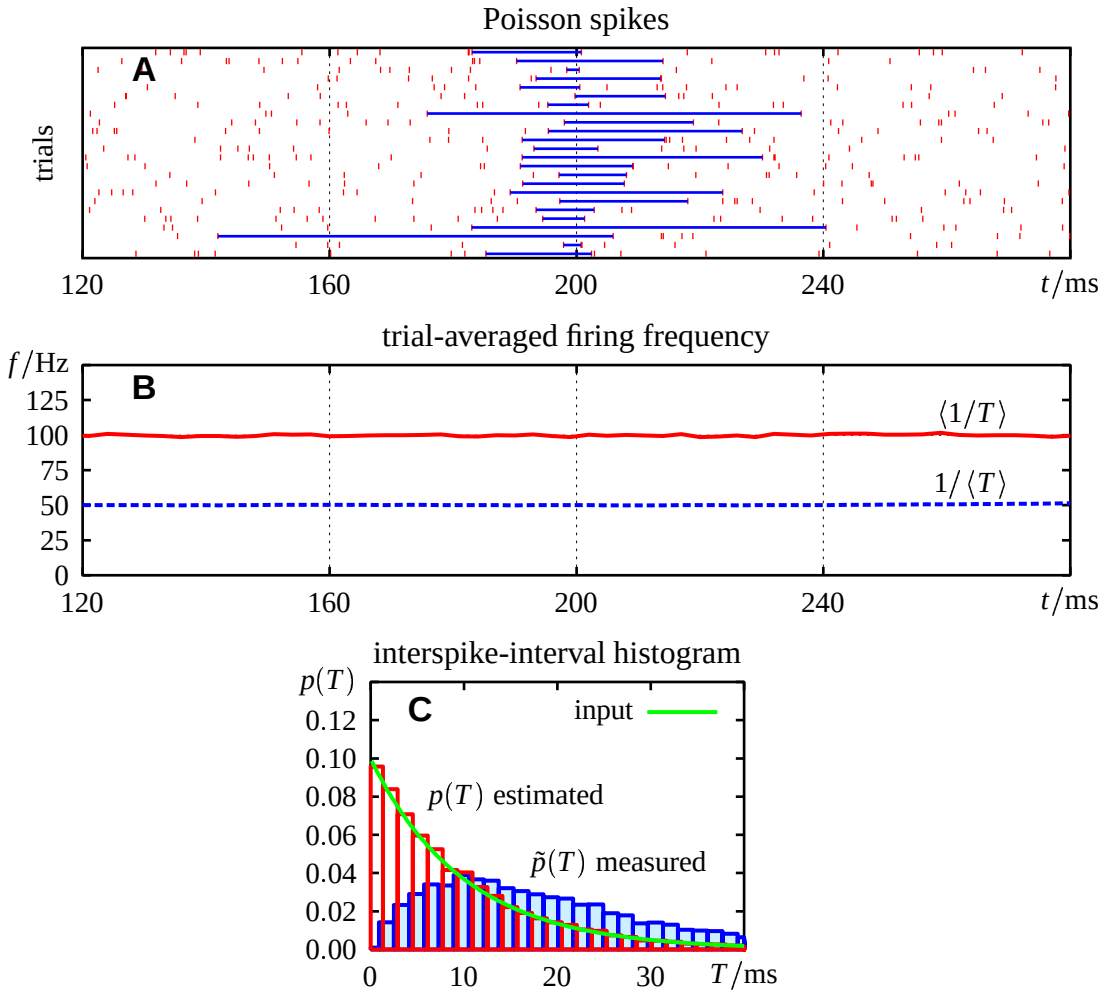

Figure 5.1: THE LOCAL *ISI*-DISTRIBUTION. **A** 24 out of 100 000 spike trains with Poisson distributed spikes (rate $r = 100$ Hz) are shown. As an example the interspike intervals T containing the time $t = 200$ ms are marked by horizontal lines. From these interspike intervals the local *ISI*-distribution and the firing frequency at time $t = 200$ ms have to be calculated. **B** The mean firing frequency, estimated for every millisecond of the shown traces, either as $f = 1/\langle T\rangle$ or as $f = \langle 1/T\rangle$ (5.5). Only the latter coincidences with the true frequency $f = r = 100$ Hz expected for these particular Poisson spike-trains. In contrast, the reciprocal of the averaged interspike intervals results in half of the rate. **C** The local interspike-interval distribution $\tilde{p}(T)$ at $t = 200$ ms determined directly from the interspike intervals marked in A differs dramatically from the true one (solid line) used to generate the spikes. Using (5.2), however, results in an excellent estimate $p(T)$ of the real distribution.

For any variable x the average with respect to $p(T)$ given $\tilde{p}(T)$ is

$$\langle x\rangle_p = \int_0^\infty x p(T)\,\mathrm{d}T = \int_0^\infty x \frac{\tilde{p}(T)/T}{\int_0^\infty \tilde{p}(T')/T'\,\mathrm{d}T'}\,\mathrm{d}T = \frac{\int_0^\infty \frac{x}{T}\tilde{p}(T)\,\mathrm{d}T}{\int_0^\infty \tilde{p}(T)/T\,\mathrm{d}T} \tag{5.8}$$

$$\boxed{\langle x\rangle_p = \frac{\left\langle \frac{x}{T}\right\rangle_{\tilde{p}}}{\left\langle \frac{1}{T}\right\rangle_{\tilde{p}}} = \frac{1}{f}\left\langle \frac{x}{T}\right\rangle_{\tilde{p}}}\,. \tag{5.9}$$

In particular, for the variance of the interspike intervals

$$\sigma_T^2 = \left\langle (T - \langle T \rangle_p)^2 \right\rangle_p \tag{5.10}$$

one obtains with $\langle T \rangle_p = 1/f$ and $\langle 1/T \rangle_{\tilde{p}} = f$

$$\sigma_T^2 = \frac{1}{f} \left\langle \frac{(T - 1/f)^2}{T} \right\rangle_{\tilde{p}} = \frac{1}{f} \left(\langle T \rangle_{\tilde{p}} - 2/f + \frac{1}{f^2} \left\langle \frac{1}{T} \right\rangle_{\tilde{p}} \right) = \frac{\langle T \rangle_{\tilde{p}}}{f} - \frac{1}{f^2} \,. \tag{5.11}$$

The standard deviation of the interspike intervals is thus given by

$$\sigma_T = \frac{1}{f} \sqrt{f \langle T \rangle_{\tilde{p}} - 1} \,, \tag{5.12}$$

and the standard deviation of the firing frequency is

$$\boxed{\sigma_f = f \sqrt{f \langle T \rangle_{\tilde{p}} - 1}} \,, \tag{5.13}$$

since according to the law of error propagation $\sigma_f = \sigma_T / T^2 = f^2 \sigma_T$.

Usually the firing rate $r(t)$, defined as the number of spikes per time bin divided by the width of the bin, is used to characterize the time course of the activity of a neuron. This measure is also frequently denoted as peri-stimulus time histogram (PSTH). A variant is the firing rate obtained by convolving the spike trains with a normalized kernel (Dayan & Abbott, 2001). With these methods the probability density of a spike to occur at some time t is measured. In contrast, the firing frequency $f(t)$ (5.5) is a measure of the reciprocal interspike-interval, which is a completely different concept. To differentiate between these two measures throughout this thesis, the term "firing frequency" with the abbreviation f is reserved to denote the reciprocal of the trial-averaged interspike interval, while "firing rate" r is used for the probability of a spike event. The firing frequency f is designed to give a measure of the deterministic component of a spike response, independent of the amount of variability between the trials. The firing rate r, however, relies on the exact timing of the spikes and reflects stochastic components of the spike response (see Fig. 5.3 on page 110).

5.2 Spike jitter and precision

In addition to the firing frequency f (5.5) a measure of the jitter of spikes from trial to trial is needed to quantify the stochastic component of the evoked spike response. The coefficient of variation (CV) is defined as the ratio of the standard deviation to the mean of the interspike-interval distribution and serves as a global measure of firing variability (Softky & Koch, 1993; van Steveninck et al., 1997; Shadlen & Newsome, 1998; Stevens & Zador, 1998a). The coefficient of variation provides only a single number for the total time interval considered and does not separate between variability of the interspike-intervals evoked by either the variability of the stimulus or intrinsic noise of the neuron. A different approach is to calculate the variance of the number of spikes counted in time windows of different lengths. The Fano factor F is the ratio of this variance to the mean

spike count. Both measures are global, too (Dayan & Abbott, 2001). As it turns out the Fano factor is independent of the variability of the stimulus for inhomogeneous Poisson processes (Rieke et al., 1997). There exist many additional algorithms to quantify the precision of spikes. However, they either cannot be used in general (Mainen & Sejnowski, 1995), or they depend on the choice of an additional time scale (Kistler et al., 1997; van Rossum, 2001). The firing rate $r(t)$ belongs to the latter category, too, and is one of the examples of a time-resolved measure of the precision of spike timing.

Why not measure the jitter of spikes directly as the standard deviation of the timing of the spikes? Consider the jitter σ_J defined by

$$\sigma_J = \sigma_\tau \tag{5.14}$$

as the standard deviation σ_τ of the timing τ_k of the spikes of interest from each trial k. Such a measure of spike jitter differs from the standard deviation of the local interspike-interval distribution (5.12). The latter combines the jitter of the left and the right spike of a considered interspike interval, while a measure of jitter like (5.14) focuses on a single spike from each trial.

Which spikes should be selected to calculate σ_J at a given time t ? One possibility is to take from each trial k the spike t_i^k which is the nearest to the time of interest t, i.e.

$$\tau_k^{(n)} = \begin{cases} t - t_{i-1}^k & ; \quad |t - t_{i-1}^k| \le |t - t_i^k| \\ t - t_i^k & ; \quad |t - t_{i-1}^k| > |t - t_i^k| \end{cases} \quad , \quad t_{i-1}^k \le t < t_i^k \, . \tag{5.15}$$

Fig. 5.2 B shows an example. The jitter σ_{J_n} is calculated according to (5.14) and (5.15) for every millisecond. If the clusters of jittered spikes are well separated (like the one at the time indicated by the left dotted vertical line in panel A) this measure coincidences well with the standard deviation used to generate the jitter of the spikes. However, between the clusters (for example at the right dotted line) the jitter is strongly overestimated. The reason is that by (5.15) some spikes are selected from the cluster to the left and some from the one to the right, which results in a bimodal distribution of the $\tau_k^{(n)}$ with a standard deviation more similar to that of the interspike-interval.

Another possibility is to take the first spike to the left for calculating the jitter σ_{J_l}:

$$\tau_k^{(l)} = t - t_{i-1}^k \, , \quad t_{i-1}^k \le t < t_i^k \, . \tag{5.16}$$

Such a measure has an advantage in that it takes causality into account. As can be seen in the example shown in Fig. 5.2 C this works fine except during the spike clusters (for example at the left dotted line), where one half of the spikes are selected from the cluster centered at the considered time t, but the other half is selected from the preceeding cluster of spikes.

Combining both σ_{J_n} and σ_{J_l} such that the smallest value of the two is taken

$$\sigma_J(t) = \min\{\sigma_{J_n}(t), \, \sigma_{J_l}(t)\} \, , \tag{5.17}$$

results in a suitable measure of spike jitter (Fig. 5.2 D). Of course it is conceivable that there are different possibilities to implement the idea (5.14) of a measure of spike jitter based on the standard deviation of the timing of spikes.

Another example with varying spike jitter is shown in Fig. 5.3. The measure of spike jitter (5.17) is indeed in good agreement with the jitter used to generate the spikes. There are only small fluctuations which deviate from the real jitter.

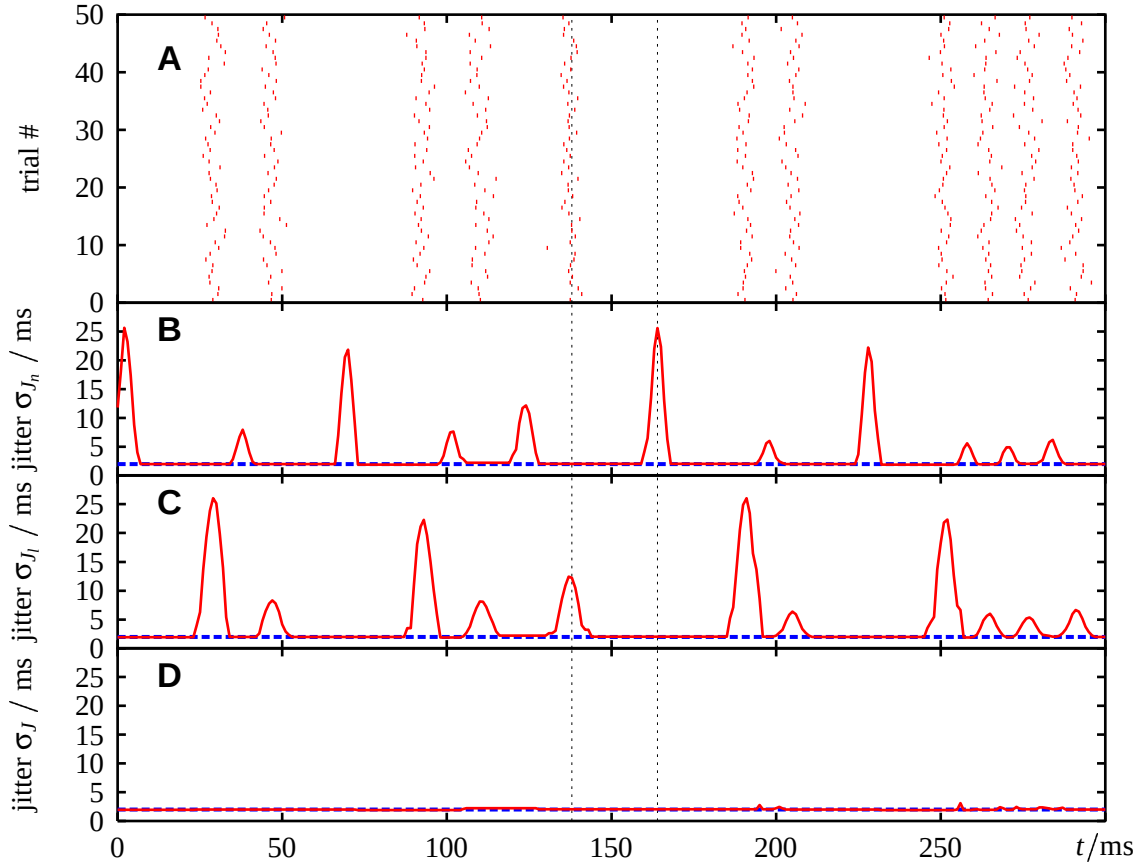

Figure 5.2: MEASURES OF SPIKE-JITTER. **A** First, the spikes of trial #1 were generated randomly. The spikes of the remaining 199 trials (50 are shown) were copied from the first trial and jittered by some time, which was drawn from a Gaussian distribution with a standard deviation of 2 ms. Thus, the spikes of all the trials cluster around the spikes of the first trial. The two vertical lines mark the center of a cluster of spikes and the center between two clusters of spikes. **B** The jitter σ_{J_n} of the spikes calculated according to (5.15) as the standard deviation of the nearest spike of each trial to time t (solid line). The dashed line indicates the standard deviation of the jitter used to generate the spikes. **C** The jitter σ_{J_l} of the spikes calculated according to (5.16) as the standard deviation of the spikes preceeding time t (solid line). **D** The combined measure of jitter σ_J (5.17) is the smaller value of the two from B & C. It reveals a good estimate of the real spike jitter.

For a Poisson spike-train with rate r, the distribution of the distance of the nearest $\tau_k^{(n)}$ as well as of the preceeding spikes $\tau_k^{(l)}$ to a given time t is identical to the interspike-interval distribution

$$p(\tau) = re^{-r\tau} . \tag{5.18}$$

It has the standard deviation $1/r$ and therefore the jitter of Poisson spike-trains is $\sigma_J(t) = 1/r$.

It is often more convenient to have a measure of precision π, which is high for low spike jitter and vice versa. The reciprocal of σ_J would be such a measure:

$$\pi = \frac{1}{\sigma_J} . \tag{5.19}$$

This measure has the advantage to have the unit Hertz, so that it is also directly comparable to the firing frequency. See Fig. 5.3 D for an example, where the time course of the spike precision $\pi(t)$ is shown in comparison with the one of the firing rate $r(t)$ and the

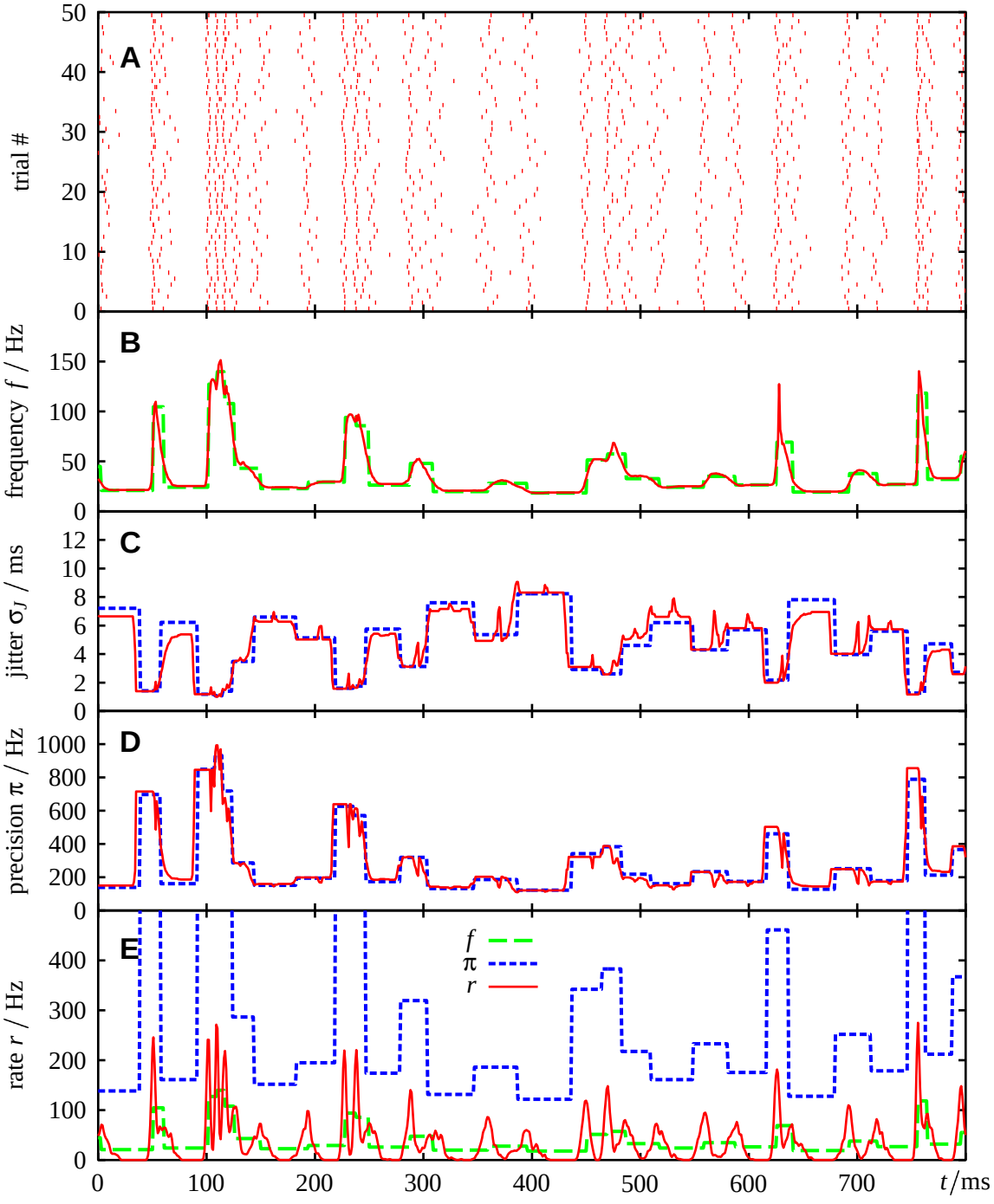

Figure 5.3: FIRING FREQUENCY, SPIKE JITTER, PRECISION AND FIRING RATE. **A** First, the spikes of trial #1 were generated randomly. Then the spikes of the remaining trials were jittered randomly from Gaussian distributions with different standard deviations around the spikes of the first trial. 50 out of 200 trails are shown. **B** The mean firing frequency (5.5) as the average of the reciprocal interspike intervals (solid line) is very close to the one used to generate the spikes (dashed line). **C** The jitter measure σ_J (5.17) (solid line) compared to the standard deviation of the Gaussian distributed jitter used to generate the spikes (dashed line). **D** The precision π (5.19) defined as the reciprocal of the spike jitter σ_J in comparison to the reciprocal of the standard deviation of the jitter used to generate the spikes. **E** The firing rate $r(t)$ as the number of spikes per one millisecond time bin divided by the width of the bin. For comparison, the firing frequency $f(t)$ and the precision $\pi(t)$ as the reciprocal of the standard deviation of the jitter used to generate the spikes are shown.

firing frequency $f(t)$. Note that for a deterministic neuron the spike jitter σ_J equals zero and the precision π diverges to infinity.

5.3 Summary

- To obtain the local interspike-interval distribution, the measured interspike intervals lying over a given time *t* have to be weighted by the reciprocal of their length (5.2).
- The firing frequency at time *t* as a measure of the mean distance of two succeeding spikes is the average of the reciprocal interspike intervals (5.5).
- A measure for the jitter of spikes (5.17) based on the standard deviation of timing of spikes is proposed. It has the advantage to denote the jitter directly in units of time.

Part II

Experiments

6

Auditory Receptor Neurons of Locusts

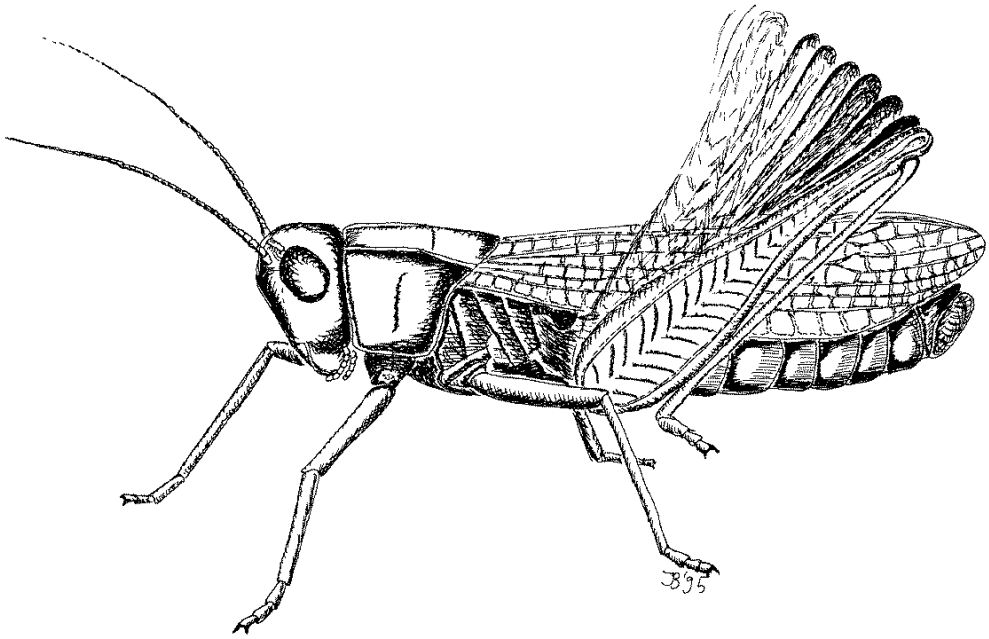

Contents

6.1 Introduction ***116***
6.2 Methods ***117***
Animals *117*
Preparation *117*
Recordings *117*
Online stimulus generation and data analysis *118*
f-I-curves *118*
Phase-resetting curves *120*
Adaptation model *121*
6.3 Results ***121***
Spike-frequency adaptation *123*
Phase-resetting curves *125*
Performance of the models *125*
6.4 Discussion ***131***
Class-I or class-II neuron? *131*
Properties of f-I-curves *132*
Adaptation mechanisms *134*
Model for spike-frequency adaptation *134*
Adaptation and the distribution of stimulus amplitudes *135*
Song recognition *135*
6.5 Summary ***136***

Cover: Stridulating male of the field-grasshopper *Chorthippus dorsatus*.

6.1 Introduction

Models of the generation of spikes and of spike-frequency adaptation were introduced in the first part of this thesis. These single-compartment models are tested on real neurons in this and the following chapter. Auditory receptor cells of grasshoppers are well suited to apply the proposed models, since they lack a dendritic tree and intermediate synapses. The signal-transmission properties of the auditory receptor cells are of great interest for investigations on subsequent stages of auditory processing.

The auditory system of grasshoppers plays an important role in their reproduction. With their legs and/or wings they produce calling songs to attract their mates. The receiver has to recognize a con-specific song among other songs, assess it, and respond or move towards it. This behavior has been studied extensively (von Helversen, 1997).

The auditory system of grasshopper is therefore well suited for studying how this pattern-recognition task is implemented on the neural level.

Acridid grasshoppers have their ears at the abdomen (see Fig. 1.2). A sound wave excites the oval tympanum (Michelsen, 1971; Michelsen & Rohrseitz, 1995), which is exposed to the outside world. The auditory ganglion (Müller's organ) is attached to the inner surface of the tympanum (Gray, 1960; Breckow & Sippel, 1985). The ganglion contains the auditory receptor neurons, which pick up the oscillations of the tympanum (Hill, 1983a,b; Oldfield & Hill, 1986). The receptor neurons translate the sound wave into a sequence of spikes. The axons of the receptor cells form the auditory nerve and make contact with auditory interneurons in the metathoracic ganglion (Halex et al., 1988; Boyan, 1999; Jacobs et al., 1999).

Electrophysiological recordings from auditory receptor cells of adult *Locusta migratoria* are analyzed in this chapter. Onset, steady-state and adapted f-I-curves, and adaptation time constants were measured, in order to quantify spike-frequency adaptation observed in the receptor cells (Michelsen, 1966). These findings are compared with the expectations of the theoretical considerations about adaptation from chapter 4. Phase-resetting curves were measured to determine whether the receptor neurons are class-I or class-II neurons (see chapter 2), and to choose an appropriate phase-oscillator model from chapter 3. Finally, implications on the transmission of calling songs are discussed.

6.2 Methods

Animals

All experiments were performed on adult *L. migratoria*. The animals were obtained from commercial cultures.

Preparation

The legs, the wings, head and gut were removed and the animal was waxed ventral side uppermost on a platform. Then the dorsal part of the thorax was cut open to expose the metathoracic ganglion and auditory nerve. The auditory nerve was fixed with a special forceps mounted on a micromanipulator.

Recordings

Receptor cells were recorded intracellularly in the auditory nerve with standard glass micro-electrodes (borosilicate, $50 - 110\,\mathrm{M}\Omega$ resistance), filled with 1 M KCl solution. Neural responses were amplified (NPI, BRAMP-01) and recorded by a data acquisition board (National Instruments, PCI-MIO-16E-1) with a sampling rate of 10 kHz. If not stated otherwise, the animals were heated to a temperature of about 35 °C. The phase-resetting curves were measured at room-temperature (about 20 °C). The experiments were performed by Hartmut Schütze, Olga Kolesnikova, Tim Gollisch, and myself.

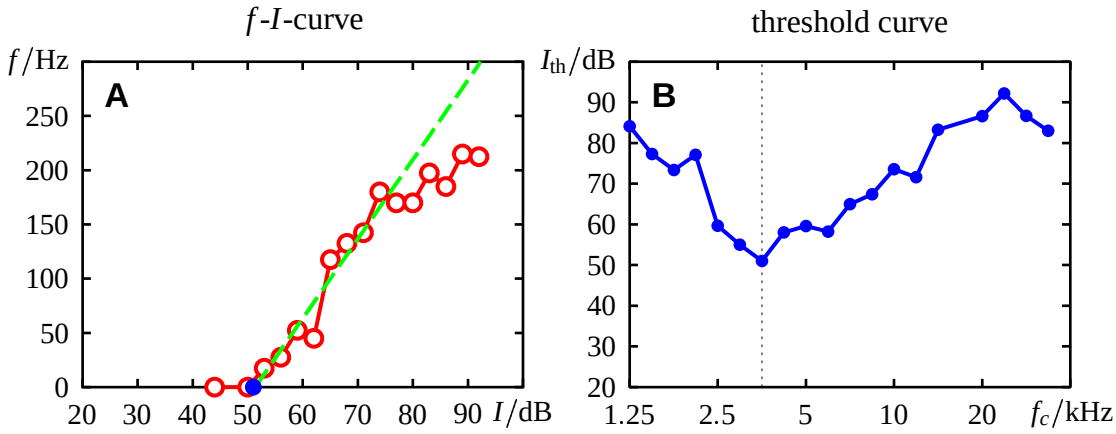

Figure 6.1: MEASURING THE THRESHOLD-CURVE OF AN AUDITORY RECEPTOR NEURON. **A** An f-I-curve calculated from the mean spike count evoked by 40 ms long stimuli with carrier frequency 3.5 kHz. A line is fitted into the dynamic range (dashed line) to determine the threshold intensity (dot at 50 dB). **B** The threshold intensities I_{th} for different carrier frequencies f_c of the stimulating sound waves. The threshold-curve shown is typical for a low-frequency receptor. The cell shown here is most sensitive at about 3.5 kHz. The data were recorded at room temperature.

Online stimulus generation and data analysis

For online stimulus generation and data analysis together with Christian Machens I developed the OEL-software (Online-Electrophysiology-Laboratory). It is written in C++ under Linux and uses the Qt-library (Troll Tech) for graphical user interface. Two character-device driver were implemented as loadable kernel modules for the communication with the data-acquisition board (National Instruments, PCI-MIO-16E-1) and the attenuator of the acoustic signal (Chrystal semiconductors, CS3310). OEL handles the output of stimuli, reads continuously the recorded voltage trace, and detects the spikes, using an adaptive threshold of the first derivative of the voltage trace. So called RePros (Research Programs) can be written in C++ and added to OEL, which analyze the spike trains and then generate the next stimulus. Stimuli were sampled with 200 to 240 kHz. Their intensity is measured in decibel sound pressure level (dB SPL).

f-I-curves

First, the carrier frequency for which the cell is most sensitive was determined (Fig. 6.1). For that purpose stimuli of 40 ms duration and 1 ms ramps were used. Each stimulus with a particular carrier frequency and intensity was repeated two times. The response of the cell was measured as the mean spike count of the two trials during stimulation. If a stimulus evoked a response, the next stimulus was applied after a pause of 260 ms. Otherwise the next stimulus followed after 5 ms. An f-I-curve was measured at each carrier frequency for intensities ranging from 20 to 100 dB SPL. Starting with a resolution of 24 dB, which then was successively divided by two, the response to different intensities down to a resolution of 6 dB was measured. Intensities below a higher intensity, which did not evoke any response, were skipped. The response to intensities spaced by 3 dB was only determined for intensities, were the slope of the already measured f-I-curve was larger than 5 Hz/dB. With this procedure the measurement of the f-I-curve focused on its dynamic range. A line was fitted into the dynamic range and its intersection with the

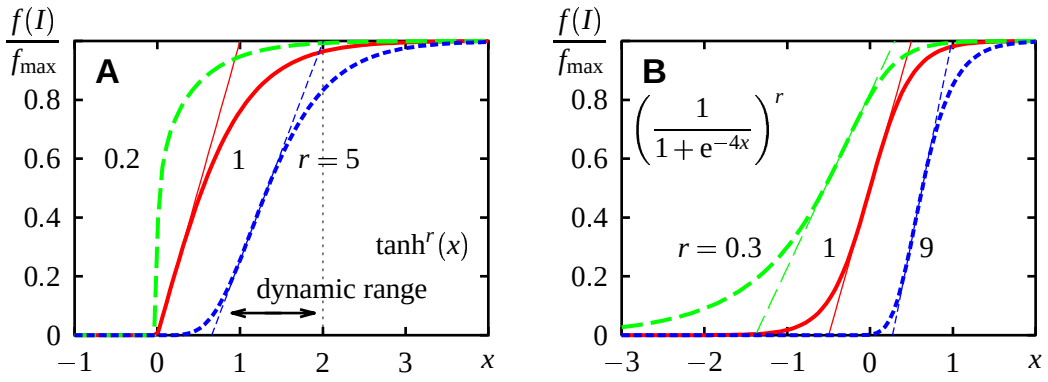

Figure 6.2: SIGMOIDAL FUNCTIONS USED TO FIT THE f-I-CURVES. **A** The rectified hyperbolic tangent (6.1) has a sharp foot-point, which is smeared out for values of r greater than one. **B** The Boltzmann function (6.3) has smooth transitions at both the lower and upper part of its dynamic range. The parameter r makes the Boltzmann function asymmetric. Values of r larger than one result in a sharper foot-point. The thin lines are the tangents to the sigmoids at their turning points. Their slopes are given by (6.2) and (6.4).

intensity-axis was taken as the threshold intensity of the receptor neuron. The f-I-curves were measured at maximal 21 different carrier frequencies between 1.25 and 40 kHz. The carrier frequencies were spaced by a factor of $\sqrt[4]{2} \approx 1.1892$, i.e. the carrier frequencies were 1.25, 1.49, 1.77, 2.1, 2.5, ... 40 kHz. The carrier frequency of the lowest threshold intensity was taken as the best carrier frequency of the receptor cell. All stimuli of the following experiments used this frequency for the carrier sound wave.

Next, a more detailed f-I-curve was measured using stimuli of 300 ms duration, which were repeated six times. The minimum resolution of intensities was 1.5 dB. The peak of the trial-averaged time course of the firing frequency (equation (5.5) on page 105) was taken to construct the onset f-I-curve $f_0(I)$. The steady-state f-I-curve $f_\infty(I)$ was calculated from the mean response between 240 and 290 ms after stimulus onset (Fig. 6.3). A single exponential was fitted into the time course of the firing frequency to obtain the effective adaptation time-constant τ_{eff} (Fig. 6.4).

For a parameterization of the onset f-I-curve the positive part of a hyperbolic tangent

$$f_0(I) = \begin{cases} f_{\max} \tanh^r(k(I - I_{\text{th}})) & ; \quad I > I_{\text{th}} \\ 0 & ; \quad I \le I_{\text{th}} \end{cases} \tag{6.1}$$

was used, where $f_{\max}$ is the maximum firing frequency and I_{th} is the threshold intensity (see Fig. 6.2 A). k determines the initial slope and the exponent $r > 0$ distorts the hyperbolic tangent. The slope s_0 at the turning point of (6.1) is

$$s_0 = 2 f_{\max} k \frac{r}{r+1} \sqrt{\frac{r-1}{r+1}}^{r-1} . \tag{6.2}$$

The width of the dynamic range of the sigmoidal is approximately $f_{\max}/s_0$.

For the steady-state f-I-curve the Boltzmann function was fitted on the data

$$f_\infty(I) = f_{\max} \left(\frac{1}{1 + e^{-k(I - I_{1/2})}} \right)^r \tag{6.3}$$

(see Fig. 6.2 B). $I_{1/2}$ is the intensity where the firing frequency is one half of the maximum frequency $f_{\max}$, provided $r = 1$. The slope at the turning point is

$$s_\infty = f_{\max} k \left(\frac{r}{1+r} \right)^{1+r} . \tag{6.4}$$

The time constant of recovery from adaptation was measured as described in Fig. 4.10. A 200 ms stimulus was used to adapt the cell. The test stimuli of 40 ms duration were repeated eight times. Between test stimulus and the next adaptation stimulus was a pause of one second.

To measure the adapted f-I-curves, a special stimulus as described in Fig. 6.5 was used. Appropriate background intensities were calculated online based on the onset and steady-state f-I-curves measured before.

Phase-resetting curves

The latency λ of the system (transduction of the sound wave, transformation and time of the spikes traveling down the axon to the microelectrode; the time of the sound wave to reach the ear was already subtracted from the spike data) was determined with perturbations of 12 dB strength and one millisecond duration on top of a background intensity that evoked a firing frequency of approximately 100 Hz. After 400 ms to let the cell adapt to its steady-state firing frequency, the perturbations were randomly spaced from 30 to 60 ms. The entire stimulus was two seconds long, contained 35 perturbations and was repeated five times. The latency of the system was determined as the time shift that maximized the number of spikes, which were directly initiated by the perturbations, i.e. a spike occurred within 0.5 ms after the time of the perturbation plus the time shift.

Phase-resetting curves were measured with stimuli similar to the one used to determine the latency of the system. The perturbations were smaller (3–9 dB) and shorter (0.3 and 0.6 ms) and were randomly spaced from 50 to 100 ms. These stimuli were repeated 20 times. The period T_0 of the unperturbed oscillation was calculated as the mean interspike interval before the first perturbation. The time of a perturbation t_p plus the latency of the system λ minus the time of the preceeding spike t_i normalized by T_0 is the phase of the perturbation

$$\varphi = \frac{t_p + \lambda - t_i}{T_0} , \; t_i < t_p + \lambda \leq t_{i+1} . \tag{6.5}$$

The phase shift $\Delta\varphi$ is the difference of the unperturbed period T_0 and the interspike interval $t_{i+1} - t_i$ over the perturbation

$$\Delta\varphi = \frac{T_0 + t_i - t_{i+1}}{T_0} , \; t_i < t_p + \lambda \leq t_{i+1} . \tag{6.6}$$

The phase shifts were binned in 1/10 phases and the median as well as the second and third quartile was calculated for each bin to get a phase-resetting curve.

Adaptation model

With the following adaptation model the firing frequency to arbitrary stimuli $I(t)$ was predicted:

$$\begin{aligned} f(t) &= f_0(I-A) \\ \tau\dot{A} &= \frac{I - f_0^{-1}(f_\infty(I))}{f_\infty(I)} f(t) - A\,. \end{aligned} \tag{6.7}$$

In this equation A is the state of adaptation and τ is the adaptation time-constant. The model (6.7) is a variant of the model for encoder adaptation (4.22), which can be applied to neurons with saturating f-I-curves. The original model for encoder adaptation (4.22) is not applicable, since the inverse function of the steady-state f-I-curve is not defined for firing frequencies greater than its maximum firing frequency. To overcome this problem, the steady-state adaptation strength in (6.7) is forced to be proportional to the firing frequency $f(t)$. All deviations from this proportionality are handled by the intensity dependence of the proportionality factor. See discussion for a validation of this model.

The firing frequency from the model (6.7) was smoothed by applying the non-leaky phase oscillator (3.5) in the following way: At a given time t a time interval T centered over t is determined such that

$$\int_{t-T(t)/2}^{t+T(t)/2} f(t')dt' = 1\,. \tag{6.8}$$

The resulting firing frequency $\nu(t) = 1/T(t)$ was compared with the experimentally measured firing frequency $f_{\text{exp}}(t)$.

The prediction error

$$p.e. = \sigma^2_{\text{diff}}/\sigma^2_{\text{exp}} \tag{6.9}$$

relates the mean squared difference

$$\sigma^2_{\text{diff}} = \frac{1}{T_s}\int_0^{T_s} (f_{\text{exp}}(t) - \nu(t))^2\,\mathrm{d}t \tag{6.10}$$

of the experimentally measured firing frequency $f_{\text{exp}}(t)$ and the firing frequency $\nu(t)$ of the model to the variance σ^2_{exp} of $f_{\text{exp}}(t)$ over the entire duration of the stimulus T_s. For a perfectly predicted firing frequency the mean squared difference σ^2_{diff} equals zero and the prediction error $p.e.$ becomes zero.

To test the performance of the models, two types of stimuli were applied: (i) the envelope of a calling song of a male of the grasshopper *Chorthippus biguttulus*. (ii) white noise stimuli of ten seconds duration with an amplitude distribution similar to the grasshopper song and different cut-off frequencies (Machens et al., 2001). All these stimuli were filled with a sine wave with their frequency set to the neurons best frequency.

6.3 Results

Data from still ongoing experiments are presented in the following.

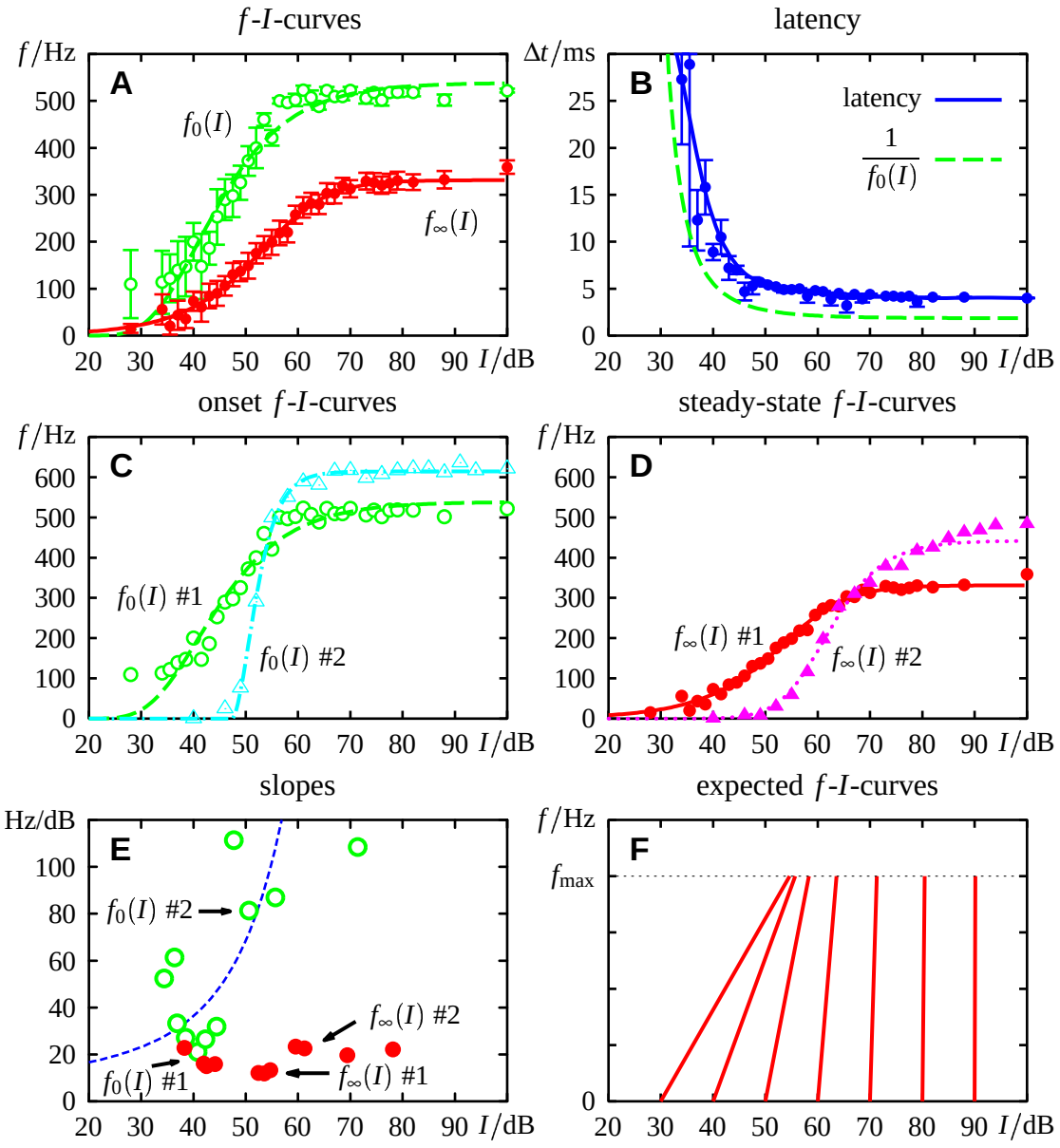

Figure 6.3: f-I-CURVES AND LATENCIES OF LOW-FREQUENCY RECEPTORS. The animals were heated to 35 °C. Each stimulus was 300 ms long and was repeated $n = 6$ times. **A** The onset f-I-curve $f_0(I)$ and the steady-state f-I-curve $f_\infty(I)$ of a low-frequency receptor with its best carrier-frequency at 2.5 kHz. Errorbars denote the standard error of the firing frequency. The dashed line is the fit of the hyperbolic tangent (6.1) used for the onset f-I-curve. The solid line is the fit of the Boltzmann function (6.3) used for the steady-state f-I-curves. **B** Latencies to the first spike with standard errors in comparison with the mean interspike interval $1/f_0(I)$ of the onset f-I-curve. Note that also the (unknown) latency of the system λ contributes to the latencies shown here, which has to be subtracted from the data. **C** The onset f-I-curve of the cell shown in A compared with the onset f-I-curve of a different low-frequency receptor with best frequency at 2.97 kHz. **D** Comparison of the steady-state f-I-curves of the same cells from C. **E** The dependence of the slopes of both the onset (open circles) and the steady-state f-I-curves (filled circles) on the intensity of their turning point. The values of the two cells from C & D are indicated by the arrows. The dashed line is the expected slope (6.14) of the onset f-I-curves, if they all would have the same width in terms of sound-wave amplitudes. A fit on the data revealed a value of 507 for the ratio $\Delta p/p_0$ of the amplitude interval Δp to the reference sound pressure $p_0 = 20\,\mu$Pa. **F** Linear parts of f-I-curves with different threshold intensities as expected from the dashed line in D.

Table 6.1: PROPERTIES OF f-I-CURVES OF LOW-FREQUENCY RECEPTOR NEURONS.

f-I-curve	f_{max} Hz	s Hz/dB	ΔI dB
onset	570 ± 38	58 ± 32	13 ± 7
steady-state	370 ± 50	18 ± 4	22 ± 4

Summarized are the averaged maximum firing frequency f_{max}, slope s, and width ΔI of the dynamic range of $n = 11$ f-I-curves measured in seven different receptor cells. The slopes were calculated by means of (6.2) and (6.4).

Spike-frequency adaptation

To characterize spike-frequency adaptation the onset and the steady-state f-I-curve of a neuron is needed (see chapter 4). A typical example of f-I-curves of a low-frequency receptor is illustrated in Fig. 6.3 A. On average (see tab. 6.1) the onset f-I-curves had a maximum firing frequency of 570 Hz. The maximum firing frequency of the steady-state f-I-curves was 370 Hz. This is about two third of the onset f-I-curves ($f_0/f_\infty = 1.6 \pm 0.1$). The percentage of adaptation $F_{adap} = \frac{f_0 - f_\infty}{f_0}$ (Wang, 1998) is 56 ± 12 %. Both the slope of the onset f-I-curves (mean 58 Hz/dB) and the width of their dynamic range (mean 13 dB) vary strongly. As demonstrated in Fig. 6.3 C, D & E, the onset f-I-curves become steeper with higher threshold intensity. In contrast, the slopes of the steady-state f-I-curves and the widths of their dynamic range are independent of their threshold intensity (18 Hz/dB and 22 dB, respectively). On average the slopes of the onset f-I-curves are three times larger than the slopes of the steady-state f-I-curves ($s_0/s_\infty = 3.1 \pm 1.2$). Consequently, the width of the dynamic range of the onset f-I-curves is smaller than the width of the steady-state f-I-curves ($\Delta I_0/\Delta I_\infty = 0.6 \pm 0.2$).

The Boltzmann function (6.3) is a good model for a parameterization of the steady-state f-I-curves. It fits them for the whole range of intensities fairly well. The situation is more complicated for the onset f-I-curves. A slight spontaneous activity of the neurons implicates that there is even for subthreshold stimuli an enlarged activity somewhere during the stimulus, which is taken as the onset response. Therefore for low intensities the onset f-I-curves level out at a non-zero frequency, and it is not clear, whether the onset f-I-curves start smoothly or as a straight line with finite slope. However, they show a wide linear range, which is better fitted by the hyperbolic tangent (6.1).

Latencies to the first spike after stimulus onset are of the order of magnitude of the corresponding interspike interval from the onset f-I-curve. The latencies become very large close to the threshold as can be seen in Fig. 6.3 B.

The time courses of the firing frequency to constant stimuli with different intensities are shown in Fig. 6.4 A. A fit with a single exponential reveals the effective time constant of adaptation. The effective time constants for different stimulus intensities are plotted in comparison with the f-I-curves in Fig. 6.4 C. For intensities near threshold the time constants of adaptation are small (about 10 ms). They increase with stimulus intensity and approach on average a maximum value of $\tau_{eff} = 75 \pm 12$ ms[1].

In $n = 6$ cells the time constant of recovery from adaptation was measured (see

[1] Preliminary results from experiments performed at room temperature reveal similar maximum time constants of adaptation of about 80 ms.

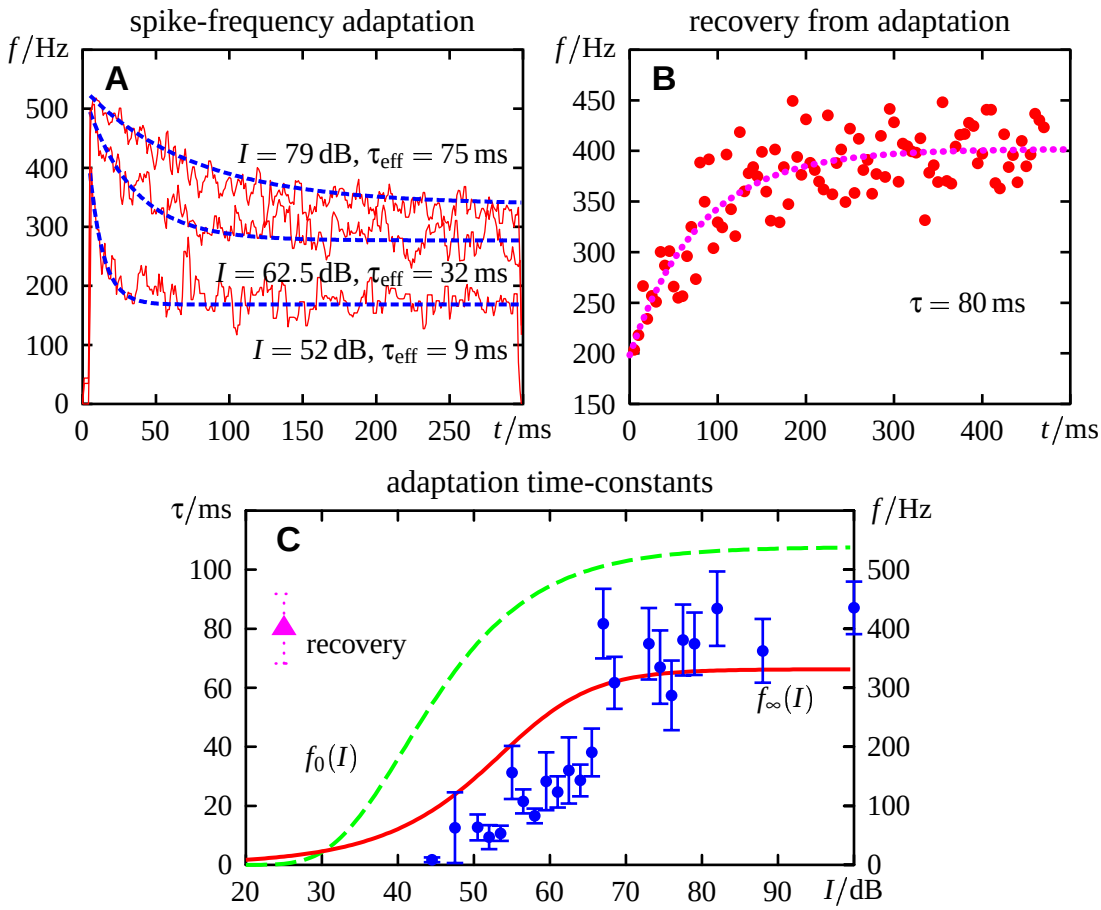

Figure 6.4: ADAPTATION TIME-CONSTANTS OF A LOW-FREQUENCY RECEPTOR. Same cell as in Fig. 6.3. **A** Three traces of the trial averaged firing frequency ($n = 6$) evoked by constant stimuli with different intensities as indicated are shown (carrier frequency 2.5 kHz, duration 300 ms). Single exponentials were fitted into the traces (dashed lines) to determine the effective adaptation time-constant τ_{eff}. **B** The firing frequencies evoked by test stimuli of 40 ms duration at time t after an initial adaptation stimulus of 200 ms duration with intensity $I = 51.2$ dB SPL. A fit with a single exponential (dashed line) revealed a time constant from recovery of adaptation of $\tau = 80$ ms. **C** The dependence of the effective adaptation time-constants (dots) from A on stimulus intensity. For comparison the fits of the f-I-curves from Fig. 6.3 are superimposed. The triangle marks the time constant of recovery from adaptation from B. The errorbars denote the uncertainty of the fits.

Fig. 6.4 B). On average the time constants were $\tau = 50 \pm 17$ ms. They were smaller than the corresponding maximum effective time constants of adaptation, but clearly larger than the time constants measured close to threshold (Fig. 6.4 C).

Adapted f-I-curves were measured successfully in $n = 9$ cells. Three examples are illustrated in Fig. 6.6. With increasing background intensity the adapted f-I-curves are shifted appropriately to higher intensities. In six cells the slope of the adapted f-I-curves remained unchanged, while in three cells the slope decreased a little at high background intensities. The maximum firing frequency of the adapted f-I-curves decreased with increasing background intensity towards the maximum firing frequency of the steady-state f-I-curve. The adapted f-I-curves shifted not beyond the saturation of the onset f-I-curve. The maximum difference between the threshold intensity of the onset f-I-curve and the threshold intensity of an measured adapted f-I-curve was about 10 dB.

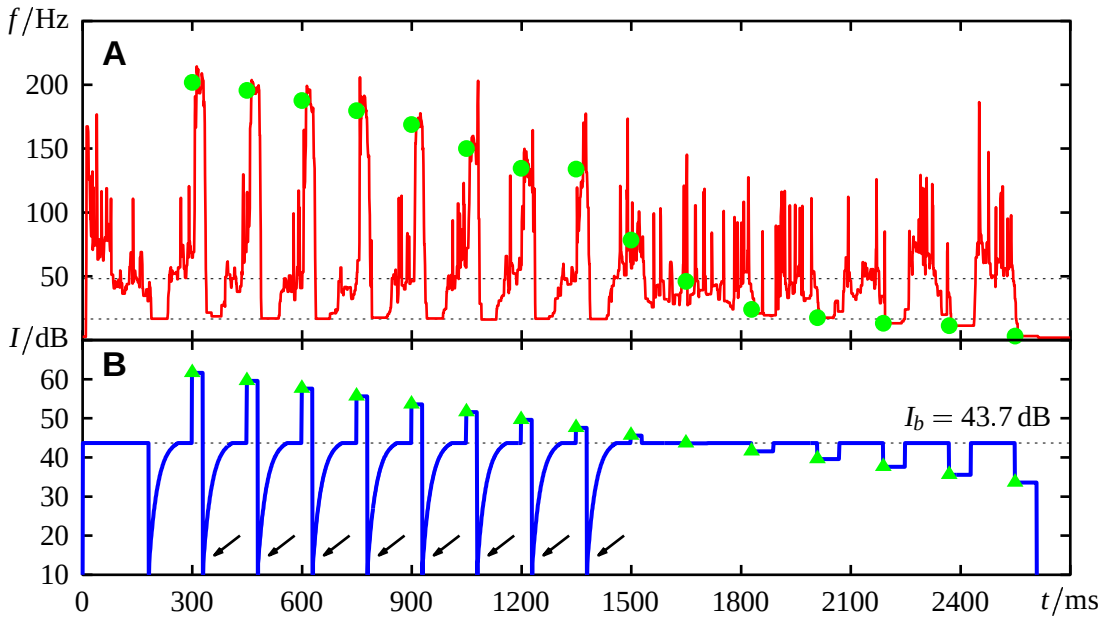

Figure 6.5: MEASURING AN ADAPTED f-I-CURVE. **A** Time course of the firing frequency $f(t)$ evoked by the stimulus $I(t)$ shown in B. First the neuron was adapted to the background intensity I_b (dotted line in B). Beginning at $t = 300$ ms the response (filled circles in A) to different intensities in an descending order (triangles in B) was tested. Directly after the test stimuli above background intensity the stimulus was set to zero (arrows in B) in order to minimize the total activity of the neuron, since very often the neuron's response to the background intensity (upper dotted line in A) between the test stimuli decreased slowly during the entire stimulus. The duration of the test stimuli was 30 ms for $I > I_b$ and 60 ms otherwise. The lower dotted line in A is the reciprocal of the 60 ms stimuli, which is approximately the lowest firing frequency that can be measured (see also Fig. 4.12 in chapter 4).

Phase-resetting curves

Phase-resetting curves were measured successfully in $n = 5$ cells. The data from one example cell are illustrated in Fig. 6.7. The latency λ of the system was on average 6.4 ± 0.6 ms. The phase-resetting curves for the weak perturbations were always positive, except at very late phases, which is an effect of noise (see Fig. 6.7 B for an explanation). The response function of the θ-model (3.20) corresponds well with the measured phase-resetting curves of the receptor neurons in that both are positive (at least for phase angles < 0.7) and both have a single peak approximately at intermediate phases. Even perturbations, which consist only of a single oscillation of the carrier sound-wave, still had an effect on the following spikes.

Performance of the models

To test the models, first the onset and the steady-state f-I-curves of the receptor cell were measured. Then the cell was stimulated with the calling song and the white-noise stimuli. The evoked firing frequency was then compared with the prediction of the proposed adaptation model (6.7), whose output firing-frequency $f(t)$ was smoothed with the non-leaky phase oscillator (3.6).

The model reproduced the measured firing frequency with high accuracy (see Fig. 6.8,

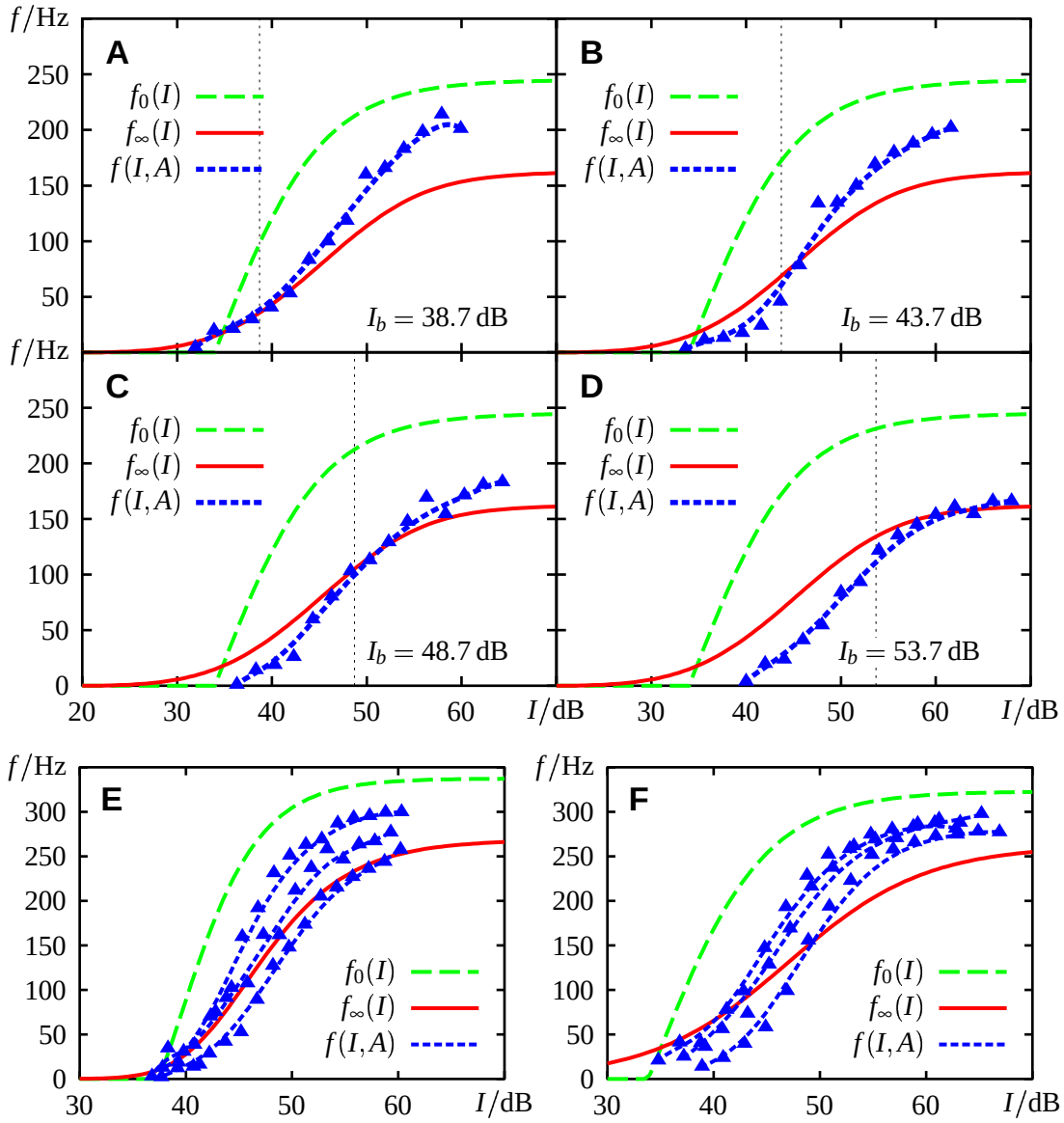

Figure 6.6: ADAPTED f-I-CURVES OF RECEPTOR NEURONS. **A, B, C & D** Adapted f-I-curves $f(I,A)$ of a low-frequency receptor with best frequency at 2.97 kHz. Four different background intensities I_b as indicated (vertical lines) were used. For comparison the onset f-I-curve $f_0(I)$ and the steady-state f-I-curve $f_\infty(I)$ of the same cell are drawn. At background intensity the adapted f-I-curves are expected to intersect the steady-state f-I-curve. Increasing background intensity shifts the adapted f-I-curves and decreases their saturation level towards the one of the steady-state f-I-curve. **D** The adapted f-I-curve at the background intensity is below the steady-state f-I-curve. This may be caused by additional very slow (> 1 s) processes, which further weaken the response of the cell. **E** Some adapted f-I-curves in comparison to the onset and steady-state f-I-curves of a low-frequency receptor with best frequency at 3.54 kHz. With increasing background intensity the slope of the adapted f-I-curves is slightly decreasing. **F** Adapted f-I-curves of a high-frequency cell with best frequency at 40 kHz. In this cell the slope of the adapted f-I-curves does not change.

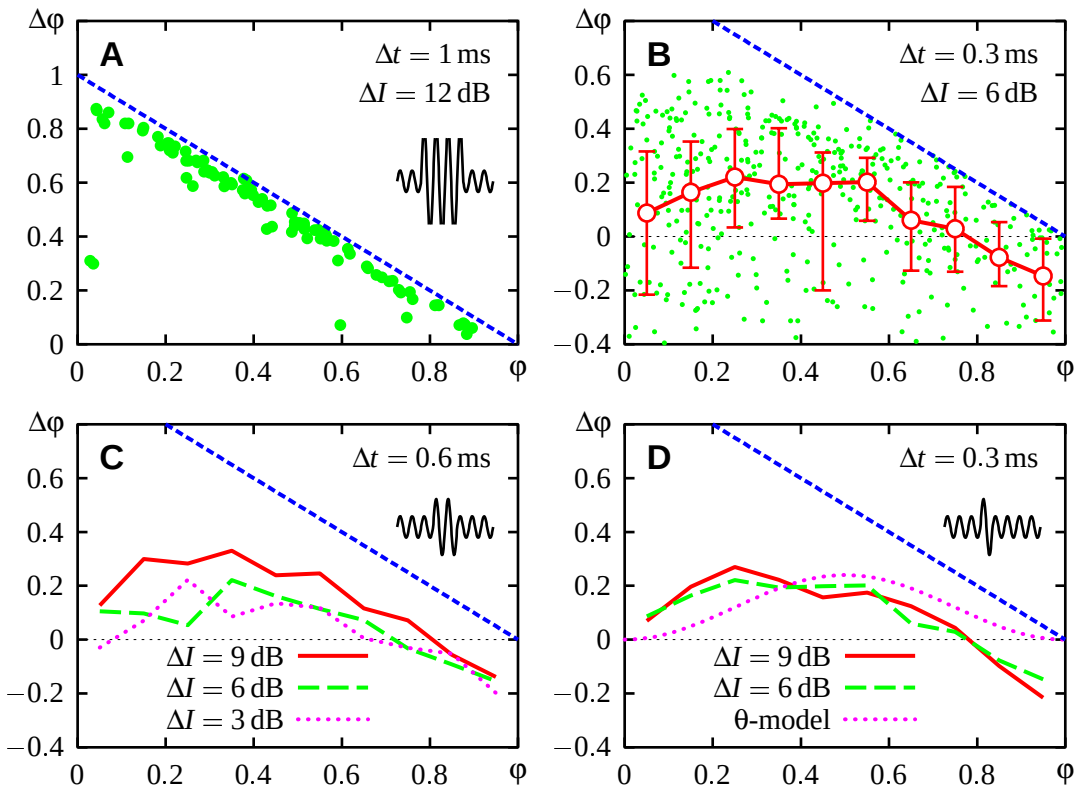

Figure 6.7: PHASE-RESETTING CURVES OF A LOW-FREQUENCY RECEPTOR. **A** The latency λ of the system was measured using strong perturbations of $\Delta I = 12\,\mathrm{dB}$ and $\Delta t = 1\,\mathrm{ms}$ duration (a part of the sound wave is sketched in the inset). Such perturbations force almost immediately the generation of a spike. For the calculated system latency of 6.7 ms the phase shifts line up very closely to the $1 - \varphi$-line (dashed line). This line indicates spikes which were generated at the same time as the perturbation. **B, C & D** To measure the phase-resetting curves, shorter and weaker perturbation stimuli as indicated were used. **B** The resulting phase shifts are very noisy (dots), since the timing of the spikes is very irregular even without perturbations. However, the medians of the data binned into ten bins reveal a clear phase-resetting curve. The errorbars denote the second and third quartile. The phase-resetting curve is always positive, except at very late phases. The negative values of the data there is an effect of the noisy spikes. The data cannot be higher than the $1 - \varphi$-line (dashed line) to ensure causality. Therefore they only can fluctuate below this line. **C** Phase-resetting curves (median) evoked by perturbations of 0.6 ms duration. This corresponds to two oscillations of the carrier frequency of 3.54 kHz used for the stimuli (inset). The strength ΔI of the perturbations was varied as indicated. **D** Same as in C, but with the duration of the perturbation of only 0.3 ms, which corresponds to one oscillation of the sound wave (inset). Superimposed is an appropriately scaled response function of the θ-model (dotted line).

Fig. 6.9, and Fig. 6.10). A model without adaptation, i.e. a mapping of the stimulus directly through the neuron's onset f-I-curve, clearly failed to reproduce the experimentally measured firing frequency (Fig. 6.8 A). To the white-noise stimuli the cell adapted quickly to an approximately constant state of adaptation (Fig. 6.8 C and Fig. 6.9 C). The intensity of the calling song slowly increases with time. The state of adaptation followed this slow component of the stimulus and kept the output firing frequency of the cell at a nearly constant level (Fig. 6.10 B & D).

The f-I-curve of the neuron is shifted dynamically by the state of adaptation $A(t)$.

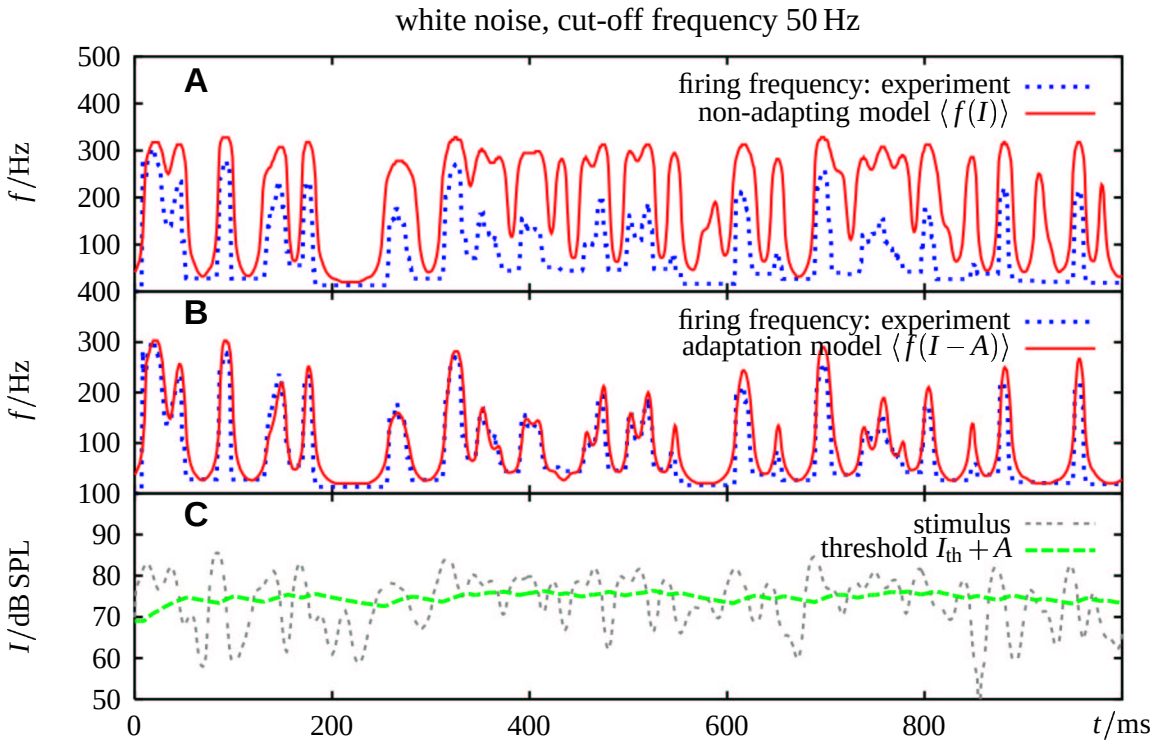

Figure 6.8: PERFORMANCE OF THE ADAPTATION MODEL FOR A WHITE-NOISE STIMULUS. The stimulus is a white-noise modulation of a 5 kHz sound wave with cut-off frequency 50 Hz. Only the first part of the ten second long stimulus is displayed. **A** The firing frequency of the cell (dashed line) evoked by the white-noise stimulus shown in C. A simple mapping of the stimulus through the neuron's onset f-I-curve and smoothing with (6.8) to account for the spike-dynamics yields the firing frequency of a non-adaptating neuron (solid line). The prediction error (6.9) over ten seconds is 570 %. Thus, such a model cannot reproduce the experimentally measured firing frequency. **B** Using both the onset and steady-state f-I-curves, the prediction of the time course of the firing frequency of the adaptation model (6.7) was computed and smoothed by (6.8) (solid line). It closely follows the experimentally measured firing frequency (prediction error (6.9) over ten seconds is 36 %). In **C** the threshold of the adapted f-I-curve (dashed line) as the threshold of the onset f-I-curve I_{th} plus the state of adaptation A is drawn in comparison with the stimulus (solid line).

The varying threshold of the adapted f-I-curve is given by the threshold of the onset f-I-curve I_{th} plus the state of adaptation A. Only parts of the stimulus above the current threshold are transmitted by the neuron. As can be seen in the examples of Fig. 6.8 C, Fig. 6.9 C, and Fig. 6.10 B & D, adaptation keeps most of the stimulus below the neuron's threshold. Subtracting the state of adaptation $A(t)$ from the stimulus $I(t)$ results in an effective stimulus, which is then transmitted via the onset f-I-curve, provided the slope of the adapted f-I-curves does not change. In Fig. 6.11 the original amplitude distribution of a white-noise stimulus is compared with the amplitude distribution of the effective stimulus. Without adaptation most of the original stimulus is above threshold. Due to adaptation, however, for the receptor cell the stimulus becomes softer and is shifted to lower intensities from the point of view of the onset f-I-curve. Finally one half of the stimulus remains sub-threshold.

The strong effect of the non-leaky phase oscillator (6.8) on the output firing frequency of the adaptation model (6.7) is illustrated in Fig. 6.9 A & B. The adaptation model (6.7)

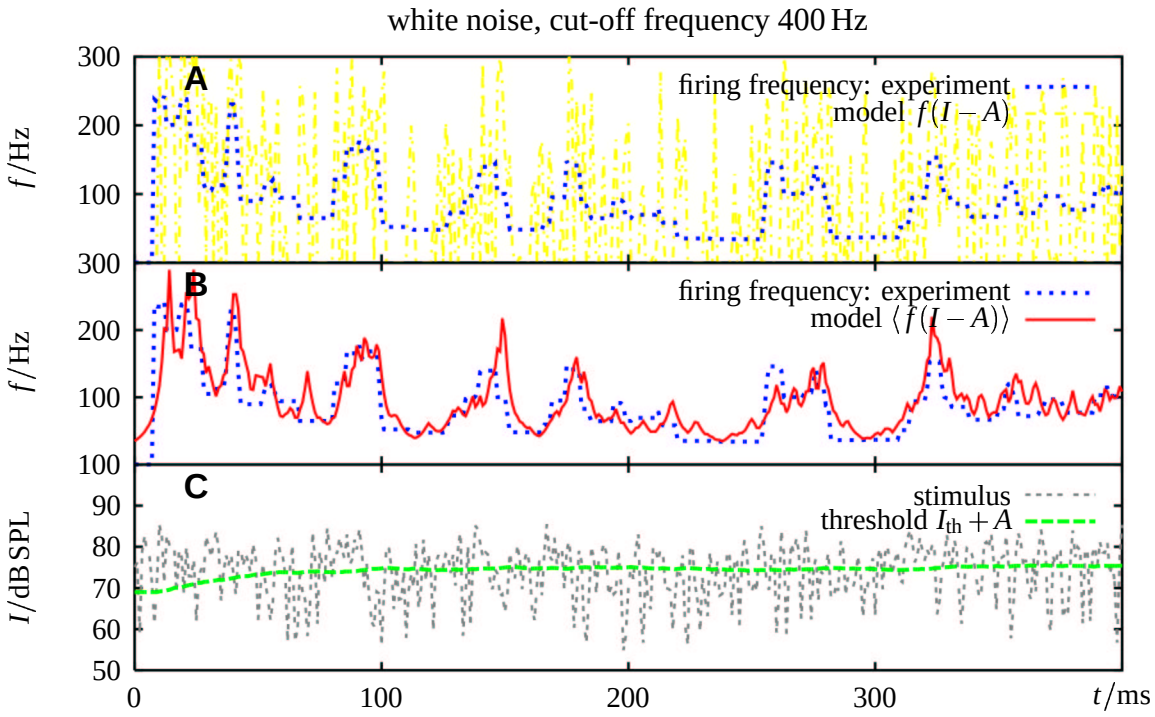

Figure 6.9: THE ADAPTATION MODEL AND THE SMOOTHING EFFECT OF THE SPIKE DYNAMICS. **A** The firing frequency of the same cell as in Fig. 6.8 (dashed line) evoked by a white-noise stimulus with cut-off frequency 400 Hz. The firing frequency $f(I-A)$ of the adaptation model (6.7) fluctuates as fast as the stimulus (solid line) and does not match the experimentally measured firing frequency. **B** Applying the filter (6.8) to account for the spike-dynamics, results in a firing frequency (solid line), which is much closer to the measured one (dashed line). **C** Similar as for the 50 Hz stimulus used in Fig. 6.8, the threshold of the adapted f-I-curve adapts quickly to the upper part of the stimulus.

only maps the input $I(t)$ through the onset f-I-curve. Therefore it transmits the stimulus independently of how fast it fluctuates (panel C), resulting in firing frequencies which can vary much faster than the observed firing frequency of the real receptor cell. In fact, the adaptation models are high-pass filters (see page 88). However, fluctuations of the stimulus between two succeeding spikes in general cannot be resolved from the firing frequency (see Fig. 3.7 on page 37). The simplest way to account for this effect is to generate spikes out of the output firing-frequency of the adaptation model (6.7), and compute the final firing frequency from these spikes (such spikes are shown in Fig. 6.10 E). A more continuous way to implement this procedure is the filter (6.8), which is based on the non-leaky phase oscillator (3.2). The fluctuations of the resulting firing frequency are then on a similar time scale as the measured firing frequency.

In Fig. 6.10 E the spike trains simulated by the non-leaky phase oscillator (3.2) and the θ-model (3.22) are directly compared with spike trains of a receptor cell. These are preliminary data and still have to be analyzed quantitatively. Both models produce spike patterns, which match the experimentally measured spikes quite well.

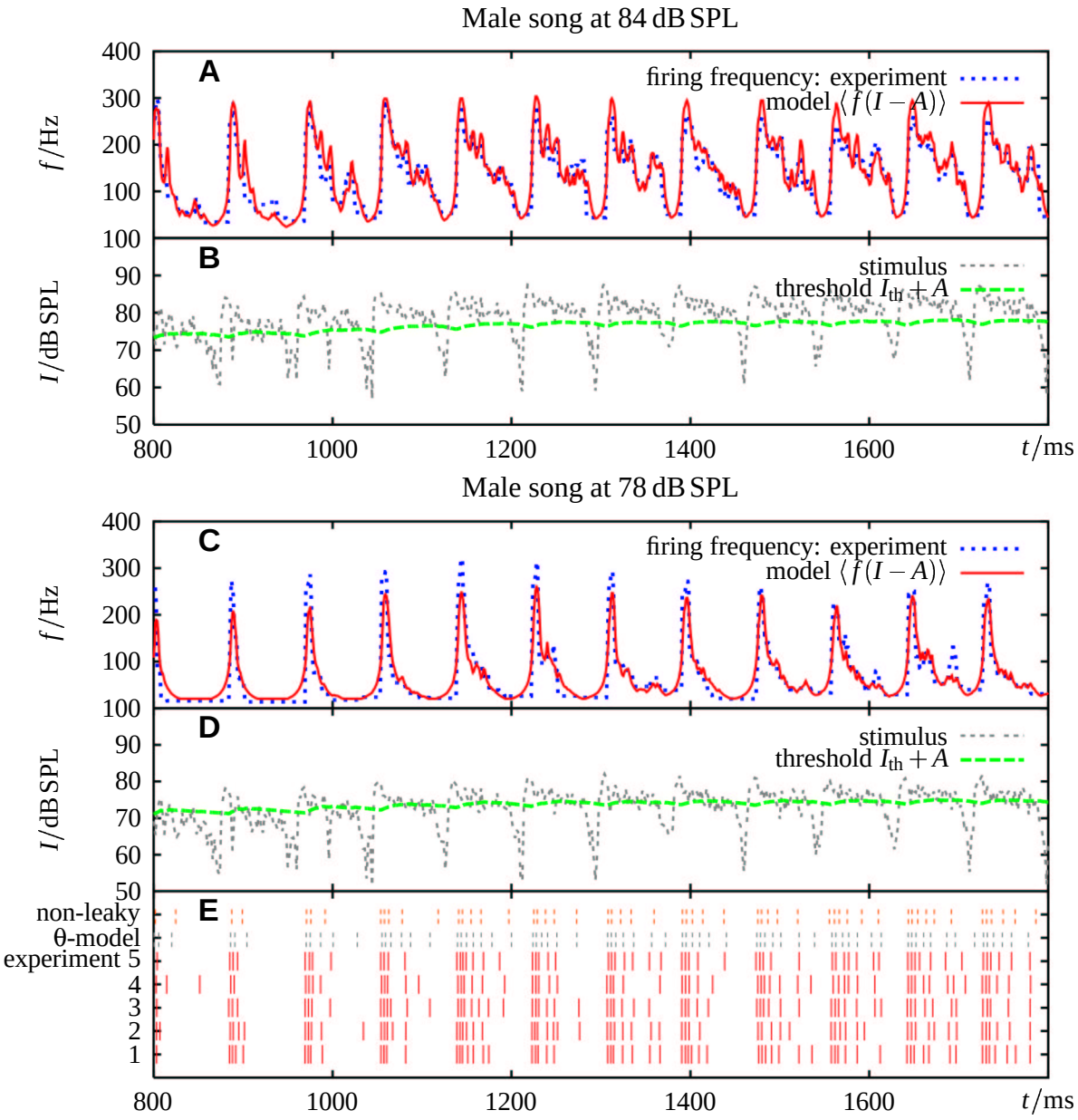

Figure 6.10: PERFORMANCE OF THE ADAPTATION MODEL FOR CALLING SONGS. The stimulus is the envelope of the calling song of a male of the grasshopper *Chortippus biguttulus*, filled with a 5 kHz carrier sound-wave. The song starts at $t = 0$ and lasts 2.7 s. **A** The response of the same receptor cell as in Fig. 6.8 (dashed line) to the song with its mean intensity during the loudest syllables at 84 dB SPL. The measured firing frequency is predicted with high accuracy by the firing frequency of the adaptation model (6.7) smoothed by (6.8). The prediction error (6.9) for the entire song is 11 %. Without including adaptation into the model, i.e. just mapping the stimulus through the onset f-I-curve, the prediction error is 278 %. **B** The stimulus (solid line) in comparison with the threshold of the adapted f-I-curve (dashed line). The actual threshold follows the slow increase of the stimulus intensity. **C & D** Same as in A for the song with mean intensity 78 dB SPL, which was more closely to the neuron's threshold at $I_{\text{th}} = 69$ dB SPL. The prediction error of the model is 14 %. Without adaptation it is 351 %. **E** The five spike trains obtained experimentally from the receptor cell (lower five rows) and the spike trains simulated with the non-leaky phase oscillator (3.2) and the θ-model (3.22).

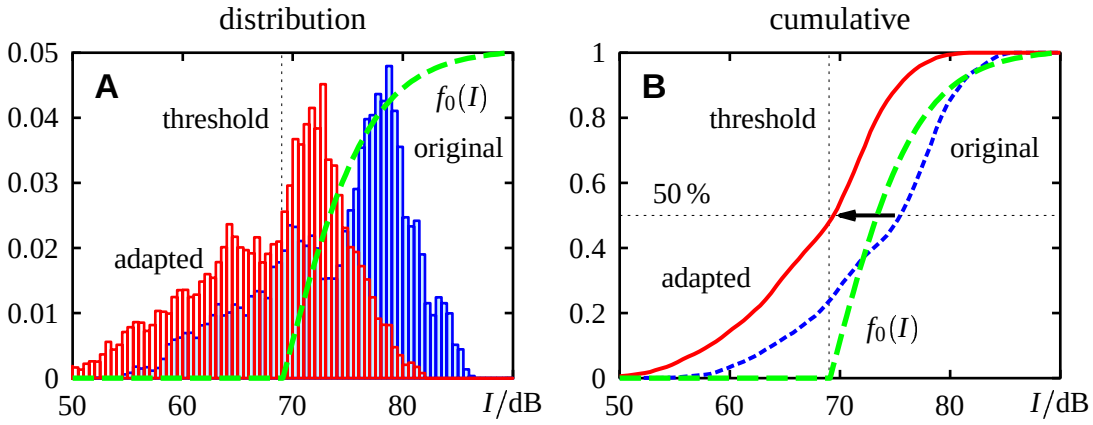

Figure 6.11: DISTRIBUTION OF STIMULUS AMPLITUDES COMPARED TO THE NEURON'S f-I-CURVE. **A** The histogram with its peak to the right is the amplitude distribution of the white-noise stimulus from Fig. 6.8. Adaptation dynamically shifts the neuron's f-I-curve. The distribution of the stimulus the neuron "sees" is therefore different. The amplitude distribution with the peak to the left is obtained from the stimulus minus the state of adaptation $A(t)$. For comparison the onset f-I-curve is drawn (dashed line). **B** Same as in A with the cumulatives of the two amplitude distributions. Since for the white-noise stimuli the state of adaptation is most of the time approximately constant, the cumulative of the original stimulus is mainly shifted to the left. In this example the neuron adapts so that about one half of the stimulus is transmitted, while the lower half does not evoke any response, since it is below threshold.

6.4 Discussion

Receptor neurons of locusts were subject of many studies during the past five decades. The work of Suga (1960), Michelsen (1966), Römer (1976), and Sippel & Breckow (1984) already showed that these neurons exhibit spike-frequency adaptation to constant stimulation. However, this was never examined quantitatively from a dynamical point of view. A test for class-I or class-II dynamics of a spiking cell was so far never addressed with the measurement of phase-resetting curves.

Class-I or class-II neuron?

To decide whether a neuron is a class-I or a class-II neuron, the properties of its f-I-curve, latencies, and phase-resetting curve can be used as summarized in chapter 2. All these properties measured in the auditory receptor neurons support that they are class-I neurons. The receptor cells can fire with arbitrary low firing frequencies. However, for two reasons this is not a strong argument. First, it is hard to measure arbitrary low firing frequencies experimentally. Very long stimuli are needed to test for frequencies below about 10 Hz. Spontaneous activity observed in some cells sets a lower limit to firing frequencies. Second, even a class-II neuron can exhibit class-I f-I-curves, if the discontinuity of its f-I-curve is smeared out by noise. Indeed, the spike pattern of auditory receptor cells to constant stimuli is very noisy. For intermediate firing frequencies the CV (standard deviation of interspike intervals divided by their mean) measured during steady-state is high (about 0.5).

Latencies and phase-resetting curves are much stronger cues. The latencies of the first

spike after stimulus onset can be arbitrary long for stimulus intensities close to threshold (Fig. 6.3 B). Furthermore, the latencies are of the order of magnitude of the corresponding interspike interval of the onset f-I-curve. Note that from the measured latencies the latency of the system has to be subtracted, i.e. the time of the transduction process plus the time the spikes need to travel down the axon to the microelectrode. For receptor neurons at room temperature this system latency is about 6 – 7 ms. For receptor neurons heated to 35 °C the system latency was not measured. Since the minimal latencies measured at this temperature were about 4 ms, the system latency has to be shorter to ensure causality. Without knowing the exact value of the system latency it cannot be decided whether the latencies are longer or shorter than the corresponding interspike intervals. This is an interesting issue for the performance of the phase oscillators from chapter 3.

Due to the high variability of the interspike intervals even in the steady-state (after more than 200 ms) the resulting data of the phase-shift measurements were very noisy, too (Fig. 6.7 B). However, the median values reveal a monophasic phase-resetting curve of a class-I neuron. Phase-resetting curves were measured at room temperature, to have a steady-state firing frequency that is not too high. The shortness of the perturbations is limited by the period of the carrier sound wave. For low-frequency receptors stimulated at their best frequency the duration of one oscillation is in the range of 0.2 – 0.4 ms. Perturbations consisting of two oscillations make about one twentieth of an interspike interval at 100 Hz firing frequency. Therefore the firing frequency should not be higher. On the other hand, the variability (CV) of the interspike intervals increases with decreasing firing frequency (not shown). Thus, measuring the phase-resetting curves at room temperature and firing frequencies of about 100 Hz seemed to be a good compromise.

Properties of f-I-curves

In previous electrophysiological studies of receptor cells, f-I-curves were measured as the mean spike-count per the entire duration of the stimulus (ranging from 10 to 1000 ms). If short stimuli of less than about 20 ms were used, such f-I-curves are close to the onset f-I-curve. The longer the stimuli are, the more these f-I-curves are dominated by the steady-state f-I-curve. However, the distinction between onset and steady-state f-I-curves is necessary to quantify the properties of spike-frequency adaptation and to distinguish between transducer and encoder adaptation (see chapter 4).

The onset f-I-curve $f_0(I)$ is the result of the transduction of the intensity I of the sound wave into a conductance change $g(I)$ of the receptor membrane and of the processes generating spikes:

$$f_0(I) = f(g(I)) \,, \tag{6.11}$$

where $f(g)$ is the dependence of the firing frequency on the conductance g, which is a property of the spike generator. The transduction of the sound wave $g(I)$ most probably is a sigmoidal function. At some intensity I equal to or below the threshold of the onset f-I-curve, $g(I)$ activates and it saturates at a higher intensity. Since the receptor cells are class-I neurons, the transformation of the conductance into spikes $f(g)$ is expected to be approximately a square-root function

$$f(g) \approx c\sqrt{g - g_{\text{th}}} \,. \tag{6.12}$$

Important is that $f(g)$ does not saturate for arbitrary high conductances g. The f-I-curves of different neurons measured with current injections indeed do not saturate at plausi-

ble firing frequencies (Madison & Nicoll, 1984; Lanthorn et al., 1984). Therefore the observed saturation of the onset f-I-curves has to be attributed to the transduction process $g(I)$. Note also, that the f-I-curves of the receptor neurons are remarkable similar to the simple model for encoder adaptation shown in Fig. 4.8, where such an saturating transduction is implemented.

As shown in Fig. 6.3 D the slope of the onset f-I-curves increases with increasing threshold intensity. Imaizumi & Pollack (2001) reported similar findings in auditory receptor neurons of the cricket *Teleogryllus oceanicus*. This might be an effect of the logarithmic decibel scale. Sound waves are pressure waves with an amplitude p. The intensity measured in dB SPL (decibel sound pressure level) is defined as

$$I/\mathrm{dB\,SPL} = 20\log_{10}\frac{p}{p_0}\,, \tag{6.13}$$

where p_0 is the reference pressure of $p_0 = 20\,\mu\mathrm{Pa}$, which corresponds to the human hearing threshold at 1 kHz. Assume the transducer properties of all receptor cells to be similar except for their sensitivity, i.e. the spike generation $f(g)$ is the same as well as the shape of the transduction function $g(I)$. Thus, the width of the dynamic range of the transduction $g(I)$ is assumed to be the same for all receptor cells. However, is this width measured in decibel, pressure amplitude, or squared pressure-amplitude? Obviously the data in Fig. 6.3 C & D cannot be explained with a constant width measured in decibel.

Alternatively, the width of the transduction $g(I)$ could be a constant difference in sound pressure Δp. Then the width ΔI measured in decibel is

$$\Delta I = 20\cdot\log_{10}\left(1+\frac{\Delta p}{p_0}10^{-I_0/20}\right)\,, \tag{6.14}$$

which depends on the threshold intensity I_0 of the transduction. The corresponding slope $s = f_{\max}/\Delta I$ with $f_{\max} = 570\,\mathrm{Hz}$ was fitted into the data of Fig. 6.3 D. It describes the data well, but more data are needed to verify this relation especially at high threshold intensities. In Fig. 6.3 E f-I-curves resulting from this relation are sketched. A similar relation can be obtained for a constant width measured in squared pressure amplitudes. The resulting function is very similar to (6.14) and the data do not allow to distinguish between these two alternatives. In a companion work, Gollisch et al. (2001) showed that the variance of the sound pressure-wave, i.e. the squared pressure amplitude is the relevant signal for the receptor cells.

An other hint concerning the time scales of the transduction process comes from the measurements of phase-resetting curves. Perturbation stimuli much shorter than the time constant of the transduction process may be filtered out and may have no or only a little effect on the spike generator, since the tympanum (Schiolten et al., 1981; Breckow & Sippel, 1985) and the transduction process constitute a low-pass filter. However, even perturbations as short as one oscillation of the carrier sound-wave (0.3 ms) still have an effect. Therefore, the cut-off frequency of this low-pass filter cannot be much lower. This is in good agreement with the work of Schiolten et al. (1981), who measured the damping time constant of the tympanum to be 90 µs. The fact that even a single oscillation of the sound wave has an effect on the following spike does not imply that the spikes lock on the oscillations of the sound wave. The timing of the spikes is only slightly advanced by the oscillations. Suga (1960) and Hill (1983a) already showed that the spikes of auditory receptor neurons of locusts do not lock on the oscillation of the stimulating sound wave.

Adaptation mechanisms

There are mainly two possibilities to explain the spike-frequency adaptation of the auditory receptor cells. First, the transducer process of the sound wave may adapt in dependence on the sound intensity (transducer adaptation). Second, additional ionic currents adapt the spike generator in dependence on the output firing frequency (encoder adaptation).

The decrease of the effective adaptation time-constants for decreasing intensities and the time constant of recovery from adaptation in the order of the maximum adaptation time constants (Fig. 6.4 C), is a strong hint for encoder adaptation. For transducer adaptation such a strong dependence of the effective time constants on intensity in relation to the f-I-curves is not expected (recall Fig. 4.11 on page 82).

The decreasing maximum firing frequency of the adapted f-I-curves (Fig. 6.6), and the fact that their dynamic range is always below the intensity, where the onset f-I-curves saturates, is in accordance with the view of equation (6.11), where encoder adaptation acts subtractive on the transducer conductance g and not on the stimulus. Encoder adaptation does not influence the transduction of the sound wave into a change of a conductance. Therefore, the intensity, where the onset and the adapted f-I-curves saturate, remains the same, independently of the state of adaptation. See also Fig. 4.8 on page 76 for an illustration of this issue.

In summary, spike-frequency adaptation in auditory receptor cells of locusts on timescales below 100 ms is caused by encoder adaptation. Various mechanosensory receptor cells of invertebrates were investigated using current injections. By this direct method encoder adaptation was found to be the main contribution to the observed spike-frequency adaptation, too (French, 1989b,a; Purali & Rydqvist, 1998; Torkkeli et al., 2001).

There is an additional adaptation process, which was not investigated in this study, acting on much slower time scales of several seconds (Michelsen, 1966). This type of adaptation seems to shift the adapted f-I-curves below the saturation of the onset f-I-curve, as can be seen for example in Fig. 6.4 D. Thus, this slow adaptation may take place in the transducer process.

Model for spike-frequency adaptation

Encoder adaptation acts subtractive on the input current, which is approximately proportional to the input conductance $g(I)$, as derived in chapter 4. Thus,

$$f(t) = f(g(I) - A) \tag{6.15}$$

would be the right equation for encoder adaptation in the receptor cells. However, the exact form of $g(I)$ is not known, but it is very likely that the function $g(I)$ is approximately linear near the threshold of the onset f-I-curve. In this linear regime adaptation acts also subtractive on the input directly

$$f(t) \approx f_0(I - A)\ . \tag{6.16}$$

The model (6.7) used here is a variant of the original model (4.22) of encoder adaptation. It accounts phenomenologically for the observed spike-frequency adaptation. The assumption of this model that $A_\infty(I)$ is proportional to the firing frequency f is at least satisfied for the linear part of the steady-state f-I-curve, since such linear adaptation keeps

linear f-I-curves linear as shown in section 4.3.2 on page 85. However, the model (6.7) does not reproduce the decreasing saturation of the adapted f-I-curves. It is valid only for stimuli which are close to the receptor's threshold. This restriction is not a problem for the examples shown in Fig. 6.8, Fig. 6.9, and 6.10, since these stimuli stay in the lower part of the f-I-curve.

Adaptation and the distribution of stimulus amplitudes

By means of the adaptation model (6.7) the time course of the state of adaptation, which shifts the neuron's f-I-curve, for particular stimuli was accessible. The effective stimulus for a specific neuron has been calculated by subtracting the state of adaptation from the stimulus intensity (Fig. 6.11). Therefore, it was possible to compare the distribution of stimulus amplitudes with and without adaptation with the neuron's onset f-I-curve. Adaptation made the stimuli for the neuron effectively softer without changing the shape of the amplitude distribution too much. Thus, spike-frequency adaptation only compensates for the mean intensity of a stimulus. It does not change the slope of the f-I-curve in order to adapt to the standard deviation of the stimulus, as proposed for modulatory mechanisms (Shin et al., 1999). Note that these results depend on the time scales of the stimulus in comparison to the adaptation time constant. The stimuli of the examples shown have most of their power in frequency components which are much faster than the adaptation process. The situation is different for stimuli which vary on a time scale which is comparable to the spike-frequency adaptation.

Song recognition

What is the role of spike-frequency adaptation in auditory receptor neurons for the transmission of calling songs of the grasshoppers? Adaptation shifts the neuron's f-I-curve according to the mean intensity of the stimulus. First, this keeps the louder parts of the stimulus in the dynamic range of the receptor neuron. Thus, the substructure of syllables of the songs can be encoded in different firing frequencies. Second, gaps in the signal become more distinct since softer parts of the stimulus are effectively shifted below the neuron's threshold. This helps to suppress the influence of background noise on the detectability of gaps (c.f. chapter 4). Third, the neuron recovers from adaptation during pauses in the signal. Thus, the onset of the next syllable is more pronounced. However, the capabilities of the receptor neurons to adjust their f-I-curve according to the mean intensity of a stimulus are limited. Their f-I-curves can only be shifted over about 10 dB as shown in the Results. Römer (1976) investigated the distribution of threshold intensities of receptor neurons. The thresholds of low-frequency receptors are distributed in three clusters over a range from 20 up to 60 dB. Therefore, it is likely that there are always some receptors which are stimulated in their dynamic range. It would be interesting to explore how an interneuron which receives input from the receptor neurons uses them. Response properties of such an interneuron are investigated in a cricket species in the next chapter.

6.5 Summary

- Response properties of auditory receptor neurons were studied in *Locusta migratoria*.
- Spike-frequency adaptation in receptor neurons has a maximum effective time constant of about 80 ms.
- The dependence of the effective time constants on stimulus intensity and the time constant of recovery from adaptation, as well as the shape of the adapted f-I-curves in relation to the onset f-I-curve show that spike-frequency adaptation is mainly caused by intrinsic mechanisms of the spike encoder.
- A variant of the model for encoder adaptation (6.7) predicts the firing frequency for arbitrary stimuli with high accuracy.
- The width of the onset f-I-curves decreases with increasing threshold intensity. This probably implies that receptor neurons perceive the amplitudes of sound waves not in logarithmic units.
- Auditory receptor neurons are class-I neurons:
  - They can fire with arbitrary low frequencies.
  - Latencies to the first spike are of the order of magnitude of the corresponding interspike interval from the onset f-I-curve and can be arbitrary long.
  - Perturbations always advance the following spike. The resulting phase-resetting curves are similar to the one of the θ-model.
- A single stronger oscillation of the carrier sound-wave is sufficient to advance the following spike.

7

Intensity invariance in a primary auditory interneuron

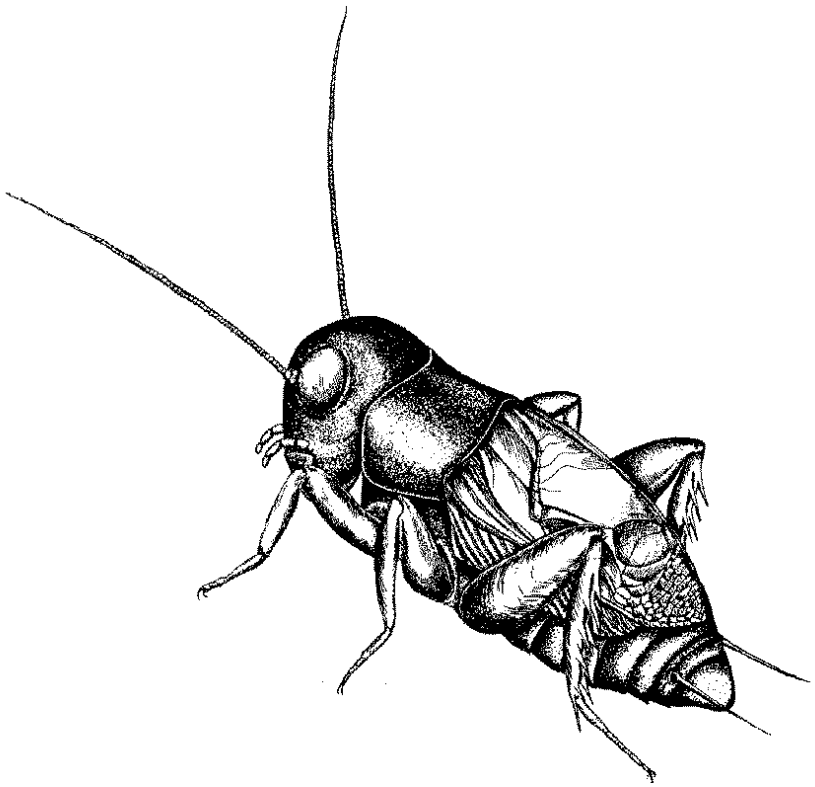

Contents

7.1 Introduction ***138***
7.2 Methods ***140***
Animals *140*
Preparation *140*
Recordings *140*
Stimulation *141*
f-I-curves *141*
White-noise stimuli and pulse patterns *144*
Adaptation model *145*
7.3 Results ***146***
Spike-frequency adaptation *147*
Intensity invariance *149*
Performance of the adaptation model *150*
Transfer function *153*
7.4 Discussion ***153***
Properties of f-I-curves *154*
Possible mechanisms for spike-frequency adaptation *154*
Receptor neurons *155*
Intensity invariance *155*
Pulse patterns *156*
Adaptation model *157*
7.5 Summary ***158***

Cover: The cricket *Gryllus campestris* (drawn by Uta Grünert).

7.1 Introduction

The adaptation models derived in chapter 4 assume that the input is applied directly to the spike generator. The auditory receptor neurons of locusts approximately satisfy this assumption and the adaptation models describe their response properties well, as shown in the previous chapter. Here, the models are tested on the AN1, a first order interneuron of the auditory system of crickets. The response properties of the AN1 are similar to the response properties of the auditory receptor neurons which have direct connections to the AN1 (Hennig, 1988). The question is whether the adaptation models are still capable to describe the activity of this interneuron, or whether the transformation of the stimulus by the receptor cells, the synapses, and the dendritic tree exhibits an additional dynamics

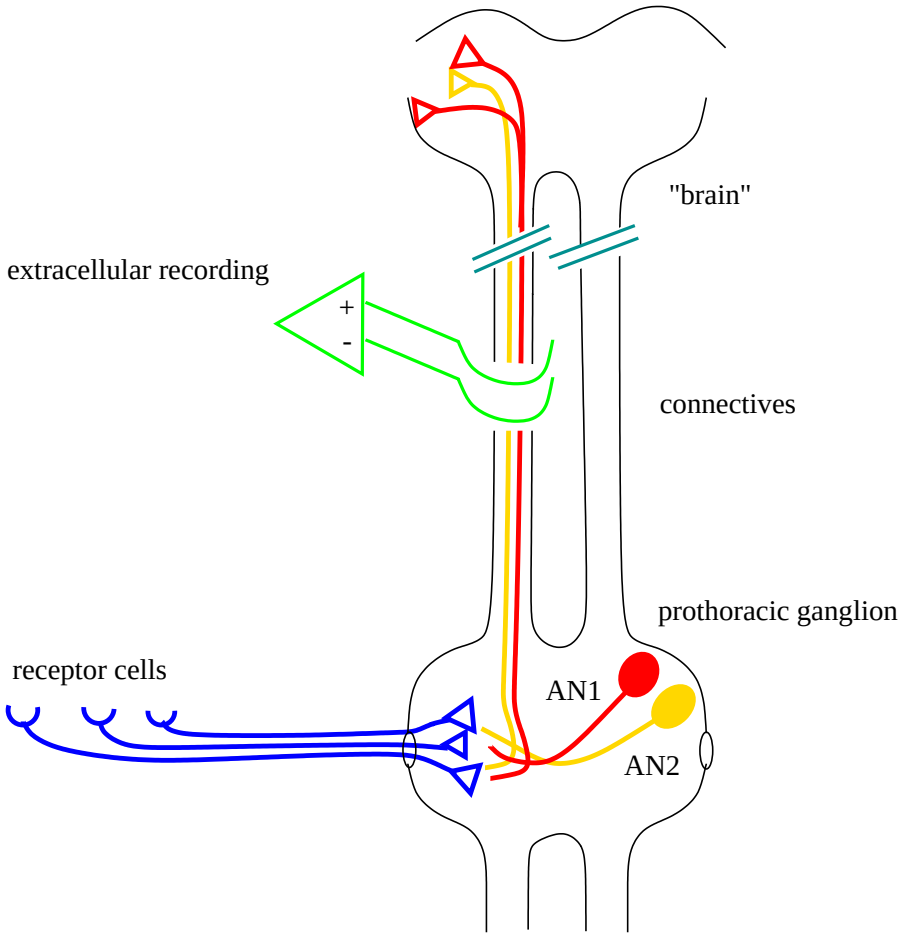

Figure 7.1: THE AUDITORY SYSTEM OF CRICKETS. Receptor cells transform the sound-wave into spikes. Their axons project into the prothoracic ganglion and make contact to several interneurons. The AN1 and the AN2 are ascending interneurons which transmit the information into the cricket's "brain". For the extracellular recordings the connectives are cut.

which cannot be described by the models. For that purpose, extracellular recordings of the AN1 were performed in the cricket *Teleogryllus oceanicus*.

The calling song of this cricket species can last for minutes or even hours. The structure of these songs is determined by the duration of syllables and pauses, which are of the order of magnitude of 10–100 ms. Crickets recognize their conspecific partners based on these fast patterns (Hennig & Weber, 1997).

Auditory receptor afferents project into the prothoracic ganglion (Esch et al., 1980), where they connect to several interneurons directly (Hennig, 1988). From the ascending interneurons the AN1 is most sensitive. In addition, the AN1 is a bottleneck for the information transmission about the recepted calling songs to the brain (Schildberger & Hörner, 1988). The auditory system of the cricket is sketched in Fig. 7.1.

On condition that one of the adaptation models from chapter 4 explains the response properties of the AN1, the signal-transmission properties of this interneuron can be analyzed quantitatively. The high-pass properties of adaptation would support to compensate for varying intensities of the calling songs perceived from different distances.

7.2 Methods

All experiments were performed by R. Matthias Hennig, Berlin.

Animals

Laboratory-reared *T. oceanicus* females were used in all experiments.

Preparation

Both pairs of wings and the meso- and metathoracic legs were removed and the animal was fixed ventral side uppermost to a platform. The prothoracic legs with the ears were waxed to pins at the coxae and the tarsi in a normal walking position. The ventral nerve cord was cut at both sides of the prothoracic ganglion in order to reduce background activity from ascending and descending neurons. See Hennig (1988) for a more detailed description.

Recordings

Extracellular hook-electrode recordings were made from the connectives between the prothoracic and subesophageal ganglia that also contain the axons of the AN1 and of the AN2, another ascending auditory interneuron. The electrodes were electrically isolated with a vaseline – mineral oil mixture. Two tungsten wires were used as electrodes in differential mode. The voltage trace was digitized with an AD-board (National instruments: AT-MIO-16E-1 using 12 bit) at 10 kHz sampling rate and stored on disk. Spikes were detected offline using Labview software (National Instruments). For the AN1 every event with its peak in an appropriate voltage range was counted as a spike. Spikes less than 2.8 ms apart from the preceeding spike were discarded to minimize background activity. Interspike intervals shorter than 2.8 ms very likely originate from the detection of spikes from other neurons, since previously reported firing frequencies of the AN1 were below the corresponding maximum of 357 Hz (Schildberger & Hörner, 1988). Occasionally high activity in the connectives caused by breathing of the animal induced a strong increase in detected spikes probably not due to AN1- or stimulus related activity. Such spike trains were discarded from the analysis. The recordings were necessarily noisy, since the AN1 is a small neuron in the large connective, which contains axons of more than 1000 cells. Furthermore, the activity of the AN2 may mask the AN1 activity with its larger spikes, especially at high intensities. As illustrated in Fig. 7.2 B the interspike-interval distribution of the background activity is close to an exponential distribution, which is expected for a Poisson spike train (Dayan & Abbott, 2001). The time courses of the firing frequency averaged from upto 25 repetitions of the same stimulus still were very noisy (see Fig. 7.2 and Fig. 7.3 for examples).

Out of 24 cells $n = 13$ cells were used for the analysis. The remaining cells were excluded since either the background activity of the recording was above 50 Hz or the onset f-I-curves (see below) were not stable throughout the experiment. The background activity before stimulus onset of the cells included into the analysis was still above 30 Hz.

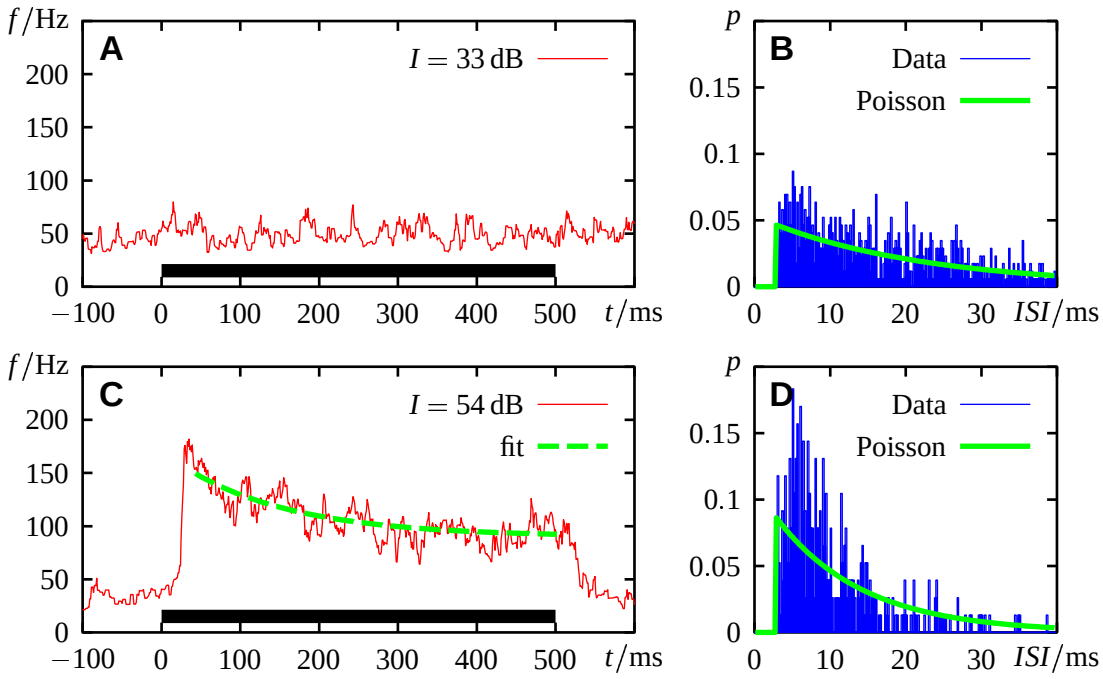

Figure 7.2: RESPONSE OF AN AN1 TO CONSTANT STIMULATION. The left column (**A & C**) shows the mean firing frequency of a cell evoked by stimulation with a sound wave of constant amplitude and carrier frequency 4.5 kHz as indicated by the bottom bar. The spikes evoked by 22 repetitions of the same stimulus were used to calculate the averaged time course of the firing frequency. The corresponding interspike-interval histograms (right column, **B & D**) are compared with the one of a Poisson spike-train of equal firing rate and refractory period (2.8 ms) (solid line). **A** The extracellularly recorded response to a stimulus intensity of $I = 33$ dB SPL. The activity is most probably due to the detection of spikes not originating from the AN1. **B** Most of the interspike intervals are in the tail of the corresponding exponential distribution of a Poisson spike-train. The coefficient of variation (standard deviation of the interspike intervals divided by their mean) is $CV = 0.75$. **C** At a sound level of $I = 54$ dB SPL the cell clearly responds with a firing frequency of about 170 Hz. It decays back to 100 Hz with a time constant of $\tau_{\text{eff}} = 166$ ms. **D** The interspike-interval histogram now has a distinct peak between 5 and 10 ms, but still has a CV of 0.7. The tail of the distribution probably originates from failures of the detection of AN1-spikes.

Stimulation

The recording setup was lined with sound-absorbing foam to reduce echos. An advantage of the extracellular recordings is that the recording chamber is free of large obstacles like a micro-manipulator, which further enhances the quality of the sound stimulation. The stimuli were multiplicated analogically with a carrier sine-wave of frequency 4.5 kHz, which corresponds to the calling song of *T. oceanicus* and is at the same time the best frequency of the AN1 (Hennig, 1988). Rectangular and step-like stimuli had rise and fall times of 2 ms. Stimuli were presented frontal by a dynamical loudspeaker at a distance of 50 cm.

f-I-curves

The onset and steady-state f-I-curves, $f_0(I)$ and $f_\infty(I)$, are important to characterize spike-frequency adaptation (see chapter 4). Both f-I-curves were measured once at the

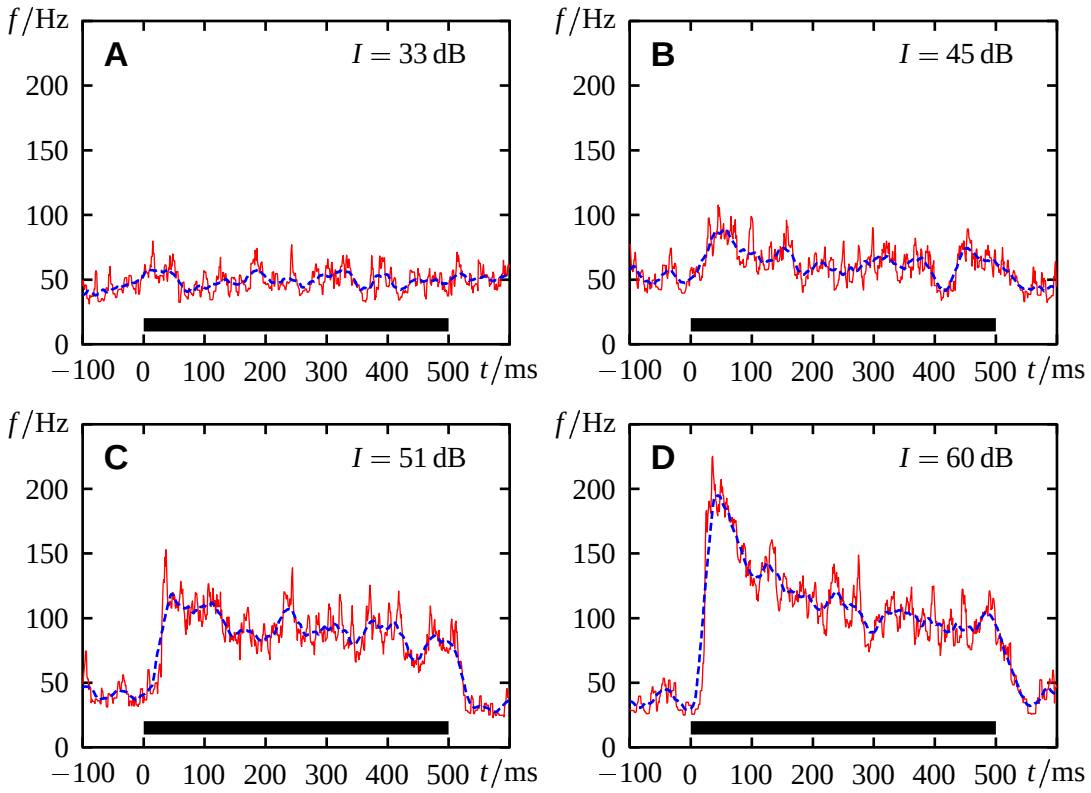

Figure 7.3: RESPONSES OF AN AN1 TO DIFFERENT INTENSITIES. **A, B, C & D** The time courses of the firing frequency (solid line) evoked by constant stimuli (bottom bar) with different intensities as indicated (same cell as in Fig. 7.2). Note the prominent adaptation at $I = 60\,\mathrm{dB}$. The firing frequency smoothed with a 30 ms averaging-window is overlaid (dashed line).

beginning and once at the end of an experiment. Rectangular stimuli of 500 ms duration were applied at intensities every 3 dB from 30 to 93 dB SPL. Each stimulus was repeated 25 times, the pauses between the stimuli were 1.5 s long. Single spike trains were discarded in order to control for the quality of the recording, if their mean firing frequency during 100 ms before stimulus onset was greater than the mean firing frequency of the 25 trials in this interval plus 1.8-times the standard deviation. The time course of the firing frequency was calculated every millisecond as the trial-averaged inverse interspike interval (equation (5.5) on page 105). The maxima of the time courses smoothed with a rectangular 30 ms averaging window were taken for the onset f-I-curve (see Fig. 7.3 for such smoothed firing frequencies). For the steady-state f-I-curve the mean firing frequencies from 350 to 450 ms after stimulus onset were calculated directly from the interspike intervals in this range. In order to obtain the effective time constant of spike-frequency adaptation a single exponential function was fitted into the data (Fig. 7.2 C).

The resulting f-I-curves were fitted by a rectified hyperbolic tangent

$$f(I) = \begin{cases} f_{\min} + (f_{\max} - f_{\min}) \tanh(k(I - I_{\mathrm{th}})) & ; \quad I > I_{\mathrm{th}} \\ f_{\min} & ; \quad I \leq I_{\mathrm{th}} \,. \end{cases} \tag{7.1}$$

The spontaneous activity for sub-threshold stimuli $f_{\min}$ was set to the average value of all sub-threshold steady-state responses. The "maximum firing frequency" $f_{\max}$ was set to the average over three data points around the one with the largest measured firing frequency. The threshold intensity I_{th} was set to the intensity of the largest intensity point

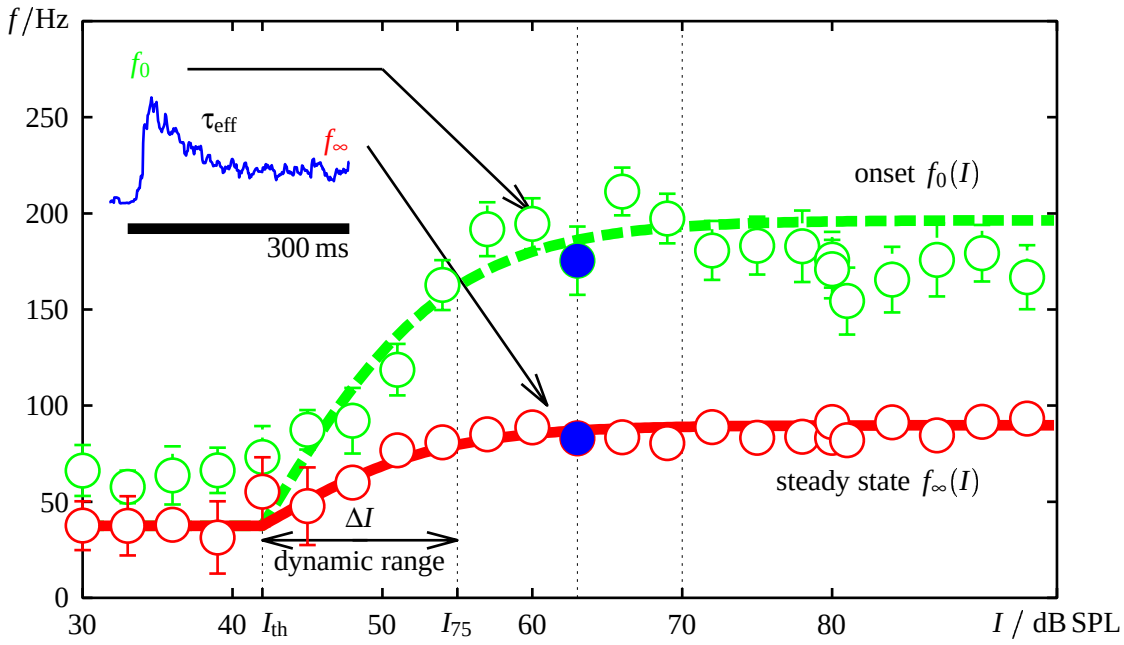

Figure 7.4: f-I-CURVES OF AN AN1. From the firing frequencies evoked by constant stimuli in Fig. 7.3 the onset and the steady-state f-I-curve, $f_0(I)$ and $f_\infty(I)$, were constructed. The open circles denote the mean values of the firing frequency and the error bars the standard error of the mean ($n = 22$). The inset shows the time course of the firing frequency evoked by a constant stimulus of $I = 63$ dB SPL. The initial peak response f_0 approximately resembles the properties of the unadapted neuron. The fitted lines concentrate on the dynamic range of the f-I-curves and neglect the decrease of the onset f-I-curve $f_0(I)$ at high sound levels (above 70 dB). The dynamic range ΔI of the onset f-I-curve is marked by the horizontal arrow and is defined as the intensity I_{75} that evoked 75 % of the maximum response minus the threshold intensity I_{th}. The high firing frequencies of the onset f-I-curve data below threshold I_{th} are an effect of noise, since they are measured as the peak response of the smoothed time course of the firing frequency (compare with Fig. 7.3).

that evoked less than 10 % of $f_{\max} - f_{\min}$ above $f_{\min}$ of the steady-state response. The remaining slope factor k was fitted using the Levenberg-Marquardt method as described in Press et al. (1992). Data upto the maximum response were used for the fit. Thus, the observed decrease of the firing frequency at high intensities was neglected (Fig. 7.4). The slope s of the f-I-curve at threshold I_{th} is given by

$$s = \left.\frac{\mathrm{d}f}{\mathrm{d}I}\right|_{I=I_{\text{th}}^+} = k(f_{\max} - f_{\min}) \,. \tag{7.2}$$

The adapted f-I-curves were measured as described in Fig. 7.5 to further specify the adaptation properties. With a 500 ms stimulus the neuron was adapted to some background intensity I_b. Then the onset response to a different intensity was tested by a subsequent 100 ms stimulus and the cell was adapted back to I_b during the following 300 ms. This was repeated for 12 different test intensities every 3 dB. Five background intensities were used: $I_b = 35$, 47, 59, 71 and 83 dB SPL. The average firing frequencies over the first half of the test stimuli were used to construct the adapted f-I-curves. Again, (7.1) was used as a parameterization of the adapted f-I-curves. $f_{\min}$ and k were taken from the previously measured onset f-I-curve. $f_{\max}$ was set to the average of all the data points at

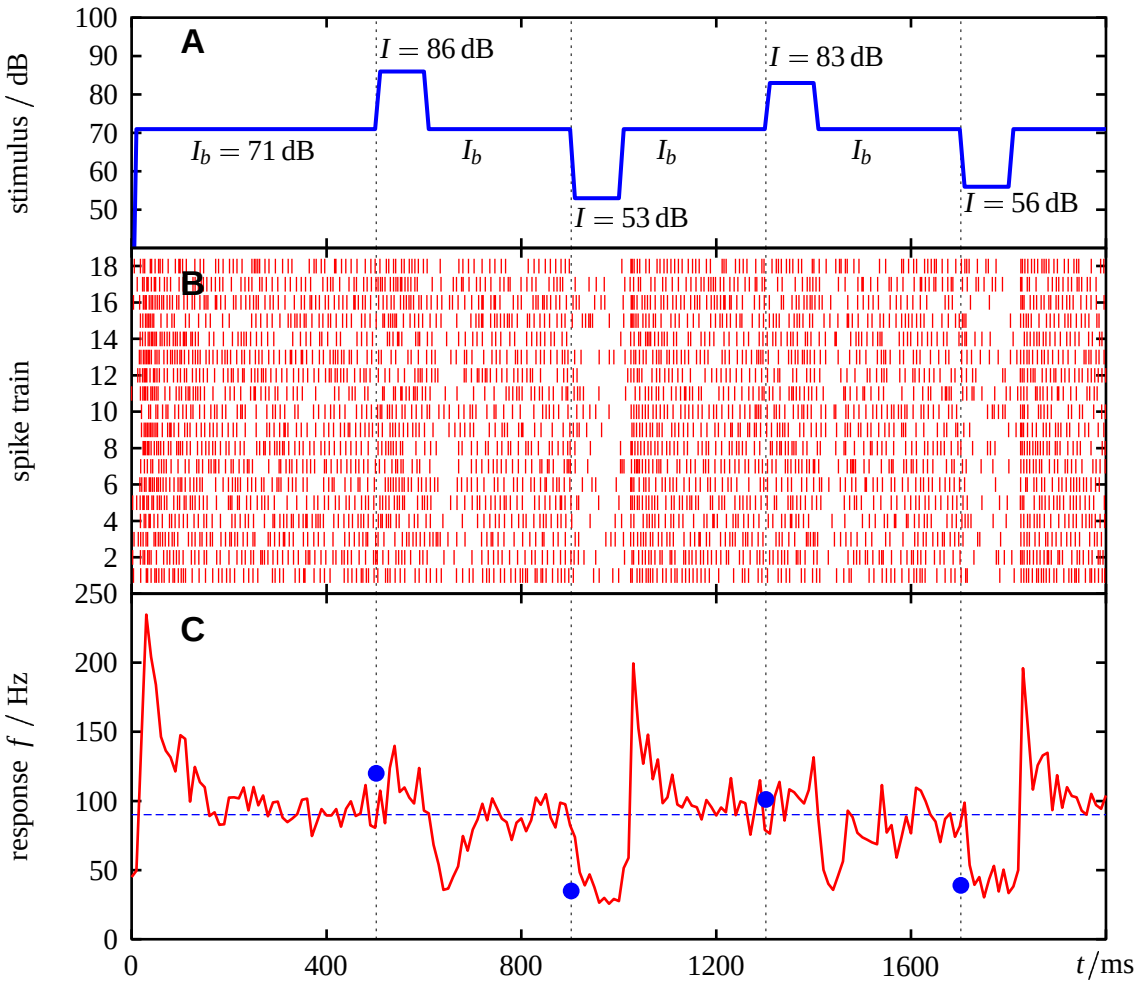

Figure 7.5: MEASURING AN ADAPTED f-I-CURVE. **A** The stimulus used to measure the adapted f-I-curve for the neuron adapted to $I_b = 71\,\text{dB SPL}$. During the first 500 ms the neuron was adapted to the background intensity I_b. Then with a louder stimulus (100 ms, $I = 86\,\text{dB SPL}$) the response of the adapted neuron to this intensity was tested. Again the neuron was adapted to I_b and the response to a lower intensity ($I = 53\,\text{dB SPL}$) was tested. This procedure was repeated for different test intensities in an alternating order. The entire stimulus was 4.8 s long and tested for 12 different intensities (every 3 dB). **B** The 18 spike trains evoked by such a stimulus. **C** The time course of the firing frequency calculated from the spike trains. Note that the response is delayed for about 10 ms due to latency of the entire system. The mean values of the responses during 50 ms after onset of the test stimuli plus latency (dots) were used for constructing the adapted f-I-curve (see Fig. 7.7 lower left panel). The horizontal line marks the averaged steady-state response to the background intensity.

the highest intensities measured whose firing frequency decreased with intensity. Finally, I_{th} was fitted to the data.

White-noise stimuli and pulse patterns

To investigate the dynamics of adaptation and to test the adaptation model, the responses to different Gaussian white-noise stimuli and pulse patterns were recorded. Each stimulus was repeated 25 times. The 8 different white-noise stimuli had cut-off frequencies of 50, 100, 200 and 400 Hz, standard deviations of 4 and 6 dB, and a duration of 1000 ms. They

Table 7.1: PROPERTIES OF f-I-CURVES OF THE AN1.

f-I-curve	$f_{\min}$ Hz	$f_{\max}$ Hz	I_{th} dB SPL	I_{90} dB SPL	ΔI dB	s Hz/dB
onset	32 ± 14	200 ± 23	42 ± 6	61 ± 5	12.4 ± 3.0	13.8 ± 3.3
steady-state	32 ± 14	107 ± 17	42 ± 6	73 ± 7	20.1 ± 5.6	3.8 ± 1.1

The table summarizes averaged values of $n = 26$ f-I-curves measured in 13 animals. The minimum and maximum firing frequencies, $f_{\min}$ and $f_{\max}$, and the threshold I_{th} correspond to the parameter in (7.1). Note that both $f_{\min}$ and I_{th} are equal for the onset and steady-state f-I-curve by definition. The initial slope of the f-I-curves is given by (7.2). The intensity where the f-I-curve reaches 90 % of its maximum value is I_{90}. The dynamic range of the f-I-curves, ΔI, is the intensity of 75 % maximum firing frequency minus I_{th}. s is the initial slope (7.2) of the f-I-curves.

were first presented at 80 dB SPL and then at 90 and 70 dB SPL (peak intensities, which is three times the standard deviation of the stimuli above their mean).

All pulse patterns had a duty cycle of 50 % (duration of the syllable as compared to the period), were about 500 ms long and were presented at 80 dB SPL. The durations of syllables and pauses used were 5, 8, 10, 15, 20, 30, 40, and 60 ms.

Between those measurements 10 onset f-I-curves were measured to monitor the stability of the sensitivity of the cell. For this purpose stimuli of 100 ms duration and intensities ranging from 30 to 93 dB SPL in steps of 3 dB were repeated 10 times spaced by pauses of 300 ms duration. The resulting firing frequencies were smoothed with a 30 ms averaging window. From the maximum values the onset f-I-curves were constructed.

Adaptation model

To model the time course of the AN1-response to the white-noise and pulse stimuli, the following phenomenological model was used:

$$\begin{aligned} f(t) &= \frac{f_0(I-A)}{1+\gamma s_0 A} \\ \tau_{\text{eff}}\dot{A} &= \frac{I - f_0^{-1}(f_\infty(I))}{1+\gamma f_\infty(I)} - A\,, \end{aligned} \tag{7.3}$$

where s_0 is the slope of the onset f-I-curve as defined by (7.2). The model (7.3) is the transducer-adaptation model (4.27) extended by a linear γf-term from equation (4.34). The first equation is adopted from the linearized equation for the f-I-curve (4.42) to account for the compression of the adapted f-I-curves as observed in the experiments. Note, that the steady-state f-I-curve of this model is only for $\gamma = 0$ identical to $f_\infty(I)$. For the f-I-curves the parameterization given by (7.1) was used. The measured adapted f-I-curves revealed a value of about 0.002 for γ (Fig. 7.8). See discussion for more details about the model.

With the filter (6.8) (page 121) derived from the non-leaky phase-oscillator (3.2) the firing frequency from the model (7.3) was smoothed. The resulting firing frequency $\nu(t)$ was compared with the experimentally measured firing frequency $f_{\text{exp}}(t)$. The prediction error *p.e.* (6.9) from page 121 is the mean squared difference σ_{diff} of the experimentally

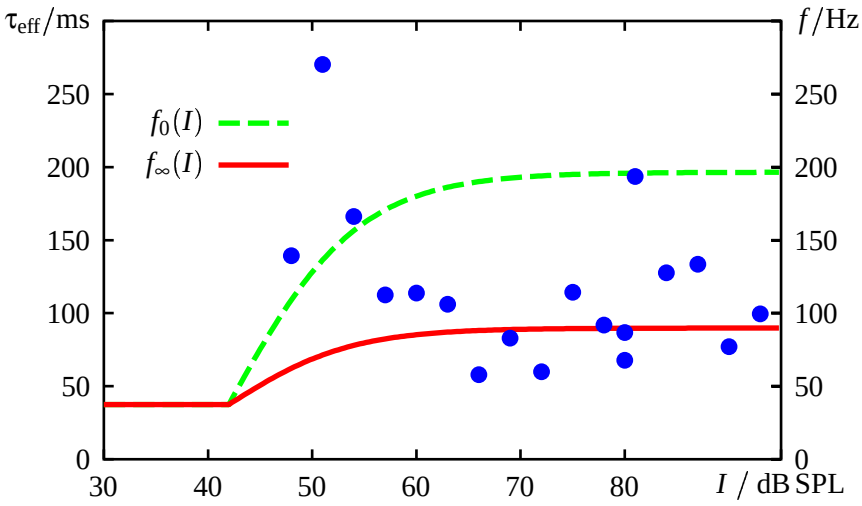

Figure 7.6: TIME CONSTANTS OF ADAPTATION. The effective time constants measured from the decay of the firing frequency as in Fig. 7.2 C for different stimulus intensities (dots). For comparison the fits of the onset and the steady-state f-I-curves from Fig. 7.4 are also shown. Since the data have large errors, the values of the time constants are not reliable. The trend to larger time constants at low stimulus intensities seen here was not observed in most other cells.

measured firing frequency f_{exp} to the firing frequency of the model ν related to the variance σ^2_{exp} of f_{exp}.

The standard deviation σ_{exp} of the firing frequency f_{exp} is a measure for the modulation depth of the response f_{exp} of the neuron. It was used to quantify the intensity invariance of the response f_{exp} to different white-noise stimuli.

In order to asses the prediction error of the model for firing frequencies evoked by pulse-patterns as stimuli, the dependence of the modulation depth σ_{exp} on the length of the syllables and pauses of the pulse patterns used as stimuli is of importance. The basic effect is that during the pauses of duration Δt between the pulses the firing frequency equals $1/\Delta t$ if a spike occurred right at the end of the preceeding syllable and the following spike occurred right at the beginning of the succeeding syllable. Thus, the firing frequency measured between the syllables increases with decreasing duration of the pauses. The corresponding modulation depth of the firing frequency can be estimated roughly as follows. Assume the neuron to fire during a syllable of the same duration Δt as the pauses with a firing frequency f_s. The firing frequency between the pauses equals approximately $1/\Delta t$ as just discussed. Both the syllables and pauses have the same duration Δt and the resulting standard deviation of the firing frequency is then

$$\sigma_{exp} \approx \frac{1}{2}\left(f_s - \frac{1}{\Delta t}\right) . \tag{7.4}$$

7.3 Results

The data from $n = 13$ cells were included in the following analysis. The data shown in the figures are all from the same cell. Its parameters are close to the averaged results as summarized in tab. 7.1.

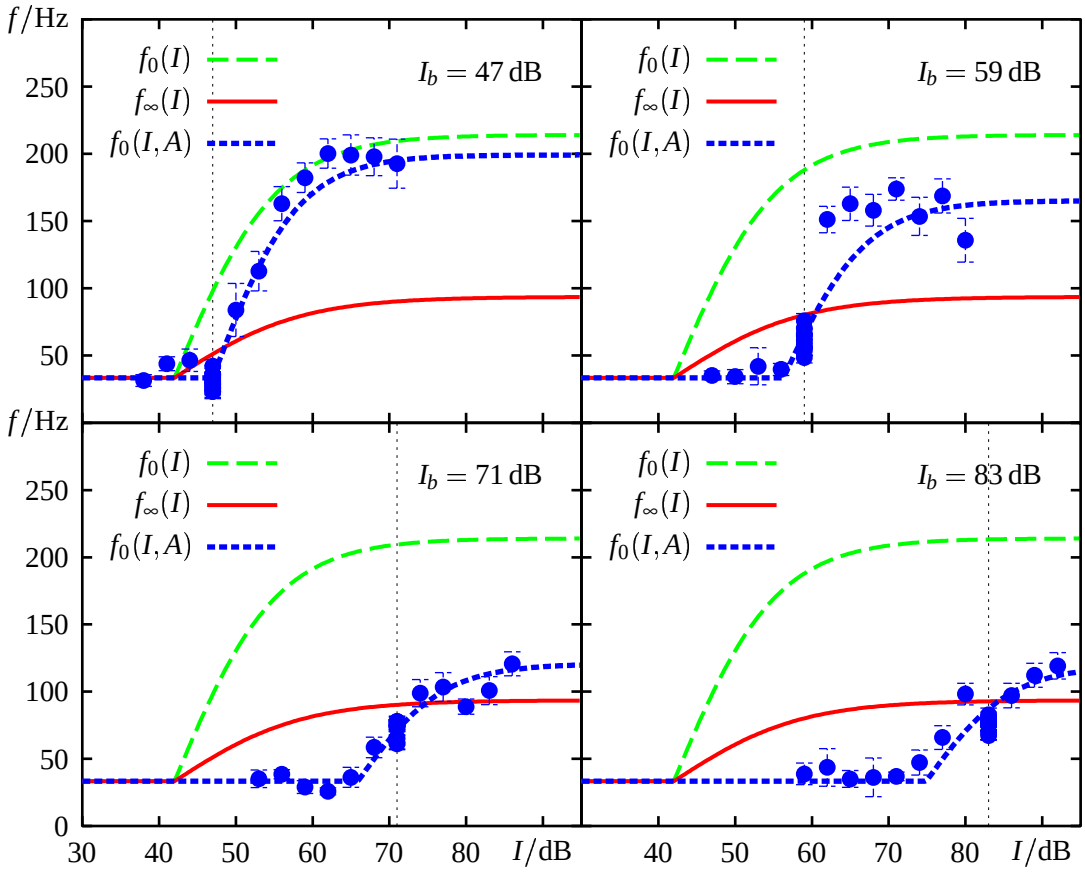

Figure 7.7: ADAPTED f-I-CURVES. With the procedure described in Fig. 7.5 the adapted f-I-curves for different background intensities I_b were measured. Four such curves are shown in comparison with the onset and steady-state f-I-curves from Fig. 7.4. The filled circles denote the mean of the firing frequency and the error bars the corresponding standard errors ($n = 18$). With increasing background intensity I_b these f-I-curves are shifted to higher input intensities. Furthermore their saturation value decreases dramatically and their slope seems to decrease, too. The adapted f-I-curves should cross the stead-state f-I-curve at the background intensity I_b. However, the adapted f-I-curves are always slightly below. This may be attributed to the very long stimulus used for measuring the adapted f-I-curves, during which a slower type of adaptation further desensitizes the neuron.

Spike-frequency adaptation

An example of the time courses of the firing frequencies evoked by stimuli of 500 ms duration and different intensities is shown in Fig. 7.3. Their properties are summarized in the f-I-curves and adaptation time-constants shown in Fig. 7.4 and 7.6, respectively. The data of the peak responses form the onset f-I-curve $f_0(I)$, and the steady-state firing frequencies result in the steady-state f-I-curve $f_\infty(I)$. On average (see tab. 7.1) both f-I-curves have their threshold at $I_{\text{th}} = 42$ dB SPL. The onset f-I-curves raise approximately linearly with a slope of 14 Hz/dB for about $\Delta I = 12$ dB. At $I_{90} = 61$ dB SPL they reach 90 % of their maximum response of $f_{\max} = 200$ Hz. The maximum firing frequency of the steady-state f-I-curves $f_{\max} = 107$ Hz is about half of the onset firing frequency ($f_0/f_\infty = 1.9 \pm 0.2$). The corresponding percentage of adaptation $F_{\text{adap}} = \frac{f_0 - f_\infty}{f_0}$ (Wang, 1998) is 46 ± 6 %. The dynamic range of the steady-state f-I-curves over $\Delta I = 20$ dB is nearly twice as large as the one of the onset f-I-curves, resulting in a slope, which is almost a

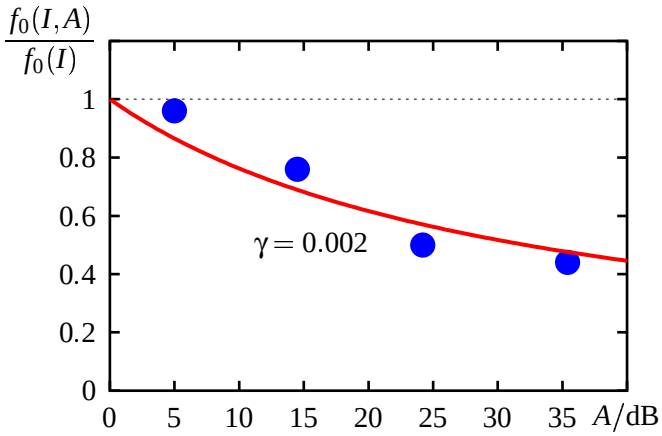

Figure 7.8: COMPRESSION OF ADAPTED f-I-CURVES. From the data of the adapted f-I-curves shown in Fig. 7.7 the compression factor as the ratio of the adapted to the unadapted f-I-curve $f_0(I,A)/f_0(I)$ in dependence on the state of adaptation A was calculated. In order to obtain a value for γ needed for the model (7.3), these data were fitted with the compression factor $1/(1+\gamma s_0 A)$ of the phenomenological adaptation model (7.3) (solid line). Note that this function is bounded to one at $A = 0$. The data revealed $\gamma \approx 0.002$ for most of the cells.

quarter ($1/3.7$) of the one of the onset f-I-curves (tab. 7.1). At around 80 dB SPL the data of the onset f-I-curves decrease again by about several ten Hertz, which very likely can be attributed to the masking of spikes by the AN2.

The effective time constants τ_{eff} of adaptation obtained from the data are very variable, as can be seen in Fig. 7.6, probably due to the noisiness of the data. However, the mean time constant calculated from the averaged time constants of each single cell is nevertheless determined relatively precisely as $\tau_{\text{eff}} = 141 \pm 23$ ms.

In 9 cells the adapted f-I-curves were successfully measured. The adapted f-I-curves of one cell are shown in Fig. 7.7 (see Fig. 7.5 for the stimulus used). What can be clearly seen in all measurements is the shift of these f-I-curves to higher input intensities, even beyond the saturation of the onset f-I-curve (see Fig. 7.7, lower right panel: $I_b = 83$ dB). The maximum possible shift as the difference between the threshold of the adapted f-I-curve measured for the largest background intensity and the threshold of the onset f-I-curve is quite large. On average this difference was 33 ± 8 dB and a maximum shift of 45 dB was observed in two cells. This capability of the AN1 to shift its f-I-curve by more than about 40 dB is the reason for the intensity invariance of its response as discussed below.

The maximum firing frequency of the adapted f-I-curves drops with increasing background intensity to the one of the steady-state f-I-curve. Whether this results from an overall compression of the adapted f-I-curves, or whether it is the consequence of a saturating input, cannot be decided from the data. A compression of the f-I-curves implies a decreasing slope within the dynamic range, while a saturating input leaves the slope untouched. However, especially at high background intensities I_b only three data points determine the slope. The fits in Fig. 7.7 are shifted and scaled versions of the onset f-I-curve, but an unchanged slope fits the data, too (not shown). From the compression of the adapted f-I-curves a value of 0.002 for the factor γ in the model (7.3) was obtained as illustrated in Fig. 7.8.

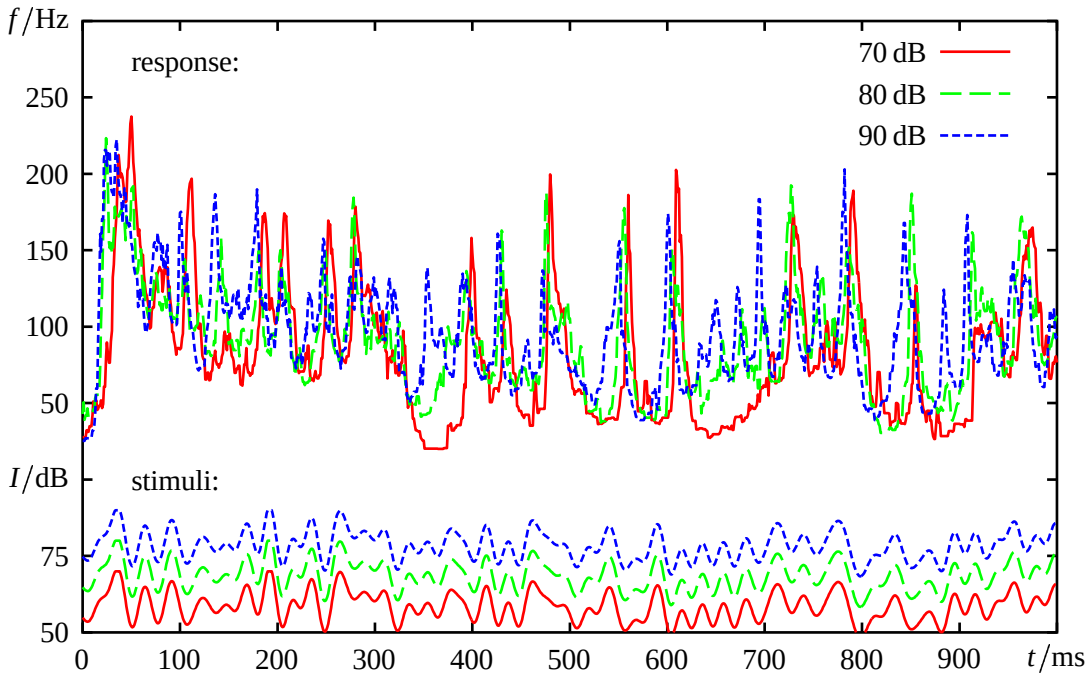

Figure 7.9: INTENSITY INVARIANCE. The time course of the firing frequency evoked by Gaussian white-noise stimuli with cut-off frequency 50 Hz and standard deviation 4 dB of different peak intensities as indicated. All three stimuli were transmitted with very similar modulation depths of the firing frequency. The differences between the three responses are not significant as can be seen in Fig. 7.10.

Intensity invariance

Adaptation can shift the f-I-curve of the AN1 over a wide range of more than 30 dB. This suggests that the time course of the firing frequency is almost invariant of the mean intensity of the stimulus. Thus, the modulation depth of the firing frequency evoked by a fluctuating stimulus is expected to be approximately independent of the mean intensity of the stimulus. If the AN1 would not adapt, i.e. the stimuli would be transmitted via the onset f-I-curve, a stimulus fluctuating for example between 70 and 90 dB would cause a constant firing frequency of about 200 Hz, since it is completely above the dynamic range of the onset f-I-curve. The resulting modulation depth would be close to zero.

This was tested with the white-noise stimuli. In four out of thirteen cells they were successfully applied at three different peak intensities of $I = 70$, 80, and 90 dB SPL as shown in Fig. 7.9 for one particular example. After the neuron was adapted to these stimuli (after about 200 ms), the modulation depths of the evoked firing frequencies were very similar, showing that all three stimuli used the whole dynamic range of the cell.

In Fig. 7.10 this phenomenon is quantified. The modulation depth was calculated as the standard deviation of the firing frequency from 200 ms to 950 ms after stimulus onset. Each value was related to the corresponding stimulus at 70 dB SPL. These relative modulation depths were averaged for each stimulus over the four cells and are shown in the figure. The values are in the range from 80 to 110 %, thus confirming the observation made in Fig. 7.9 that due to spike-frequency adaptation the responses to stimuli of different intensities are similar.

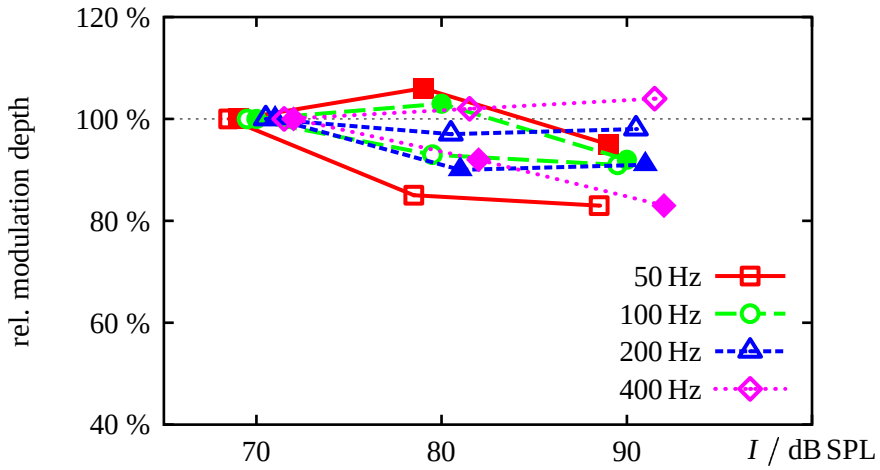

Figure 7.10: RELATIVE MODULATION DEPTHS FOR DIFFERENT INTENSITIES. In four cells Gaussian white-noise stimuli were measured successfully at three different peak intensities (I = 70, 80, and 90 dB SPL, for clarity the data points are jittered around the corresponding intensity). Shown are the averaged modulation depths (standard deviation of the firing frequency from 200 ms to 950 ms after stimulus onset) evoked by the different white-noise stimuli as compared to the one at $I = 70$ dB SPL. The cut-off frequencies of the stimuli were $f_c = 50$, 100, 200, and 400 Hz as indicated. Open symbols denote stimuli with standard deviation $\sigma = 4$ dB, filled symbols such with $\sigma = 6$ dB. On average the standard deviation of the relative modulation depths at 80 and 90 dB SPL was 14 %.

Performance of the adaptation model

After measuring the f-I-curves and adaptation time constant of a cell the parameters of the phenomenological model (7.3) are completely defined. The predicted time course of the model for different Gaussian white-noise stimuli and pulse patterns was compared with experimental data. Two typical examples are shown in Fig. 7.11. A model without adaptation, which just mapped the stimulus through the neuron's onset f-I-curve, predicted the experimentally measured firing frequency much worse (not shown).

In Fig. 7.12 the performance of the model is analyzed quantitatively for the different stimuli. The firing frequency evoked by slow stimuli with a cut-off frequency of f_c = 50 and 100 Hz are better predicted by the model than the response to fast stimuli with $f_c = 200$ and 400 Hz. In addition, the prediction error for the slow stimuli increases with intensity, while for the fast stimuli it slightly decreases.

The firing frequency evoked by pulse patterns with long syllables (≥ 30 ms) is predicted very well (Fig. 7.13). With decreasing duration of the syllables the prediction error increases. However, the absolute deviation σ_{diff} of the measured firing frequency from the prediction is nearly independent of syllable duration, but the modulation depth σ_{exp} of the AN1 response decreases dramatically and becomes even smaller than the deviation σ_{diff}. The decrease of the modulation depth σ_{exp} can be mainly explained by the increasing firing frequency during the pauses due to decreasing duration of the pauses. The graph of the function (7.4), which is a rough sketch of this consideration, is close to the data for durations of the syllables and pauses greater than 10 ms. This simple model fails at shorter syllables, since then only one ore two spikes occur during a syllable and the assumption of a constant firing frequency during the whole syllable is no longer valid.

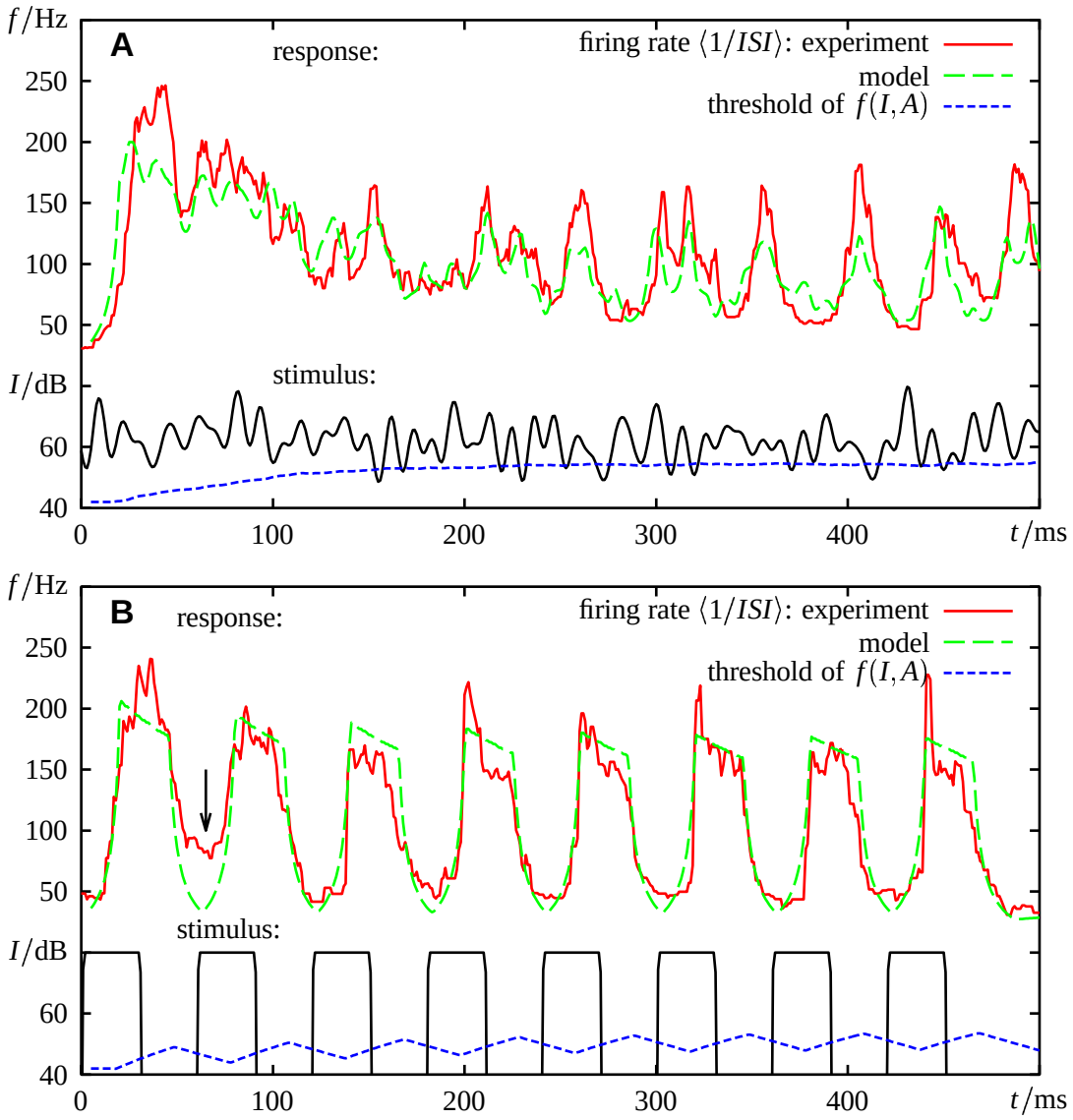

Figure 7.11: PERFORMANCE OF THE ADAPTATION MODEL. Shown is the firing frequency measured experimentally and that predicted from the adaptation model (7.3) for two stimuli applied at 70 dB SPL peak intensity. Superimposed on the stimulus-trace is the threshold of the adapted f-I-curve, i.e. $I_{\text{th}}+A$. Only parts of the stimulus above this line are transmitted. **A** Gaussian white-noise stimulus with a cut-off frequency of 100 Hz and standard deviation 6 dB. After onset of the stimulus the neuron adapts to a steady-state value which remains nearly unchanged throughout the whole stimulus. This is due to the high cut-off frequency compared to the adaptation time constant. The fast fluctuations do not affect the state of adaptation. The root mean squared difference σ_{diff} of the measured and predicted firing frequency was 28 Hz, resulting in a prediction error of 47 %. Without adaptation included into the model ($A(t)=0 \;\; \forall t$) the prediction error is 513 %. **B** A pulse pattern with 30 ms pulses and 30 ms pauses. The cell does not completely recover from adaptation during the pauses. Therefore the mean state of adaptation increases during the stimulus. This helps to suppress the enhanced activity of the neuron during the first pause (arrow). The decay of the response during the pulses is due to the decrease of the saturation value of the adapted f-I-curves. The prediction error was 15 % (59 % for a model without adaptation) at an absolute error of $\sigma_{\text{diff}} = 22$ Hz. The firing frequency during the first pause is usually larger than during the following pauses and is not reproduced by the model (arrow). The peaks in the firing frequency evoked by every second pulse are most likely caused by noise, since this systematic effect was not observed in the recordings of other cells.

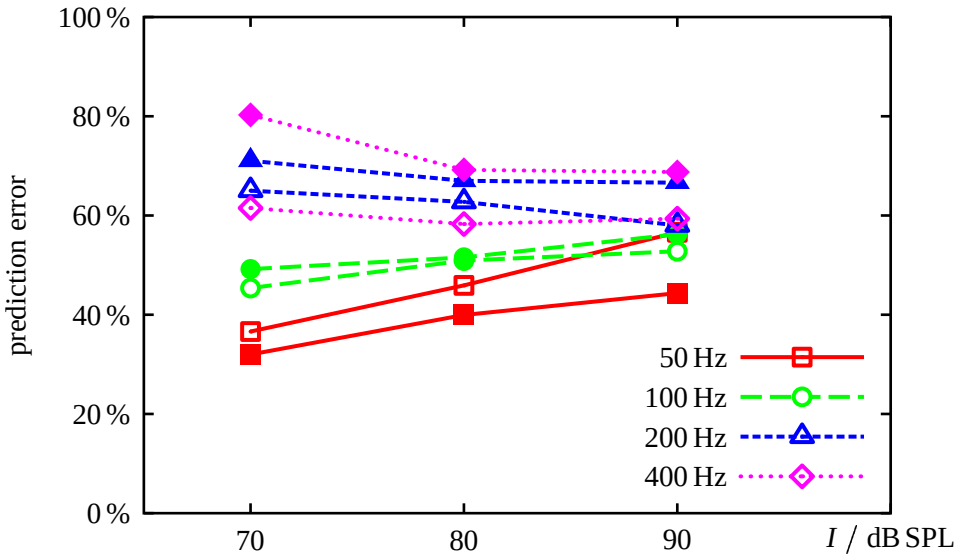

Figure 7.12: MODEL PERFORMANCE FOR WHITE-NOISE STIMULI. The prediction error of the model for the different types of Gaussian white-noise stimuli in dependence on the peak intensity I averaged over $n = 13$ cells. Open symbols denote stimuli with standard deviation $\sigma = 3\,\mathrm{dB}$, filled symbols such with $\sigma = 6\,\mathrm{dB}$. The cut-off frequencies of the noise stimuli were as indicated. The averaged absolute deviation σ_{diff} of the prediction from the measured response was 26 Hz.

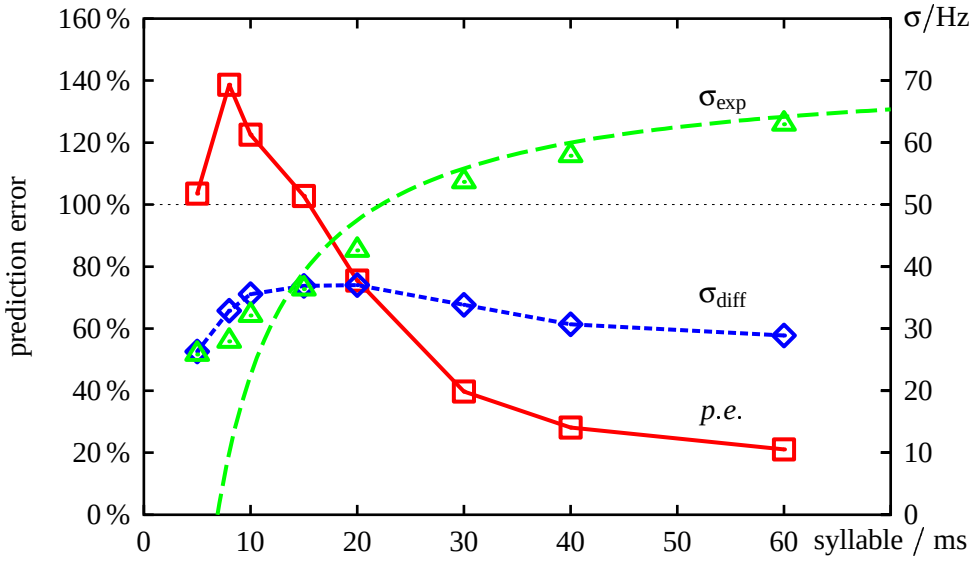

Figure 7.13: MODEL PERFORMANCE FOR PULSE PATTERNS. The mean dependence of the prediction error of the model (7.3) on syllable length is shown ($n = 13$ cells). For comparison the standard deviation of the experimentally measured firing frequency σ_{exp}, and the root mean squared difference σ_{diff} to the model prediction are plotted (right axis). While the deviation σ_{diff} is approximately constant, the modulation depth σ_{exp} of the measured firing frequency decreases with decreasing syllable length. The corresponding dashed line is the function (7.4) for $f_s = 145\,\mathrm{Hz}$. This function assumes a firing frequency f_s during the syllables and a maximum firing frequency of $1/\Delta t$ during the pauses. For syllable durations longer than about 10 ms it explains the decrease of the standard modulation of the firing frequency quite well.

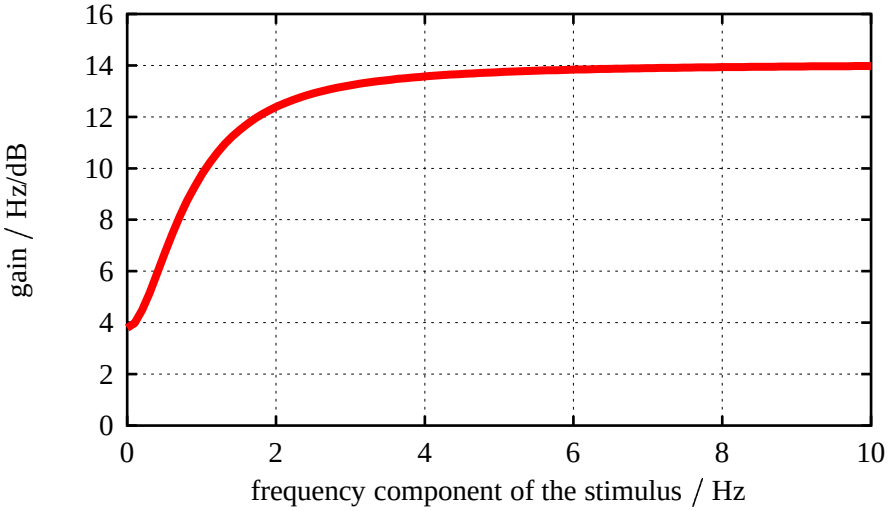

Figure 7.14: THE AMPLITUDE OF THE TRANSFER FUNCTION OF AN AN1. It was calculated using (4.54) from the mean values of the slopes of the unadapted and the steady-state f-I-curves from tab. 7.1 and the mean adaptation time constant $\tau_{\text{eff}} = 141$ ms. The gain is the evoked change in firing frequency per amplitude of the input oscillation.

Transfer function

For the dynamic range of the f-I-curves the transfer function for the firing frequency of the AN1 can be calculated by means of (4.53) as shown in Fig. 7.14. Frequency components of the stimulus above 2 Hz are transmitted with a high gain of about 14 Hz/dB through the shifted onset f-I-curve $f_0(I-A)$. Very slow components below 0.5 Hz and the mean are transmitted only with a gain of about 4 Hz/dB. Note, that the gain in this linear approximation is given by the slopes of the onset and the steady-state f-I-curves, not by their maximum values (tab. 7.1).

7.4 Discussion

Measuring f-I-curves with 500 ms stimuli and a high resolution of intensities requires long and stable recordings. With 25 repetitions of each stimulus the measurement of a single f-I-curve lasted about twenty minutes. Then adapted f-I-curves at five different background intensities (twelve minutes), Gaussian white-noise stimuli at three different intensities (twenty minutes), pulse patterns (seven minutes) and ten f-I-curves with 100 ms stimuli (each two minutes) were measured. Testing all these stimuli in one cell lasted at least one and a half hour. For this reason extracellular recordings were performed, which allowed routinely such long lasting recordings. Since the AN1 is a small neuron, intracellular recordings of this duration are nearly impossible. The penetration with a microelectrode could also damage the AN1, which may change the properties of the neuron. Extracellular recordings disturb the AN1 much less. However, the detection of the AN1 spikes from the extracellular signal was not perfect as mentioned already in the methods section. In the absence of any stimulation there was a high background activity of about 30 Hz. Such a high spontaneous activity was usually not observed in intracellular recordings (Hennig, 1988). The long tail of the interspike-interval histograms indicate that some AN1 spikes were not detected. One reason for such failures is the masking of AN1 spikes

by the larger spikes of the AN2. It is much less sensitive compared to the AN1, so that this masking effect plays a role at high stimulus intensities only. This masking effect is therefore probably the reason for the decrease of the onset f-I-curve of the AN1 at intensities above 79 dB SPL (Fig. 7.4). Nevertheless, the resulting firing frequencies were clearly correlated to the stimulation and in good agreement with previous intracellular recordings (Hennig, 1988; Horseman & Huber, 1994a).

Properties of f-I-curves

Horseman & Huber (1994b) measured f-I-curves of the AN1 in another cricket species (*Gryllus bimaculatus*) as the number of spikes per chirp consisting of four syllables and pauses with a duration of 20 ms. They reported a similar threshold slightly above 40 dB SPL. However, their f-I-curve rose slowly until it saturated above 80 dB at approximately 200 Hz. Since the stimulus was composed of 20 ms short syllables, in principle their f-I-curve should be very close to the onset f-I-curve. However, due to the presentation of four syllables in a chirp, there is a likely effect of the steady-state f-I-curve that leads to the less steeper and wider dynamic range compared to the onset f-I-curve from *T. oceanicus* of this study.

Possible mechanisms for spike-frequency adaptation

Several mechanism may explain the strong adaptation in AN1. First, it can reflect the adaptation of the receptor neurons. Second, the synapses of the receptors to the AN1 may adapt. Both possibilities are of the category transducer adaptation introduced in chapter 4. Third, the AN1 may exhibit encoder adaptation due to intrinsic slow ionic currents. Fourth, there is the possibility of inhibitory inputs (Stumpner, 1998), either as an additional feed-forward input or as recurrent inhibition.

Encoder and transducer adaptation can be differentiated based on (1) the dependence of the effective time constant of adaptation on input intensity, and (2) the shift of the adapted f-I-curves in comparison with the intensity where the onset f-I-curve saturates.

(1) The time constants of adaptation measured in the AN1 scatter strongly. Thus, they do not allow to make any statement about their dependence on input intensity (Fig. 7.6), and no statement about the type of adaptation is possible (recall Fig. 4.11).

(2) The onset f-I-curve clearly saturates. This is a strong sign of a saturating transducer process to the AN1. As shown in Fig. 4.8 encoder adaptation for such onset f-I-curves cannot be the reason for a shift of the adapted f-I-curve beyond the saturation of the onset f-I-curve. Since once the conductance mediating the stimulus is saturated, stronger inputs do not make any difference for the neuron. Therefore, intrinsic mechanisms like encoder adaptation cannot influence the point of saturation. Thus, the main contribution of the adaptation observed in the AN1 is of the category transducer adaptation, provided saturation of its onset f-I-curve indeed reflects the saturation of the transduction of its input.

This transducer adaptation can be evoked by the adaptation in the receptor neurons as it is the case in locusts (chapter 6), by depressing synapses, and by additional slow feed-forward inhibitory input. There are several hints for an inhibitory input via the Omega-neuron, a local auditory interneuron, but this inhibition acts on a much shorter time scale than the adaptation observed here (Schildberger & Hörner, 1988; Horseman & Huber,

1994a).

It cannot be ruled out that in addition to the transducer adaptation there is also a contribution of encoder adaptation. For adaptation on time scales of several seconds, a calcium dependent adaptation mechanism may be the reason (Sobel & Tank, 1994). This type of adaptation could also explain that the adapted f-I-curves measured with stimuli of nearly five seconds duration resemble the state of the neuron which is less sensitive than expected from the fast adaptation investigated here (Fig. 7.7).

The last possibility is some recurrent inhibitory input. As well as encoder adaptation its strength depends on the firing frequency of the AN1. Thus, it can have only a minor contribution on the AN1's adaptation, too.

Receptor neurons

The AN1 receives direct input from the auditory receptor neurons (Hennig, 1988). Since the main contribution to the observed spike-frequency adaptation in the AN1 arises very likely from an already adapting input, the receptor neurons are possible candidates as a source of this adaptation.

Imaizumi & Pollack (2001) analyzed extensively the f-I-curves of auditory receptor neurons in *T. oceanicus*. The f-I-curves they measured reflect mainly the onset f-I-curves, since their stimuli were 30 ms long. The dynamic ranges of the receptor neurons with best frequencies around 4.5 kHz cover approximately 15 to 35 dB, which is about twice the dynamic range of the AN1 onset f-I-curve measured here. The thresholds of the receptor neurons are distributed between about 35 and 80 dB SPL. This range agrees with the possible shift of the adapted f-I-curve in the AN1 from 42 to about 80 dB SPL. Similar properties of receptor cells were observed in the cricket *G. bimaculatus* (Oldfield et al., 1986).

To my knowledge no data exist about adaptation of auditory receptor neurons of crickets. However, since receptor cells of grasshoppers and crickets are part of chordotonal organs that occur as serial homologous in the segments of Orthopteran insects, the principal properties of the receptor cells in crickets and locusts are expected to be similar. Indeed, the onset f-I-curves measured by Imaizumi & Pollack (2001) in *T. oceanicus* are similar to the onset f-I-curves of grasshoppers (chapter 6). Thus, the adaptation properties of auditory receptor cells in both taxa can be assumed to be similar. Adaptation in receptor neurons of locusts shifts their f-I-curve only over a range of about 10 dB, while the AN1 uses a range of at least 40 dB. Future modeling studies have to show whether a simple linear summation of the receptor cell responses is sufficient to describe these adaptation properties of the AN1, or whether more sophisticated computations take place in the AN1. Such a study may show how the AN1 pools the response of receptor neurons with different sensitivities in order to achieve the observed intensity invariance.

Intensity invariance

Slow adaptation over several seconds in auditory interneurons was already observed in the omega neuron of crickets and bush-crickets (Pollack, 1988; Römer & Krusch, 2000). In these studies the forward masking effect of adaptation was emphasized, i.e. the suppression of less intense stimuli by a preceeding louder one. In this study, adaptation on a much shorter time scale of about 100 ms and its implications for intensity invariance

was investigated. The observed range of the shift of the f-I-curve over more than 40 dB is the reason for the intensity invariance. Since the AN1 in crickets is probably the main carrier of information about calling songs to the brain, the data suggest that the cricket should hardly perceive slow changes in sound intensity. Interestingly, phonotactic orientation towards calling songs stimuli measured on a locomotion compensator also showed constant values at intensities for 50–80 dB in this species (R. Hennig 2001, personal communication). Thus, the adaptation properties of the AN1 correspond well in threshold and range of adaptation to the behavior (see also Doolan & Pollack, 1985, for similar measurements). However, the intensity invariance in the AN1 is not perfect, since the steady-state f-I-curve does not vanish and the saturation level of the adapted f-I-curves decreases with increasing mean intensity.

Pulse patterns

Calling songs of crickets are composed of syllables separated by pauses, which are repeated many times. The period of these patterns in *T. oceanicus* is between 10 and 100 ms long (Hennig & Weber, 1997). Due to adaptation the firing frequency evoked by the syllables is reduced (Fig. 7.11 B). However, to be able to resolve short syllables or even the sub-structure of the syllables, high firing frequencies are needed, since only fluctuations of the input which are slower than about half of the firing frequency can be transmitted as discussed in chapter 3. In order to estimate the firing frequency evoked by a syllable, in the following the state of adaptation right at the beginning of the syllable is calculated. Let Δt_s and Δt_p be the duration of the syllables and the pauses, respectively, and $A_\infty(I)$ the steady-state value of the adaptation A evoked by the intensity I of the syllables. During the pauses A_∞ is assumed to be zero. Then, in the steady state the state of adaptation A_0 right at the beginning of a syllable is

$$A_0 = A_\infty(I)\frac{1-\mathrm{e}^{-\Delta t_s/\tau_{\mathrm{eff}}}}{\mathrm{e}^{\Delta t_p/\tau_{\mathrm{eff}}}-\mathrm{e}^{-\Delta t_s/\tau_{\mathrm{eff}}}}\,, \tag{7.5}$$

where τ_{eff} is the effective adaptation time-constant. The dependence of this function on the duration of the pause Δt_p is illustrated in Fig. 7.15 A. Only for pauses much longer than the adaptation time-constant the neuron recovers completely from adaptation resulting in $A_0 \approx 0$. If both syllables and pauses are very short, $A_0/A_\infty(I)$ equals the duty cycle.

The neuron adapts completely to its steady-state f-I-curve $f_\infty(I)$, if it is stimulated with a constant intensity I without interruption. To a pulse pattern it adapts less, as quantified by (7.5). Thus, the response to the syllable is greater than the steady-state response $f_\infty(I)$. The response is only limited by the saturation level of the corresponding adapted f-I-curve. The higher values the steady-state f-I-curve has, the higher the firing frequency during the syllables has to be. This is important to resolve pulse patterns with short periods. With a spike frequency of $f = 50$ Hz, for example, the minimum period is $1/50\,\mathrm{Hz} = 20$ ms. Every syllable evokes just one spike. To resolve shorter syllables, a higher firing frequency is needed. As illustrated in Fig. 7.15 B pulse patterns applied at 10 dB above threshold already evoke firing frequencies of more than 100 Hz, thus allowing to detect syllables down to 5 ms duration (duty cycle 50 %). This lower limit of detectable syllable durations is in good agreement with results of both temporal modulation transfer functions measured in the AN1 and behavioral studies (R.M. Hennig (2001), personal communication). The saturation frequency of the AN1 steady-state f-I-curve of

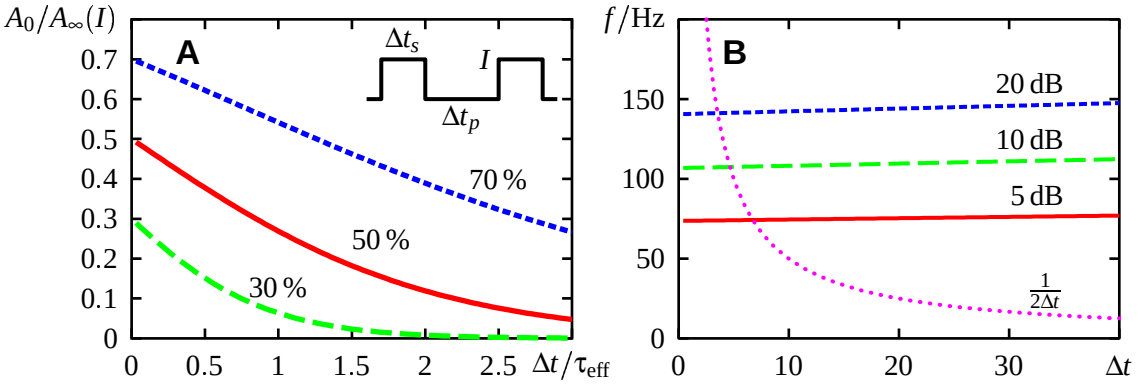

Figure 7.15: ADAPTATION TO REPEATED PULSES. **A** The state of adaptation A_0 at the beginning of a syllable related to its steady-state value $A_\infty(I)$ for the intensity I of the syllable in dependence of the duration of the pauses Δt_p related to the adaptation time-constant τ_{eff} is shown for different duty cycles $\Delta t_s/(\Delta t_s + \Delta t_p)$ as indicated. Equation (7.5) was used for the plot. If the duration of both the syllable and the pause approaches zero, $A_0/A_\infty(I)$ equals the duty cycle. **B** The initial firing frequency evoked by a syllable-pause pattern with duty-cycle 50 % in dependence on the length of the syllable Δt for different intensities relative to threshold as indicated in decibel. For the f-I-curves used for this calculation the mean values from tab. 7.1 and the state of adaptation given by (7.5) was used. The frequency $0.5/\Delta t$ of the pulse pattern is marked by the dotted line.

about 100 Hz ensures this resolution over a wide range of intensities. Note that the corresponding periods are a lower bound of the capability of the AN1 to transmit the structure of the pulse pattern, if no assumptions about the stimulus are made.

Adaptation model

Due to the properties of the observed f-I-curves in the AN1, the adaptation model (7.3) was chosen. In addition to the shift of the onset f-I-curve $f_0(I-A)$ it is scaled down appropriately by the denominator $1+\gamma s_0 A$. It is not possible to model the compression by a multiplicative term on the state of adaptation A similarly as for encoder adaptation (4.22), since such a term does not affect the saturation level. The dynamics of the state of adaptation A is driven solely by the input as it is required for any kind of transducer adaptation.

The overall performance of the model (7.3) is quite well. However, there are some deviations between the modeled and the measured firing frequencies, which can be seen in all comparisons. First, the initial response is underestimated by the model. It is determined by the maximum frequency of the unadapted f-I-curve $f_0(I)$. The procedure of calculating the maximum frequency $f_{\max}$ included two averaging processes. The time course of the firing frequency was smoothed with a 30 ms running average, and values at three intensities were averaged to get $f_{\max}$. In addition, at high intensities AN2 spikes mask the AN1 response. Thus, the maximum value of the unadapted f-I-curve used to model the firing frequency is very likely too small. Second, peaks of the firing frequency throughout the response to white-noise stimuli are much weaker in the prediction of the model. In addition to the too small maximum value of the unadapted f-I-curve an underestimation of the slope of the adapted f-I- curve could be the reason for that phenomenon. From the data of the adapted f-I-curves as in Fig. 7.7 it is not clear, however, whether adaptation compresses their initial slope. If this slope would be independent of adaptation, then the model (7.3), which compresses it, produces smaller responses. Third, the

activity evoked by the pulse patterns continued after the syllables into the pauses during the first approximately 100 ms after stimulus onset (arrow in Fig. 7.11 B). This after discharge is not reproduced by the model. It is a phenomenon which also can be observed in receptor neurons of bush crickets (Schütze, 1995). Therefore it originates probably from the transduction of the sound waves into changes of the membrane conductance.

Altogether, the slow dynamics of spike-frequency adaptation of the AN1 can be explained by the model (7.3) of transducer adaptation. Thus, all processes preceeding the generation of spikes in the AN1 (transduction of the sound wave, adaptation of the receptor cells, synaptic transmission to the AN1, integration on the dendritic tree) are captured sufficiently by the single first-order differential equation of the model. All deviations of the model from the real firing frequency arise on a faster time scale and therefore have to be attributed to the faster dynamics of the spike generator. However, due to the noisiness of the data it is not possible to check different models for the generation of spikes as proposed in chapter 3.

7.5 Summary

- Spike-frequency adaptation in the AN1, an ascending primary auditory interneuron, was studied in the Australian cricket *Teleogryllus oceanicus*.
- The dynamic range of its onset f-I-curve is about 12 dB wide. Adaptation shifts the f-I-curve over a range of more than 40 dB. The adaptation time constant is on average 140 ms.
- Due to this adaptation the AN1 response is approximately invariant of intensity on slow time scales > 500 ms, which is in good agreement with phonotactic behavior of this species.
- The non-vanishing steady-state f-I-curve forces the firing frequency evoked by pulse patterns to be at least 100 Hz. This makes it possible to resolve pulse patterns with periods down to less than 10 ms.
- The dynamics of adaptation in the AN1 can be described well by a phenomenological model of transducer adaptation, taking the decreasing saturation level into account.

8

Conclusion

The objective of this work was to derive models for single neurons, which capture their essential functional features and which can be tested directly on experimental data of real neurons.

The distinction of class-I and class-II neurons played an important role in the development of these phenomenological models. This classification is based on functional properties like f-I-curves, latencies, and phase-resetting curves (Hodgkin, 1948; Ermentrout, 1996). It is described by two different bifurcations (Rinzel & Ermentrout, 1998). In the experimental literature, however, this important classification is still neglected. Many different phenomena such as, for example, sub-threshold oscillations, short latencies and spike clustering (c.f. Fig. 2.17 on page 24), which were observed by Alonso & Klink (1993) and Fricker & Miles (2000) in hippocampal neurons, have been treated as completely independent mechanisms, but are all the expression of the underlying Hopf bifurcation.

The shapes of f-I-curves reported in the experimental literature give evidence that most neurons are class-I neurons. Therefore, I have concentrated on setting up models for class-I neurons. Until now there has been a tendency to neglect class-I neurons in the theoretical literature, since the Hodgkin-Huxley model, which constitutes a class-II neuron, often served as a neuron prototype (for example in Schneidman et al., 1998; Wang et al., 2000). However, the commonly used integrate-&-fire model is more closely related to a class-I neuron.

For sub-threshold stimuli, a class-I neuron remains quiet. Super-threshold stimuli are necessary to initiate spikes. In this super-threshold regime the neuron fires repetitively — it oscillates. The dynamics of a neuron as a nonlinear oscillator was analysed in chapter 3. Phase oscillators, and especially the θ-model (Ermentrout, 1996), were introduced as suitable models for repetitively spiking neurons and made applicable for experimental work. The neuron's f-I-curve is a key property for setting up phase oscillators. The phase-resetting curves of a neuron are required for a further refinement of the models. Extensive tests of the phase oscillators on conductance-based models revealed that the neuron's super-threshold dynamics can be reproduced well by these simple models. However, the spike latencies are not correctly explained by these models. Thus, the super-threshold dynamics differs from the neuron's sub-threshold dynamics. The interplay of these two dynamical regimes is of great importance especially for neurons operating near threshold. Therefore, the combination of the sub- and super-threshold dynamics into a single model,

which is simple and experimentally testable, is desired for a more realistic description of the spiking behavior of a neuron.

A large part of this thesis is concerned with the analysis of spike-frequency adaptation. Various mechanism can be responsible for the phenomenon spike-frequency adaptation: encoder adaptation is caused by slow ionic currents of the spike generator, transducer adaptation results from the fatigue of the transduction process of a stimulus, and depressing synapses also decrease the effectivity of the input. Adaptation acts either subtractive or divisive on the input and is driven by the input strength or by the output firing frequency. In chapter 4 a derivation of an universal phenomenological model is presented for various different mechanisms of encoder adaptation. Encoder adaptation is subtractive, it shifts the neuron's onset f-I-curve to higher input intensities. The dynamics of encoder adaptation is covered by a single differential equation for the state of adaptation A. The important nonlinearities of this model arise only from the nonlinear shape of the f-I-curves. Thus, linearizing the f-I-curves results in a linear model for adaptation, which can be used to calculate transfer functions in order to quantify signal-transmission properties of an adapting neuron. Basically, spike-frequency adaptation turns a neuron into a high-pass filter. The shorter its adaptation time-constant, the more the neuron's response resembles the time-derivative of the input.

The purpose of the second part of this work was to demonstrate (i) that the adaptation models presented in this thesis can reproduce the firing frequency of real neurons, (ii) that they provide a simple tool to quantify signal-transmission properties, and (iii) that they give some hints about the mechanisms causing spike-frequency adaptation.

The auditory receptor neurons of locusts are ideally suited for testing the models (chapter 6). They directly convert the sound-wave stimuli into sequences of spikes. They lack a dendritic tree and there are no intermediate synapses. For the first time, phase-resetting curves were measured to show that these neurons are indeed class-I neurons. To investigate spike-frequency adaptation, onset, steady-state and adapted f-I-curves, as well as effective time-constants of adaptation and the time constant of recovery from adaptation were measured. The data suggest that the observed spike-frequency adaptation is mainly caused by encoder adaptation. With a corresponding model the firing frequency to white-noise and grasshopper-song stimuli was predicted with high accuracy. Spike-frequency adaptation in the auditory receptor neurons enhances the detection of gaps, especially in the grasshopper songs. During the syllables of the songs the receptors adapt and become less sensitive. Between the syllables the receptors therefore are quiet even in the presence of background noise and recover a little from adaptation. The cell is then able to respond clearly to the onset of the following syllable.

The models for spike-frequency adaptation presented in this work are created for single neurons, which are stimulated directly. In chapter 7, however, it is demonstrated that these models can be also used to describe the activity of an interneuron which receives the applied stimulus via receptor neurons. This was tested on the AN1, a first-order interneuron of the cricket, which receives its input from auditory receptor neurons. The adaptation properties of the AN1 stimulated via the receptor neurons by sound waves are in accordance with the expectations for transducer adaptation, i.e. the observed spike-frequency adaptation arises from an already adapting input to the AN1. The corresponding model reproduced the firing frequency evoked by sound stimuli quite well. Adaptation in the AN1 makes its response approximately invariant of the mean intensity of the stimulus. The specific properties of adaptation in the AN1 ensure a firing frequency of at least one

hundred Hertz when it is stimulated with pulse patterns that are typical for the calling songs of crickets. Thus, pulse patterns with periods down to about ten milliseconds can still be resolved by the spikes.

Both the phase oscillators as models for the generation of spikes and the models for spike-frequency adaptation proposed in this study are valid only for sufficiently high firing frequencies. This is a strong restriction for many cortical neurons, which often exhibit very low firing frequencies. Other neurons, however, including the two types of auditory neurons discussed in this thesis, operate at high firing frequencies. Their typical natural stimuli, calling songs of grasshoppers and crickets, consists of syllables separated by pauses. The syllables stimulate the neurons in their super-threshold regime, where the models are in good agreement with the experimental data. During the pauses the neurons usually remain silent and thus settle on a fixed point in the sub-threshold regime. It is only the generation of the first spike evoked by the following syllable, which is not covered by the models, since for this spike the interaction of the sub- and super-threshold dynamics becomes important. However, on the level of firing frequencies the models are still accurate. A comparison on the level of spikes would be of much more interest. To do so, noise has to be added to the models appropriately, in order to reproduce the variability of the timing of the observed spikes. The interspike-interval distributions from f-I-curve measurements could be used for defining a noise model. In addition to the firing frequency, the precision of the spikes could then be compared with the data, using the measure for spike precision proposed in chapter 5. Such an approach should reproduce the importance of the precision of the first spike to a syllable observed by Ronacher & Römer (1985).

The results of this thesis show that it is indeed possible to derive simple and universal phenomenological models which are at the same time directly applicable to experimental data and amenable to theoretical investigations. These models help to understand functional aspects of neurons qualitatively as well as quantiatively. It will be a challenge to extend this approach to more complex neurons and small neural networks in the near future.

A

Conductance-Based Models

In the following the specifications of the conductance-based models used in this thesis are given. All potentials are measured in mV, conductances in $\mathrm{mS/cm^2}$, capacitances in $\mu\mathrm{F/cm^2}$, and currents in $\mu\mathrm{A/cm^2}$.

A–1 Hodgkin-Huxley model

The original model of Hodgkin & Huxley (1952) with the resting potential set to $-65\,\mathrm{mV}$. The Hodgkin-Huxley model is an example of a class-II neuron.

$$C\dot{V} = -I_{\mathrm{Na}} - I_{\mathrm{K}} - I_{\mathrm{L}} + I$$

Membrane capacitance: $C = 1\,\mu\mathrm{F/cm^2}$.

Sodium current

$$\begin{aligned} I_{\mathrm{Na}} &= \bar{g}_{\mathrm{Na}} m^3 h (V - E_{\mathrm{Na}}) \\ \dot{m} &= \alpha_m(V)(1-m) - \beta_m(V) m \\ \dot{h} &= \alpha_h(V)(1-h) - \beta_h(V) h \end{aligned}$$

$\bar{g}_{\mathrm{Na}} = 120\,\mathrm{mS/cm^2}$, $E_{\mathrm{Na}} = +50\,\mathrm{mV}$,
$\alpha_m(V) = 0.1(V+40)/(1-\exp(-(V+40)/10))$,
$\beta_m(V) = 4\exp(-(V+65)/18)$,
$\alpha_h(V) = 0.07\exp(-(V+65)/20)$,
$\beta_h(V) = 1/(1+\exp(-(V+35)/10))$.

Potassium delayed-rectifier current

$$\begin{aligned} I_{\mathrm{K}} &= \bar{g}_{\mathrm{K}} n^4 (V - E_{\mathrm{K}}) \\ \dot{n} &= \alpha_n(V)(1-n) - \beta_n(V) n \end{aligned}$$

$\bar{g}_{\mathrm{K}} = 36\,\mathrm{mS/cm^2}$, $E_{\mathrm{K}} = -77\,\mathrm{mV}$,
$\alpha_n(V) = 0.01(V+55)/(1-\exp(-(V+55)/10))$,
$\beta_n(V) = 0.125\exp(-(V+65)/80)$.

Leakage current

$$I_{\mathrm{L}} = \bar{g}_{\mathrm{L}}(V - E_{\mathrm{L}})$$

$\bar{g}_{\mathrm{L}} = 0.3\,\mathrm{mS/cm^2}$, $E_{\mathrm{L}} = -54.384\,\mathrm{mV}$.

A–2 Traub-Miles model

A version of the model of Traub et al. (1991) is used in chapter 3, which has only a single compartment and includes only the sodium, delayed rectifier and leakage current. This model is a simple example of a class-I neuron. Note that it contains the same currents as the Hodgkin-Huxley model. Only their parameters are slightly changed. The resting potential is at $V = -66.6\,\mathrm{mV}$.

$$C\dot{V} = -I_{\mathrm{Na}} - I_{\mathrm{K}} - I_{\mathrm{L}} + I$$

Membrane capacitance: $C = 1\ \mu\mathrm{F/cm^2}$

Sodium current

$$\begin{aligned} I_{\mathrm{Na}} &= \bar{g}_{\mathrm{Na}} m^3 h (V - E_{\mathrm{Na}}) \\ \dot{m} &= \alpha_m(V)(1-m) - \beta_m(V) m \\ \dot{h} &= \alpha_h(V)(1-h) - \beta_h(V) h \end{aligned}$$

$\bar{g}_{\mathrm{Na}} = 100\,\mathrm{mS/cm^2}$, $E_{\mathrm{Na}} = +48\,\mathrm{mV}$,
$\alpha_m(V) = 0.32(V+54)/(1-\exp(-(V+54)/4))$,
$\beta_m(V) = 0.28(V+27)/(\exp((V+27)/5)-1)$,
$\alpha_h(V) = 0.128\exp(-(V+50)/18)$,
$\beta_h(V) = 4/(1+\exp(-(V+27)/5))$.

Potassium delayed-rectifier current

$$\begin{aligned} I_{\mathrm{K}} &= \bar{g}_{\mathrm{K}} n^4 (V - E_{\mathrm{K}}) \\ \dot{n} &= \alpha_n(V)(1-n) - \beta_n(V) n \end{aligned}$$

$\bar{g}_{\mathrm{K}} = 200\,\mathrm{mS/cm^2}$, $E_{\mathrm{K}} = -82\,\mathrm{mV}$,
$\alpha_n(V) = 0.032(V+52)/(1-\exp(-(V+52)/5))$,
$\beta_n(V) = 0.5\exp(-(V+57)/40)$.

Leakage current

$$I_{\mathrm{L}} = \bar{g}_{\mathrm{L}}(V - E_{\mathrm{L}})$$

$\bar{g}_{\mathrm{L}} = 0.1\,\mathrm{mS/cm^2}$, $E_{\mathrm{L}} = -67\,\mathrm{mV}$.

A–3 Modified Traub-Miles model

A variant of the Traub-Miles model from above is used in chapter 4.

$$C\dot{V} = -I_{\mathrm{Na}} - I_{\mathrm{K}} - I_{\mathrm{L}} - I_{\mathrm{Ca}} + I$$

There are only slight differences in the conductances and reversal potentials of the sodium and the potassium current (Ermentrout, 1998) and an additional calcium current.

$\bar{g}_{\mathrm{Na}} = 100\,\mathrm{mS/cm^2}$, $E_{\mathrm{Na}} = +50\,\mathrm{mV}$,
$\bar{g}_{\mathrm{K}} = 80\,\mathrm{mS/cm^2}$, $E_{\mathrm{K}} = -100\,\mathrm{mV}$,
$\bar{g}_{\mathrm{L}} = 0.1\,\mathrm{mS/cm^2}$, $E_{\mathrm{L}} = -67\,\mathrm{mV}$.

Calcium current

$$\begin{aligned} I_{\mathrm{Ca}} &= \bar{g}_{\mathrm{Ca}} s (V - E_{\mathrm{Ca}}) \\ s &= 1/(1+\exp(-(V+25)/5)) \end{aligned}$$

$\bar{g}_{\mathrm{Ca}} = 5\,\mathrm{mS/cm^2}$, $E_{\mathrm{Ca}} = 120\,\mathrm{mV}$.

Traub-Miles model with M-type current

An M-type current was added to the modified Traub-Miles model to simulate spike-frequency adaptation (Ermentrout, 1998):

$$C\dot{V} = -I_{\mathrm{Na}} - I_{\mathrm{K}} - I_{\mathrm{L}} - I_{\mathrm{Ca}} - I_{\mathrm{M}} + I$$

M-type current

$$\begin{aligned} I_{\mathrm{M}} &= \bar{g}_{\mathrm{M}} w (V - E_{\mathrm{M}}) \\ \tau_w(V)\dot{w} &= w_\infty(V) - w \end{aligned}$$

$\bar{g}_{\mathrm{M}} = 8\,\mathrm{mS/cm^2}$, $E_{\mathrm{M}} = -100\,\mathrm{mV}$,
$\tau_w(V) = 100\,\mathrm{ms}$,
$w_\infty(V) = 1/(1+\exp(-(V+20)/5))$.

Traub-Miles model with AHP current

Alternatively, an AHP current and calcium dynamics was added to the modified Traub-Miles model (Ermentrout, 1998):

$$C\dot{V} = -I_{\mathrm{Na}} - I_{\mathrm{K}} - I_{\mathrm{L}} - I_{\mathrm{Ca}} - I_{\mathrm{AHP}} + I$$

AHP current and calcium dynamics

$$\begin{aligned} I_{\mathrm{AHP}} &= \bar{g}_{\mathrm{AHP}} q (V - E_{\mathrm{AHP}}) \\ q &= [Ca]/(30+[Ca]) \\ [\dot{Ca}] &= -0.002 I_{\mathrm{Ca}} - 0.0125[Ca] \end{aligned}$$

$\bar{g}_{\mathrm{AHP}} = 4\,\mathrm{mS/cm^2}$, $E_{\mathrm{AHP}} = -100\,\mathrm{mV}$.

A–4 Connor model

The A-current is a potassium current, which is present in many neurons. Connor et al. (1977) added this current to the Hodgkin-Huxley model. The resulting equations show class-I neuron properties. The resting potential of the Connor model is at $V = -73\,\mathrm{mV}$.

$$C\dot{V} = -I_{\mathrm{Na}} - I_{\mathrm{K}} - I_{\mathrm{A}} - I_{\mathrm{L}} + I$$

Membrane capacitance: $C = 1\,\mu\mathrm{F/cm^2}$.

Sodium current

$$\begin{aligned} I_{\mathrm{Na}} &= \bar{g}_{\mathrm{Na}} m^3 h (V - E_{\mathrm{Na}}) \\ \dot{m} &= \alpha_m(V)(1-m) - \beta_m(V) m \\ \dot{h} &= \alpha_h(V)(1-h) - \beta_h(V) h \end{aligned}$$

$\bar{g}_{\mathrm{Na}} = 120\,\mathrm{mS/cm^2}$, $E_{\mathrm{Na}} = +50\,\mathrm{mV}$,
$\alpha_m = 0.1(V+34.7)/(1-\exp(-(V+34.7)/10))$,
$\beta_m = 4\exp(-(V+59.7)/18)$,
$\alpha_h = 0.07\exp(-(V+53)/20)$,
$\beta_h = 1/(1+\exp(-(V+23)/10))$.

Potassium delayed-rectifier current

$$\begin{aligned} I_{\mathrm{K}} &= \bar{g}_{\mathrm{K}} n^4 (V - E_{\mathrm{K}}) \\ \dot{n} &= \alpha_n(V)(1-n) - \beta_n(V) n \end{aligned}$$

$\bar{g}_{\mathrm{K}} = 20\,\mathrm{mS/cm^2}$, $E_{\mathrm{K}} = -77\,\mathrm{mV}$,
$\alpha_n(V) = 0.005(V+50.7)/(1-\exp(-(V+50.7)/10))$,
$\beta_m(V) = 0.0625\exp(-(V+60.7)/80)$.

Potassium A-current

$$\begin{aligned} I_{\mathrm{A}} &= \bar{g}_{\mathrm{A}} a^3 b (V - E_{\mathrm{A}}) \\ \tau_a(V)\dot{a} &= a_\infty(V) - a \\ \tau_b(V)\dot{b} &= b_\infty(V) - b \end{aligned}$$

$\bar{g}_{\mathrm{A}} = 47.7\,\mathrm{mS/cm^2}$, $E = -80\,\mathrm{mV}$,
$a_\infty(V) = (0.0761\exp((V+99.22)/31.84)/(1+\exp((V+6.17)/28.93)))^{1/3}$,
$\tau_a(V) = 0.3632 + 1.158/(1+\exp((V+60.96)/20.12))$,
$b_\infty(V) = 1/(1+\exp((V+58.3)/14.54))^4$,
$\tau_b(V) = 1.24 + 2.678/(1+\exp((V+55)/16.072))$.

Leakage current

$$I_{\mathrm{L}} = \bar{g}_{\mathrm{L}}(V - E_{\mathrm{L}})$$

$\bar{g}_{\mathrm{L}} = 0.3\,\mathrm{mS/cm^2}$, $E_{\mathrm{L}} = -22\,\mathrm{mV}$.

A–5 Crook model

The model of Crook et al. (1998) was used as an additional example of an adapting neuron. It is a two-compartment model. One compartment is the membrane equation for the potential V_s of the soma. It contains all the voltage dependent currents for the generation of spikes and possible adaptation currents. The other compartment is a linear membrane equation and models the whole dendritic tree. Its potential is V_d. Both compartments are coupled by the coupling current I_{C}. Note that the input current I is injected into the soma. Therefore the adaptation currents are still additive to the input current. The resting potential of the Crook model is at $-77\,\mathrm{mV}$.

$$\begin{aligned} C\dot{V}_s &= -I_{\mathrm{Na}} - I_{\mathrm{K}} - I_{\mathrm{Ca}} - I_{\mathrm{LS}} - I_{\mathrm{C}}/P + I/P \\ C\dot{V}_d &= -I_{\mathrm{LD}} + I_{\mathrm{C}}/(1-P) \end{aligned}$$

Membrane capacitance: $C = 0.8\,\mu\mathrm{F/cm^2}$,
Proportion of the cell area taken up by the soma: $P = 0.05$.

Sodium current

$$\begin{aligned} I_{\mathrm{Na}} &= \bar{g}_{\mathrm{Na}} m^2 h (V_s - E_{\mathrm{Na}}) \\ \dot{m} &= \alpha_m(V)(1-m) - \beta_m(V)m \\ \dot{h} &= \alpha_h(V)(1-h) - \beta_h(V)h \end{aligned}$$

$\bar{g}_{\mathrm{Na}} = 221\,\mathrm{mS/cm^2}$, $E_{\mathrm{Na}} = +55\,\mathrm{mV}$,
$\alpha_m(V) = 0.32(-47.1 - V_s)/(\exp(0.25(-47.1 - V_s)) - 1)$,
$\beta_m(V) = 0.28(V_s + 20.1)/(\exp((V_s + 20.1)/5) - 1)$,
$\alpha_h(V) = 0.128\exp((-43 - V_s)/18)$,
$\beta_h(V) = 4/(\exp((-20 - V_s)/5) + 1)$.

Potassium delayed-rectifier current

$$\begin{aligned} I_{\mathrm{K}} &= \bar{g}_{\mathrm{K}} n (V_s - E_{\mathrm{K}}) \\ \dot{n} &= \alpha_n(V)(1-n) - \beta_n(V)n \end{aligned}$$

$\bar{g}_{\mathrm{K}} = 47\,\mathrm{mS/cm^2}$, $E_{\mathrm{K}} = -90\,\mathrm{mV}$,
$\alpha_n(V) = 0.59(-25.1 - V_s)/(\exp((-25.1 - V_s)/5) - 1)$,
$\beta_n(V) = 0.925\exp(0.925 - 0.025(V_s + 77))$.

Calcium current

$$\begin{aligned} I_{\mathrm{Ca}} &= \bar{g}_{\mathrm{Ca}} s^2 r (V_s - E_{\mathrm{Ca}}) \\ \dot{s} &= \alpha_s(V)(1-s) - \beta_s(V)s \\ \tau_r(V)\dot{r} &= r_\infty(V) - r \end{aligned}$$

$\bar{g}_{\mathrm{Ca}} = 8.5\,\mathrm{mS/cm^2}$, $E_{\mathrm{Ca}} = +120\,\mathrm{mV}$,
$\alpha_s(V) = 0.912/(\exp(-0.072(V_s - 5)) + 1)$,
$\beta_s(V) = 0.0114(V_s + 8.9)/(\exp((V_s + 8.9)/5) - 1)$,
$r_\infty(V) = \min(\exp(-(V_s + 60)/20), 1)$,
$\tau_r(V) = 200\,\mathrm{ms}$.

Soma leakage-current

$$I_{\mathrm{LS}} = \bar{g}_{\mathrm{LS}}(V_s - E_{\mathrm{LS}})$$

$\bar{g}_{\mathrm{LS}} = 2\,\mathrm{mS/cm^2}$, $E_{\mathrm{LS}} = -70\,\mathrm{mV}$.

Dendrite leakage-current

$$I_{\mathrm{LD}} = \bar{g}_{\mathrm{LD}}(V_d - E_{\mathrm{LD}})$$

$\bar{g}_{\mathrm{LD}} = 0.05\,\mathrm{mS/cm^2}$, $E_{\mathrm{LD}} = -70\,\mathrm{mV}$.

Coupling current

$$I_{\mathrm{C}} = \bar{g}_{\mathrm{C}}(V_s - V_d)$$

$\bar{g}_{\mathrm{C}} = 1.1\,\mathrm{mS/cm^2}$

Crook model with M-type current

To simulate the effect of an M-type adaptation current it was added to the Crook-model.

$$C\dot{V}_s = -I_{\mathrm{Na}} - I_{\mathrm{K}} - I_{\mathrm{Ca}} - I_{\mathrm{M}} - I_{\mathrm{LS}} - I_{\mathrm{C}}/P + I/P$$

M-type current

$$\begin{aligned} I_{\mathrm{M}} &= \bar{g}_{\mathrm{M}} w (V_s - E_{\mathrm{K}}) \\ \tau_w(V)\dot{w} &= w_\infty(V) - w \end{aligned}$$

$\bar{g}_{\mathrm{M}} = 6.5\,\mathrm{mS/cm^2}$, $E_{\mathrm{K}} = -90\,\mathrm{mV}$,
$w_\infty(V) = 1/(\exp(-(V_s+35)/10)+1)$,
$\tau_w(V) = 92\exp(-(V_s+35)/20)/(1+0.3\exp(-(V_s+35)/10))$.

Crook model with AHP current

To simulate the effect of an AHP-type adaptation current it was added together with the calcium dynamics to the Crook-model.

$$C\dot{V}_s = -I_{\mathrm{Na}} - I_{\mathrm{K}} - I_{\mathrm{Ca}} - I_{\mathrm{AHP}} - I_{\mathrm{LS}} - I_{\mathrm{C}}/P + I/P$$

AHP current and calcium dynamics

$$\begin{aligned} I_{\mathrm{AHP}} &= \bar{g}_{\mathrm{AHP}} q (V_s - E_{\mathrm{K}}) \\ \tau_q(V)\dot{q} &= q_\infty(V) - q \\ [\dot{Ca}] &= -BI_{\mathrm{Ca}} - [Ca]/\tau_{\mathrm{Ca}} \end{aligned}$$

$\bar{g}_{\mathrm{AHP}} = 7\,\mathrm{mS/cm^2}$, $E_{\mathrm{K}} = -90\,\mathrm{mV}$,
$q_\infty(V) = (0.0005[Ca])^2$,
$\tau_q(V) = 0.0338/(\min(0.00001[Ca], 0.01) + 0.001)$,
$B = 3$, $\tau_{\mathrm{Ca}} = 60\,\mathrm{ms}$.

B

Deutschsprachige Zusammenfassung

B–1 Einleitung

Das zentrale Element eines jeden Nervensystems ist das Neuron. Es spielt eine wichtig Rolle bei der Verarbeitung von Informationen. Grundlegende Eigenschaften von Neuronen in den verschiedensten Nervensystem sind sich sehr ähnlich. Diese Ähnlichkeit reicht von den Membran-Proteinen, welche die Ionenkanäle bilden, über die Zellmorphologie mit den dünnen und verzweigten Fortsätzen (Dendriten und Axone), bis hin zum Membranpotential als Informationsträger. Ziel der Arbeit ist es, universelle Modelle ausgehend von bekannten mikroskopischen Eigenschaften von Neuronen herzuleiten, die sowohl direkt auf experimentelle Daten anwendbar sind als auch einfach genug sind um theoretische Untersuchung zuzulassen. Damit soll eine Brücke zwischen experimentellen Untersuchungen und abstrakten theoretischen Betrachtungen geschlagen werden.

B–2 Spikende Neurone

Zur Einführung in die Modellierung spikender Neurone wird ein kurzer Überblick über die Grundlagen von Leitfähigkeitsmodellen gegeben. Am Beispiel des Hodgkin-Huxley Models wird das Konzept der Torvariablen erläutert. Nachdem kurz auf die verschiedenen Zeitskalen neuronaler Dynamik eingegangen worden ist, wird das Verfahren von Kepler et al. (1992) zur Reduzierung der Anzahl von Variablen in Leitfähigkeitsmodellen vorgestellt. Ein Punkt, der leider immer noch viel zu sehr vernachlässigt wird, ist die bereits von Hodgkin (1948) eingeführte funktionelle Einteilung von spikenden Neuronen in zwei Klasssen. Typ-I-Neurone können mit beliebig niedriger Frequenz feuern, zeigen beliebig lange Latenzen, und kleine Störungen ziehen den Zeitpunkt des folgenden Spikes vor. Im Gegensatz dazu haben Typ-II-Neurone eine Diskontinuität in ihrer Kennlinie, die Latenzen sind relativ kurz und kleine Störungen können den Zeitpunkt des folgenden Spikes verzögern. Diesen Phänomenen liegen zwei unterschiedliche Bifurkationen zugrunde. Typ-I-Neurone haben eine Sattel-Knoten Bifurkation, während bei Typ-II-Neuronen eine Hopf Bifurkation vorliegt.

B–3 Modellierung spikender Neurone

Die zentrale Idee in diesem Kapitel ist, die Kennlinie eines Neurons direkt als Parameter zur Modellierung von Spikezeitpunkten zu verwenden. Die Kennlinie unterteilt die Dynamik eines Typ-I-Neurons in einen unter- und einen überschwelligen Bereich. Die unterschwellige Dynamik ist durch die Existenz eines Fixpunkts — das Ruhepotential — gekennzeichnet, während die überschwellige Dynamik von Grenzzyklen bestimmt wird, deren Umlauffrequenz von der Kennlinie angegeben wird. Deshalb kann die Feuerrate, die von der Kennlinie bestimmt wird, als Phasengeschwindigkeit eines Phasenoszillators aufgefasst werden. Zur weiteren Verbesserung des Phasenoszillators wird die Phasen-Antwort-Kurve des Neurons benötigt. Diese einfachen Modelle sind erstaunlich gut in der Lage, die Zeitpunkte von Spikes, simuliert mit verschiedenen Leitfähigkeitsmodellen, vorherzusagen. Latenzen, gemessen in Leitfähigkeitsmodellen, lassen sich aber nicht mit diesen Modellen erklären. Dies zeigt, daß die überschwellige Dynamik sich von der unterschwelligen Dynamik eines Neurons unterscheidet. Für eine realistischere Beschreibung des Spikeverhaltens von Neuronen ist deshalb ein mindestens zwei-dimensionales Model notwendig.

B–4 Dynamik der Feuerraten-Adaptation

Feuerraten-Adaptation ist ein weit verbreitetes Phänomen in spikenden Neuronen. Die Ursachen der Feuerraten-Adaptation sind vielfältig. Encoder-Adaptation wird durch intrinsische, langsame Ionen-Ströme des Spike-Generators verursacht. Transducer-Adaptation beruht auf der Ermüdung der Transduktion eines externen Stimulus. Auch die Übertragung von Signalen durch Synapsen kann adaptieren. Adaptation wirkt sich entweder subtraktiv oder multiplikativ auf den Stimulus aus und wird entweder durch den Stimulus oder die Feuerrate verursacht. Ein universelles phänomenologisches Modell für Encoder-Adaptation wird von verschiedenen ihr zugrundeliegendenen biophysikalischen Mechanismen hergeleitet. Das Modell ist durch Kenntnis der Kennlinien und Adaptations-Zeitkonstanten eines Neurons vollständig bestimmt und lässt sich deshalb leicht auf experimentelle Daten anwenden. Gleichzeitig können mit diesem Modell die mit der Feuerraten-Adaptation verbundenen Hochpass-Filtereigenschaften quantifiziert werden.

B–5 Analyse von Spike-Folgen

Der Begriff “Feuerrate”, der von den bisher vorgestellten Modellen verwendet wird, bezeichnet den Kehrwert des Interspike-Intervalls. Eine kurze Analyse zeigt, daß zur Berechnung einer solchen zeitaufgelösten Feuerrate über die Kehrwehrte der Interspike-Intervalle verschiedener Spike-Folgen gemittelt werden muss. Ausserdem wird in diesem Kapitel ein Maß für die Präzision von Spikes vorgestellt, welches direkt auf der Standardabweichung von Spikezeiten basiert.

B–6 Auditorische Rezeptorneurone von Heuschrecken

Auditorische Rezeptorneurone der Wanderheuschrecke eignen sich hervoragend zum Testen der vorgestellten Modelle, da sie den Schall-Stimulus direkt in eine Spike-Folge umsetzen, ohne dendritische Verarbeitung und dazwischengeschaltete Synapsen. Die Messung von Kennlinien, Latenzen und Phasen-Antwort-Kurven zeigt, daß die Rezeptorneurone Typ-I-Neurone sind. Die Untersuchung ihres Feuerraten-Adaptationsverhaltens zeigt, daß Adaptation in den Rezeptorzellen durch langsame Ionen-Ströme des Spike-Generators verursacht wird. Mit einem entsprechenden Modell kann die Feuerrate, welche durch Weiße-Rauschen-Stimuli und Heuschrecken-Gesängen hervorgerufen wird, mit großer Genauigkeit vorhergesagt werden. Adaptation in den Rezeptorzellen ist wichtig, um die Detektion von kurzen Pausen im Stimulus zu verbessern.

B–7 Intensitätsinvarianz eines auditorischen Interneurons

In diesem Kapitel werden die Adaptationsmodelle auf das AN1, ein primäres auditorisches Interneuron von Grillen, angewandt. Obwohl dieses Neuron die Antworten vieler Rezeptorzellen über Synapsen erhält, kann dessen Feuerrate immer noch gut mit den Modellen hervorgesagt werden. Der Hauptbeitrag zu der beobachteten Adaptation wird nicht durch das Interneuron selbst verursacht, sonder rührt sehr wahrscheinlich von den bereits adaptierenden Antworten der Rezeptorzellen her. Adaptation verschiebt die Kennlinie des AN1 von etwa 40 dB im unadaptierten Zustand bis hinauf zu ungefähr 80 dB. Dadurch wird die Antwort des AN1 weitestgehend unabängig von der mittleren Intensität des Stimulus.

B–8 Schlußfolgerung

Die hier vorgestellte Arbeit zeigt, daß es möglich ist, einfache universelle Modelle von Neuronen herzuleiten, die gleichzeitig für experimentelle als auch für theoretische Arbeiten nutzbar sind. Mit Hilfe dieser Modelle können die Informationsübertragungseigenschaften von Neuronen quantitativ untersucht werden. Dies wurde am Beispiel der auditorischen Rezeptorzellen von Heuschrecken und eines Interneurons der Grille gezeigt.

B–9 Leitfähigkeitsmodelle

Im Anhang werden die verschiedenen Leitfähigkeitsmodelle, die in dieser Arbeit als Modellneurone verwendet wurden, spezifiziert. Es sind dies das Hodgkin-Huxley Modell, das Connor Modell, eine vereinfachte Form des Traub-Miles Modells, sowie das Crook Modell.

Bibliography

L. F. Abbott & T. B. Kepler (1990): Model neurons: From Hodgkin-Huxley to Hopfield. In L. Garrido, editor, *Statistical Mechanics of Neural Networks*, pages 5–18. Springer-Verlag, Berlin.

A. Alonso & R. Klink (1993): Differential electroresponsiveness of stellate and pyramidal-like cells of medial entorhinal cortex layer II. *J. Neurophysiol.*, **70**(1): 128–141.

M. Avoli, G. G. Hwa, J.-C. Lacaille, A. Olivier, & J.-G. Villemure (1994): Electrophysiological and repetitive firing properties of neurons in the superficial/middle layers of the human neocortex maintained in vitro. *Exp. Brain Res*, **98**: 135–144.

F. Awiszus (1992): Reduction of a Hodgkin-Huxley-type model for a mammalian neuron at body temperature. *Biological Cybernetics*, **67**(5): 427–432.

F. Baldissera & B. Gustafsson (1974): Firing behaviour of a neurone model based on the after-hyperpolarization conductance time course and algebraical summation. adaptation and steady state firing. *Acta physiol. scand.*, **92**: 27–47.

F. Baldissera, B. Gustafsson, & F. Parmiggiani (1973): Adaptation in a simple neurone model compared to that of spinal motoneurones. *Brain Res*, **52**: 382–384.

E. Barkai & M. E. Hasselmo (1994): Modulation of the input/output function of rat piriform cortex pyramidal cells. *Journal of Neurophysiology*, **72**(2): 644–658.

M. J. Berridge (1998): Neuronal calcium signaling. *Neuron*, **21**: 13–26.

W. Bialek, F. Rieke, R. R. de Ruyter van Steveninck, & D. Warland (1991): Reading a neural code. *Science*, **252**: 1854–1857.

J. G. G. Borst & F. Helmchen (1998): Calcium influx during an action potential. *Methods in Enzymology*, **293**: 352–371.

G. Boyan (1999): Presynaptic contributions to response shape in an auditory neuron of the grasshopper. *J Comp Physiol A*, **184**: 279–294.

J. Breckow & M. Sippel (1985): Mechanics of the transduction of sound in the tympanal organ of adults and larvae of locusts. *J Comp Phys A*, **157**: 619–629.

D. Brown & P. Adams (1980): Muscarinic supression of a novel voltage-sensitive K^+ current in a vertebrate neuron. *Nature*, **183**: 673–676.

D. Brown & W. Griffith (1983): Calcium-activated outward current in voltage-clamped hippocampal neurones of the guinea-pig. *J Physiol*, **337**: 287–301.

B. Cartling (1995): A generalized neuronal activation function derived from ion-channel characteristics. *Network*, **6**: 389–401.

B. Cartling (1996)a: A low-dimensional, time resolved and adapting model neuron. *International Journal of Neural Systems*, **7**(3): 237–246.

B. Cartling (1996)b: Response characteristics of a low-dimensional model neuron. *Neural Computation*, **8**: 1643–1652.

C. C. Chow & J. A. White (1996): Spontaneous action potentials due to channel fluctuations. *Biophysical Journal (in press)*, .

K. S. Cole, R. Guttman, & F. Bezanilla (1970): Nerve membrane excitation without threshold. *Proceedings of the National Academy of Sciences*, **65**(4): 884–891.

J. A. Connor & C. Stevens (1971): Prediction of repetitive firing behaviour from voltage clamp data on an isolated neurone soma. *J. Physiol.*, **213**: 31–53.

J. A. Connor, D. Walter, & R. McKown (1977): Neural repetitive firing. *Biophysical Journal*, **18**: 81–102.

B. W. Connors & M. J. Gutnick (1990): Intinsic firing patterns of diverse neocortical neurons. *TINS*, **13**(3): 99–104.

F. Coro, M. Perez, E. Mora, D. Boada, W. E. Conner, M. V. Sanderford, & H. Avila (1998): Receptor cell habituation int the a_1 auditory receptor of four noctuid moths. *The Journal of Experimental Biology*, **201**: 2879–2890.

S. M. Crook, G. B. Ermentrout, & J. M. Bower (1998): Spike frequency adaptation affects the synchronization properties of networks of cortical oscillators. *Neural Computation*, **10**: 837–854.

P. Dayan & L. F. Abbott (2001): *Theoretical Neuroscience: Computational and Mathematical Modeling of Neural Systems.* MIT, Cambridge.

B. Delord, P. Baraduc, R. Costalat, Y. Burnod, & E. Guigon (2000): A model study of cellular short-term memory produced by slowly inactivating potassium conductances. *Journal of Computational Neuroscience*, **8**: 251–273.

J. M. Doolan & G. S. Pollack (1985): Phonotactic specifity of the cricket *Teleogryllus oceanicus*: intensity-dependent selectivity for temporal parameters of the stimulus. *J. Comp. Physiol. A*, **157**: 223–233.

Å. Edman, S. Gestrelius, & W. Grampp (1987)a: Analysis of gated membrane currents and mechanisms of firing control in the rapidly adapting lobster stretch receptor neurone. *J. Physiol.*, **384**: 649–669.

Å. Edman, S. Gestrelius, & W. Grampp (1987)b: Current activation by membrane hyperpolarization in the slowly adapting lobster stretch receptor neurone. *J. Physiol.*, **384**: 671–690.

J. Engel, H. A. Schultens, & D. Schild (1999): Small conductance potassium channels cause an activity-dependent spike frequency adaptation and make the transfer function of neurons logarithmic. *Biophysical Journal*, **76**: 1310–1319.

B. Ermentrout (1996): Type I membranes, phase resetting curves, and synchrony. *Neural Computation*, **8**: 979–1001.

B. Ermentrout (1998): Linearization of f*-I* curves by adaptation. *Neural Computation*, **10**: 1721–1729.

B. Ermentrout, M. Pascal, & B. Gutkin (2001): The effects of spike frequency adaptation and negative feedback on the synchronization of neural oscillators. *Neural Computation*, **13**: 1285–1310.

H. Esch, F. Huber, & D. W. Wohlers (1980): Primary auditory neurons in crickets: Physiology and central projections. *J. Comp. Physiol. A*, **137**: 27–38.

R. Fitzhugh (1961): Impulses and physiological states in theoretical models of nerve membrane. *Biophys. J.*, **1**: 445–466.

I. A. Fleidervish, A. Friedman, & M. J. Gutnick (1996): Slow inactivation of Na^+ current and slow cumulative spike adaptation in mouse and guinea-pig neocortical neurones in slices. *Journal of Physiology*, **493.1**: 83–97.

A. S. French (1989)a: Ouabain selectively affects the slow component of sensory adaptation in an insect mechanoreceptor. *Brain Research*, **504**: 112–114.

A. S. French (1989)b: Two components of rapid sensory adaptation in a cockroach mechanoreceptor neuron. *Journal of Neurophysiology*, **62**(3): 768–777.

A. S. French, U. Höger, S.-I. Sekizawa, & P. Torkkeli (2001): Frequency response functions and information capacities of paired spider mechanoreceptor neurons. *Biological Cybernetics*, **85**: 293–300.

A. S. French & M. J. Korenberg (1989): A nonlinear cascade model for action potential encoding in an insect sensory neuron. *Biophysical Journal*, **55**: 655–661.

D. Fricker & R. Miles (2000): EPSP amplification and the precision of spike timing in hippocampal neurons. *Neuron*, **28**: 559–569.

T. Gloveli, D. Schmitz, R. Empson, T. Dugladze, & U. Heinemann (1997): Morphological and electrophysiological characterization of layer III cells of the medial entorhinal cortex of the rat. *Neuroscience*, **77**(3): 629–648.

T. Gollisch, J. Benda, H. Schütze, & A. V. Herz (2001): Phenomenological model for sound-intensity coding in auditory receptor neurons of locusts. In *Proceedings of the 28th Gttingen Neurobiology Conference*, volume I, Stuttgart. Georg Thieme Verlag.

R. Granit, D. Kernell, & K. Shortess (1963): Quantitative aspects of repetitive firing of mammalian motoneurons, caused by injected currents. *J Physiol*, **168**: 911–931.

E. Gray (1960): The fine structure of the insect ear. *Philos. Trans. R. Soc. Lond. [Biol]*, **243**: 75–94.

J. Guckenheimer & I. Labouriau (1993): Bifurcation of the Hodgkin and Huxley equations: a new twist. *Bulletin of Mathematical Biology*, **55**(5): 937–952.

B. Gustafsson & H. Wigström (1981): Shape of frequency-current curves in CA1 pyramidal clls in the hippocampus. *Brain Research*, **223**: 417–421.

B. S. Gutkin & G. B. Ermentrout (1998): Dynamics of membrane excitability determine interspike interval variability: a link between spike generation mechanisms and cortical spike train statistics. *Neural Computation*, **10**(5): 1047–1065.

R. Guttman & R. Barnhill (1970): Oscillation and repetitive firing in squid axons. *The Journal of General Physiology*, **55**: 104–118.

H. Halex, W. Kaiser, & K. Kalmring (1988): Projection areas and branching patterns of the tympanal receptor cells in migratory locusts, *Locusta migratoria* and *Schistocerca gregaria*. *Cell Tissue Res.*, **253**: 517–528.

J. V. Halliwell & P. R. Adams (1982): Voltage-clamp analysis of muscarinic excitation in hippocampal neurons. *Brain Res*, **250**(1): 71–92.

B. N. Haman, T. E. Kennedy, A. Alonso, & D. G. Amaral (2000): Morphological and electrophysiological characteristics oflayer V neurons of the rat medial entorhinal cortex. *The Journal of Comparative Neurology*, **418**: 457–472.

D. Hansel, G. Mato, & C. Meunier (1993): Phase reduction and neural modeling. *Concepts in Neuroscience*, **4**(2): 193–210.

D. Hansel, G. Mato, & C. Meunier (1995): Synchrony in excitatory neural networks. *Neural Computation*, **7**: 307–337.

F. Helmchen, K. Imoto, & B. Sakmann (1996): Ca^{2+} buffering and action potential-evoked Ca^{2+} signaling in dendrites of pyramidal neurons. *Biophysical Journal*, **70**: 1069–1081.

R. Hennig (1988): Ascending auditory interneurons in the cricket *Teleogryllus commodus* (Walker): comparative physiology and direct connections with afferents. *J Comp Physiol A*, **163**: 135–143.

R. Hennig & T. Weber (1997): Filtering of temporal parameters of the calling song by cricket females of two closely related species: a behavioural analysis. *J Comp Phys A*, **180**: 621–630.

J. Hertz, A. Krogh, & R. G. Palmer (1991): *Introduction to the theory of neural computation.* Perseus Books.

K. Hill (1983)a: The physiology of locust auditory receptors: I. discrete depolarizations of receptor cells. *J. Comp. Physiol.*, **152**: 475–482.

K. Hill (1983)b: The physiology of locust auditory receptors: II. membrane potentials associated with the response of the receptor cell. *J. Comp. Physiol.*, **152**: 483–493.

B. Hille (1992): *Ionic membranes of excitable membranes.* Sinauer Associates, Sunderland, Mass., 2. edition.

J. Hindmarsh & R. Rose (1982): A model of the nerve impulse using two first order differential equations. *Nature*, **296**: 162–164.

J. Hindmarsh & R. Rose (1984): A model of neuronal bursting using three coupled first order differential equations. *Proc. R. Soc. Lond. B*, **221**: 87–102.

B. Hirschberg, J. Maylie, J. P. Adelman, & N. V. Marrion (1998): Gating of recombinant small-conductance Ca-activated K^+ channels by calcium. *J. Gen. Physiol.*, **111**: 565–581.

S. D. Hocherman, R. Werman, & Y. Yarom (1992): An analysis of the long-lasting after-hyperpolarization of guinea-pig vagal motoneurons. *Journal of Physiology*, **456**: 325–349.

A. Hodgkin (1948): The local electric changes associated with repetitive action in a non-medullated axon. *J. Physiol.*, **107**: 165–181.

A. Hodgkin & A. Huxley (1952): A quantitative description of membrane current and its application to conduction and excitation in nerve. *J. Physiol.*, **117**: 500–544.

J. R. Holt, D. P. Corey, & R. A. Eatock (1997): Mechanoelectrical transduction and adaptation in hair cells of the mouse utricle, a low-frequency vestibular organ. *The Journal of Neuroscience*, **17**(22): 8739–8748.

F. C. Hoppensteadt & E. M. Izhikevich (1997): *Weakly connected neural networks.* Applied Mathematical Sciences 126. Springer, New York.

G. Horseman & F. Huber (1994)a: Sound localisation in crickets I: Contralateral inhibition of an ascending auditory interneuron (AN1) in the cricket *Gryllus bimaculatus*. *J. Comp. Physiol. A*, **175**: 389–398.

G. Horseman & F. Huber (1994)b: Sound localisation in crickets II: Modelling the role of a simple neural network in the prothoracic ganglion. *J. Comp. Physiol. A*, **175**: 399–413.

K. Imaizumi & G. S. Pollack (2001): Neural representation of sound amplitude by functionally different auditory receptors in crickets. *J. Acoust. Soc. Am*, **109**(3): 1247–1260.

E. M. Izhikevich (2000): Neural excitability, spiking, and bursting. *International Journal of Bifurcation and Chaos*, **10**: 1171–1266.

K. Jacobs, B. Otte, & R. Lakes-Harlan (1999): Tympanal receptor cells of *schistocerca gregaria*: Correlation of soma positions and dendrite attachment sites, central projections and physiologies. *Journal of Experimental Zoology*, **283**: 270–285.

D. B. Jaffe, W. N. Ross, J. E. Lisman, N. Lasser-Ross, H. Miyakawa, & D. Johnston (1994): A model for dendritic Ca^{2+} accumulation in hippocampal pyramidal neurons based on fluorescence imaging measurements. *Journal of Neurophysiology*, **71**(3): 1065–1077.

E. Javel (1996): Long-term adaptation in cat auditory-nerve fiber responses. *J. Acoust. Soc. Am.*, **99**(2): 1040–1052.

D. Johnston & S. M.-S. Wu (1997): *Foundations of Cellular Neurophysiology.* MIT Press, Cambridge, Massachusetts.

A. R. Kay & R. K. Wong (1987): Calcium current activation kinetics in isolated pyramidal neurones of the CA1 region of the mature guinea-pig hippocampus. *J Physiol*, **392**: 603–16.

T. B. Kepler, L. F. Abbott, & E. Marder (1992): Reduction of conductance-based neuron models. *Biol. Cybern.*, **66**: 381–387.

D. Kernell (1965): The adaptation and the relation between discharge frequency and current strength of cat lumbosacral motoneurons stimulated by long-lasting injected currents. *Acta physiol. scand.*, **65**: 65–73.

W. M. Kistler, W. Gerstner, & J. L. van Hemmen (1997): Reduction of the Hodgkin-Huxley equations to a single-variable threshold model. *Neural Computation*, **9**: 1069–1100.

C. Koch (1999): *Biophysics of computation.* Oxford University Press, New York.

C. Koch, O. Bernander, & R. J. Douglas (1995): Do neurons have a voltage or a current threshold for action potential initiation?. *Journal of Computational Neuroscience*, **2**: 63–82.

M. Köhler, B. Hirschberg, C. Bond, J. Kinzie, N. Marrion, J. Maylie, & J. Adelman (1996): Small-conductance, calcium activated potassium channels from mammalian brain. *Science*, **273**: 1709–1714.

H. Koike, N. Mano, Y. Okada, & T. Oshima (1970): Repetitive impulses generated in fast and slow pyrammidal tract cells by intracellularly applied current steps. *Exp. Brain Res.*, **11**: 263–281.

J.-C. Lacaille & S. Williams (1990): Membrane properties of interneurons in stratum oriens-alveus of te CA1 region of rat hippocampus in vitro. *Neuroscience*, **36**(2): 349–359.

T. Lanthorn, J. Storm, & P. Andersen (1984): Current-to-frequency transduction in CA1 hippocampal pyramidal cells: Slow prepotentials dominate the primary range firing. *Exp. Brain Res*, **53**: 431–443.

Y.-H. Liu & X.-J. Wang (2001): Spike-frequency adaptation of a generalized leaky integrate-and-fire model neuron. *Journal of Computational Neuroscience*, **10**: 25–45.

G. Maccaferri, M. Mangoni, A. Lazzari, & D. DiFrancesco (1993): Properties of the hyperpolarization-activated current in rat hippocampal CA1 pyramidal cells. *Journal of Neurophysiology*, **69**: 2129–2136.

R. MacGregor & R. Oliver (1974): A model for repetitve firing in neurons. *Kybernetic*, **16**: 53–64.

C. K. Machens, M. B. Stemmler, P. Prinz, R. Krahe, & A. V. Herz (2001): Representation of acoustic communication signals by insect auditory receptor neurons. *The Journal of Neuroscience*, **21**(9): 3215–3227.

M. T. Madigan, J. M. Martinko, & J. Parker (1997): *Brock: Biology of Microorganisms.* Prentive Hall, eighth edition.

D. Madison, B. Lancaster, & R. Nicoll (1987): Voltage clamp analysis of cholinergic action in the hippocampus. *The Journal of Neuroscience*, **7**(3): 733–741.

D. Madison & R. Nicoll (1984): Control of the repetitive discharge of rat CA1 pyramidal neurones in vitro. *J. Physiol.*, **354**: 319–331.

Z. F. Mainen & T. J. Sejnowski (1995): Reliability of spike timing in neocortical neurons. *Science*, **268**: 1503–1506.

H. Markram, P. J. Helm, & B. Sakmann (1995): Dendritic calcium transients evoked by single back-propagating action potentials in rat neocortical pyramidal neurons. *Journal of Physiology*, **485.1**: 1–20.

N. V. Marrion (1997): Control of M-current. *Annu. Rev. Physiol.*, **59**: 483–504.

M. Martina & P. Jonas (1997): Functional differences in Na^+ channel gating between fast-spiking interneurones and principal neurones of rat hippocampus. *Journal of Physiology*, **505.3**: 593–603.

D. A. McCormick, B. W. Connors, J. W. Lighthall, & D. A. Prince (1985): Comparative electrophysiology of pyramidal and sparsley spiny stellate neurons of the neocortex. *Journal of Neurophysiology*, **54**(4): 782–806.

A. Michelsen (1966): Pitch discrimination in the locust ear: observations on single sende cells. *J. Insect Physiol.*, **12**: 1119–1131.

A. Michelsen (1971): The physiology of the locust ear: III. acoustical properties of the intact ear. *Z. vergl. Physiologie*, **71**: 102–128.

A. Michelsen & K. Rohrseitz (1995): Directional sound processing and interaural sound transmission in a small and a large grasshopper. *The Journal of Experimantal Biology*, **198**: 1817–1827.

M. Migliore, E. Cook, D. Jaffe, D. Turner, & D. Johnston (1995): Computer simulations of morphologically reconstructed CA3 hippocampal neurons. *Journal of Neurophysiology*, **73**(3): 1157–1168.

C. Morris & H. Lecar (1981): Voltage oscillations in the barnacle giant muscle fiber. *Biophys. J.*, **35**: 193–213.

R. Numann, W. Wadman, & R. Wong (1987): Outward currents of single hippocampal cells obtained from the adult guinea-pig. *J Physiol*, **393**: 331–53.

B. Oldfield & K. Hill (1986): Functional organization of insect auditory sensilla. *J. Comp. Physiol.*, **158**: 27–34.

B. Oldfield, H. Kleindienst, & F. Huber (1986): Physiology and tonotopic organization of auditory receptors in the cricket gryllus bimaculatus. *J. Comp. Physiol. A*, **159**: 457–464.

G. S. Pollack (1988): Selective attentiion in an insect auditory neuron. *The Journal of Neuroscience*, **8**(7): 2635–2639.

W. H. Press, S. A. Teukolsky, W. T. Vetterling, & B. P. Flannery (1992): *Numerical recipes in C.* Cambridge University Press, second edition.

N. Purali & B. Rydqvist (1998): Action potential and sodium current in the slowly and rapidly adapting stretch receptor neurons of the crayfish (astacus astacus). *J Neurophysiol*, **80**(4): 2121–2132.

A. D. Reyes & E. E. Fetz (1993): Two modes of interspike interval shortening by brief transient depolarizations in cat neocortical neurones. *Journal of Neurophysiology*, **69**(5): 1661–1672.

A. Ricci, Y.-C. Wu, & R. Fettiplace (1998): The endogenous calcium buffer and the time course of transducer adaptation in auditory hair cells. *The Journal of Neuroscience*, **18**(20): 8261–8277.

F. Rieke, D. Warland, R. de Ruyter van Steveninck, & W. Bialek (1997): *Spikes: exploring the neural code.* MIT Press, Cambridge.

J. Rinzel & B. Ermentrout (1998): Analysis of neural excitability and oscillations. In C. Koch & I. Segev, editors, *Methods in neural modeling.*, pages 251–292. MIT.

H. Römer (1976): Die Informationsverarbeitung tympanaler Rezeptorelemente von *Locusta migratoria* (Acrididae, Orthoptera). *Journal of Comparative Physiology*, **109**: 101–122.

H. Römer & M. Krusch (2000): A gain-control mechanism for processing of chorus sounds in the afferent auditory pathway of the bushcricket *Tettigonia viridissima* (Orthoptera; Tettigoniidae). *J Comp Phys A*, **186**: 181–191.

B. Ronacher & H. Römer (1985): Spike synchronization of tympanic receptor fibres in a grasshopper (*Chorthippus biguttulus* l., Acrididae). *J Comp Physiol A*, **157**: 631–642.

R. Rose & J. Hindmarsh (1989): The assembly of ionic currents in the thlamic neuron I. the three-dimensional model. *Proc. R. Soc. Lond. B*, **237**: 267–288.

P. Sah (1996): Ca^{2+}-activated K^+ currents in neurones: types, physiological roles and modulation. *TINS*, **19**(4): 150–154.

P. Sah & J. D. Clements (1999): Photolytic manipulation of $[Ca_{2+}]_i$ reveals slow kinetics of potassium channels underlying the afterhyperpolarization in hippocampal pyramidal neurons. *The Journal of Neuroscience*, **19**(10): 3657–3664.

M. V. Sanchez-Vives, L. G. Nowak, & D. A. McCormick (2000): Cellular mechanisms of long-lasting adaptation in visual cortical neurons *in vitro*. *The Journal of Neuroscience*, **20**(11): 4286–4299.

V. M. Sandler & J.-G. Barbara (1999): Calcium-induced calcium release contributes to action potential-evoked calcium transients in hippocampal CA1 pyramidal neurons. *The Journal of Neuroscience*, **19**(11): 4325–4336.

K. Schildberger & M. Hörner (1988): The function of auditory neurons in cricket phonotaxis. *J. Comp. Physiol. A*, **163**: 621–631.

J. Schiller, F. Helmchen, & B. Sakmann (1995): Spatial profile of dendritic calcium transients evoked by action potentials in rat neocortical pyramidal neurones. *Journal of Physiology*, **487.3**: 583–600.

P. Schiolten, O. N. Larsen, & A. Michelsen (1981): Machanical time resolution in some insect ears. *J. Comp. Physiol.*, **143**: 289–295.

J. Schnapf, B. Nunn, M. Meister, & D. Baylor (1990): Visual transduction in cones of the monkey *Macaca fascicularis*. *Journal of Physiology*, **427**: 681–713.

E. Schneidman, B. Freedman, & I. Segev (1998): Ion channel stochasticity may be critical in determining the reliability and precision of spike timing. *Neural Computation*, **10**: 1679–1703.

B. C. Schroeder, M. Hechenberger, F. Weinreich, C. Kubisch, & T. J. Jentsch (2000): KCNQ5, a novel potassium channel broadly expressed in brain, mediates M-type currents. *The Journal of Biological Chemistry*, **275**(31): 24089–24095.

E. D. Schutter & P. Smolen (1998): Calcium dynamics in large neuronal models. In C. Koch & I. Segev, editors, *Methods in neural modeling.*, pages 211–250. MIT.

H. Schütze (1995): Untersuchungen zu Nachentladungen der Antworten von Rezeptoren des komplexen Tibialisorgans von Laubheuschrecken (Tettigionidae). Master's thesis, Philipps Universität Marburg.

L. Schwabe, P. Adorján, & K. Obermayer (2001): Spike-frequency adaptation as a mechanism for dynamic coding in V1. *Neurocomputing*, **38–40**: 351–358.

P. Schwindt, W. Spain, R. Foehring, C. Stafstrom, M. Chubb, & W. Crill (1988): Multiple potassium conductances and their functions in neurons from cat sensorimotor cortex in vitro. *Journal of Neurophysiology*, **59**(2): 424–449.

P. E. Schwindt (1973): Membrane-potential trajectories underlying motoneuron rhythmic firing at high rates. *Journal of Neurophysiology*, **36**: 434–449.

I. Segev (1992): Single neurone models: oversimple, complex and reduced. *TINS*, **15**(11): 414–421.

I. Segev & R. E. Burke (1998): Compartmental models of complex neurons. In C. Koch & I. Segev, editors, *Methods in neural modeling.*, pages 93–136. MIT.

A. A. Selyanko & D. A. Brown (1999): M-channel gating and simulation. *Biophysical Journal*, **77**: 701–713.

M. N. Shadlen & W. T. Newsome (1998): The variable discharge of cortical neurons: Implications for connectivity, computation, and information coding. *The Journal of Neuroscience*, **18**(10): 3870–3896.

J. Shin, C. Koch, & R. Douglas (1999): Adaptive neural coding dependent on the time-varying statistics of the somatic input current. *Neural Computation*, **11**: 1893–1913.

M. Sippel & J. Breckow (1984): Non-monotonic response intensity characteristics of acoustic receptor cells of *Locusta migratoria*. *J Comp Physiol A*, **155**(1): 633–638.

D. Smetters (1999): Detecting action potentials in neuronal populations with calcium imaging. *Methods*, **18**(2): 215–221.

E. Sobel & D. Tank (1994): In vivo Ca^{2+} dynamics in a cricket auditory neuron: an example of chemical computation. *Science*, **263**: 823–826.

W. R. Softky & C. Koch (1993): The highly irregular firing of cortical cells is inconsistent with temporal integration of random EPSPs. *The Journal of Neuroscience*, **13**(1): 334–350.

C. E. Stafstrom, P. C. Schwindt, & W. E. Crill (1984): Repetitive firing in layer V neurons from cat neocortex in vitro. *Journal of Neurophysiology*, **52**(2): 264–277.

P. N. Steinmetz, A. Manwani, C. Koch, M. London, & I. Segev (2000): Subthreshold voltage noise due to channel fluctuations in active neuronal membranes. *Journal of Computational Neuroscience*, **9**: 133–148.

C. F. Stevens (1972): Inferences about membrane properties from electrical noise measurements. *Biophysical Journal*, **12**: 1028–1047.

C. F. Stevens & A. M. Zador (1998)a: Input synchrony and the irreguler firing of cortical neurons. *nature neuroscience*, **1**(3): 210–217.

C. F. Stevens & A. M. Zador (1998)b: Novel integrate-and-fire-like model of repetitive firing in cortical neurons. In *Proceedings of the 5th Joint Symposium on Neural Computation*.

M. Stocker, M. Krause, & P. Pedarzani (1999): An apamin-sensitive Ca^{2+}-activated K^+ current in hippocampal pyramidal neurons. *PNAS*, **96**: 4662–4667.

J. F. Storm (1988): Temporal integration by a slowly inactivating K^+ current in hippocampal neurons. *Nature*, **336**: 379–381.

J. F. Storm (1989): An after-hyperpolarization of medium duration in rat hippocampal pyramidal cells. *Journal of Physiology*, **409**: 171–190.

A. F. Strassberg & L. J. DeFelice (1993): Limitations of the Hodgkin-Huxley formalism: Effects of single channel kinetics on transmembrane voltage dynamics. *Neural Computation*, **5**: 843–855.

S. H. Strogatz (1994): *Nonlinear Dynamics and Chaos: With Applications in Physics, Biology, Chemistry, and Engineering.* Perseus Books, Cambridge.

A. Stumpner (1998): Picrotoxin eliminates frequency sensitivity of an auditory interneuron in a bushcricket. *J. Neurophysiol.*, **79**: 2408–2415.

N. Suga (1960): Peripheral mechanism of hearing in locust. *Jpn. J. Physiol.*, **10**: 533–546.

P. Torkkeli, S.-I. Sekizawa, & A. French (2001): Inactivation of voltage-activated Na^+ currents contributes to different adaptation properties of paired mechanosensory neurons. *Journal of Neurophysiology*, **85**: 1595–1602.

R. D. Traub, R. K. Wong, R. Miles, & H. Michelson (1991): A model of a CA3 hippocampal pyramidal neuron incorporating voltage-clamp data on intrinsic conductances. *Journal of Neurophysiology*, **66**(2): 635–650.

T. W. Troyer & K. D. Miller (1997): Physiological gain leads to high ISI variability in a simple model of a cortical regular spiking cell. *Neural Computation*, **9**(4): 733–745.

M. Tsodyks & H. Markram (1997): The neural code between neocortical pyramidal neurons depends on neurotransmitter release probability. *Proc. Natl. Acad. Sci. USA*, **94**: 719–723.

M. Tsodyks, K. Pawelzik, & H. Markram (1998): Neural networks with dynamic synapses. *Neural Computation*, **10**: 821–835.

M. van Rossum (2001): A novel spike distance. *Neural Computation*, **13**: 751–763.

R. R. R. van Steveninck, G. D. Lewen, S. P. Strong, R. Koberle, & W. Bialek (1997): Reproducibility and variability in neural spike trains. *Science*, **275**: 1805–1808.

D. von Helversen (1997): Acoustic communication and orientation in grasshoppers. In M. Lehrer, editor, *Orientation and Communication in Arthropods.*, pages 301–341. Birkhäuser Verlag, Basel/Switzerland.

H.-S. Wang, Z. Pan, W. Shi, B. S. Brown, R. S. Wymore, I. S. Cohen, J. E. Dixon, & D. McKinnon (1998): KCNQ2 and KCNQ3 potassium channel subunits: molecular correlates of the M-channel. *Science*, **282**: 1890–1893.

X.-J. Wang (1998): Calcium coding and adaptive temporal computation in cortical pyramidal neurons. *J. Neurophysiology*, **79**: 1549–1566.

Y. Wang, D. T. Chik, & Z. Wang (2000): Coherence resonance and noise-induced synchonization in globally coupled Hodgkin-Huxley neurens. *Physical Review E*, **61**(1): 740–746.

J. A. White, R. Klink, A. Alonso, & A. R. Kay (1998): Noise from voltage-gated ion channels may influence neuronal dynamics in the entorhinal cortex. *J. Neurophysiol.*, **80**: 262–269.

J. A. White, J. T. Rubinstein, & A. R. Kay (2000): Channel noise in neurons. *TINS*, **23**(3): 131–137.

X.-M. Xia, B. Fakler, A. Rivard, G. Wayman, T. Johnson-Pais, J. Keen, T. Ishii, B. Hirschberg, C. Bond, S. Lutsenko, J. Maylie, & J. Adelman (1998): Mechanisms of calcium gating in small-conductance calcium-activated potassium channels. *Nature*, **395**: 503–507.

W. M. Yamada, C. Koch, & P. R. Adams (1998): Multiple channels and calcium dynamics. In C. Koch & I. Segev, editors, *Methods in neural modeling.*, pages 137–170. MIT.

Acknowledgments

Without many inspiring discussions with people from the ITB, other neuroscientists from all over the world, and even people not familiar with the subjects of this thesis (especially my wife!) this work would not have been possible. Therefore I want to thank them all very much.

First of all I want to thank my supervisor *Andreas Herz* for the opportunity to work at the ITB, where he built up a great environment for research on challenging topics. His never ending good spirits, the hundreds of interesting researchers he invited for a talk and the workshops he organized, and the special support for the grasshopper group created an atmosphere which gave me the feeling to be right in the center of the computational-neuroscience community. His very critical and constructive comments on every kind of manuscript was a valuable help. Also his effort in teaching students was a great enrichment.

I am very grateful to all the grasshoppers. It was a great team. *Christian Machens* is the master of white-noise and information theory. He powered the OEL-project with many good ideas. *Hartmut Schütze*, our electrophysiologist, is a brilliant engineer. It was a great time to build up the electrophysiology setup together with him and to celebrate nice recordings in the lab. *Tim Gollisch* will explain the world. He enriched our group with his knowledge about theoretical physics as well as with his sophisticated experimental work on the transduction process in auditory receptor neurons. *Olga Kolesnikova* set the three-hours world record in intracellular recordings on locust auditory receptor neurons. And *Fredrik Edin* never stopped asking questions.

Special thanks to *Astrid Franz* for teaching me the secrets of intracellular recordings. *Matthias Hennig* supported my models with his knowledge and with a huge amount of data from the crickets. He also organized the traditional excursions to the Gülper See. *Rüdiger Krahe* helped me to find into the world of grasshoppers with his enthusiasm. I will follow him to the weakly electric fishes. *Bernd Ronacher* had always time for lots of helpful advice on grasshoppers. There are also *Gerald Pollack* and his student *Kazuo Imaizumi*, *Andreas Stumpner*, and *Dagmar* and *Otto von Helversen* who all enriched my work on grasshoppers with comments and advice.

Sincere thanks go to the excellent theoreticians in our lab. *Laurenz Wiskott* supported my work on chapter 3 with many valuable and long discussions. Playing Klezmer with him was also a great experience. *Raphael Ritz* knows everything and everybody in neuroscience.

For stimulating discussion I thank *Carsten Ebbinghaus* for his ideas on spike thresholds. *Gunter Kreck, Irina Erchova, Nikolai Axmacher* and *Roland Müller* complemented the discussion about class-I and class-II neurons with their work on hippocampal neurons. There were also *Roberto Fernandez Galan*, *Susanne Schreiber*, *Daniel Cremers*, and *Tobias Blaschke* with their interesting projects. The little project of *Stefanie Hertel* and *Ilka Diester* expanded my knowledge about noise in spiking neurons, and the Studienjahresar-

beit of *Wiebke Krambeck* keeps me thinking on class-I and class-II neurons.

My thanks go also to my other colleges from the ITB. *Christian Zemlin* was very interested in my work. *Arndt Telschow*, *Jürgen Neubauer*, and *Hanspeter Herzel* also helped in mathematical questions and were great soccer players. *Jennifer Davis* supplied us with her snacks and her wonderful cake. *Karin Winklhöfer*, *Stefan Beirer*, *Nils Blüthgen*, *Christian Waltermann*, *Thomas Förster*, and *Willi Schiegel* kept the ITB and the computers running. I thank *Matthias Flor* for his fast and reliable literature service.

I am very grateful to *Matthias Bethge* for his constructive attendance at my work about spike-frequency adaptation. With *Martin Nawrot* and *Jutta Kretzberg* I shared exciting discussions and cooperation.

I am also grateful to *Klaus Pawelzik* and *Martin Egelhaaf* for their interesting work, for inviting me to their labs, and writing the reports. *Paola Pedarzani* taught me the biological secrets about spike-frequency adaptation, and *Lorenzo Cingolani* provided me with his excellent recordings from hippocampal neurons that forced me to rethink my models. I want to thank *David MacAlpine* for his interest on my adaptation models, and his student *Nicole Harper*, who applied my ideas on the MSO in the auditory system of vertebrates.

I especially thank *Uta Grünert* for her patience, constant encouragement and love. She was always interested in my work and helped to improved the layout of my posters with her precise ideas.